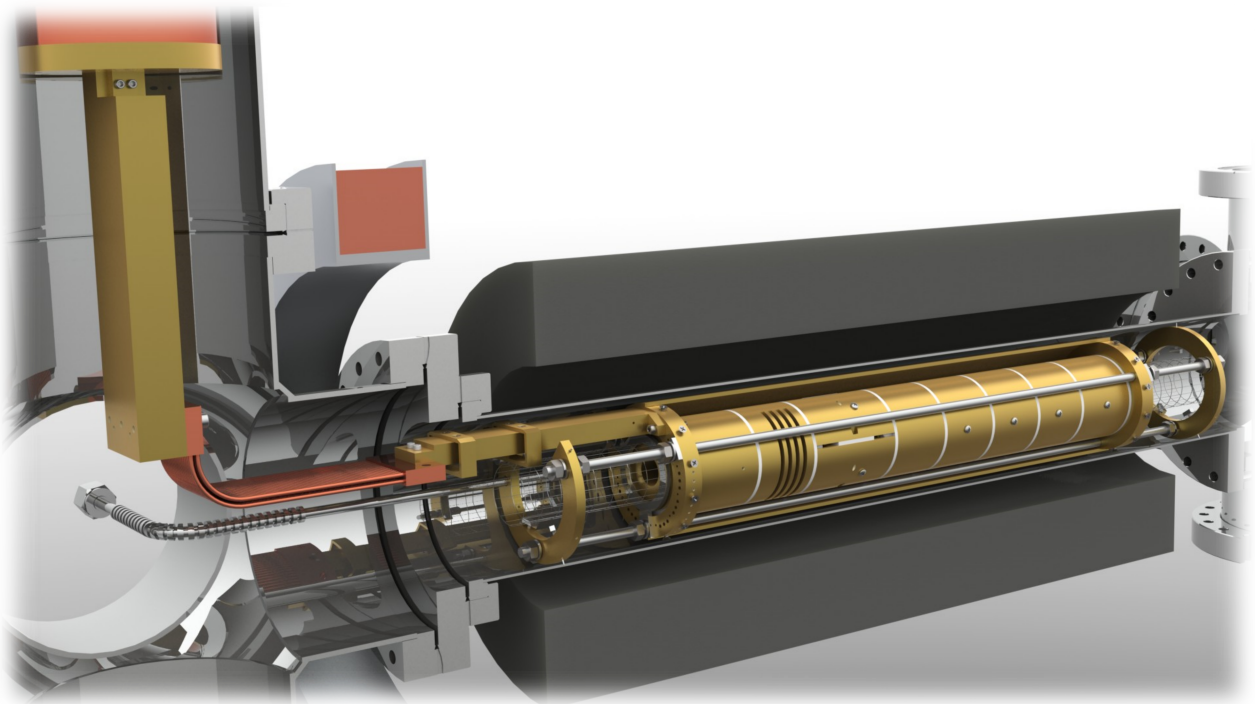


Trap-Based Beam Formation Mechanisms and the Development of an Ultra-High-Energy-Resolution Cryogenic Positron Beam

Michael Ryan Natisin
Ph.D. Thesis



Department of Physics
University of California, San Diego



2016

UNIVERSITY OF CALIFORNIA, SAN DIEGO

**Trap-Based Beam Formation Mechanisms and the Development of an
Ultra-High-Energy-Resolution Cryogenic Positron Beam**

A Dissertation submitted in partial satisfaction of the
requirements for the degree
Doctor of Philosophy

in

Physics

by

Michael Ryan Natisin

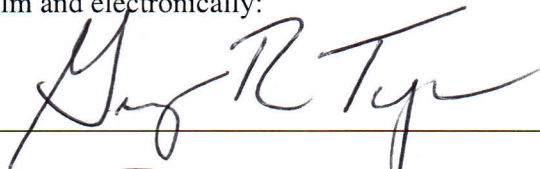
Committee in charge:

Professor Clifford M. Surko, Chair
Professor Robert E. Continetti
Professor Charles F. Driscoll
Professor Daniel H. Dubin
Professor George R. Tynan

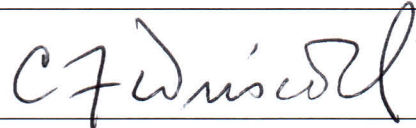
2016

Copyright
Michael Ryan Natisin, 2016
All rights reserved.

The Dissertation of Michael Ryan Natisin is approved, and
it is acceptable in quality and form for publication on micro-
film and electronically:











Chair

University of California, San Diego

2016

DEDICATION

To my three beautiful girls: Tenille, Solara, and Remi.

Your inspiration and support made this work possible.

TABLE OF CONTENTS

Signature Page	iii
Dedication	iv
Table of Contents	v
List of Figures	viii
List of Tables	xi
Acknowledgements	xii
Vita	xiv
Abstract of the Dissertation	xv
Chapter 1	1
Introduction	1
1.1 The discovery of the positron	2
1.2 Positron sources	2
1.3 Development of the modern positron beam	3
1.4 Outline of the dissertation	4
Chapter 2	6
Buffer gas trap based beams	6
2.1 Positron source and moderator	6
2.2 The buffer gas trap	9
2.3 Scattering and annihilation region	12
Chapter 3	14
Magnetized beam characterization: experimental and theoretical methods	14
3.1 Charged particle motion in a varying magnetic field	14
3.2 Analytical model of the energy distribution functions	15
3.3 Experimental measurement techniques	18
3.3.1 Energy distribution	18
3.3.2 Temporal distribution	22
3.3.3 Radial distribution	22
3.4 Characterization of the BGT-based beam	22
3.5 Factors affecting beam characterization	25
3.5.1 Magnetic field dependence	25
3.5.2 Positron number dependence	25
3.5.3 Beam reflections during measurement	27
3.5.4 Electronic noise	29
3.5.5 Potential perturbations	29

Chapter 4	Importance of high quality beams in atomic physics studies	32
	4.1 Positron annihilation on molecules	32
	4.1.1 Low-energy modes	34
	4.1.2 Infrared-inactive modes	34
	4.1.3 Multimode resonant annihilation	36
	4.1.4 Intramolecular vibrational redistribution	37
	4.2 Inelastic positron scattering	39
Chapter 5	Trap-based beam formation and optimization: simulations and experiments .	41
	5.1 Description of the simulation	42
	5.2 Results: Experimental geometry	43
	5.2.1 Dynamics during beam formation	43
	5.2.2 Dynamics during beam transport	46
	5.2.3 Comparisons and parameter studies	49
	5.3 Results: Generic geometry	55
	5.3.1 The generic Penning-Malmberg trap	55
	5.3.2 Beam formation regimes	55
	5.3.3 Optimization and parameter studies	59
	5.4 Summary: Optimal conditions for beam-formation	69
Chapter 6	Positron cooling through interactions with a molecular gas	72
	6.1 Model of positron thermalization with a molecular gas	73
	6.2 Description of the experiments	74
	6.3 Measurements and model predictions	77
	6.3.1 Carbon tetrafluoride	77
	6.3.2 Molecular nitrogen	78
	6.3.3 Carbon monoxide	80
	6.3.4 Positron cooling comparisons	84
	6.4 Model predictions using cryogenic buffer-gases	86
Chapter 7	The cryogenic beam-tailoring trap	89
	7.1 Overview of CBT design	89
	7.2 Experimental methods with the CBT	90
	7.3 Characterization of the CBT beam	94
	7.4 CBT beam results under various conditions	98
	7.5 CBT Utility in future research	100
	7.5.1 Positron annihilation on molecules	100
	7.5.2 Inelastic positron scattering	104
Chapter 8	Summary and concluding remarks	108
	8.1 Summary of the dissertation	108
	8.2 Future progress in positron beam development	109
	8.2.1 Alternative cooling techniques	109
	8.2.2 Alternative beam formation techniques	110
	8.2.3 A final obstacle to future progress	111
	8.3 Concluding remarks	112

Appendix A	Positron annihilation on molecules: experimental and theoretical methods . .	113
	A.1 Description of an annihilation experiment	113
	A.2 Calculating annihilation rates	114
	A.3 Theoretical overview	115
	A.3.1 Vibrational Feshbach resonances	115
	A.3.2 The Gribakin-Lee Model	116
	A.3.3 Multimode resonant annihilation	117
	A.3.4 Intramolecular vibrational energy redistribution	119
	A.3.5 The overall model	121
Appendix B	Measured annihilation spectra	122
Bibliography	146

LIST OF FIGURES

Figure 2.1:	Schematic diagram of the BGT-based beamline	6
Figure 2.2:	Schematic diagram of the source and moderator assembly	7
Figure 2.3:	Schematic diagram of the source and moderator region	8
Figure 2.4:	Schematic diagram of buffer gas trap and electrical potentials	10
Figure 2.5:	Typical BGT fill parameters	11
Figure 2.6:	Typical BGT ejection ramp function	12
Figure 2.7:	Measured magnetic field of BGT-based beamline	13
Figure 2.8:	Schematic diagram of annihilation region	13
Figure 3.1:	Schematic diagram of beam parallel energy distribution measurement	19
Figure 3.2:	Measured BGT beam cumulative parallel energy distribution	20
Figure 3.3:	Measured BGT beam cumulative total energy distribution	21
Figure 3.4:	Measured beam energy distributions obtained from the BGT	23
Figure 3.5:	Beam temporal and radial distributions obtained from the BGT	24
Figure 3.6:	BGT beam measurements at various magnetic field ratios	26
Figure 3.7:	BGT temporal spread dependence on positrons number	27
Figure 3.8:	Effect of beam reflections on measured parallel energy distribution	28
Figure 3.9:	Effect of electronic noise on measured parallel energy distribution	29
Figure 3.10:	Effect of potential perturbations on measured mean parallel energy	30
Figure 4.1:	Annihilation spectrum for methyl chloride	33
Figure 4.2:	Annihilation spectrum for 1,2-trans-dichloroethylene	35
Figure 4.3:	Annihilation spectrum for carbon tetrabromide	36
Figure 4.4:	Annihilation spectrum of 1,1-dichloroethylene	38
Figure 4.5:	Cross section for excitation of the ν_2 and ν_3 vibrational modes of CO_2	40
Figure 5.1:	BGT-based beamline simulation initial conditions	44
Figure 5.2:	Simulated BGT positron ejection	45
Figure 5.3:	Simulated BGT parameters during ejection	47
Figure 5.4:	BGT-based beamline simulation beam transport	48
Figure 5.5:	BGT distributions obtained from experiment and simulation	49
Figure 5.6:	Effect of ramp voltage on the BGT beam	51
Figure 5.7:	Effect of positron temperature on the BGT beam	54
Figure 5.8:	Generic PM trap simulation conditions	56
Figure 5.9:	Beam formation regimes	58
Figure 5.10:	Effect of ejection protocol on simulated beam	60
Figure 5.11:	Effect of positron temperature on simulated beam	62
Figure 5.12:	Effect of well depth on simulated beam	64
Figure 5.13:	Effect of well depth on beam formation	65
Figure 5.14:	Effect of exit-gate length on simulated beam	67
Figure 5.15:	Effect of well length on simulated beam	68
Figure 5.16:	Effect of beam formation on the shape of the beam distributions	70
Figure 6.1:	Example cutoffs used to obtain positron temperature	76
Figure 6.2:	Positron cooling using $0.51 \pm 0.05 \mu\text{torr}$ of CF_4 at 300 K	77

Figure 6.3:	Positron cooling using $15 \pm 1.5 \mu\text{torr}$ of N_2 at 300 K	79
Figure 6.4:	Positron cooling using $1.7 \pm 0.2 \mu\text{torr}$ of CO at 300 K	81
Figure 6.5:	Positron-CO cooling power per channel	83
Figure 6.6:	Positron cooling comparisons at 300 K	85
Figure 6.7:	Positron cooling comparisons at 50 K	86
Figure 6.8:	Positron cooling power at 50 K	87
Figure 7.1:	Schematic diagram of CBT-based beamline	90
Figure 7.2:	Schematic diagram of the CBT region	91
Figure 7.3:	Overview of CBT electrodes	92
Figure 7.4:	Schematic diagram of the CBT electrodes and potentials	93
Figure 7.5:	Measured magnetic field of CBT-based beamline	95
Figure 7.6:	Measured energy distributions obtained from CBT	96
Figure 7.7:	Measured time and radial distributions obtained from CBT	97
Figure 7.8:	Effect of ramp voltage on the CBT beam	99
Figure 7.9:	CBT temporal spread dependence on positrons number	100
Figure 7.10:	BGT vs. CBT annihilation spectrum for methanol	101
Figure 7.11:	BGT vs. CBT annihilation spectrum for 1,2-trans-dichloroethylene	102
Figure 7.12:	BGT vs. CBT annihilation spectrum for 1,1-dichloroethylene	103
Figure 7.13:	Simulated results of H_2 rotational scattering	105
Figure 7.14:	Simulated results of D_2 rotational scattering	106
Figure A.1:	Schematic diagram of the annihilation region	113
Figure A.2:	Overview of the vibrational Feshbach resonance	116
Figure A.3:	Multimode structure of 1,1-dichloroethylene	118
Figure A.4:	Example of IVR Analysis	120
Figure B.1:	Annihilation spectrum for 1,1-dichloroethylene	124
Figure B.2:	Annihilation spectrum for 1H-perfluorooctane	125
Figure B.3:	Annihilation spectrum for chloroform	126
Figure B.4:	Annihilation spectrum for chloroform-d	127
Figure B.5:	Annihilation spectrum for dichloromethane	128
Figure B.6:	Annihilation spectrum for dichloromethane-d2	129
Figure B.7:	Annihilation spectrum for ethanol	130
Figure B.8:	Annihilation spectrum for ethanol-d1	131
Figure B.9:	Annihilation spectrum for ethanol-d5	132
Figure B.10:	Annihilation spectrum for ethanol-d6	133
Figure B.11:	Annihilation spectrum for methanol	134
Figure B.12:	Annihilation spectrum for methanol-d1	135
Figure B.13:	Annihilation spectrum for methanol-d3	136
Figure B.14:	Annihilation spectrum for methanol-d4	137
Figure B.15:	Annihilation spectrum for 1,2-cis-dichloroethylene	138
Figure B.16:	Annihilation spectrum for 1,2-trans-dichloroethylene	139
Figure B.17:	Annihilation spectrum for bromoform	140
Figure B.18:	Annihilation spectrum for bromoform-d	141
Figure B.19:	Annihilation spectrum for tetrachloroethylene	142
Figure B.20:	Annihilation spectrum for trichloroethylene	143

Figure B.21: Annihilation spectrum for carbon tetrabromide	144
Figure B.22: Annihilation spectrum for carbon tetrachloride	145

LIST OF TABLES

Table 6.1:	Buffer gas cooling parameters	84
Table B.1:	Summary of molecular fit parameters	123
Table B.2:	Mode fit parameters for 1,1-dichloroethylene	124
Table B.3:	Mode fit parameters for 1H-perfluorooctane	125
Table B.4:	Mode fit parameters for chloroform	126
Table B.5:	Mode fit parameters for chloroform-d	127
Table B.6:	Mode fit parameters for dichloromethane	128
Table B.7:	Mode fit parameters for dichloromethane-d2	129
Table B.8:	Mode fit parameters for ethanol	130
Table B.9:	Mode fit parameters for ethanol-d1	131
Table B.10:	Mode fit parameters for ethanol-d5	132
Table B.11:	Mode fit parameters for ethanol-d6	133
Table B.12:	Mode fit parameters for methanol	134
Table B.13:	Mode fit parameters for methanol-d1	135
Table B.14:	Mode fit parameters for methanol-d3	136
Table B.15:	Mode fit parameters for methanol-d4	137
Table B.16:	Mode fit parameters for 1,2-cis-dichloroethylene	138
Table B.17:	Mode fit parameters for 1,2-trans-dichloroethylene	139
Table B.18:	Mode fit parameters for bromoform	140
Table B.19:	Mode fit parameters for bromoform-d	141
Table B.20:	Mode fit parameters for tetrachloroethylene	142
Table B.21:	Mode fit parameters for trichloroethylene	143
Table B.22:	Mode fit parameters for carbon tetrabromide	144
Table B.23:	Mode fit parameters for carbon tetrachloride	145

ACKNOWLEDGEMENTS

This dissertation is the product of years of hard work and dedication, and would not have been possible without the guidance and support of numerous people. To these people I am sincerely thankful for shaping this work, as well as myself, into something to be proud of.

I would like to start by thanking my adviser, Professor Cliff Surko, who is most responsible for transforming me into the scientist I hope to have become. Cliff has taught me how to put down the wrenches and welders from my previous life, and has instead replaced them with the less tangible tools required for the art of experimental physics (though wrenches have proven useful here as well, on occasion). One of the greatest advantages of having Cliff as an adviser is that our approaches to problem solving are so different. Where he rapidly comes to conclusions based on intuition and experience, I slowly make progress through detailed analysis. While these differences have made some aspects of research more challenging (cf. all publications), they have also provided me with countless examples of the benefits to such an approach. I hope to one day have a fraction of his talent in this regard.

I would also like to thank the current and former members of our group who have contributed to this work over the years. Of key importance was our group's resident research scientist, James Danielson. James not only contributed to all of the work described in this dissertation, but also provided the necessary assistance for smooth operation of the labs. In addition, due to his encyclopedic knowledge on all manner of eclectic topics, James' presence ensured that lunches were always long and full of conversation (even when we wished that they weren't). I would also like to thank our previous postdoc, Adric Jones, who was instrumental in getting me through my first year as a graduate student researcher. Adric taught me how to run the annihilation experiments, the beauty of MATLAB programming, and how Australians somehow never lose a game of pool.

I would like to give a special thank you to the master of all things technological; Gene Jerzewski. As our group's technical expert, Gene taught me how to troubleshoot and repair the complicated equipment that desperately and repeatedly attempted to bring all research to a grinding halt. Without a doubt, Gene made significant contributions to all of the research done by me, and many before me. Above all else, Gene was an incredibly kind individual who went out of his way to ensure the success and well-being of the students in the group. Although Gene passed away in 2015, his memory remains in the many people whose lives were improved, both professionally and personally, by his influence.

I would also like to acknowledge the help of our group assistant, Judy Winstead, for the excellent proof reading of all manner of manuscripts and abstracts. Additionally, I thank the members of my committee for their guidance during the final phases of this journey. In particular, I would like to thank Professor Fred Driscoll, without whom I likely would have never entered graduate school.

Finally, I would like to thank my wife Tenille, and my two beautiful daughters Solara and Remi, for all of the inspiration and support that they have given me throughout this process. It is through their encouragement that someone like me could have such ambition, and through their support that someone like me could actually achieve it.

Some of the work and discussion in Chapter 3 is taken from "Formation of buffer-gas-trap based positron beams," M. R. Natisin, J. R. Danielson and C. M. Surko, *Phys. Plasmas* **22**, 033501 (2015) [26]. The author of this dissertation led the research and was the principle author of the paper.

Some of the work and discussion in Chapter 5 is taken from "Formation of buffer-gas-trap based positron beams," M. R. Natisin, J. R. Danielson and C. M. Surko, *Phys. Plasmas* **22**, 033501 (2015) [26] and "Formation mechanisms and optimization of trap-based positron beams," M. R.

Natisin, J. R. Danielson and C. M. Surko, *Phys. Plasmas*, **23**, 023505 (2016) [27]. The author of this dissertation led the research and was the principle author of these papers.

Some of the work and discussion in Chapter 6 is taken from “Positron cooling by vibrational and rotational excitation of molecular gases,” M. R. Natisin, J. R. Danielson and C. M. Surko, *J. Phys. B* **47**, 225209 (2014) [25]. The author of this dissertation led the research and was the principle author of the paper.

Some of the work and discussion in Chapter 7 is taken from “A cryogenically cooled, ultra-high-energy-resolution, trap-based positron beam,” M. R. Natisin, J. R. Danielson and C. M. Surko, *App. Phys. Lett.* **108**, 024102 (2016)[70]. The author of this dissertation led the research and was the principle author of the paper.

This work was supported by the National Science Foundation, grants PHY 10-68023 and PHY 14-01794.

VITA

2010	B.S. in Physics <i>cum laude</i> , University of California, San Diego
2010-2011	Teaching Assistant, University of California, San Diego
2011-2016	Research Assistant, University of California, San Diego
2012	M.S. in Physics, University of California, San Diego
2013	C.Phil. in Physics, University of California, San Diego
2016	Ph.D. in Physics, University of California, San Diego

PUBLICATIONS

- M. R. Natisin, J. R. Danielson, and C. M. Surko, "Formation mechanisms and optimization of trap-based positron beams," *Phys. Plasmas*, **23**, 023505 (2016).
- M. R. Natisin, J. R. Danielson, and C. M. Surko, "A cryogenically cooled, ultra-high-energy-resolution, trap-based positron beam," *Appl. Phys. Lett.* **108**, 024102 (2016).
- M. R. Natisin, J. R. Danielson, and C. M. Surko, "Formation of buffer-gas-trap based positron beams," *Phys. Plasmas* **22**, 033501 (2015).
- M. R. Natisin, J. R. Danielson, and C. M. Surko, "Positron cooling by vibrational and rotational excitation of molecular gases," *J. Phys. B* **47**, 225209 (2014).
- M. R. Natisin, N. C. Hurst, J. R. Danielson, and C. M. Surko, "Recent progress in tailoring trap-based positron beams," *AIP Conf. Proc.* **1521**, 154-164 (2013).
- J. R. Danielson, A. C. L. Jones, M. R. Natisin, and C. M. Surko, "Modeling enhancement and suppression of vibrational Feshbach resonances in positron annihilation on molecules," *Phys. Rev. A* **88**, 062702 (2013).
- A. C. L. Jones, J. R. Danielson, M. R. Natisin, and C. M. Surko, "Role of vibrational dynamics in resonant positron annihilation on molecules," *Phys. Rev. Lett.* **110**, 223201 (2013).
- J. R. Danielson, A. C. L. Jones, M. R. Natisin, and C. M. Surko, "Comparisons of positron and electron binding to molecules," *Phys. Rev. Lett.* **109**, 113201 (2012).
- A. C. L. Jones, J. R. Danielson, M. R. Natisin, C. M. Surko and G. F. Gribakin, "Ubiquitous nature of multimode vibrational resonances in positron-molecule annihilation," *Phys. Rev. Lett.* **108**, 093201 (2012).
- J. R. Danielson, A. C. L. Jones, J. J. Gosselin, M. R. Natisin, and C. M. Surko, "Interplay between permanent dipole moments and polarizability in positron-molecule binding," *Phys. Rev. A* **85**, 022709 (2012).
- A. C. L. Jones, J. R. Danielson, J. J. Gosselin, M. R. Natisin, and C. M. Surko, "Positron binding to alcohol molecules," *New J. Phys.* **14**, 015006 (2012).

ABSTRACT OF THE DISSERTATION

**Trap-Based Beam Formation Mechanisms and the Development of an
Ultra-High-Energy-Resolution Cryogenic Positron Beam**

by

Michael Ryan Natisin

Doctor of Philosophy in Physics

University of California, San Diego, 2016

Professor Clifford M. Surko, Chair

The focus of this dissertation is the development of a positron beam with significantly improved energy resolution over any beam resolution previously available. While positron interactions with matter are important in a variety of contexts, the range of experimental data available regarding fundamental positron-matter interactions is severely limited as compared to analogous electron-matter processes. This difference is due largely to the difficulties encountered in creating positron beams with narrow energy spreads. Described here is a detailed investigation into the physical processes operative during positron cooling and beam formation in state-of-the-art, trap-based beam systems. These beams rely on buffer gas traps (BGTs), in which positrons are trapped and cooled to the ambient temperature (300 K) through interactions with a molecular gas, and subsequently ejected as a high resolution pulsed beam.

Experimental measurements, analytic models, and simulation results are used to understand the creation and characterization of these beams, with a focus on the mechanisms responsible for setting beam energy resolution. The information gained from these experimental and theoretical studies was then used to design, construct, and operate a next-generation high-energy-resolution beam system. In this new system, the pulsed beam from the BGT is magnetically guided into a new

apparatus which re-traps the positrons, cools them to 50 K, and re-emits them as a pulsed beam with superior beam characteristics.

Using these techniques, positron beams with total energy spreads as low as 6.9 meV FWHM are produced. This represents a factor of ~ 5 improvement over the previous state-of-the-art, making it the largest increase in positron beam energy resolution since the development of advanced moderator techniques in the early 1980's. These beams also have temporal spreads of $0.9 \mu\text{s}$ FWHM and radial spreads of 1 mm FWHM. This represents improvements by factors of ~ 2 and 10, respectively, over those of the previous beam resolutions. Future experimental applications of this new technology are also discussed.

Chapter 1

Introduction

The discovery of antimatter marked a stark change in the scientific perception of the universe we live in. As with any profound and unexpected discovery, it prompted many more questions than answers. Chief among them is a question which remains unsolved even today, more than three-quarters of a century later; if for every matter particle there exists a corresponding antiparticle, then why is the universe we live in composed almost entirely of matter? While the solution to this mystery has proven particularly illusive, its pursuit has led to many discoveries about the properties of antimatter which have elevated the topic to one of mainstream appeal.

One of the defining properties of antimatter is that an antiparticle has the same mass and spin as its matter counterpart, but opposite charge. Most notable is the changing of sign of the electric charge, resulting in electrically positive matter particles having electrically negative antiparticles, and vice versa. A key message repeatedly gleaned from the study of antimatter has been the surprising richness in new physics seen in the interactions between matter and antimatter, much of which could not have been anticipated based on this seemingly innocuous sign change.

Along with predicting a new class of particles, the discovery of antimatter also opened up new possibilities for particle interactions. Since the quantum numbers of antiparticles are additive inverses of their matter counterparts, their sum is identically zero. Therefore, according to the rules of quantum mechanics, the particle-antiparticle pair may be destroyed, and in its place any set of particles whose quantum numbers also sum to zero may be produced, provided energy and momentum are conserved. This new process is called annihilation, and has fueled much of the public interest in antimatter research.

At first glance, the presence of the annihilation process would appear to preclude other, more typical, scattering processes from occurring during particle-antiparticle interactions. Indeed, if this were the case their study would be comparatively dull. However, it is one of the amazing facets of nature that annihilation time scales are sufficiently slow compared to typical interaction time scales that the full richness of particle-particle interactions is still present within the particle-antiparticle analog, allowing for a diverse array of processes to occur before their ultimate fate is met.

The most well studied antimatter particle is the positron, which is the antiparticle to the electron. Since positrons are attracted to and distinguishable from electrons, a wide variety of electron-positron states are possible. These possibilities include such exotic states as a positron bound to an electron (positronium), or even bound states between positrons and matter molecules. It is this rich variety of interactions that continues to make positron research such a fascinating topic of study.

1.1 The discovery of the positron

The theoretical prediction and subsequent discovery of the positron was a unique event in the history of science in that, for the first time, a new particle was predicted theoretically in complete absence of empirical evidence. The first evidence for the existence of the positron, and indeed antimatter in general, was found by Paul Dirac in 1928 [1]. Here, Dirac developed for the first time a theoretical description of the electron which was consistent with both quantum mechanics and special relativity, and found that in this formulation electrons with negative energy states were predicted.

The following year, Dirac postulated that nearly all of these negative-energy states are occupied, or “filled up,” by the presence of normal electrons, and are therefore not observable [2]. The remaining unoccupied negative-energy states would then be “holes” in the distribution of negative-energy electron states, and so would behave as an ordinary particle of positive energy and electric charge, which he (mistakenly) postulated to be the proton. Dirac then took this idea further, describing the process of a positive energy electron transitioning to an unoccupied negative-energy state as “annihilation” between an electron and a proton, resulting in the emission of electromagnetic radiation [3].

Shortly after these ideas were presented, it became clear that the unoccupied holes in the negative-energy distribution were, in fact, not related to the proton. In 1931, Dirac abandoned this postulate and instead posited the existence of a new particle, unknown to experimental physics, which had the same mass but opposite charge compared to that of an electron [4]. He labeled this new particle the “anti-electron,” and went on to posit that protons would have their own unoccupied negative-energy states, similarly called “anti-protons.” In 1933 the first experimental evidence for antimatter was found when Carl Anderson examined the tracks left by cosmic rays through a cloud chamber, and showed that the results were consistent with a particle which had the same charge-to-mass ratio as the electron, but with a positive electric charge [5]. Anderson named this particle the positron.

1.2 Positron sources

While positrons are found in nature (e.g., cosmic rays, etc.), they are not available in sufficient quantities for typical experimental use. The two mechanisms useful in creating a high flux of positrons are pair production and radioactive decay. Pair production is the process of converting a photon into an electron-positron pair, and requires the photon to have greater energy than the combined rest mass of the two particles (2×511 keV). In contrast, radioactive decay produces positrons through beta-plus (β^+) decay, in which a proton is converted into a neutron, a positron, and an electron-neutrino. While pair production has been successfully used in large facilities such as reactors and linear accelerators (LINACs) to produce higher positrons fluxes than typically obtained through radioactive decay, radioisotopes offer a far simpler and more cost effective method of obtaining large numbers of positrons within a smaller experimental environment.

The first positron emitting radioisotope was discovered by Jean Frederic Joliot-Curie in 1934, when he found that ^{30}P emitted positrons with a decay half-life of approximately three minutes [6]. Since that time, many isotopes have been found to undergo β^+ decay. Short-lived positron-emitting isotopes such as ^{11}C , ^{13}N , ^{15}O , and ^{18}F have proven extremely useful for medical applications such as positron emission tomography (PET), while longer living isotopes such as ^{22}Na , ^{58}Co , ^{64}Cu and ^{68}Ge lie at the heart of many scientific applications.

Typical radioactive sources for scientific applications are able to produce as many as 10^9 positrons/s. Unfortunately, these positrons are emitted with a broad spread of energies, ranging anywhere from 0 up to ~ 500 keV. This large spread in energies makes the trapping and study of the emitted positrons prohibitively difficult. For this reason, advancements in the study of positron-matter interactions became (and in fact, still is) closely tied to advancements in the technology used to manipulate them.

1.3 Development of the modern positron beam

Positron beams, which have a population of positrons with a small spread in energies compared to their transport energy (i.e., mean energy along direction of propagation), have now become instrumental in the study of a wide variety of positron-matter interactions. The most important aspects of these beams for scientific applications are their production efficiency (i.e., the ratio of the number of positrons in the output beam to the number incident on the device used to create them) and their energy spread (although in the case of pulsed beams, pulse duration is also important). The significance of the production efficiency is due to the relative scarcity of positrons, while smaller energy spreads allow for measurements of narrower or more densely packed features, as well as enabling measurements of lower energy processes.

While artificial positron sources were discovered shortly after the discovery of the positron itself, it took several decades for the development of techniques which could produce relatively low energy positrons to be used for more precise scientific applications. The first significant advancement towards this end was the discovery by Costello *et al.* in 1972, where they found that when high energy positrons impinged upon a thin gold surface, a small fraction ($\sim 10^{-7} - 10^{-6}$) would thermalize with, and subsequently be ejected from, the surface with a low mean energy (~ 1 eV) and a low spread in energies (~ 1.5 eV FWHM) [7]. They correctly attributed this result to the presence of a negative positron-gold work function. By applying a bias voltage to the gold layer to increase the positron transport energy, they produced the first steady-state, low energy positron beam.

This process of implanting positrons into materials with negative work functions in order to have them re-emitted with lower energies is called “positron moderation,” and became crucial to the advancement of the study of positron-matter interactions. Moderators have since been developed using a variety of materials (e.g., metals, rare-gases, etc.) and configurations (i.e., transmission or reflection) to enable the production of positron beams with greater efficiency and/or decreased energy spread. Using these techniques, steady-state positron beams with efficiencies as high as $\sim 10^{-2}$ (neon moderator) [8] and energy spreads as low as ~ 0.1 eV (nickel moderator) [9] have been produced. The development of these beams enabled the study of a series of new positron-matter interactions, such as total collision cross sections [10], and even allowed the measurement of several inelastic processes, such as electronic excitation [11] and ionization [12].

The next major advancement in positron beam technology came as a significant departure from the steady-state moderated beams used previously. The key advancement which made this new technique possible was developed by Greaves and Surko in 1989, where they were able to trap and cool positrons in a modified Penning-Malmberg (PM) style trap [13]. Using electronic and rotational excitation of a molecular nitrogen buffer gas, positrons emitted from a tungsten moderator were trapped with an efficiency of 30% and cooled to the gas temperature of 300 K. This device is now known as a buffer gas trap (BGT). It has become the standard method of trapping and cooling positrons for scientific applications.

While the development of the BGT enabled the first studies of low temperature positron

plasmas, it also provided the foundation for producing positron beams with significantly improved characteristics over those available previously. In 1997, Surko *et al.* used the BGT, now paired with a neon moderator for greatly increased overall efficiency [14], to create a pulsed, magnetically guided positron beam with a total energy spread (i.e., both parallel and perpendicular to the magnetic field) of ~ 40 meV [15]. In addition to having an energy spread which was better than the best moderated beams available, the pulsed nature of the beam allowed temporally sensitive processes to be studied with minimal background noise. The development of BGT-based beams enabled the study of a wide variety of new processes, such as vibrational excitation cross sections [16], annihilation studies [17], material science [18] and antihydrogen [19].

Given the evolution of the positron beam described above, there are two significant statements to be made. One is that the evolution of positron science has been highly correlated with the evolution of positron technology. Each leap in beam technology brought new applications and new processes to be studied which were not possible with the technology that preceded it. The second statement is that leaps in positron beam technology have largely been serial in nature (i.e, the moderator takes the positrons emitted from the source as input, the BGT takes the beam emitted from the moderator as input, etc.), making the modern positron beamline a series of successive stages, each evolving the beam towards new capabilities. The work presented in this dissertation will continue with this tradition.

1.4 Outline of the dissertation

Chapter 2 describes the experimental apparatus used for the early research described in this dissertation. This includes a description of the source, moderator, buffer gas trap and beam measurement regions of the beamline.

Chapter 3 describes the experimental and theoretical techniques related to magnetized beam characterization. Here the motion of charged particles through axially varying magnetic fields is briefly summarized, followed by a discussion of an analytic model that describes the evolution of the various components of the positron beam energy distribution as the beam propagates through non-uniform magnetic fields. Experimental methods to measure the relevant beam distributions are described, and a detailed characterization of the BGT beam is given. Factors which affect the measurement of beam characteristics are also discussed.

Chapter 4 presents some of the motivation for the work discussed in this dissertation. The utility of advanced positron beams for atomic physics applications is discussed, with a focus on the current open questions which are difficult to investigate using current beam technology. Here examples of recent studies of positron annihilation on molecules are presented, such as contributions due to infrared-inactive and higher-order vibrational excitations, as well as the effects of intramolecular vibrational redistribution. Also discussed is current limitations in the study of positron scattering, such as the measurement of vibrational and rotational excitation cross sections.

In chapter 5, detailed simulations and experiments of trap-based beam-formation are described, with particular attention paid to the conditions in which optimal beam-energy resolution may be obtained. The chapter begins with a description of the simulation itself, followed by a discussion of the results obtained under simulation conditions which replicate those of the buffer gas trap apparatus. Here, a description of the dynamics undergone during beam-formation and transport is given, followed by a parameter study in which several important beam-formation parameters are varied, both in the simulation and experiment. The results are then compared to gain a better understanding of their effects on beam quality.

Also discussed in Chapter 5 are simulation results obtained using a generic Penning-Malmberg trap geometry. Here, the constraint of a specific experimental geometry is lifted, thus allowing for a wide variety of conditions and geometries to be examined. Using these results, the beam-formation process is examined in more detail. Of key significance is the identification of three distinct regimes in which beam-formation occurs, two of which yield significant improvements to beam quality over the regime which virtually all traps currently operate. Simulation results under a variety of conditions are also presented, and a discussion of the underlying processes responsible for setting beam quality are discussed. Chapter 5 ends with a summary of the conditions under which optimal beam quality may be obtained.

Chapter 6 describes experimental and theoretical results of positron cooling through vibrational and rotational excitation of a molecular gas. Here, measurements are described in which the positron temperature is measured as a function of time as they cool through interactions with a variety of buffer gases at 300 K. These measurements are then compared to the results obtained from a theoretical model of positron cooling through vibrational and/or rotational excitation under the Born approximation in order to extract estimates of the underlying cross sections. Using these estimated cross sections, the model is used to predict the effectiveness of using these buffer gases to cool the positrons to cryogenic temperatures.

Chapter 7 describes a newly built cryogenic beam system which takes the BGT-based beam as input and outputs a beam with significantly improved characteristics. The chapter begins with an overview of the design of the cryogenic beam-tailoring trap (CBT), which relies heavily on the detailed understanding of positron beam formation and cooling obtained from the studies discussed previously, followed by a description of the experimental methods and techniques used during operation of the CBT. Also presented is a detailed characterization of the CBT-based beam, which has a total energy resolution of 6.9 meV FWHM, which is a factor of ~ 5 improvement over the highest resolution positron beam available previously, while simultaneously having sub-microsecond temporal resolution and millimeter spatial resolution. The chapter ends with a discussion of some of the new applications and studies made available with this new positron beam technology.

Chapter 8 provides a summary of the new research detailed in this dissertation, as well as a discussion regarding the techniques and obstacles likely to play a role in future progress in positron beam technology. Here, alternative approaches to positron cooling and beam formation are described, and their respective advantages and disadvantages discussed. Also presented is a discussion regarding the most likely impediment to further improvements to beam energy resolutions.

The appendices describe experiments and analysis conducted by the author to study resonant positron annihilation on a variety of molecules. This work motivated the development of the new high-energy-resolution beam, which is the principal dissertation topic. Appendix A elucidates the roles of Feshbach resonances, multimode resonant annihilation, and intramolecular vibrational energy redistribution in determining annihilation rates. Appendix B contains an analysis of recently measured annihilation spectra including comparisons with the predictions of the theoretical models described in Appendix A.

Chapter 2

Buffer gas trap based beams

In this chapter, the experimental apparatus and techniques used for the atomic physics and early beam research is described. In the interest of brevity, the experimental details related to the atomic physics studies will be omitted, instead focusing on those pertaining to the positron beam studies. Experimental details related to the atomic physics studies are discussed in Appendix A, and details regarding the new positron trap are discussed in Chapter 7.

A schematic diagram of the buffer gas trap (BGT)-based beamline is shown in Fig. 2.1. Positrons emitted from a radioactive source are slowed to electron-volt energies using a moderator, then magnetically guided into a three-stage buffer gas trap. Within the BGT, the positrons are trapped and cooled to 300 K through interactions with a molecular gas, and subsequently ejected from the trap as a high resolution pulsed beam. The beam is then magnetically guided into a region in which the BGT beam may be characterized or used in a scattering or annihilation experiment. Each of the stages in this process will be described.

2.1 Positron source and moderator

The source and moderator assembly, developed by Greaves and Surko in 1997 [14], is shown schematically in Fig. 2.2. High energy positrons are emitted from a sodium-22 (^{22}Na) radioactive source through the process of beta-plus (β^+) decay. The ^{22}Na source was obtained commercially from iThemba Labs [20] and installed in 2012. It has a half-life of 2.6 years and an initial

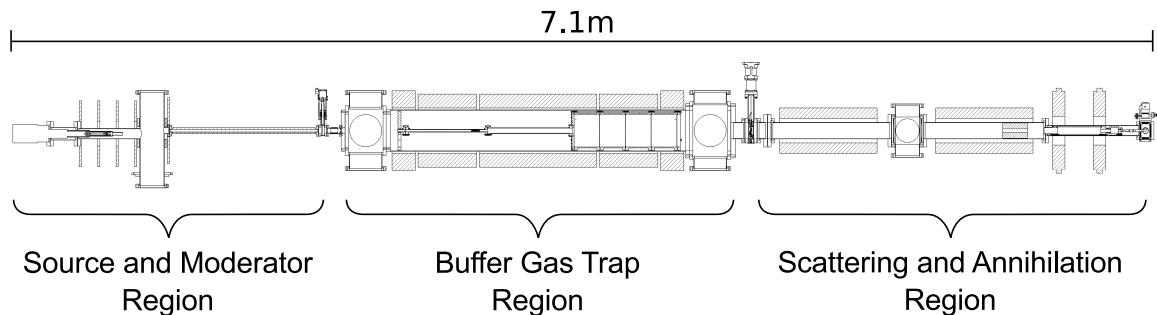


Figure 2.1: Schematic diagram of the BGT-based beamline.

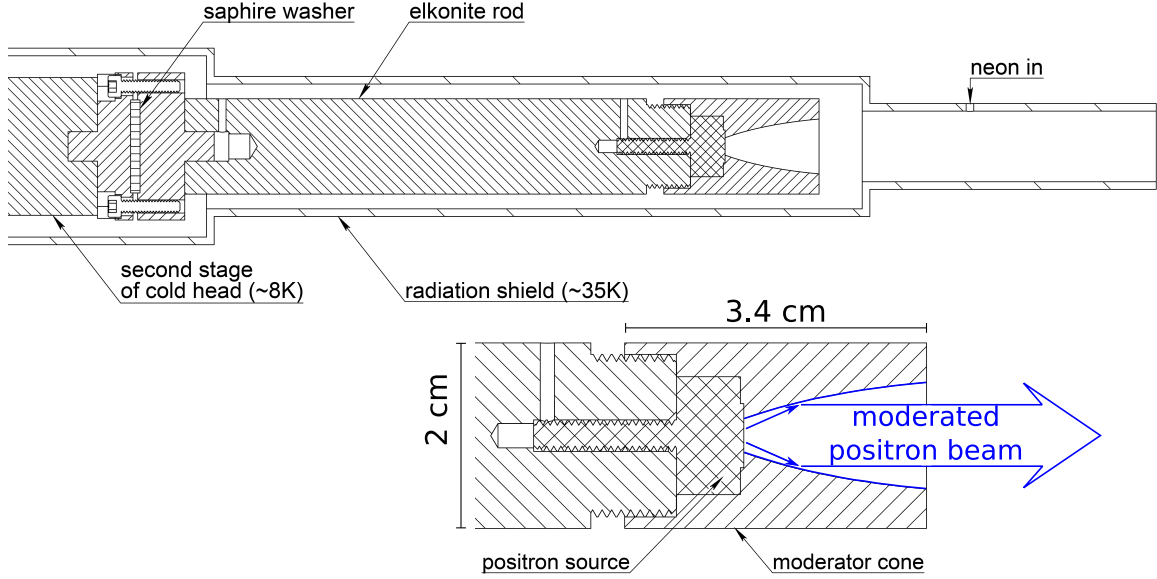


Figure 2.2: Schematic diagram of the source and moderator assembly. The ^{22}Na source and copper moderator cone are attached through an elkonite rod to the second-stage of a two-stage cryocooler which is maintained at 8 K. The assembly is surrounded by a radiation shield which is attached to the first-stage of the cryocooler and maintained at ~ 35 K.

activity of 50 mCi. The dominant decay process, which has a branching-ratio of 90.5%, is



where ν_e and γ represent an electron-neutrino and photon, respectively. For a 50 mCi source, $\sim 10^9$ positrons/s are emitted isotropically with energies ranging from 0 to ~ 500 keV.

In order to effectively use the positrons emitted from the source, their energies, and perhaps more importantly, their spread in energies, must be reduced. This is accomplished using a solid neon moderator. As seen in Fig. 2.2, a copper cone is fixed to the face of the radioactive source and attached via an elkonite rod to the second-stage of a two-stage cryocooler. Elkonite (a tungsten-copper alloy) is used for the cold-finger to reflect as much of the backward emitted positrons as possible, while maintaining good thermal and electrical conductivity. A PID temperature controller is used to adjust the current applied to a heater coil wrapped around the cold-head, allowing the cold-finger to be maintained at ~ 8 K. Neon gas is leaked into the source region and subsequently freezes onto the parabolic copper surface, forming a thin layer of solid neon.

As the high energy positrons are emitted from the source, they lose energy within the thin layer of solid neon through inelastic processes such as ionization, electron-hole creation and eventually phonon creation [8]. Since the positrons lose energy on time-scales short compared to the annihilation lifetime, a small fraction of the positrons diffuse to the surface of the neon layer and are re-emitted at electron-volt energies due to neon having a negative positron work function.

Various techniques for “growing” the neon moderator have been used [21]. Currently, the preferred technique involves doing multiple fast growth cycles rather than a single slow cycle. At the beginning of a growth cycle, the moderator cone temperature is raised to 50 K to remove the previous

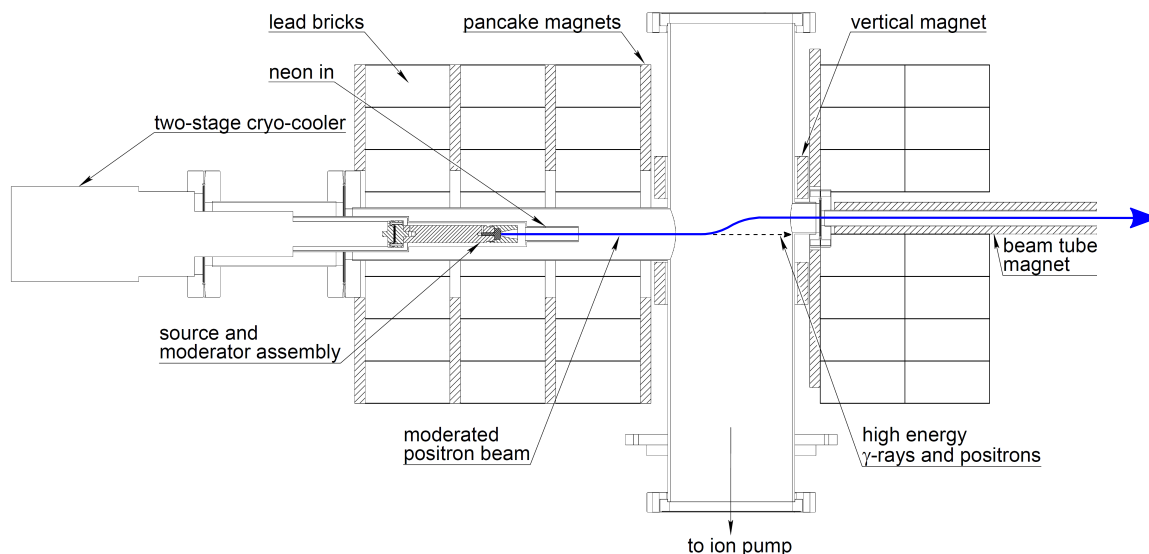


Figure 2.3: Schematic diagram of the source and moderator region. The source is vertically offset from the beam tube magnet to break line-of-sight with the downstream beamline. A series of pancake magnets generate a ~ 150 G magnetic field for radial confinement of the moderated positrons, while a vertical coil re-aligns the beam with the downstream axis.

moderator and any easily removed contaminants, after which the cone is once again cooled to 8 K and the region pumped down to the base-pressure of $\sim 1 \times 10^{-7}$ Torr. Neon gas is then introduced through a piezoelectric valve into the source region at a pressure of 3 mTorr for four minutes, at which time the neon valve is shut and the system is once-again pumped down to the base pressure. This growth cycle is typically repeated three times for a given moderator growth session.

Using the methods described above, as many as 6×10^6 positrons/s are emitted from the moderator. The efficiency and lifetime of the moderator can vary considerably between different growth cycles, however this variability is greatly reduced when multiple consecutive growths are performed. It is thought that these parameters are limited by the development of contaminants on the moderator surface, and that the multiple stripping and re-growing of the moderator helps by removing some of these contaminants.

A schematic diagram of the apparatus surrounding the source and moderator assembly is shown in Fig. 2.3. The assembly is installed within an ultra-high vacuum (UHV) chamber which is surrounded by lead bricks and vertically offset from the remaining beamline to prevent any high-energy positrons and gamma rays produced by the source from interfering with the experiment downstream. The moderator is biased to 30 V to eject the moderated positrons with a transport energy optimal for trapping in the buffer gas trap (described below). These positrons are then radially confined by the ~ 150 G magnetic field produced by a series of pancake coils, while a vertical coil perturbs the beam axis to coincide with that of the beam tube magnet and remaining beamline.

The moderated beam is a magnetized, steady-state flux of up to 6×10^6 positrons/s with a mean parallel energy of ~ 30 eV and an energy spread of ~ 2 eV FWHM. Due to the conical shape of the moderator cone, the positrons are preferentially emitted within a relatively narrow band of radii where positrons make a glancing angle with the Ne layer. This results in a moderated beam having

an annular cross section with an outer diameter of ~ 0.4 cm and an inner diameter of ~ 0.3 cm in a 150 G field. These positrons are then guided along the beam tube and into a three stage buffer gas trap.

2.2 The buffer gas trap

The buffer gas trap (BGT) was developed by Surko *et al.* in 1989 [13] and first used as a method of producing a pulsed positron beam in 1997 [15]. As seen in Fig. 2.4, the BGT consists of a series of cylindrically symmetric electrodes of varying inner diameters of 1.3 cm, 3.0 cm and 20.1 cm in the regions labeled Stage 1, Stage 2 and Stage 3, respectively. Molecular nitrogen is introduced into Stage 1, and by pumping on both sides of the trap with cryogenic pumps, the N_2 pressure drops by approximately an order of magnitude in each subsequent stage. Approximately $1 \mu\text{Torr}$ of CF_4 is added to the Stage 3 region to more rapidly thermalize the accumulated positrons (see Chapter 6). A series of magnetic coils surrounding the BGT generates an axial magnetic field which, for the experiments described here, varies from ~ 1 kG in Stage 2 to ~ 600 G in Stage 3 (cf. Fig. 2.7).

The BGT is operated in three phases; labeled fill, cool and eject, respectively. The electrostatic potential generated by the trapping electrodes during these phases are shown in Fig. 2.4. They were calculated using a finite-element method with the experimental trap geometry. During the fill phase, the voltages applied to the electrodes are such that the potential steps to consecutively lower values in each stage, with a barrier at the end of the trap to reflect the incident beam. As the moderated positrons enter on the high pressure side of the trap, they lose energy through inelastic collisions with the N_2 buffer gas and become trapped into the successively deeper potential wells until they are confined on the low pressure side of the trap.

The primary energy loss mechanism during the fill phase is electronic excitation, which removes ~ 8.6 eV with each collision [16]. However, the positronium formation threshold is 8.8 eV [22], which is a strong positron loss channel. Because of this, the potential steps heights are carefully set to maximize the electronic excitation cross section while minimizing the positronium (Ps) formation cross section through each region [23]. Molecular nitrogen is unique among atoms and molecules in having an electronic excitation at lower energies than the threshold for Ps formation [22]. This established it as the buffer gas of choice for positron trapping.

The number of positrons accumulated, and their respective trapping efficiency under typical conditions, are shown in Fig. 2.5. Here it is seen that the number of positrons accumulated is approximately linear with the duration of the fill until large fill times (> 6 s), above which the number of positrons increases more slowly and the trapping efficiency is reduced. It should be noted that while the trapping efficiency shown here is limited to $\sim 10\%$, efficiencies as high as 30% have been obtained [24]. Typical fill times for the applications discussed in this dissertation were 0.05–0.5 s, yielding $\sim 10^4$ – 10^5 accumulated positrons.

Once the desired number of positrons have been accumulated in stage 3, the cool phase is started. During the cool phase, the potential in stages 1 and 2 is raised to block the incident moderated beam from entering the trap, and the accumulated positrons are confined in a potential well determined by three sets of electrodes, labeled the trapping-gate, well, and exit-gate, respectively. The voltages applied to the trapping and exit-gate electrodes, V_T and V_E , provide axial confinement of the trapped positrons. The cool phase typically lasts ~ 0.1 s, during which time the positrons quickly thermalize with the N_2 and CF_4 buffer gases through rotational and vibrational excitation, respectively. This thermalization process has recently been studied in detail [25], and will be dis-

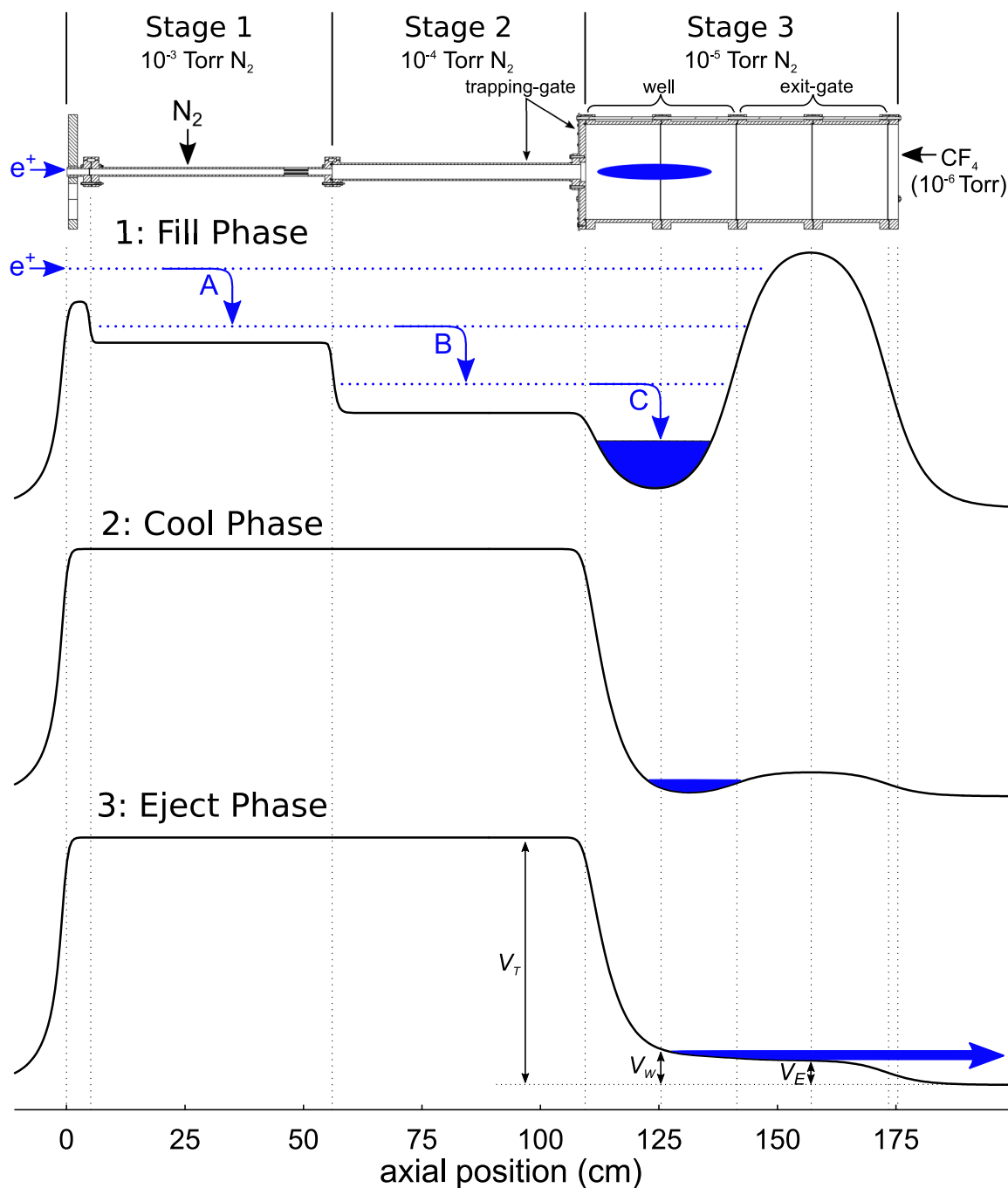


Figure 2.4: Schematic diagram of buffer gas trap and electrical potentials. (Top) three-stage buffer gas trap electrodes, and (bottom) calculated on-axis electrical potentials for each of the three phases of operation. Molecular nitrogen is introduced into stage 1 and maintained at a reduced pressure in subsequent stages, and CF_4 is introduced into stage 3. Arrows A, B and C indicate positron energy loss through electronic excitation of the N_2 the buffer gas. V_T , V_W and V_E represent voltages applied to the trapping-gate, well and exit-gate electrodes, respectively.

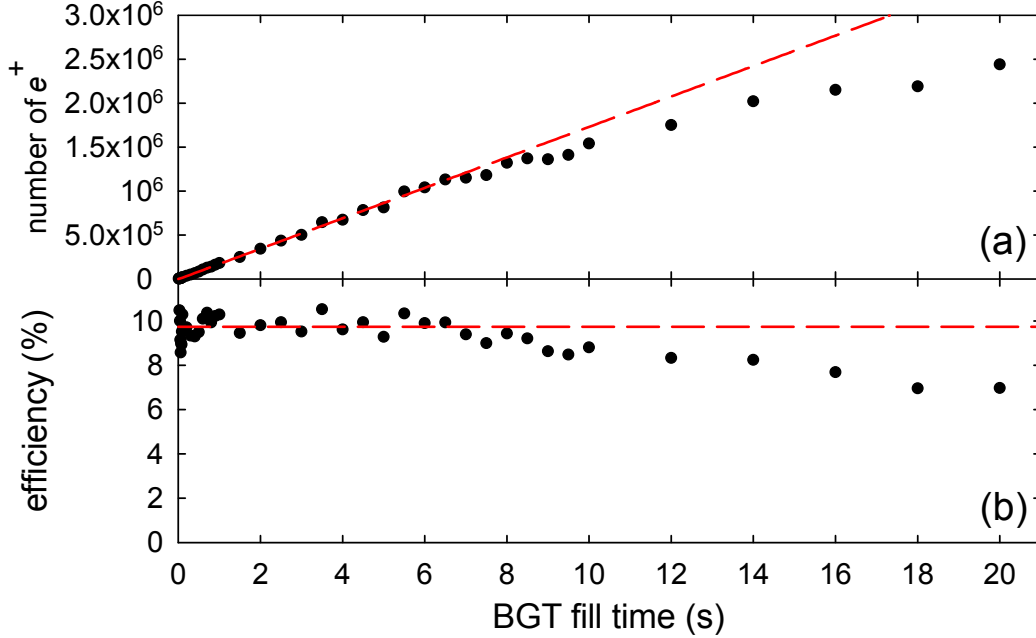


Figure 2.5: Typical BGT fill parameters, where (a) is the number of positrons accumulated and (b) is the trapping efficiency obtained using various BGT fill times. Red dashed lines show (a) linear fit to data and (b) mean trapping efficiency below ~ 6 s.

cussed in Chapter 6.

After the positrons have cooled to the ~ 300 K gas temperature, the eject phase is started. The voltages applied to the trapping and exit-gate electrodes are held fixed during ejection, with $V_E < V_T$ to give directionality to the ejected beam. The positrons are ejected from the trap by increasing the voltage applied to the well electrodes V_W , lifting the positrons over the exit-gate barrier and ejecting them as a pulsed beam.

An example of the voltage applied to the well electrode during a typical pulse is shown in Fig. 2.6. The well voltage is raised by setting a higher voltage on an amplifier. The resulting voltage ramp can be modeled as the resistance-capacitance (RC) response of an electrode to an applied voltage,

$$V_W(t) = (V_s - V_0) \left[1 - \exp\left(\frac{-t}{\tau_r}\right) \right] + V_0, \quad (2.2)$$

where V_s is the final steady-state voltage, V_0 is the initial (well) voltage and τ_r is the RC response time. The initial well voltage affects the initial well depth, with the time dependence of positron ejection set by V_s and τ_r . While the voltage on the electrode eventually reaches V_s , the positrons are ejected from the trap at $V_W \sim V_E$, which typically occurs before V_s is reached. Consequently, both V_s and τ_r affect how quickly the well voltage reaches V_E . Shown for comparison in Fig. 2.6 is the solution to Eq. (2.2) with $V_s = 3.5$ V, $V_0 = 0$ V and $\tau_r = 10$ μ s.

The transport energy of the resulting beam is largely set by the magnitude of the exit-gate barrier V_E , while the time-dependence of the voltage ramp impacts the energy and temporal resolution of the resulting beam, with slower (faster) ramps producing beams with smaller (larger) energy spreads but larger (smaller) temporal spreads. The processes undergone during beam formation and ejection have recently been studied in detail [26, 27], and will be discussed in Chapter 5.

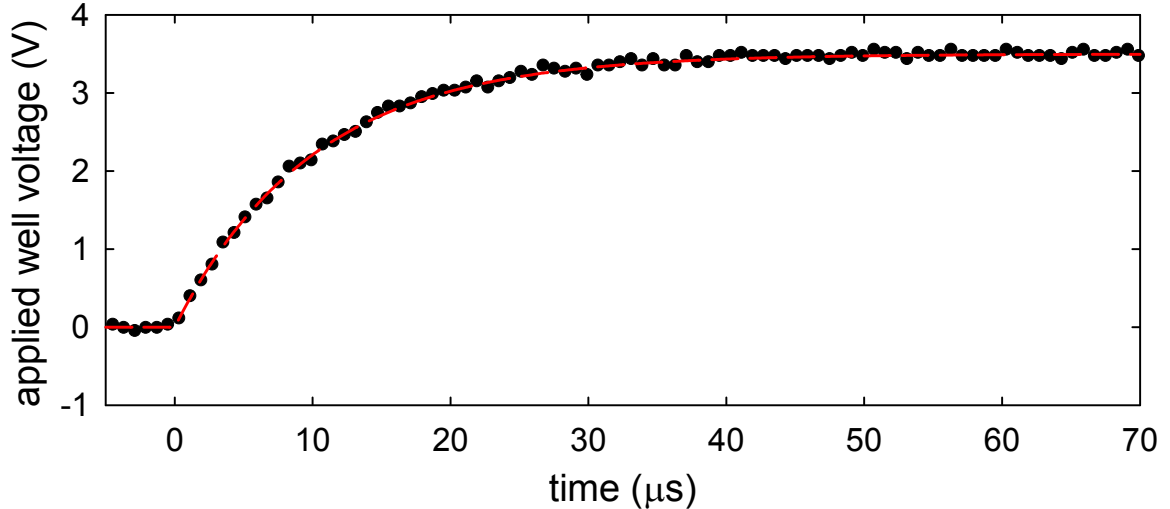


Figure 2.6: Typical BGT ejection ramp function. (•) applied voltage as measured on an oscilloscope, and (---) Eq. (2.2) with $V_s = 3.5$ V, $V_0 = 0$ V and $\tau_r = 10$ μ s.

The pulsed beam generated by the buffer gas trap has a total energy resolution as low as 35 meV FWHM [26], with a typical pulse duration of ~ 2 μ s and a beam diameter of ~ 1 cm in the 600 G magnetic field. These beam distributions will be described in Chapter 3, including discussion of the techniques used to measure and model them.

2.3 Scattering and annihilation region

A schematic diagram of the beamline from the third-stage of the BGT to the annihilation region is shown in Fig. 2.7. After the pulsed beam is emitted from the BGT, it is guided through two magnetic solenoids and into the annihilation region. In experiments prior to this dissertation work, the solenoids were used to perform scattering cross section measurements. They are now used for experiments involving a new positron trap, which is discussed in Chapter 7. For the beamline discussed in this chapter, they are simply used to transport the beam from the BGT to the annihilation region. Also shown are the measured on-axis magnetic fields in this region.

A schematic diagram of the annihilation region is shown in Fig. 2.8. The axial magnetic field is generated by a solenoid and a pair of Helmholtz coils providing a magnetic field which varies between $\sim 500 - 700$ G (as seen in Fig. 2.7), while a set of electrodes is used to adjust the incident positron beam energy. The electrodes are surrounded by lead shielding to isolate the annihilation region from any extrinsic gamma rays, while an adjustable cantilever leak valve and pressure baffle are used during an annihilation experiment to fill the region with the target molecular gas.

The annihilation cell consists of four electrodes. It was designed and used for the more recent positron annihilation experiments that are discussed in the appendices. The cell is used here to diagnose the BGT beam. The long cylindrical electrode centered in the Helmholtz coils is used as a retarding potential analyzer (RPA), which when combined with the collector and NaI gamma-ray detector, allows the parallel energy distribution of the BGT to be measured (as discussed in Chapter 3). The front and rear electrodes are used for additional beam diagnostics and during annihilation experiments.

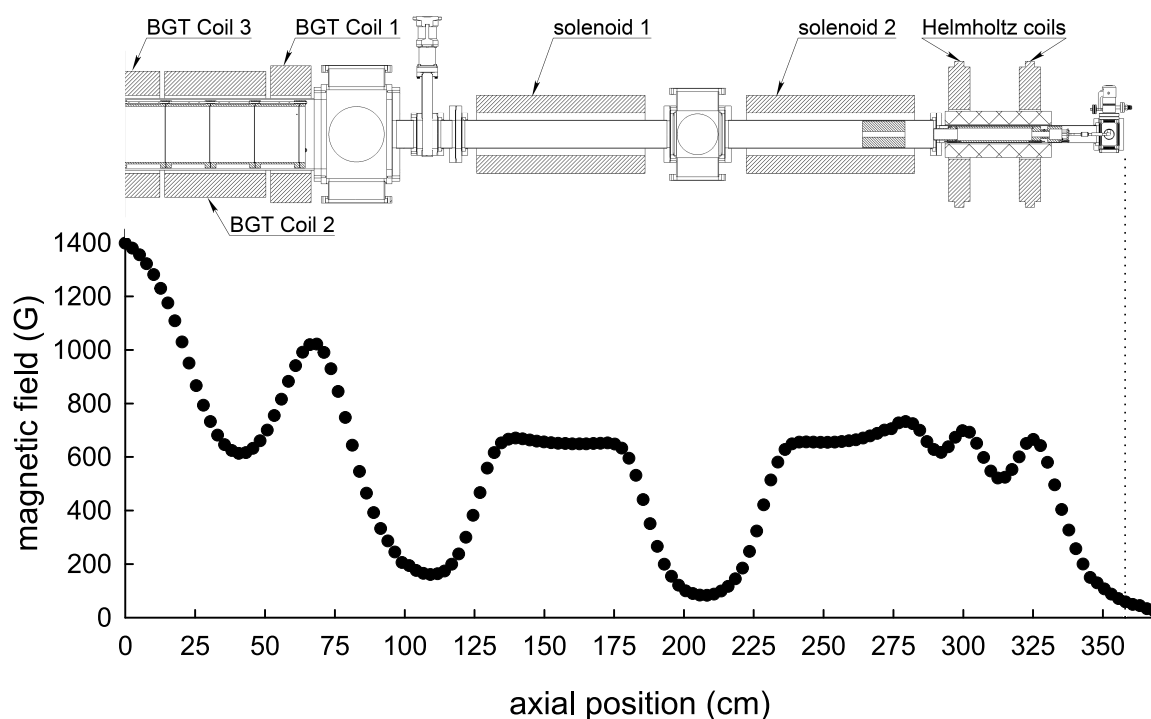


Figure 2.7: Measured magnetic field of BGT-based beamline. (Top) schematic diagram of the beamline from the third-stage of the BGT to the annihilation region, and (bottom) measured on-axis magnetic field under typical conditions over this region. Vertical dashed line indicates relative position of the end of the beamline.

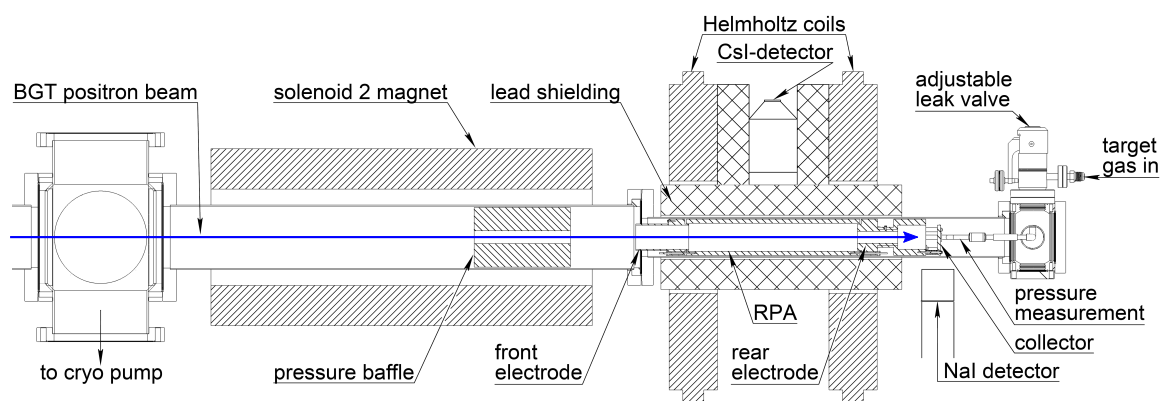


Figure 2.8: Schematic diagram of the annihilation region. A solenoidal magnet and a set of Helmholtz coils provide a magnetic field which varies between 500 and 700 G, while the front and rear electrodes, the RPA, collector and NaI gamma-ray detector are used to diagnose the BGT beam. The leak valve, pressure baffle, lead shielding, and CsI gamma-ray detector are used for positron annihilation studies.

Chapter 3

Magnetized beam characterization: experimental and theoretical methods

In this chapter the experimental and theoretical techniques used to characterize magnetized beams are described. An analytic model of the BGT-based beam energy distribution is presented that describes the evolution of the components of the energy distribution (i.e., both parallel and perpendicular to the magnetic field) as the beam propagates through regions of axially varying magnetic field. These expressions are expected to be useful in a number of applications, such as the analysis of trap-based beams and the study of elastic and inelastic scattering and annihilation processes [28, 29, 17].

The experimental techniques used to measure important aspects of the beam are also discussed. These characteristics include the energy, temporal, and radial distributions. The resulting distributions obtained from the BGT-based beamline (cf. Chapter 2) under optimal conditions are also discussed. These measurements represent the highest energy resolution positron beam available at the time. Many factors which limit the performance of these beams, either during their measurement or their production, are also discussed.

3.1 Charged particle motion in a varying magnetic field

The motion of a charged particle in a magnetic field may be decomposed into two components: the axial motion parallel to the magnetic field at velocity v_{\parallel} and the circular motion perpendicular to it at velocity v_{\perp} . The radius of the circular orbit is called the cyclotron radius,

$$r_c = \frac{mv_{\perp}}{|q|B}, \quad (3.1)$$

where m and q are the particle mass and electric charge, respectively, and B is the magnetic field strength¹.

For the beams described here, the particles experience changes in the magnetic field on time scales slow compared to the period of the cyclotron motion. This allows the orbits to be described using a guiding center approximation in which the centers of the cyclotron orbits follow the magnetic field lines. A key feature of the dynamics is that there are two invariant quantities: the

¹SI units are used here and throughout this dissertation.

positron orbital magnetic moment,

$$\mu = \frac{mv_{\perp}^2}{2B} = \frac{E_{\perp}}{B}, \quad (3.2)$$

and the positron total energy,

$$E_{tot} = E_{\parallel} + E_{\perp}, \quad (3.3)$$

where E_{\parallel} and E_{\perp} are the positron kinetic energy parallel and perpendicular to the magnetic field, respectively.

These two invariants of the system result in a coupling between the positron parallel and perpendicular motion as a particle travels through an axially varying magnetic field. The invariance of μ implies that, as the positron enters regions of lower (higher) magnetic field, its perpendicular energy decreases (increases) proportionally. Conservation of energy then requires that a decrease (increase) in perpendicular energy is accompanied by an increase (decrease) in the positron parallel energy.

Since the total energy of each positron is constant as it travels through regions of varying magnetic field, so also is the *distribution* of total energies within the beam. Therefore, the mean of the total energy distribution is constant under a changing magnetic field and may be written as

$$\bar{E}_{tot} = \bar{E}_{\parallel} + \bar{E}_{\perp}, \quad (3.4)$$

where \bar{E}_{\parallel} and \bar{E}_{\perp} are the mean of the parallel and perpendicular distributions, respectively. Additionally, since the total energy of each positron is the sum of its parallel and perpendicular energies, the standard deviation of the total energy distribution is also constant, and may be written as

$$\sigma_{tot} = \sqrt{\sigma_{\parallel}^2 + \sigma_{\perp}^2 + 2\sigma_{\parallel,\perp}}, \quad (3.5)$$

where σ_{\parallel} and σ_{\perp} are the standard deviations of the parallel and perpendicular distributions, respectively, and $\sigma_{\parallel,\perp}$ is their covariance. For the case of a uniform B the last term vanishes, while for non-uniform fields the contribution is non-zero.

3.2 Analytical model of the energy distribution functions

Since the total energy distribution of the beam includes both the parallel and perpendicular motions, it is most easily understood by separately analyzing the constituent components. The parallel energy distribution, as will be shown, is largely set by beam formation processes, such as the geometry of the trapping well and the speed at which the positrons are ejected. In contrast, because of the invariance of μ , the perpendicular distribution is independent of the manner in which the beam is formed, and depends only on the initial positron temperature and magnetic field.

Experimental measurements (described below) and simulations (see Chapter 5) show that under typical conditions the parallel energy distribution closely resembles a Gaussian distribution,

$$f(E_{\parallel}) = \frac{1}{\sqrt{2\pi}\sigma_0} \exp\left[-\frac{(E_{\parallel} - \bar{E}_0)^2}{2\sigma_0^2}\right], \quad (3.6)$$

where σ_0 and \bar{E}_0 are the standard deviation and mean of the Gaussian distribution. In contrast, because the beam formation does not affect the perpendicular energy distribution of the beam, it is

well described by a Maxwell-Boltzmann (MB) distribution in two dimensions,

$$f(E_{\perp}) = \frac{1}{k_b T_{\perp}} \exp\left[-\frac{E_{\perp}}{k_b T_{\perp}}\right], \quad (3.7)$$

where T_{\perp} represents the positron temperature perpendicular to the magnetic field, and k_b is Boltzmann's constant.

Since the positron energies parallel and perpendicular to the magnetic field are well described by Gaussian and MB distributions, respectively, the beam can be modeled using a joint energy distribution function, $f(E_{\parallel}, E_{\perp})$, which is the product of Eqs. (3.6) and (3.7) [30],

$$f(E_{\parallel}, E_{\perp}) = \frac{1}{\sqrt{2\pi}k_b T_{\perp} \sigma_0} \exp\left[-\frac{E_{\perp}}{k_b T_{\perp}} - \frac{(E_{\parallel} - \bar{E}_0)^2}{2\sigma_0^2}\right]. \quad (3.8)$$

The total energy distribution is obtained by convolving Eq. (3.8) with an energy conserving delta function, $\delta(E_{\parallel} + E_{\perp} - E_{tot})$, yielding an exponentially-modified Gaussian distribution (EMG),

$$f(E_{tot}) = \frac{1}{2k_b T_{\perp}} \exp\left[-\frac{1}{k_b T_{\perp}} \left(E_{tot} - \frac{\sigma_0^2}{2k_b T_{\perp}} - \bar{E}_0\right)\right] \operatorname{erfc}\left[-\frac{1}{\sqrt{2}\sigma_0} \left(E_{tot} - \frac{\sigma_0^2}{k_b T_{\perp}} - \bar{E}_0\right)\right]. \quad (3.9)$$

Here, erfc is the complementary error function, with \bar{E}_0 and σ_0 the mean and standard deviation of the Gaussian component of the distribution, as in Eq. (3.6). The mean and standard deviation of the overall total energy distribution are

$$\bar{E}_{tot} = \bar{E}_0 + k_b T_{\perp}, \quad (3.10)$$

and

$$\sigma_{tot} = \sqrt{\sigma_0^2 + (k_b T_{\perp})^2}. \quad (3.11)$$

The above characterization of the BGT-based beam is an accurate description of the beam provided the magnetic field is constant. However, when the beam propagates through an axially varying magnetic field, the parallel and perpendicular energy distributions become correlated due to conservation of the positron magnetic moment and energy, leading to a deviation from the simple Gaussian and MB distributions given above. The *total* energy distribution (Eq. (3.9)), however, is unaffected by the changing magnetic field.

The effects of an axially varying magnetic field on the positron energy distributions may be examined by re-writing the joint distribution function, $f(E_{\parallel}, E_{\perp})$, in a magnetic field different from the field in which the beam was formed. Using invariance of the positron magnetic moment and conservation of energy (Eqs. (3.2) and (3.3), respectively), the joint distribution function of the beam as it propagates through an axially varying magnetic field may be written as

$$f(E'_{\parallel}, E'_{\perp}) = \frac{1}{\sqrt{2\pi}Mk_b T_{\perp} \sigma_0} \exp\left[-\frac{E'_{\perp}}{Mk_b T_{\perp}} - \frac{(E'_{\parallel} - E'_{\perp}(1-M)/M - \bar{E}_0)^2}{2\sigma_0^2}\right], \quad (3.12)$$

where M is the magnetic field ratio (often called the ‘‘mirror ratio’’), defined as

$$M \equiv \frac{B'}{B_0}, \quad (3.13)$$

with B_0 and B' the magnetic fields where the beam is formed and measured, respectively. Note that in the limit $M \rightarrow 1$ (i.e., a uniform field), $f(E'_\parallel, E'_\perp) \rightarrow f(E_\parallel, E_\perp)$.

The parallel energy distribution of the beam as it propagates through an axially varying magnetic field can be obtained by integrating Eq. (3.12) over the perpendicular energy, yielding

$$f(E'_\parallel) = \frac{1}{2|\sigma_e|} \exp\left[-\frac{1}{\sigma_e} \left(E'_\parallel - \frac{\sigma_0^2}{2\sigma_e} - \bar{E}_0\right)\right] \operatorname{erfc}\left[-\frac{\operatorname{sgn}(1-M)}{\sqrt{2}\sigma_0} \left(E'_\parallel - \frac{\sigma_0^2}{\sigma_e} - \bar{E}_0\right)\right], \quad (3.14)$$

where

$$\sigma_e \equiv (1-M)k_b T_\perp \quad (3.15)$$

is the standard deviation of the exponential component of the distribution, and $\operatorname{sgn}(1-M)$ is +1 for $M < 1$, and -1 for $M > 1$. The mean and standard deviation of the magnetic field dependent parallel energy distribution can then be written as

$$\bar{E}'_\parallel = \bar{E}_0 + (1-M)k_b T_\perp \quad (3.16)$$

and

$$\sigma'_\parallel = \sqrt{\sigma_0^2 + (1-M)^2 (k_b T_\perp)^2}. \quad (3.17)$$

In general, the parallel energy distribution takes the form of an EMG distribution. In the limit that $M \rightarrow 1$ (uniform magnetic field), Eq. (3.14) simplifies to a Gaussian distribution, as described by Eq. (3.6). However, as the beam propagates through regions of lower ($M < 1$) or higher ($M > 1$) magnetic field, a tail develops on the right or left side of the distribution, respectively. Note that in the limit $M \rightarrow 0$, where all perpendicular energy has been transferred into the parallel, Eqs. (3.14)-(3.17) simplify to the total energy distribution given by Eqs. (3.9)-(3.11), and in this limit, $E'_\parallel \rightarrow E_{tot}$.

The perpendicular energy distribution in any magnetic field is obtained by integrating Eq. (3.12) over the parallel energy, giving

$$f(E'_\perp) = \frac{1}{2Mk_b T_\perp} \exp\left[-\frac{E'_\perp}{Mk_b T_\perp}\right] \operatorname{erfc}\left[\frac{1}{\sqrt{2}\sigma_0} \left(\frac{E'_\perp(M-1)}{M} - \bar{E}_0\right)\right]. \quad (3.18)$$

Here it is seen that perpendicular energy distribution is no longer strictly a MB distribution when the beam propagates through an axially varying magnetic field. However, provided $\bar{E}_0 \gg \sigma_0$ (i.e., a relatively cold beam), and $M \ll \bar{E}_0/E'_\perp$ (which ensures that no particles are reflected due to “magnetic mirroring”), Eq. (3.18) simplifies to a MB distribution characterized by a temperature $T'_\perp = MT_\perp$. Under these conditions, the mean and standard deviation of the perpendicular energy distribution may be written as

$$\bar{E}'_\perp = \sigma'_\perp = Mk_b T_\perp. \quad (3.19)$$

In the limit $M \rightarrow 1$, Eq. (3.18) reduces to Eq. (3.7). In the limit of $M \ll 1$, Eq. (3.18) is equivalent to a MB distribution with $T'_\perp \ll T_\perp$, indicating that perpendicular energy has been transferred into the parallel.

In summary, the complete beam energy distribution functions at any magnetic field (i.e., and M value) can be expressed analytically: Eq. (3.12) gives the joint distribution as a function of both E_\parallel and E_\perp , while the single-variable distributions for the total, parallel and perpendicular energies are given by Eqs. (3.9), (3.14) and (3.18), respectively.

3.3 Experimental measurement techniques

In this section the experimental techniques used to characterize the various beam distributions are described. This includes the beam energy distributions (parallel, perpendicular and total) as well as the temporal and radial distributions.

3.3.1 Energy distribution

As described above, the positron beam energy distribution may be separated into components both parallel and perpendicular to the magnetic field. Historically, the parallel component was typically all that was measured, though the perpendicular and total energy distributions may be measured or estimated using a variety of techniques.

Parallel energy distribution

The method used to measure the parallel energy distribution is shown schematically in Fig. 3.1. Positrons are ejected from the third stage of the BGT with a range of parallel energies. The beam is then passed through a retarding potential analyzer (RPA) electrode set to a potential V_A , allowing only particles with $E_{\parallel} > V_A$ to pass through and annihilate on a metal plate. The resulting gamma radiation is measured using a NaI detector, allowing the number of positrons with $E_{\parallel} > V_A$ to be counted. By repeating this procedure using a variety of RPA potentials, the average cumulative parallel energy distribution of the beam is constructed.

While the parallel energy distribution varies as the beam propagates through a non-uniform field, its value when measured in the same field in which it was produced ($M = 1$) is special in that, at that point, the parallel distribution is unaffected by the perpendicular distribution. This allows the effects due to beam formation to be examined more clearly.

An example of the measured cumulative parallel energy distribution at $M \approx 1$ is shown in Fig. 3.2. As discussed above, in a uniform magnetic field the parallel energy distribution closely resembles a Gaussian distribution. However, in general, it is described by an EMG distribution (Eq. (3.14)). For this reason, the data are fit to the cumulative distribution function of an EMG distribution. This allows the mean and standard deviation of the parallel energy distribution to be quantified, as defined as in Eqs. (3.16) and (3.17), respectively. The parallel energy distribution may then be obtained by either taking the negative-derivative of the fit cumulative distribution, or by inserting the obtained fit parameters into Eq. (3.14).

Perpendicular energy distribution

The perpendicular energy distribution cannot be measured directly using the techniques described above. However, both the mean and standard deviation of the perpendicular energy distribution may be calculated using a variety of techniques.

Using Eqs. (3.2) and (3.3), the mean perpendicular energy of the beam at magnetic field B may be found by measuring the parallel energy distribution at two different magnetic fields,

$$\bar{E}_{\perp}(B) = \frac{\bar{E}'_{\parallel} - \bar{E}_{\parallel}}{1 - B'/B}, \quad (3.20)$$

where \bar{E}_{\perp} and \bar{E}_{\parallel} are the mean perpendicular and parallel energies at the RPA, B is the magnetic field in the RPA region, and the primes distinguish parameters evaluated at the two different RPA

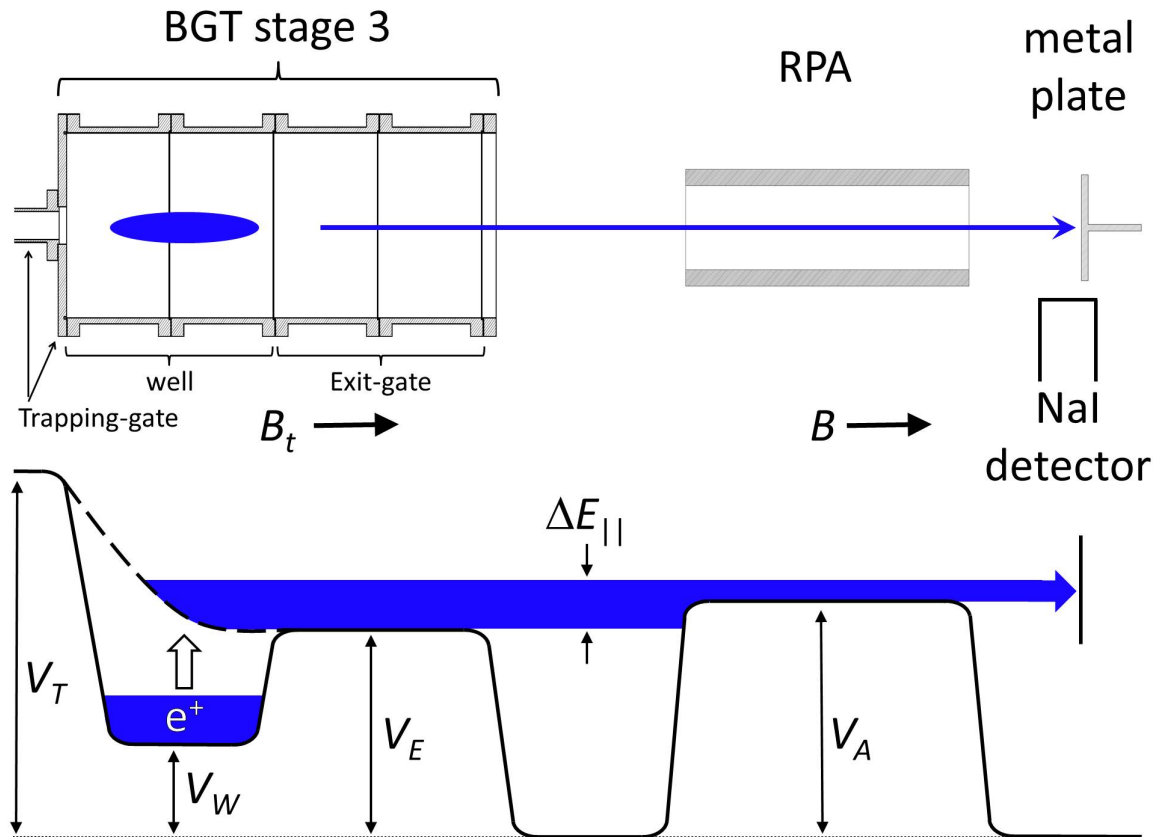


Figure 3.1: Schematic diagram of beam parallel energy distribution measurement. (Top) experimental components, and (bottom) potentials used to measure the beam parallel energy distribution. Cooled positrons are initially confined in a potential well in the third stage of the BGT. Then V_W is increased, lifting the positrons over V_E , thus forming a beam with parallel energy spread $\Delta E_{||}$. The beam is passed through an RPA, allowing only positrons with $E_{||} > V_A$ to annihilate on a metal plate and be counted using a NaI detector. This process is repeated at a variety of V_A values, allowing the cumulative parallel energy distribution to be constructed.

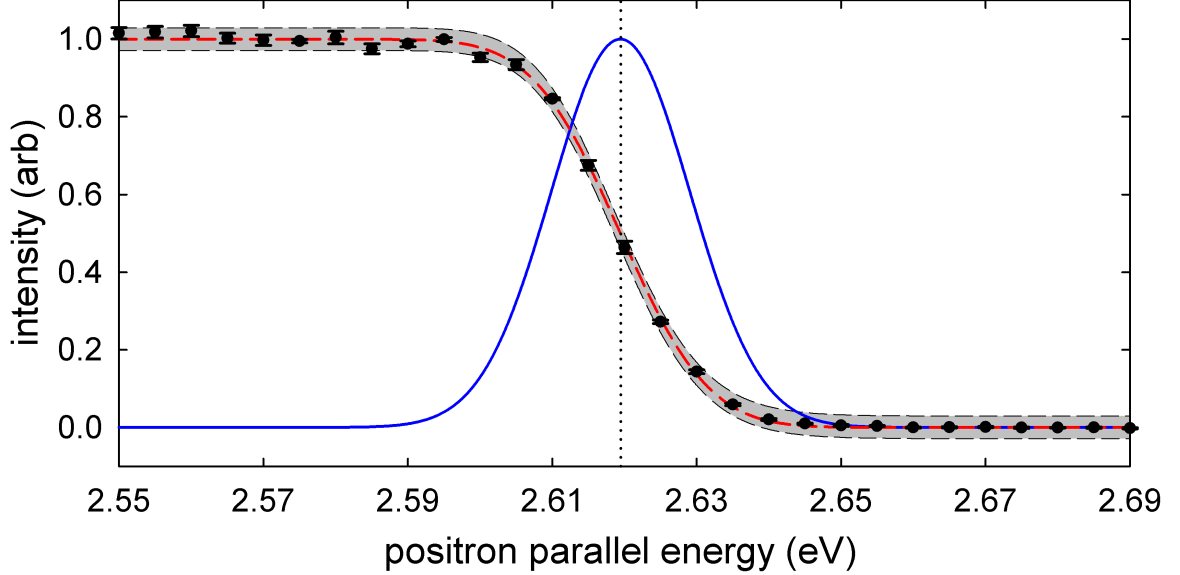


Figure 3.2: Measured BGT beam cumulative parallel energy distribution. (•) cumulative energy distribution measured at an RPA magnetic field of $B \sim 650$ G ($M \approx 1$), (— —) EMG fit to data, and (—) negative-derivative of fit, thus representing the parallel energy distribution. Shaded areas and vertical dotted lines show the 95 % confidence interval and mean parallel energy obtained from the fit, respectively.

magnetic fields. Equivalently, the mean perpendicular energy may be obtained by measuring the mean parallel energy at several magnetic fields and fitting the slope of the obtained curve,

$$\bar{E}_{\perp}(B) = -\frac{dE_{\parallel}}{dB}B. \quad (3.21)$$

Alternatively, the standard deviation of the perpendicular energy distribution may also be estimated. Re-organizing Eq. (3.5),

$$\sigma_{\perp}^2 = \sqrt{\sigma_{tot}^2 - \sigma_{\parallel}^2 - 2\sigma_{\parallel,\perp}}, \quad (3.22)$$

which allows calculation of σ_{\perp} by using the σ_{\parallel} and σ_{tot} obtained from direct measurements (see below), and assuming $\sigma_{\parallel,\perp} = 0$ (or using simulations to estimate its value). Additionally, since $\sigma_{\perp} = k_b T_{\perp}$ from Eq. (3.9), the perpendicular energy spread may be obtained from the EMG fit to the measured total energy distribution.

If the perpendicular energies are assumed to be Maxwell-Boltzmann (MB) distributed at all times, then $\bar{E}_{\perp} = \sigma_{\perp} \equiv k_b T_{\perp}$. This allows the perpendicular energy distribution to be fully characterized using any of the techniques described above. Measurements have shown that the values obtained using the methods described above are in excellent agreement with one-another [26], further supporting the assumption that the perpendicular energy distribution is MB distributed.

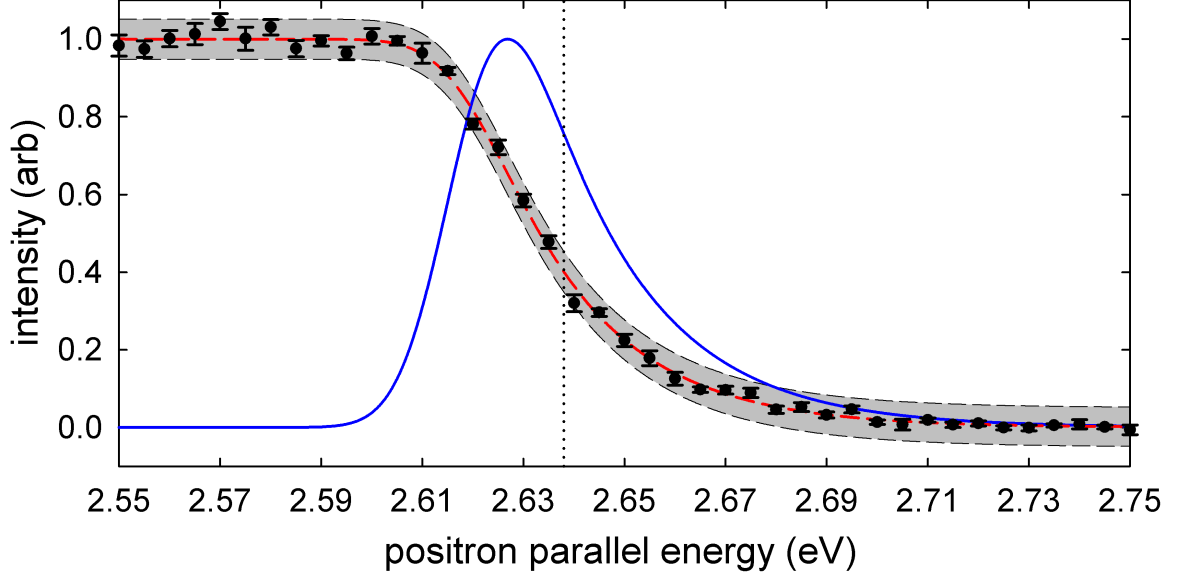


Figure 3.3: Measured BGT beam cumulative total energy distribution. (•) cumulative energy distribution measured at an RPA magnetic field of $B \sim 20$ G ($M \approx 1/30$), (—) EMG fit to data (Eq. (3.14)). Measurements are at a sufficiently reduced field to effectively provide a measure of the total energy distribution. Shaded areas and vertical dotted lines show the 95 % confidence interval and mean parallel energy obtained from the fit.

Total energy distribution

While the constituent components have been discussed separately, the approximate total energy distribution can be measured directly, and to a high degree of accuracy, using a variation of the technique for E_{\parallel} described above. As seen in Eq. (3.14), if the beam enters a region in which the magnetic field is small compared to that in the beam formation region, then the parallel energy distribution approaches the total energy distribution (i.e., the $M \rightarrow 0$ limit). Therefore, reducing the RPA magnetic field to a value small compared to the trapping magnetic field allows direct measurement of the total energy distribution using the RPA procedure described above.

Figure 3.3 shows the measured cumulative “parallel” energy distribution with the RPA in a magnetic field reduced by a factor of 30 from that of the BGT, thus effectively measuring the total energy distribution. As in the parallel energy case, the measured total energy distribution is fit to an EMG distribution, allowing the mean and standard deviation to be quantified, as defined in Eqs. (3.10) and (3.11), respectively. The data fit very well to the EMG distribution, providing further confirmation that the perpendicular energy distribution of the beam is indeed Maxwell-Boltzmann.

As an alternative to direct measurement, the total energy distribution can also be calculated using measurements of the parallel distribution at two different magnetic fields, thus enabling \bar{E}_{\perp} to be obtained using Eq. (3.20). The measured parallel distribution is then convolved with the MB characterized by $\bar{E}_{\perp} = k_b T_{\perp}$. The results obtained using this technique are in excellent agreement with direct measurements [26].

3.3.2 Temporal distribution

The temporal distribution of the beam can be measured by allowing positrons ejected from the BGT to impinge upon, and subsequently annihilate at, a metal plate. The emitted gamma radiation is then measured as a function of time using a NaI detector. The response time of the NaI detector and associated electronics corresponds to a full-width at half-maximum (FWHM) of $\sim 0.5 \mu\text{s}$, which provides a non-negligible contribution to measurements of temporal distributions near or below this value. The measurement is fit to a Gaussian distribution, allowing the spread of the time distribution to be quantified.

It should be noted that, due to the small but finite parallel energy spread of the beam, the temporal spread varies as the beam propagates. Under typical conditions, the first positrons ejected have energies comparable to the magnitude of the exit-gate barrier, while those emitted later are lifted by the rising potential well, thus releasing them with greater energies. This can result in a temporal spread which converges as the beam propagates, due to the higher energy positrons catching up to those with lower energy released before them. However, experiments show no appreciable change in the time spread over the lengths available ($\sim 3 \text{ m}$), and simulations (discussed in Chapter 5) show that, under the conditions described here, the beam is converging to a minimum $\sim 100 \text{ m}$ from the source. Thus, the time spread may be safely treated as a constant.

3.3.3 Radial distribution

The radial distribution is measured by accelerating the beam to -10 kV and allowing it to impinge on a phosphor screen. The phosphor emits light proportional to the number of particles impinging upon it. When measured using a CCD camera, this allows the number of particles at a given radial and azimuthal position to be counted. Using these data, the center of the beam is determined by finding the peak light integrated along both the horizontal and vertical directions, and the average radial distribution is obtained by averaging the data azimuthally around the center point.

3.4 Characterization of the BGT-based beam

An example of the measured parallel, perpendicular and total energy distributions obtained from the BGT are shown in Fig. 3.4. Spreads in the energy distributions are characterized by either their standard deviations or full-width at half-maximum (FWHM). The standard deviation provides a better representation of the physics of the beam distributions, while the FWHM correlates better with the effective resolving-power of the beam. For the special case of a Gaussian distribution, the FWHM, ΔE , is related to the standard deviation σ by $\Delta E = 2\sqrt{2\ln 2}\sigma$. However in the general case of an EMG distribution, no such simple relationship exists.

As seen in Fig. 3.4 (a), the parallel energy distribution is well described by a Gaussian distribution with a standard deviation of $\sigma_{\parallel} = 9.7 \text{ meV}$ ($\Delta E_{\parallel} = 22.8 \text{ meV}$ FWHM), while the perpendicular energy distribution shown in Fig. 3.4 (b) is an assumed Maxwell-Boltzmann with $\bar{E}_{\perp} = \sigma_{\perp} = 19.1 \text{ meV}$. The total energy distribution is shown in Fig. 3.4 (c), and is EMG distributed with $\sigma_{tot} = 22.5 \text{ meV}$ ($\Delta E_{tot} = 33 \text{ meV}$ FWHM). This represents the best total energy resolution for a positron beam produced at that time.

While the energy distribution of the positron beam is typically the most important characteristic with regards to experimental utility, other aspects of the beam are also important. The measured temporal and radial distributions, obtained from the BGT under the same conditions as those shown

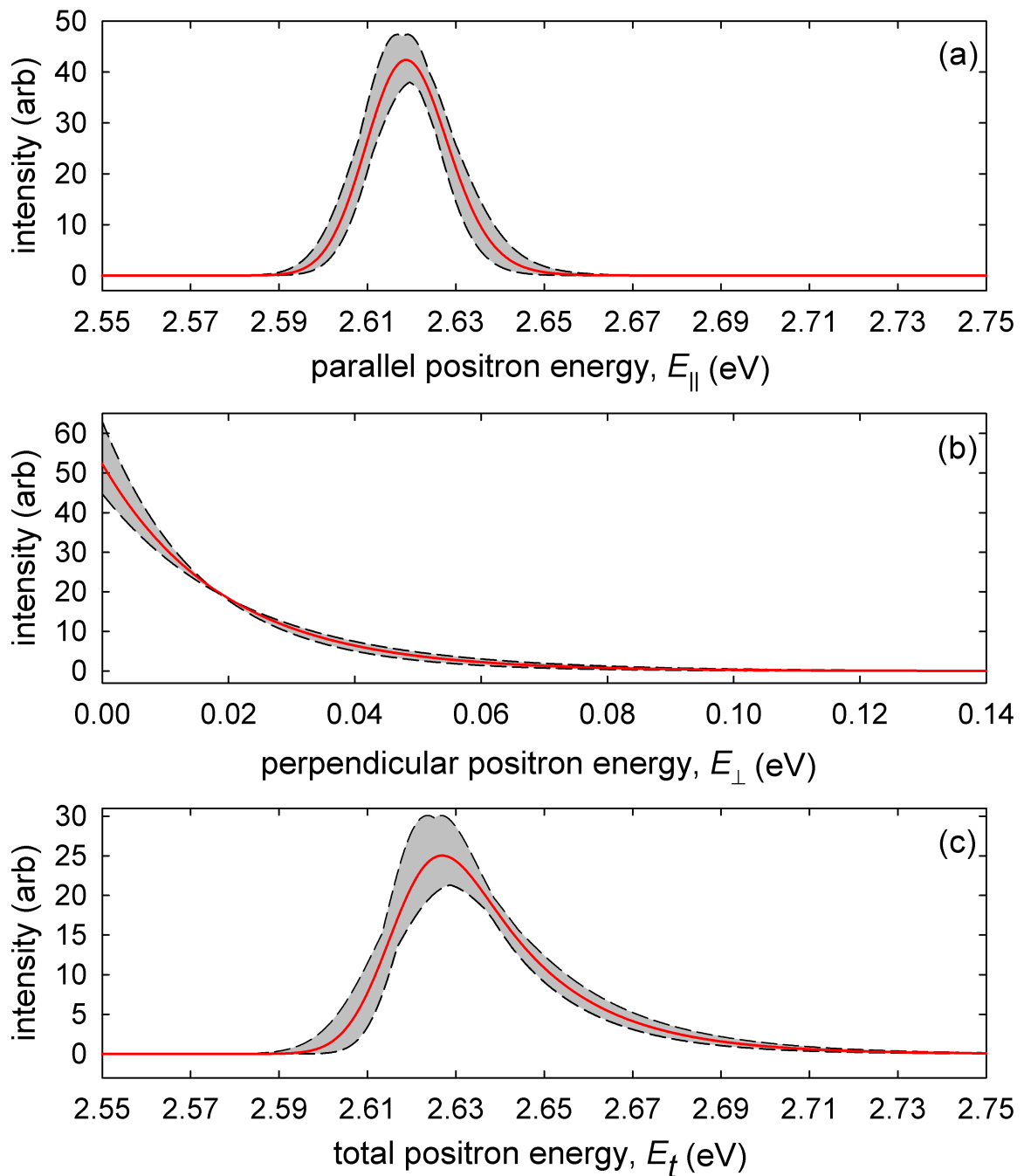


Figure 3.4: Measured beam energy distributions obtained from the BGT: (a) Parallel energy distribution with $\Delta E_{\parallel} = 22.8$ meV FWHM ($\sigma_{\parallel} = 9.7$ meV), (b) MB perpendicular energy distribution corresponding to the measured value of $\sigma_{\perp} = 19.1$ meV, which was obtained using Eq. (3.20), and (c) total energy distribution with $\Delta E_{tot} = 33$ meV FWHM ($\sigma_{tot} = 22.5$ meV). Shaded regions show 95 % confidence intervals estimated from the fits.

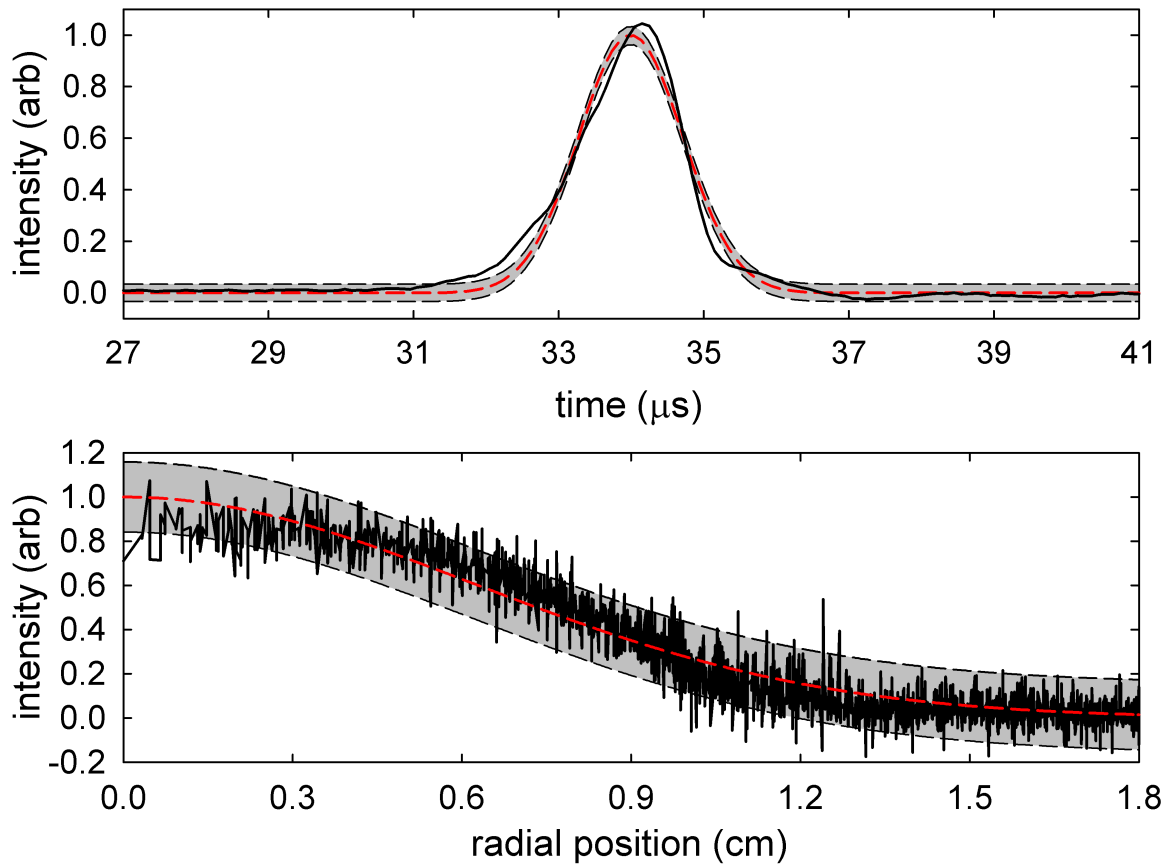


Figure 3.5: Beam temporal and radial distributions obtained from the BGT: (a) temporal distribution yielding $\Delta\tau = 1.7 \mu\text{s}$ FWHM ($\sigma_\tau = 0.71 \mu\text{s}$), and (b) radial distribution yielding $\Delta R = 1.4 \text{ cm}$ FWHM at 320 G ($\Delta R = 1.0 \text{ cm}$ FWHM in $\sim 650 \text{ G}$ trap field). Shaded regions show 95 % confidence intervals estimated from the fits.

in Fig. 3.4, are shown in Fig. 3.5. Here it is seen that the temporal distribution is roughly Gaussian in shape with a spread of $\Delta\tau = 1.7 \mu\text{s}$ FWHM. The radial distribution may also be roughly described as Gaussian, with a spread of $\Delta R = 1.4 \text{ cm}$ FWHM in the 320 G magnetic field. This corresponds to a beam diameter of $\Delta R = 1.0 \text{ cm}$ FWHM in the $\sim 650 \text{ G}$ field of the beam formation region of the BGT.

3.5 Factors affecting beam characterization

Many factors have been found to affect the measured beam characteristics. These factors range from the physical processes that affect the beam itself, to processes that occur during beam measurements and so affect the measured beam characteristics. In many cases, these effects limit the ability to produce or measure narrow beam distributions. For this reason, improvements in beam technology also require improvements in the technology used to measure them. Several of these factors are briefly discussed here.

3.5.1 Magnetic field dependence

The measured energy distributions described above are for the “special” case in which the RPA magnetic field is approximately equal to the magnetic field in the beam formation region (i.e., $M \approx 1$). Under these conditions, the parallel and perpendicular energy distributions may be treated as independent. However, as described by the analytic model presented in Sec. 3.2, these distributions become correlated as the beam propagates into regions of varying magnetic field.

By adjusting the RPA magnetic field relative to the BGT magnetic field, the dependence of the beam energy distributions on the magnetic field may be measured. Shown in Fig. 3.6 are the mean and standard deviation of the parallel and perpendicular energy distributions measured at various magnetic field ratios, $M \equiv B_{RPA}/B_{BGT}$. Here it is seen that \bar{E}_{\parallel} decreases linearly with magnetic field ratio, as expected from Eq. (3.16). In contrast, σ_{\parallel} is a minimum at $M = 1$ and increases when the beam enters regions of higher or lower magnetic field, as described by Eq. (3.17). Finally, the mean perpendicular energy (calculated using Eq. (3.20)) increases linearly with M , as described in Eq. (3.19).

It should be noted that for $M > 1$, both the parallel and perpendicular spreads are seen to increase with M . At first glance this may appear to violate conservation of energy since the total energy spread must be constant under a varying magnetic field. However, for values $M > 1$ the covariance $\sigma_{\parallel,\perp}$ becomes negative, therefore maintaining σ_{tot} constant, as seen in Eq. (3.5).

3.5.2 Positron number dependence

The primary effect of positron number on the measured beam distributions is seen in the temporal spread. Shown in Fig. 3.7 is the measured FWHM of the temporal distribution obtained as the number of positrons per pulse is varied. Here the temporal spread is seen to increase with increasing positron number, however the effect is relatively weak, particularly at low positron number. This effect is thought to be due to the positron space-charge potential, which increases as the number of positrons per unit length (along the magnetic axis) increases. By comparison, the parallel energy spread is less sensitive to the positron number, having no significant effect at least until the space-charge becomes comparable to the parallel energy spread (not shown).

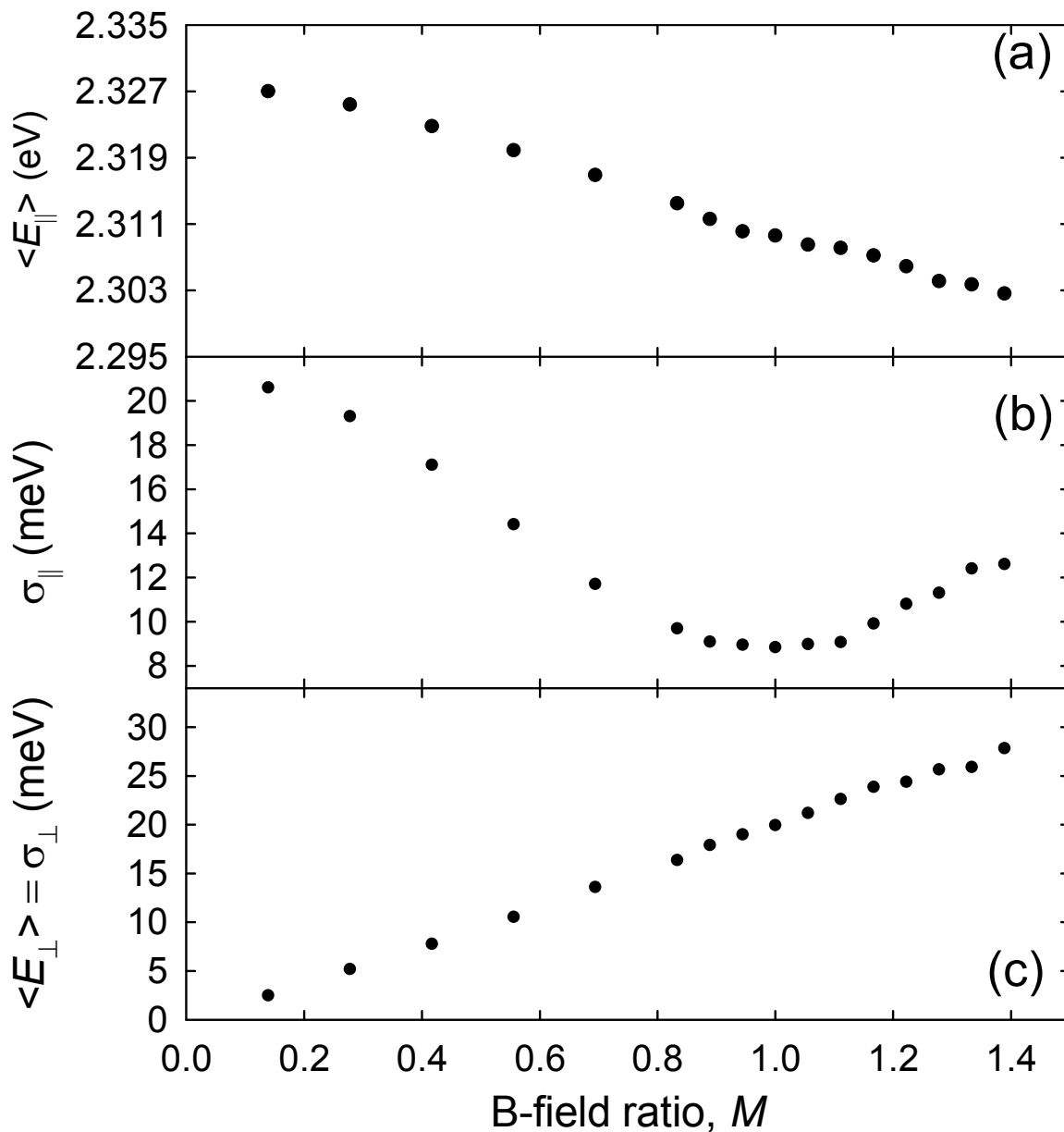


Figure 3.6: BGT beam measurements at various magnetic field ratios. (a) mean parallel energy, (b) standard deviation of the parallel energy distribution, and (c) mean perpendicular energy (calculated using Eq. (3.20)) at various magnetic field ratios, $M = B_{RPA}/B_{BGT}$. Note that, for the case of a MB perpendicular distribution, $\bar{E}_{\perp} = \sigma_{\perp}$.

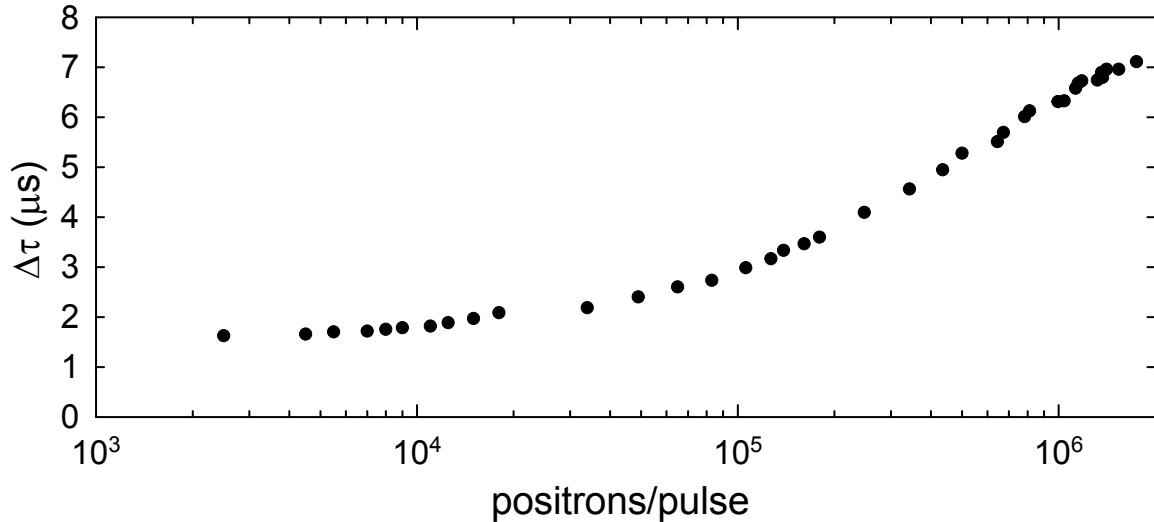


Figure 3.7: BGT temporal spread dependence on positrons number.

3.5.3 Beam reflections during measurement

As described above, the average cumulative parallel energy distribution is measured by counting the number of positrons that pass through an RPA at various RPA potentials. The number of positrons to pass through the RPA is determined by integrating the gamma radiation signal emitted as the beam annihilates on a metal plate downstream from the RPA. As the RPA voltage is increased, some or all of the positrons in the beam will be reflected and therefore not reach the metal plate, thus resulting in a decrease to the the emitted gamma radiation signal.

In practice, however, the positrons which are reflected by the RPA potential propagate back upstream and re-enter the BGT, where the well potential is typically still rising in order to eject the positrons from the trap. These reflected positrons are then further lifted by the rising potential well and re-ejected from the trap as a “secondary” beam which has a higher parallel energy than the initial pulse of positrons. Through this process, positrons within the initial “primary” beam which did not have sufficient energy to overcome the RPA potential are able to overcome it after repeated reflections. This leads to a broadening of the measured parallel energy distribution.

The effect of these secondary beams depends on several factors, including the beam transport energy, the beam temporal spread, and the relative distance between the trap and RPA electrodes. For example, under typical conditions for the BGT beamline, the primary and secondary pulses are sufficiently separated in time to allow the primary pulse to be independently determined when measuring the parallel energy distribution. However, if the pulse duration is increased (e.g., by reducing the positron ejection rate), then the reflected positrons are able to re-enter the BGT while the primary positrons are still being ejected, resulting in an overlap of the measurements of the radiation from both the primary and secondary pulses. Under these conditions, time-windowing the signal integration does not prevent a broadening of the measured parallel energy distribution.

The effect of reflected pulses on the measured parallel energy distribution is shown in Fig. 3.8. Here, the integration time-window is adjusted to include multiple secondary peaks in order to examine their effect on the measured distribution. As described above, the secondary pulses have a larger mean energy than the primary pulse, and therefore integrating over them results in an increase to both the mean and the spread of the measured parallel energy distribution.

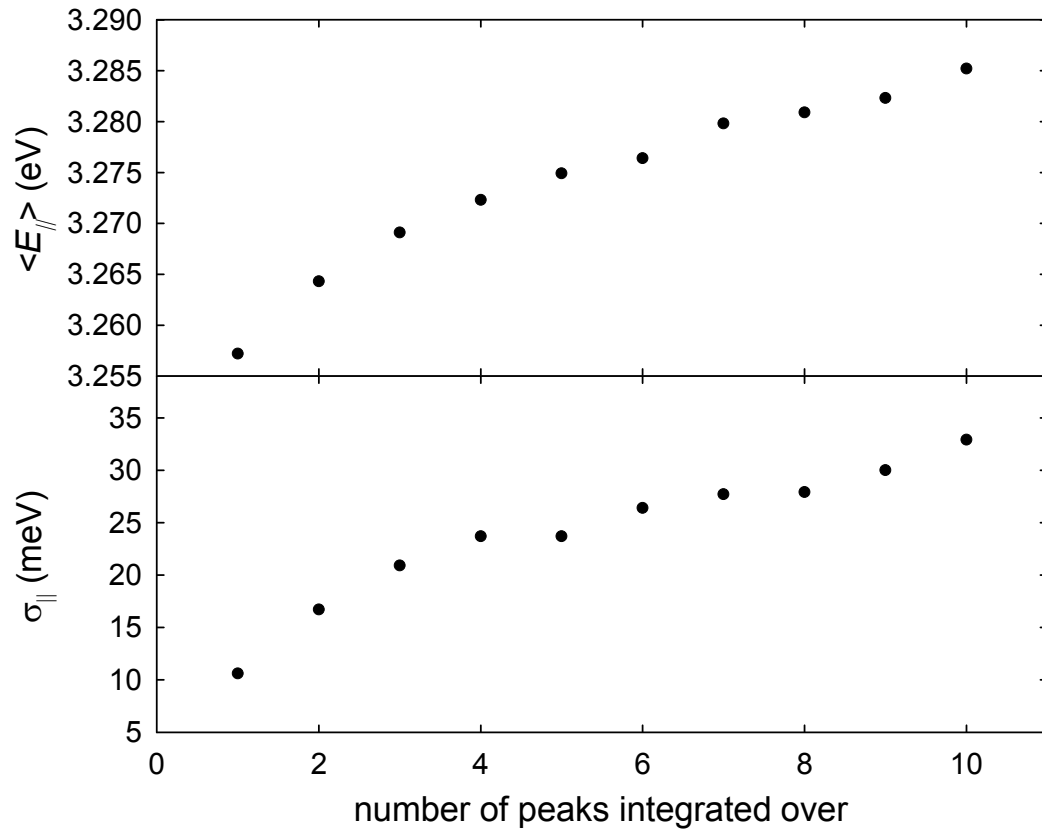


Figure 3.8: Effect of beam reflections on measured parallel energy distribution. (a) mean and (b) standard deviation of the parallel energy distribution as the time window of integration is increased to include multiple peaks (i.e., “secondary” beams). See text for details.

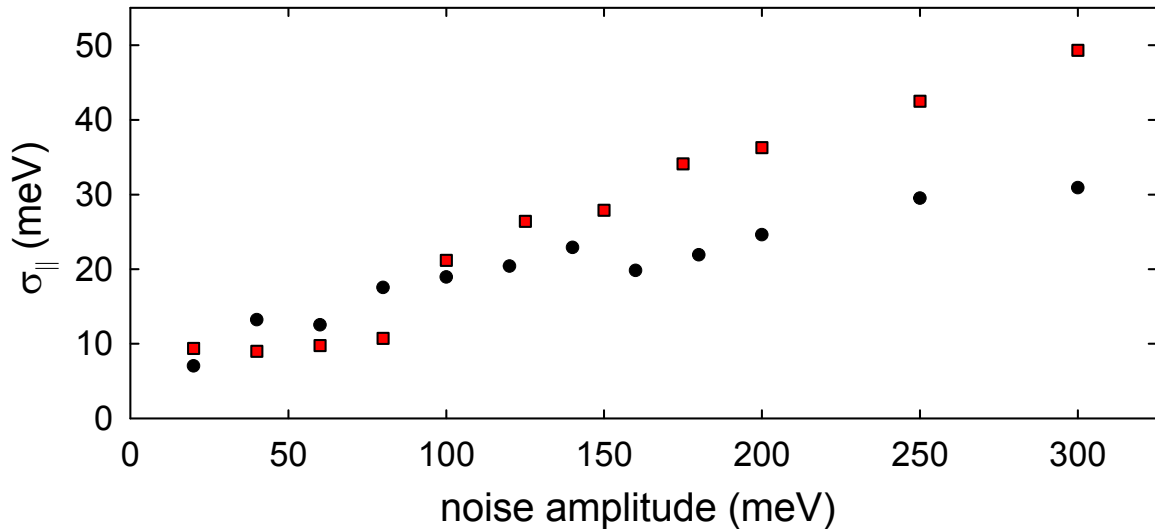


Figure 3.9: Effect of electronic noise on measured parallel energy distribution. Measured standard deviation of the parallel energy distribution as Gaussian noise is applied to the (●) exit-gate and (■) RPA. The horizontal axis is the peak-to-peak noise amplitude, as measured on an oscilloscope.

3.5.4 Electronic noise

Electronic noise on the electrodes can also affect the parallel energy distribution. The two electrodes most sensitive to electronic noise are the exit-gate and RPA electrodes. Noise on the exit-gate results in a fluctuation of the energies required for the positrons to escape the trap, thereby affecting the beam itself, while noise on the RPA results in fluctuations of the reflecting potential, thereby affecting the measurement of the beam.

The mechanism by which electronic noise broadens the parallel energy spread depends on the time scale of the noise. For electronic fluctuations on time scales short compared to positron ejection times, the noise acts to provide additional fluctuations in the parallel energy of each positron, thereby increasing the parallel energy spread of a given pulse. Alternatively, if the noise occurs on time scales long compared to the ejection time, the noise contributes the same random perturbation to the energies of *all* of the positrons in a given pulse, thus shifting the mean parallel energy. Over multiple pulses, these random shifts cause a broadening of the *average* parallel energy distribution.

An example of the effect of electronic noise on the measured parallel energy spread is shown in Fig. 3.9. Here Gaussian noise of varying amplitude with a bandwidth of 9 MHz of is added to either the exit-gate or RPA electrode. In both cases, increasing the amplitude of the noise leads to an increase in the spread of the measured parallel energy distribution. The effect of electronic noise on the BGT-based beam will be discussed in more detail using simulations in Chapter 5.

3.5.5 Potential perturbations

The effects of potential perturbations on the measured beam distributions are difficult to study systematically. Experience has shown that both the mean and spread of the parallel energy and temporal distributions can be affected by perturbations in the applied potentials. A few examples of these effects are briefly described here.

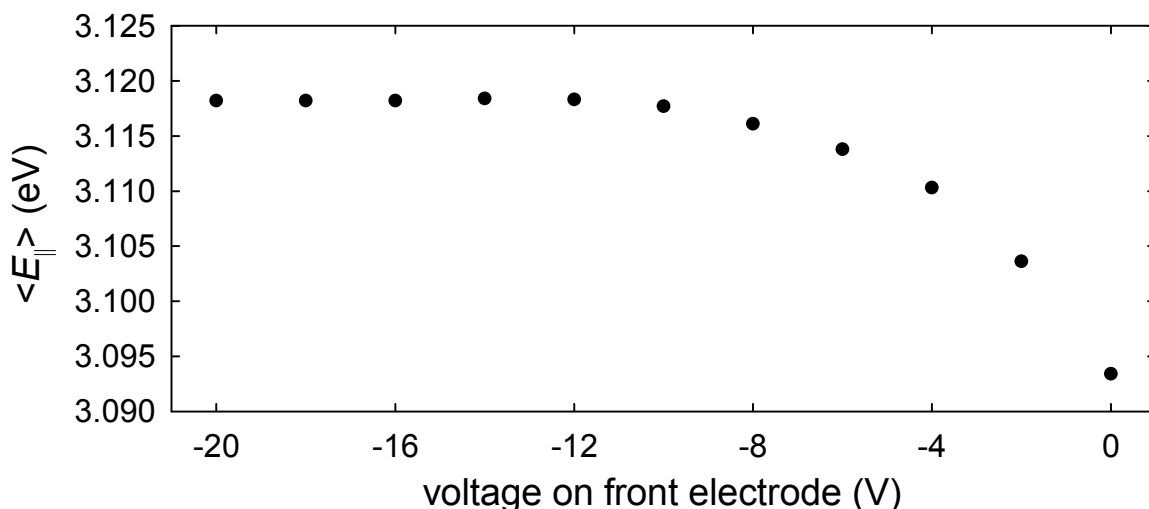


Figure 3.10: Effect of potential perturbations on energy. (●) measured mean parallel energy obtained as a negative voltage of various values is applied to an electrode immediately upstream of the RPA. This technique provides a measure of effects due to positive potential perturbations in the RPA potential.

The adsorption of molecules on the BGT and RPA electrodes produces potential “offsets” from the applied voltages. Experience has shown that these offsets depend upon the specific molecule and the electrode material (e.g., stainless steel, aluminum, gold-plated copper, etc.). The primary effect of this is that the mean beam energy, measured using an RPA, is found to shift as electrode surface conditions change. For example, measurements made before and after baking can show shifts in the mean beam energy of several electron-volts, while that measured in a nominally clean system typically drifts over time scales of days to weeks. These drifts are not problematic in typical experiments since the measurements can be calibrated to account for these offsets (i.e., the RPA, or a scattering- or annihilation-cell cutoff accurately measures the zero of beam energy at that location). However under certain circumstances, even shifts in the measured annihilation spectra have been seen (see Appendix B).

Since the technique used to measure the parallel energy distribution relies only on the maximum potential produced by the RPA (i.e., positrons only make it through the RPA if their parallel energy is greater than maximum potential produced by the RPA), positive perturbations, or “bumps,” in the RPA potential can lead to a measurement of the parallel distribution which appear to be shifted to lower energies than the actual beam. One method of probing these perturbations is to apply a large negative voltage to an electrode near the RPA in order to “pull down” any positive perturbations near the end of the RPA, thus moving the maximum RPA potential to the nominal voltage of the RPA.

An example of results obtained using this technique is shown in Fig. 3.10. Here it is seen that the measured mean parallel energy initially increases as the front electrode voltage is made more negative, then becomes constant as the voltage is reduced further. This example suggests that there was a potential perturbation near the end of the RPA with a magnitude of at most 25 meV. Using electrodes on both sides of the RPA, and combined with a high voltage power supply, would enable this technique to probe for positive perturbations relatively far into the RPA.

Similar effects to those described above have been seen on the exit-gate trap electrodes. In this case, the presence of positive perturbations in the exit-gate potential can substantially broaden

the temporal spread of the ejected beam by reflecting some fraction of the positrons during ejection, therefore requiring them to make additional bounces within the well before escaping the trap. Experiments similar to those shown in Fig. 3.10, but with the exit-gate electrode rather than the RPA, have shown sharp decreases in the temporal spread as a negative voltage is applied to an adjacent electrode.

Another example of the effects of potential perturbations is their impact on the spread of the parallel energy distribution. In this case, azimuthally asymmetric perturbations to either the exit-gate or RPA potentials can lead to a strong radial dependence of the measured energy distribution. In these cases parallel energy spreads are significantly narrower when the beam radius is reduced (either by passing it through an aperture or using a so-called “rotating wall” to radially compress the positrons). This effect is especially noticeable in measurements in which the RPA magnetic field is reduced compared to that of the trap ($M < 1$), where the positrons are radially much closer to the RPA electrode surface.

Experience has also shown that the RPA material and/or gold-plating processes can limit the ability to measure small parallel energy spreads. After testing a variety of RPAs of differing material and plating techniques, several were encountered in which measurements of spreads lower than many hundreds of meV were not possible. It is presumed that this is due to poor plating which lead ‘to ‘patches” where potential asymmetries exist.

The issues discussed here provide a real impediment to the ability to produce and measure positron beams with significantly narrower energy spreads. Unfortunately, due to the number of factors involved, systematic studies of these processes are prohibitively difficult. This leaves trial-and-error as the primary method of making improvements in these areas. One such trial which yielded good results is discussed in Chapter 7.

Some of the work and discussion in Chapter 3 is taken from “Formation of buffer-gas-trap based positron beams,” M. R. Natisin, J. R. Danielson and C. M. Surko, *Phys. Plasmas* **22**, 033501 (2015) [26]. The author of this dissertation led the research and was the principle author of the paper.

Chapter 4

Importance of high quality beams in atomic physics studies

In this chapter the utility of positron beams for scientific studies is discussed, with a focus on the limitations placed upon experiments by the current state of positron beam technology. Several examples of open questions regarding positron-molecule interactions are presented, and the difficulties encountered in answering these questions are described. Note that the goal of this chapter is not to describe in any detail the physical processes involved, but rather to give a variety of examples in which further progress in this field is made prohibitively difficult due to the limitations of the experimental technology used to probe it.

The energy dependence of positron annihilation on molecules was the principle area of study during the early stages of research for this dissertation. The limitations placed upon those studies by current beam technology were the primary motivation for the beam formation research that is the focus of this dissertation. Here, examples of recent studies are presented, such as contributions due to infrared-inactive and higher-order vibrational excitations, as well as the effects of intramolecular vibrational redistribution. Also discussed is current limitations in the study of positron scattering, such as the measurement of vibrational and rotational excitation cross sections.

4.1 Positron annihilation on molecules

The most notable feature discovered with the first energy-resolved measurements of the positron-molecule annihilation rate was the existence of resonances associated with the molecular vibrational modes [31]. These are the result of vibrational Feshbach resonances (VFRs) that are mediated by a positron-molecule bound state, and are described in detail in Appendix A. The energy of the measured resonance occurs at $\epsilon_v = \omega_v - \epsilon_b$, where ω_v is the energy of a molecular vibration and ϵ_b is the positron-molecule binding energy. For the purposes of this chapter, it is important that the natural width of these resonances is extremely small ($\sim \mu\text{eV}$), and so the widths of the measured resonances are limited only by the beam total energy resolution.

Positron-molecule annihilation rates are conventionally described in terms of the dimensionless quantity Z_{eff} [32], which is the measured annihilation rate Γ normalized to the Dirac rate

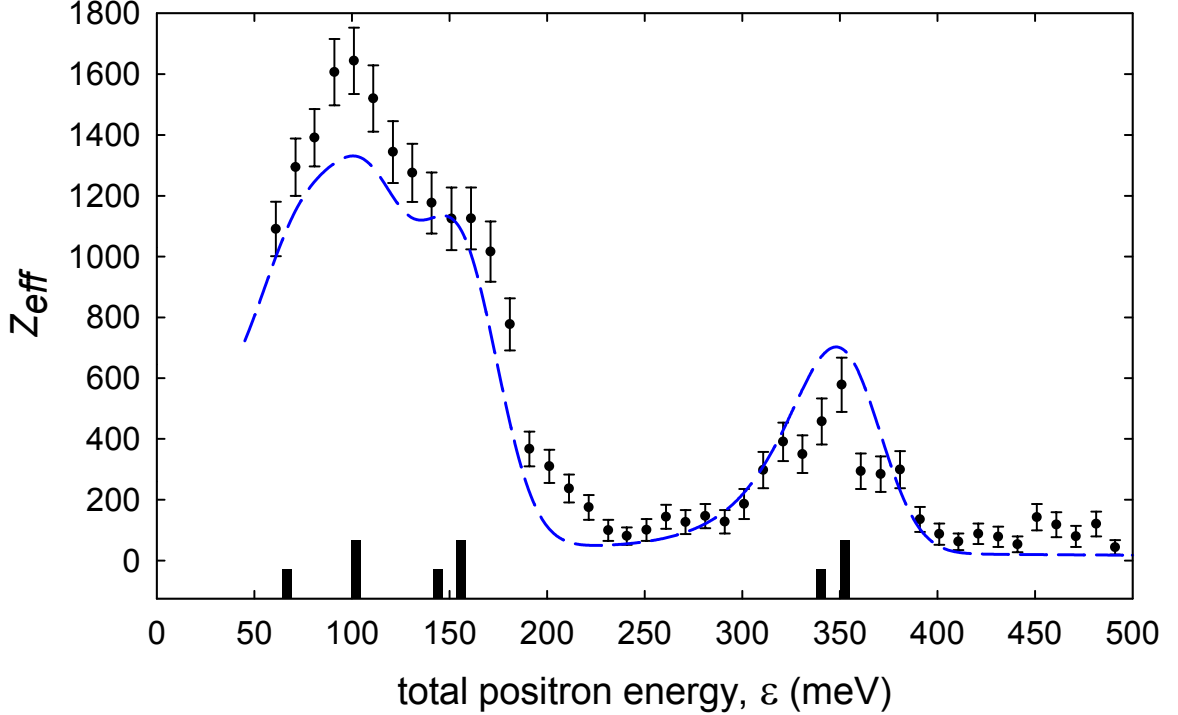


Figure 4.1: Annihilation spectrum for methyl chloride (CH_3Cl) [33]; (\bullet) measured data and ($- -$) GL model from Eq. (A.8) with $\epsilon_b = 24$ meV. Vertical bar positions represent vibrational mode energies downshifted by the binding energy and heights represent mode degeneracies.

Γ_D for two-gamma annihilation in a free-electron gas,

$$Z_{eff}(\epsilon) = \frac{\Gamma(\epsilon)}{\Gamma_D} = \frac{\Gamma(\epsilon)}{\pi r_0^2 c n_g}, \quad (4.1)$$

where r_0 is the classical electron radius, c is the speed of light and n_g is the molecular density.

An example of a measured, energy-resolved Z_{eff} is shown in Fig. 4.1. Shown here is the annihilation spectrum of methyl chloride (CH_3Cl) [33], which clearly shows the strong energy dependence of Z_{eff} . Also shown for comparison is the theoretical prediction of $Z_{eff}(\epsilon)$. This theoretical model, developed by Gleb Gribakin [30] and motivated by the first energy-resolved Z_{eff} measurements [31], is referred to as the ‘‘Gribakin-Lee’’ (GL) model. It describes the effect of isolated VFRs of infrared-active fundamental vibrational modes on the Z_{eff} spectrum. In this model, positron capture is mediated by long-range dipole coupling.

Methyl chloride is unique in that there are relatively few fundamental vibrational modes, and most of those are reasonably well separated in energy, making it an ideal candidate for an energy resolved study. However, while the measured data proved sufficient to obtain measurements of the binding energy and resolve several spectral features, even in this relatively optimal case, the BGT beam resolution is insufficient to fully resolve all of the resonances. Indeed, of the more than 60 molecules in which energy-resolved Z_{eff} has now been measured with the BGT-based beam [17], there is not one case in which all of the expected resonances are independently resolved.

The limitations of current beam technology go beyond the ability to fully resolve all of

the fundamental VFRs in a given spectrum. There is significant evidence that additional physics beyond the GL model is present within the majority of measured annihilation spectra. However, experimental measurements to probe these unexplored processes are prohibitively difficult with current beam technology. In the remainder of this section, examples of these processes are briefly described, and the difficulties involved with their investigation discussed.

4.1.1 Low-energy modes

Due to the finite spread in positron energies in the beam, there is a limit to the lowest energy with which energy-resolved features can be reliably studied. In terms of the total energy distribution, this limit is set by the energy at which a reasonable fraction of the distribution would be shifted below zero energy. For the specific case of the annihilation measurements discussed here, this effect may be better understood in terms of factors affecting the parallel and perpendicular components independently.

As described in Appendix A, the incident parallel beam energy is adjusted by applying a retarding potential using an RPA electrode. Because of this, at some RPA voltage some of the lowest energy positrons within the beam will be reflected by the retarding potential, thus distorting the parallel energy distribution within the gas cell. Simulations show that this effect becomes appreciable (i.e., $> 5\%$ positrons reflected) at an energy $\epsilon \sim \bar{E}_{\parallel} - \Delta E_{\parallel}$, where \bar{E}_{\parallel} and ΔE_{\parallel} are the beam mean parallel energy and FWHM spread in parallel energies, respectively. Therefore, the FWHM of the parallel energy distribution is a good measure of the minimum reliable parallel energy measurement.

The perpendicular energy of the beam also affects the minimum energy with which these features may be reliably measured. The perpendicular energy is unaffected by the RPA potential, although it is still able to contribute to the vibrational excitation of the molecule. For this reason, even at arbitrarily low parallel energies, the perpendicular energy sets an additional minimum on the lowest reliable energy which may be probed. The effect of the perpendicular energy on the minimum reliable measurement depends primarily on the positron temperature (more specifically, it depends on the effect of the perpendicular energy distribution on the shape of the total energy distribution). For the BGT-based beamline results discussed in this chapter (and in the appendices), the result is approximately an additional 12 meV below which features cannot be reliably measured.

Due to these effects, the minimum total energy to which the BGT-based beamline can reliably probe (under optimal conditions) is ~ 35 meV. Since the VFR resonances occur at the vibrational mode energy minus the binding energy, there are typically many interesting features around or below this value which cannot yet be experimentally studied. Examples of this are discussed in Appendix B. In order for these processes to be explored, positron beams with significantly reduced parallel energy spreads and positron temperatures must be developed.

4.1.2 Infrared-inactive modes

The GL model, as discussed above, describes resonant Z_{eff} in terms of dipole-coupled vibrational modes. Because of this, only vibrational modes that are infrared-active are predicted to have a corresponding resonance in the Z_{eff} spectrum. This simplification was necessary due to the difficulties involved in describing non-dipole coupled states. However, there are many examples of measured spectra where infrared-inactive vibrational modes appear to contribute to the annihilation rate.

One example, shown in Fig. 4.2, is the annihilation spectra for 1,2-trans-dichloroethylene ($C_2H_2Cl_2$). Of the 12 vibrational modes, 6 are infrared-inactive due to the molecular symmetry. The

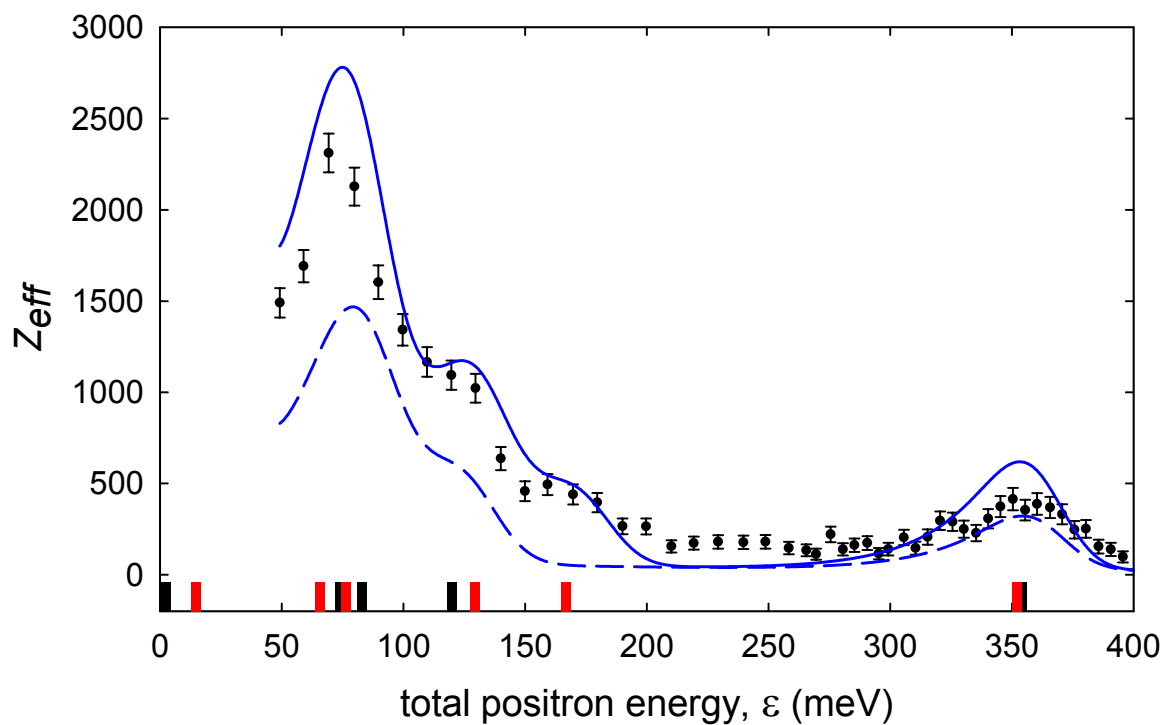


Figure 4.2: Annihilation spectrum for 1,2-trans-dichloroethylene ($C_2H_2Cl_2$); (\bullet) measured data, ($--$) GL model from Eq. (A.8) with $\varepsilon_b = 29$ meV using infrared-active modes only and ($-$) GL model using all modes. Vertical bar positions represent vibrational mode energies downshifted by the binding energy, and heights represent mode degeneracies. Black and red indicate infrared-active and inactive modes, respectively.

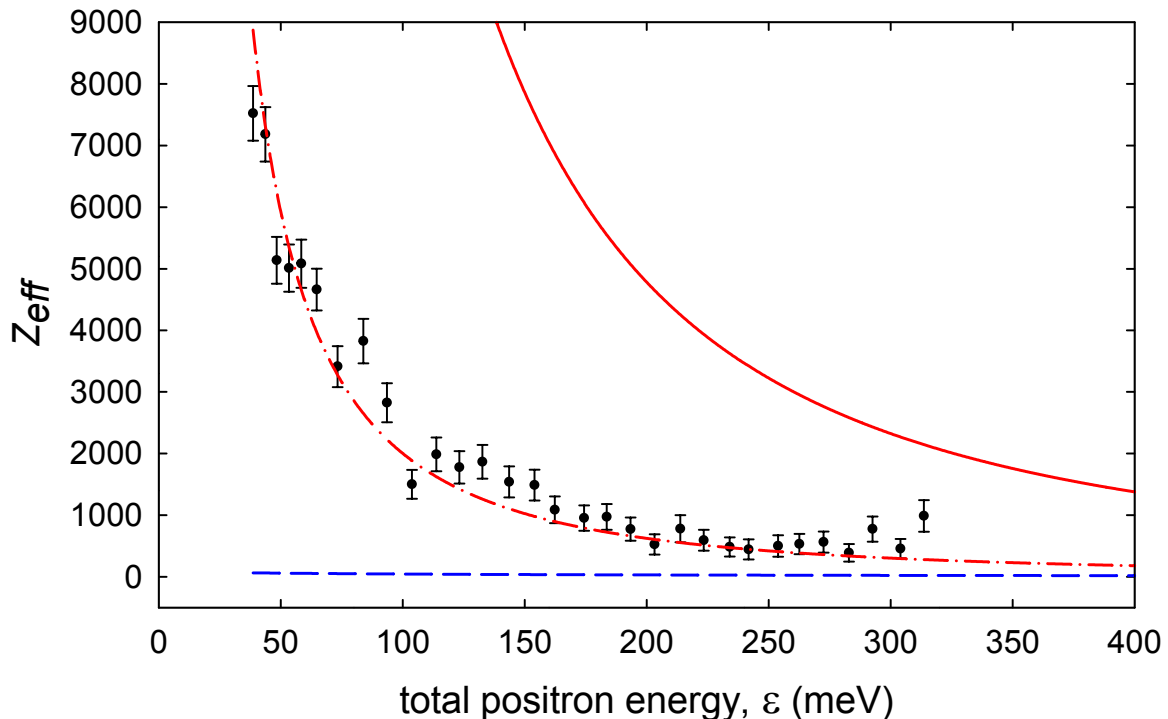


Figure 4.3: Annihilation spectrum for carbon tetrabromide (CBr_4) [35]; (\bullet) measured data, ($- -$) GL model from Eq. (A.8) with $\varepsilon_b = 115$ meV, ($-$) MRA model from Eq. (A.11) and ($- \cdot -$) MRA model scaled by factor $\eta = 0.13$.

dashed line represents the model prediction using only the infrared-active modes, as prescribed by the model. It is seen that there is considerable additional spectral weight beyond the model.

Also shown by the solid line in Fig. 4.2 is the model prediction where now *all* vibrational modes are included. While infrared-inactive modes are not expected to contribute identically to that predicted by the GL model for infrared-active modes, this shows that the additional spectral weight is likely present. In particular, there appears to be a “shoulder” in the data near the infrared-inactive mode at $\varepsilon_v = 165$ meV, which is consistent with the excitation of a VFR at that energy.

Figure 4.2 is an example in which the annihilation spectrum appears to indicate the presence of positron binding mediated by infrared-inactive vibrational modes. Several more examples are discussed in Appendix B. However, no example exists to date where the infrared-inactive resonance is fully resolved, thus preventing detailed investigation. A higher energy resolution beam would enable these infrared-inactive resonances to be independently measured, hopefully providing crucial information to assist in the development of theoretical models of this process.

4.1.3 Multimode resonant annihilation

As specified above, the GL model describes the effect of VFRs on Z_{eff} due to well isolated, fundamental vibrational modes. However, it does not account for VFRs mediated by multimode excitations (i.e., combinations and overtones of the fundamentals). Another model, also developed by Gribakin and Lee, describes the effects of positron attachment due to multimode excitations on $Z_{eff}(\varepsilon)$ [34]. The multimode resonant annihilation (MRA) model is described in Appendix A.

An example where the annihilation spectrum is apparently dominated by multimode resonant annihilation is shown in Fig. 4.3. Shown here is the annihilation spectrum of carbon tetrabromide (CBr_4) [35]. There are no VFRs in the measured spectrum, since the binding energy is sufficiently large that the expected resonant energies are all below zero. Due to this, the GL model predicts Z_{eff} to be due entirely to the small contribution from direct annihilation (see Appendix A). In contrast, the measured Z_{eff} spectrum shows a significantly larger annihilation rate which decreases as positron energy is increased. Also shown in Fig. 4.3 is the predicted Z_{eff} obtained from the MRA model due to multimode excitations. Here, the model over-predicts the annihilation rate. However, when this prediction is scaled by a constant numerical factor η , good agreement with the measured data is obtained.

While this example is relatively unique in that MRA appears to be the dominant annihilation process, evidence for multimode annihilation appears to exist in virtually all measured annihilation spectra to date. This evidence is typically in the form of a broad background of annihilation on which the fundamental VFRs sit. In almost all cases, the MRA model over-predicts the apparent effect of these processes, but provides reasonable agreement when scaled by a numerical factor $\eta < 1$ [35].

Unfortunately, while the MRA model predicts that multimode excitations produce resonances just as in the case of the fundamentals, these resonances are typically densely packed and therefore are only observable as a broad background due to the relatively broad beam energy spreads. This makes the investigation of multimode resonant annihilation prohibitively difficult with current beam technology. With a higher resolution positron beam, the first state-resolved multimode excitation by positron impact could be made, and the discrepancies with the MRA model could be investigated in detail.

4.1.4 Intramolecular vibrational redistribution

Another feature seen in virtually all annihilation spectra is that the magnitudes of the measured resonances differ from that predicted by the GL model. These discrepancies vary from the complete absence of a predicted resonance, to the enhancement of resonances by factors of 10-100 [17]. This process is thought to be due to intramolecular vibrational redistribution (IVR), where the vibrational energy of a molecule is redistributed into near-resonant multimode vibrational states [36, 37, 38]. The effect of IVR on positron annihilation is discussed in more detail in Appendix A. Briefly stated, the positron becomes bound to the molecule through the excitation of a fundamental mode (as described by the GL model). However, due to IVR, this energy may redistribute into nearby multimode states which may have significantly longer or shorter relaxation times than the entrance fundamental¹. This can result in an enhancement or suppression of the magnitude of the VFR, as compared to the GL model prediction [39, 40].

Shown in Fig 4.4 is an example where both the enhancement and suppression of resonances is seen in a single molecule. Shown here is the annihilation spectrum for 1,1-dichloroethylene ($\text{C}_2\text{H}_2\text{Cl}_2$), where the fitted MRA component of the measured data has been subtracted off to more clearly show the effects of IVR. Also shown is the GL model prediction, where it is seen that at low positron energies many of the resonances are enhanced above the GL model prediction, while at $\epsilon \approx 150$ meV the resonance is suppressed relative to the model. Also shown is a scaled solution to the GL model, where the magnitudes of the resonances have been fitted to the data using a scale

¹The relaxation time is the time for the positron to be ejected from the molecule by de-excitation of a vibrational mode.

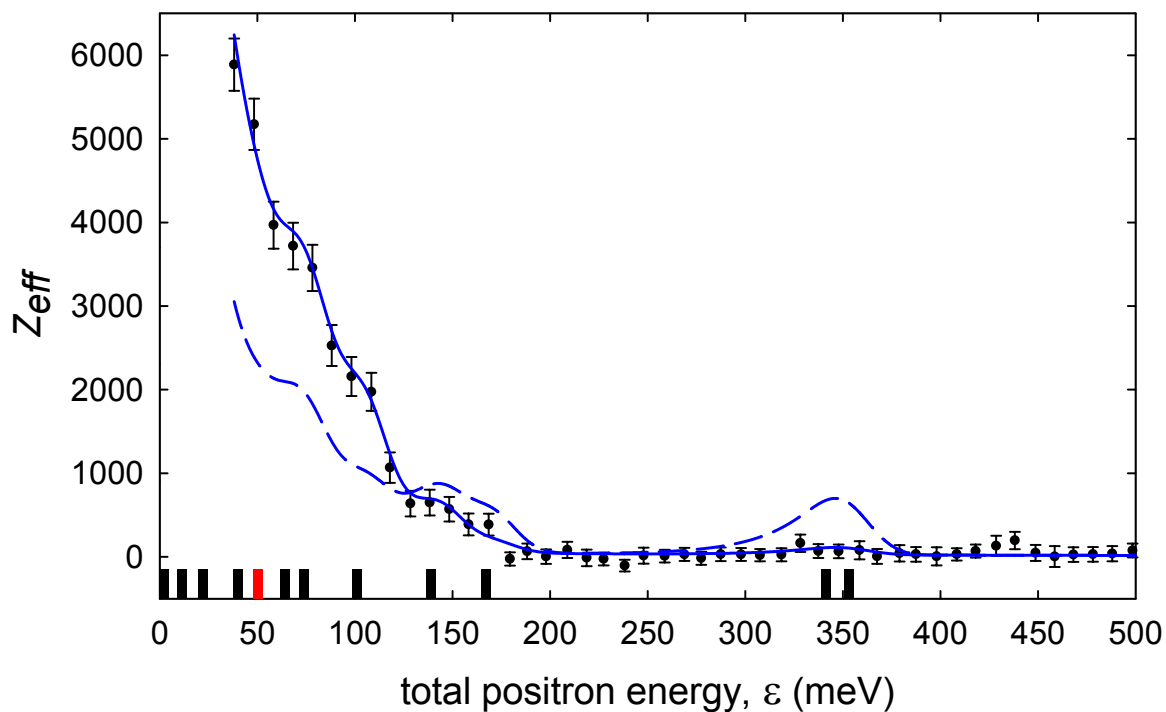


Figure 4.4: Annihilation spectrum of 1,1-dichloroethylene (C₂H₂Cl₂); (•) measured data with the fitted MRA component subtracted for clarity, (---) GL model from Eq. (A.8) with $\epsilon_b = 31$ meV, (—) scaled GL model from Eq. (A.15). Vertical bar positions represent vibrational mode energies downshifted by the binding energy and heights represent mode degeneracies, where black and red indicate infrared-active and inactive modes, respectively.

factor, to allow quantification of the relative enhancement or suppression.

The effects of IVR are difficult to investigate for several reasons. Theoretically, *ab initio* calculations would require knowledge of the mode-mode couplings between many thousands of multimodes. Experimental investigation is similarly problematic due to the rarity of well isolated fundamental vibrations in which a single resonance may be examined. For the vast majority of cases, multiple fundamental vibrations overlap within any given beam spread, making the study of the effects of IVR on any given mode prohibitively difficult. Further, due to the relatively unknown contributions of both IR-inactive and multimode resonant annihilations, even fitting mode scale factors of groups of modes for cataloging is problematic.

4.2 Inelastic positron scattering

Another active area of positron research which is inhibited by current beam technology is positron scattering. The goal of typical scattering measurements is to measure the cross sections for various positron-atom or positron-molecule interactions. This may be done by passing a positron beam through a target gas in a high magnetic field and subsequently measuring the beam parallel energy distribution using an RPA in a reduced magnetic field [28]. Due to conservation of energy and invariance of the positron magnetic moment, energy is transferred from the perpendicular component of the beam distribution into the parallel component as the beam propagates into regions of lower magnetic field (as described in Chapter 3). Because of this, in the limit that the RPA magnetic field is significantly smaller than that in the scattering region, the contributions from elastic scattering is removed from the measured beam distribution, enabling the (typically smaller) contributions from inelastic scattering to be measured. The inelastic cross section can then be obtained by comparing the scattered beam-energy distribution to the unscattered case.

Using this technique, inelastic cross sections for processes which are of higher energy than the beam total energy spread can be measured. This restriction has limited measurements to those of relatively high energy processes, such as ionization and electronic excitation [22]. However, using a variation of the BGT-based beamline described in Chapter 2, a small selection of vibrational excitation cross sections have also been measured [16, 41].

As an example, Sullivan *et al.* used the UCSD BGT beam to measure the vibrational excitation cross sections of CO₂, as shown in Fig. 4.5 [16]. The inset shows the cumulative energy distribution of the scattered beam, as measured using an RPA in a reduced magnetic field. The steps in the measured data show the positron energy loss due to excitation of the ν_2 and ν_3 vibrational modes. The magnitudes of these steps relative to the incident (i.e., unscattered) beam are then used to determine the cross sections.

Unfortunately, even with the state-of-the-art BGT-based beam (i.e., total energy spread of ~ 35 meV FWHM), the study of low energy or closely-packed vibrational excitation cross section measurements has not been possible. Even more unfortunate is the fact that state-resolved rotational excitation cross sections are not currently possible for any molecule. This limitation has significantly affected advancement in positron atomic physics, with virtually no experimental measurements of these fundamental low-energy processes.

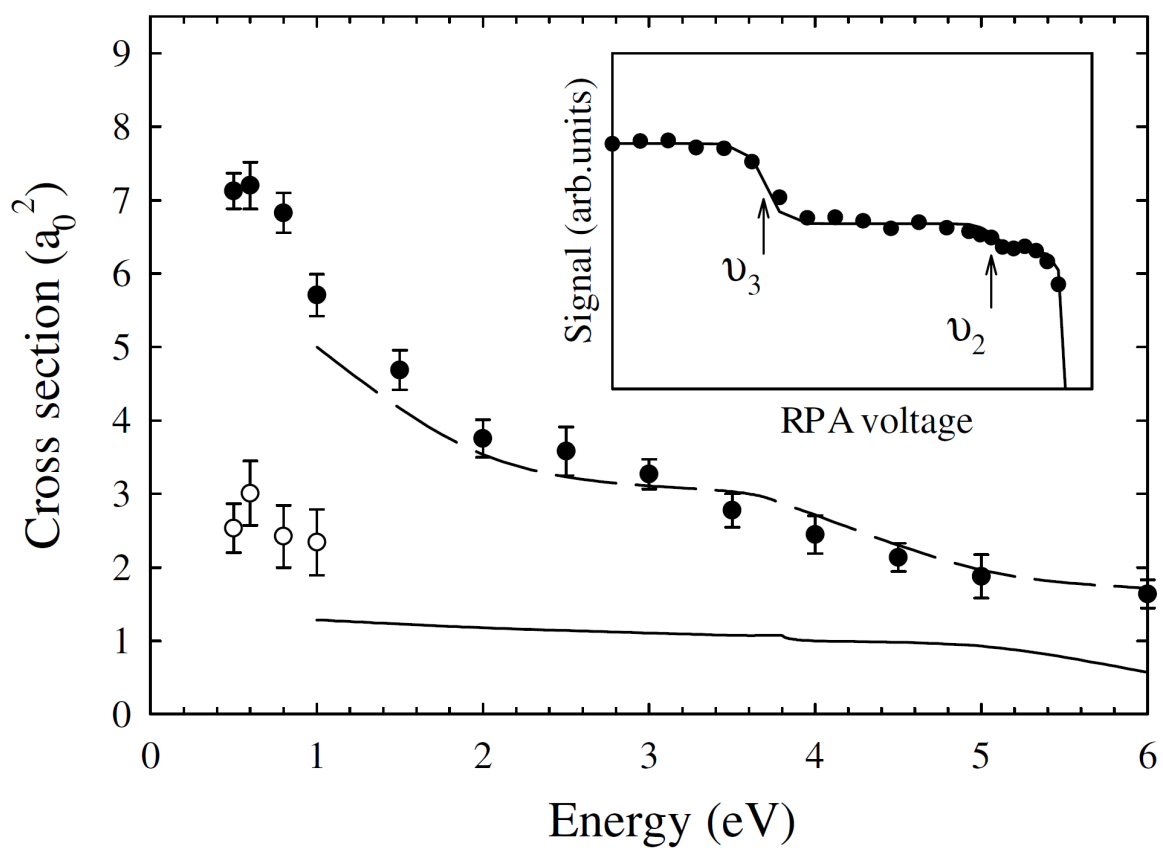


Figure 4.5: Cross section for excitation of the v_2 and v_3 vibrational modes of CO_2 from Ref. [16]. (\circ) and (\bullet) are experimental data for the v_2 and v_3 modes, respectively. (—) and (---) are theory from Kimura *et al.* [42] for the same two modes. Inset shows raw RPA data, showing steps due to both vibrational modes, with the solid line showing the fitted curve.

Chapter 5

Trap-based beam formation and optimization: simulations and experiments

Trap-based positron beams are now used in a wide variety of applications, including antihydrogen [19, 43, 44, 45], formation of dense gases of positronium atoms [46], material science [18], and atomic physics studies [29, 17]. As described in Chapter 3, positron beams with tens of millielectron volt energy spreads or sub-microsecond temporal spreads have been produced. Although this resolution is sufficient for probing well-isolated processes at energies $\gtrsim 50$ meV, many other processes are difficult or impossible to study without further advances in beam technology (as discussed in Chapter 4).

Given the limitations placed on experimental positron physics by current beam technologies, there have been surprisingly few systematic studies of the relevant beam formation processes and how beam quality depends on them. A better understanding of beam formation will aid in the development of improved experimental techniques and technology that, in turn, can then be expected to enable study of a variety of additional phenomena. While the measurement techniques described in Chapter 3 allow characteristics of the beam to be studied, the dynamics of beam formation and ejection is difficult to study experimentally. On the other hand, since the final beam parameters depend on the relative trajectories of large numbers of positrons interacting with spatially and temporally varying electric fields, first-principles calculations are prohibitively difficult. For these reasons, simulations are used here to study the underlying physical processes.

In this chapter, experimental measurements and simulation results using the BGT-based beamline are presented. The simulation conditions are chosen to replicate those found in the BGT-based beamline as accurately as possible, allowing direct comparisons between simulation and experiment to be made. Under these conditions the dynamic processes occurring during beam formation and transport are discussed, and beam results obtained under a variety of conditions are compared.

Also described are simulation results under more generic conditions not constrained by existing hardware. These simulations allow a more detailed investigation of the underlying physical phenomena operative during beam formation. They also as well as provide a practical guide for optimization of next-generation, high-energy-resolution, positron beams. Of key importance is the identification of three distinct regimes in which beam formation may occur, two of which are capable

of producing beams with significantly improved energy and temporal resolution when compared with the regime in which trap-based beams currently operate. Beam results under a wide variety of conditions are presented, and the underlying processes discussed. The chapter ends with a summary of the optimal conditions for beam formation in which high energy resolution is desired.

5.1 Description of the simulation

Described here is a Monte-Carlo simulation that follows, in the guiding center approximation, the trajectories of a large number of particles through time-dependent potentials and static magnetic fields. The simulations assume cylindrical symmetry and neglect space-charge effects and positron-positron and positron-neutral collisions. Experimental measurements show no significant dependence on positron number for the low densities used here (cf. Fig. 3.7), and beam-formation occurs on time scales which are fast compared to collision times, and so these effects are neglected. The externally applied potentials are allowed to vary axially, radially and temporally; while the magnetic field B is allowed to vary axially, but is constant in time.

The positrons are initially placed in a potential well determined by the geometry of the trapping electrodes. The parallel and perpendicular velocities are described by 1-D and 2-D MB distributions, respectively, with the initial radial positions chosen to obey a Gaussian distribution. The initial axial positions of the positrons are generated to start the particles in a thoroughly mixed state. This is done by starting each positron in the center of the potential well with prescribed perpendicular and parallel velocities and radial position, and then allowing it to make 10 bounces in the well. The measured axial position distribution at the end of these bounces is used to determine the initial axial position distribution for the simulation. The parallel and perpendicular velocities are then adjusted, depending on the potential and magnetic field, to ensure the initial velocity distribution is MB distributed. This procedure ensures that the simulations begin with the particles in an equilibrium state in phase space (*i.e.*, z and v_z).

Once the initial distributions have been determined, the axial positions and parallel velocities are calculated as the particle moves along the magnetic field line by numerically integrating the equations of motion using the velocity Verlet technique [47]:

$$z(t + \delta t) = z(t) + v_{\parallel}(t)\delta t + \frac{1}{2m}F_{\parallel}(z, r, t)\delta t^2, \quad (5.1a)$$

$$v_{\parallel}(t + \delta t) = v_{\parallel}(t) + \frac{1}{2m}[F_{\parallel}(z, r, t) + F_{\parallel}(z, r, t + \delta t)]\delta t. \quad (5.1b)$$

Here, z is the axial position, δt is the integration time step, v_{\parallel} is the velocity parallel to the magnetic field, m is the positron mass, and F_{\parallel} is the force in the magnetic field direction.

For a positively charged particle with charge e in a potential ϕ and magnetic field B ,

$$F_{\parallel}(z, r, t) = -e \frac{d\phi(z, r, t)}{dz} - \frac{mv_{\perp}^2}{2B(z)} \frac{dB(z)}{dz}. \quad (5.2)$$

The first term is the force on the particle in a spatially varying potential, while the second term is the force on the positron orbital magnetic moment (cf. Eq. (3.2)) due to the spatially varying magnetic field.

The perpendicular velocity at any axial position can be determined using Eq. (3.2) as

$$v_{\perp}(z) = v_{\perp,0} \sqrt{\frac{B(z)}{B(z_0)}}, \quad (5.3)$$

where $v_{\perp,0}$ and z_0 are the initial perpendicular velocity and axial positions as determined from the initial distributions described above. Additionally, variations in the axial magnetic field, dB/dz , lead to a non-zero radial magnetic field component which results in a radial displacement to the positron guiding centers as they move in z ,

$$r(z) = r_0 \sqrt{\frac{B(z_0)}{B(z)}}, \quad (5.4)$$

where r_0 is the initial displacement of the guiding center from the axis of symmetry.

The positron trajectories can be determined using Eqs. (5.1)-(5.4) as the particles interact with the varying potential and magnetic field. For the simulations discussed here, the trajectories of 20,000 positrons were followed for each simulation. The externally applied potentials $\phi(z, r, t)$ are calculated as a function of z , r and t on a grid of 0.05 cm, 0.25 cm, and 5 ns, respectively, using a finite-element method and the experimental electrode geometry. The magnetic fields $B(z)$ are defined on-axis only, using an axial step size of 0.05 cm. The numerical integration was done using a time step δt of 1 ns. Reducing this time step by an order of magnitude had no significant effect on the results, indicating that stable numerical solutions were reached.

5.2 Results: Experimental geometry

The simulation parameters chosen throughout this section are intended to replicate the experimental conditions as accurately as possible. The initial parallel and perpendicular velocities are chosen to form 1-D and 2-D MB distributions at 300 K (unless otherwise noted), with the initial radial positions Gaussian-distributed with a FWHM of 0.5 cm ($\sigma = 0.21$ cm). The externally applied potentials due to voltages on the electrodes are calculated using realistic electrode geometry, and $B(z)$ is taken directly from experimental measurements (cf. Fig. 2.7).

Figure 5.1 shows the geometry and initial conditions used in the simulation. The positrons are initially confined within the potential well generated by the trapping-gate, well and exit-gate electrodes, here set to 30, 0 and 3 V, respectively. They are allowed to bounce within the well for 10 μs to verify that they remain MB distributed at their initial temperature, after which the pulsed beam is formed at $t = 0$ μs by increasing the well voltage according to Eq. (2.2) with $V_s = 3.5$ V, $V_0 = 0$ V and $\tau_r = 10$ μs .

5.2.1 Dynamics during beam formation

The on-axis potential and positron positions at three different times during the ramp are shown in Fig. 5.2. At 16 μs [Fig. 5.2 (a)] the positrons are still confined within the potential well, but the well depth has decreased to ~ 75 mV. At 18.5 μs [Fig. 5.2 (b)], the well has become nearly flat, and some of the positrons have escaped, while the bulk of the positrons have been ejected at ~ 20 μs [Fig. 5.2 (c)].

The beam formation process is highly dynamic in nature. The initial positron bounce time in the potential well is ~ 1 μs , however this increases with time during the ramp, reaching ~ 2 μs

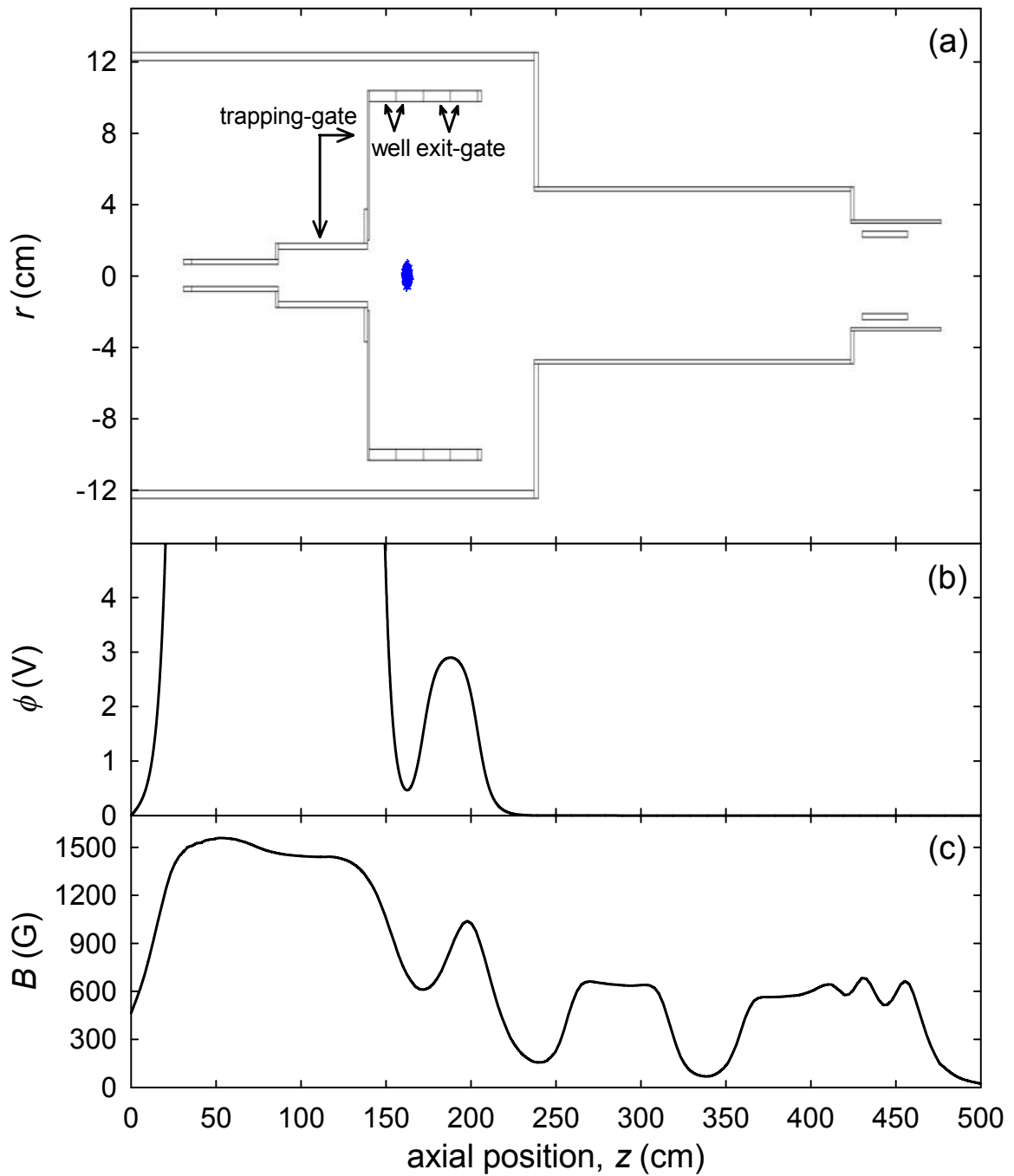


Figure 5.1: BGT-based beamline simulation initial conditions. (a) electrode geometry with (•) positron initial axial and radial positions, (b) initial on-axis potential and (c) axial magnetic field. For this example, the trapping-gate, well and exit-gate electrodes are set to 30, 0 and 3 V respectively.

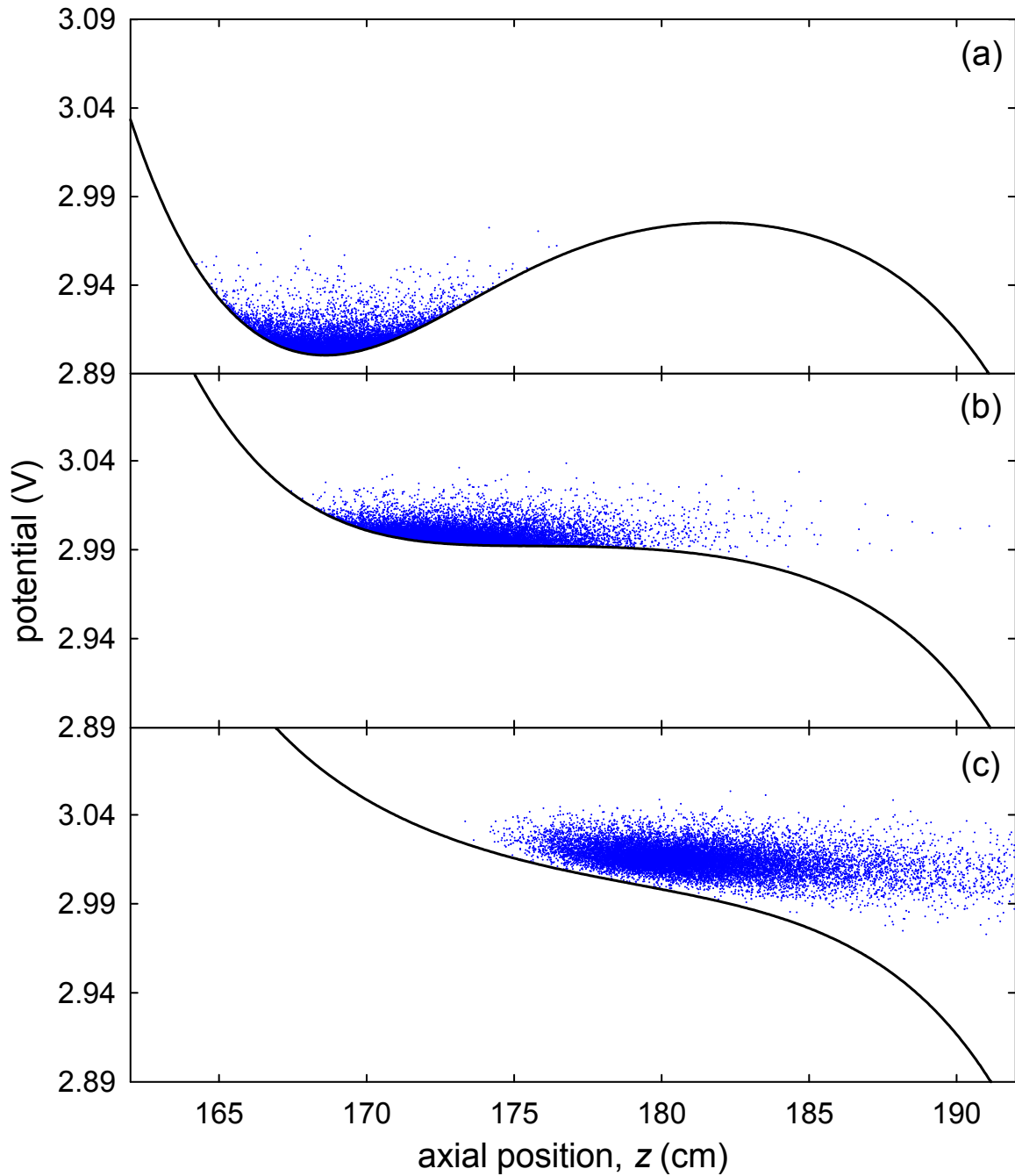


Figure 5.2: Simulated BGT positron ejection. (—) on-axis potential and (•) positron positions and energy at (a) $t = 16 \mu\text{s}$, (b) $t = 18.5 \mu\text{s}$ and (c) $t = 20 \mu\text{s}$ for the conditions described in Fig. 5.1. The ramp function is as in Eq. (2.2), with $V_s = 3.5$ V, $V_0 = 0$ V, and $\tau_r = 10 \mu\text{s}$.

during the last bounce before ejection. While each positron makes ~ 12 bounces during the time the potential well is ramped, the final bounce has the largest impact on the resulting beam characteristics.

Figure 5.3 shows the time dependence of important parameters during beam formation. The fraction of positrons remaining within the well is shown in Fig. 5.3 (a), while the average well width w , calculated by averaging the width of the well over positron energy at a given time, is seen in Fig. 5.3 (b). The well width is a constant, w_0 , until $t = 0 \mu\text{s}$, at which time the well voltage is ramped according to Eq. (2.2), causing w to increase as the positrons are raised in the approximately parabolic well. As the well potential approaches the exit-gate potential, w increases dramatically, after which time the potential becomes flat and the well disappears. Note that, for the electrode geometry and potentials used here, few positrons are ejected from the trap until after $V_W > V_E$ and the well disappears (cf. Fig. 5.3).

The parallel temperature during beam formation is shown in Fig. 5.3 (c), obtained by fitting the parallel velocities of the positrons remaining within the well to a 1-D MB distribution. Here it is seen that the parallel temperature decreases by a factor of ~ 3 during the beam formation process. This can be explained by conservation of the longitudinal adiabatic invariant, $J \sim v_{\parallel} w$, where w is the width of the potential well [48]. Expansion of the well during the ramp produces adiabatic cooling of T_{\parallel} . For comparison, the dashed line in Fig. 5.3 (c) shows the calculated T_{\parallel} due to adiabatic cooling,

$$T_{\parallel}(t) = T_{\parallel,0} (w_0/w(t))^2, \quad (5.5)$$

where $T_{\parallel,0}$ is the initial parallel temperature, and $w(t)$ is the average well width [cf. Fig. 5.3 (b)]. The two curves agree very well until the sudden increase in w just before the well vanishes. This occurs on time scales comparable to the positron bounce time, and so in this case, the longitudinal adiabatic invariant is no longer conserved.

The parallel cooling process during beam formation is beneficial for both the energy and time resolution (discussed below). By tailoring the initial potential well geometry and ejection conditions, this effect can be of further benefit. However, beam formation and ejection must take place on time scales fast compared to the positron-neutral collision time scales to ensure that the positrons are not re-heated during ejection. For the experiments described here, the positron-neutral collision time was $\sim 1 \text{ ms}$, and so the effect of collisions is negligible during the $\sim 10 \mu\text{s}$ time required for beam formation.

5.2.2 Dynamics during beam transport

Once the positrons are ejected from the trap, they continue downstream in the spatially varying magnetic field. Figure 5.4 shows the axial and radial particle positions, the on-axis potential and magnetic field at $t = 22 \mu\text{s}$ for a simulation under the conditions described in Fig. 5.2. Here, the effects of the spatially non-uniform magnetic field is clearly seen as the radial expansion of the beam in regions of low B .

The parallel, perpendicular, and total energies are calculated for each particle at each axial location. To compare with experimental results, the beam energy distributions are recorded in the RPA region, while the temporal distribution is calculated at the location of the annihilation plate. Random, time-dependent voltage fluctuations with a root-mean-squared (rms) voltage of 7 mV were added to the potential of each electrode, and the distributions are obtained by taking the average of 50 separate simulations. This most accurately replicates the procedures and parameters used to experimentally measure the energy distribution using the RPA technique described earlier. Finally,

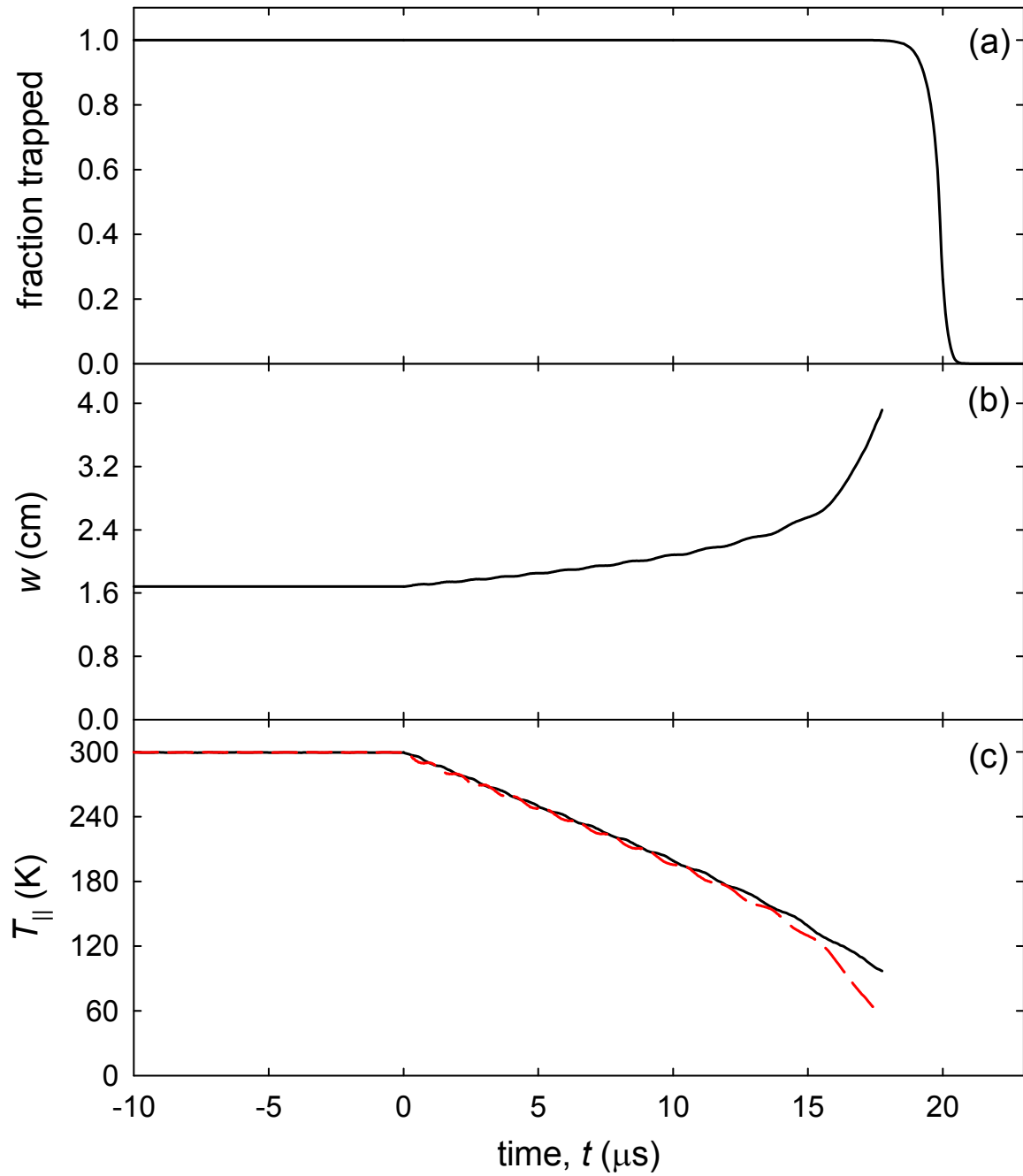


Figure 5.3: Simulated BGT parameters during ejection. (a) fraction of positrons remaining in the trap, (b) average width w of the potential well as seen by the positrons and (c) parallel positron temperature for the conditions described in Figs. 5.1 and 5.2. (- -) shows positron temperature obtained from Eq. (5.5) using $w(t)$ shown in (b).

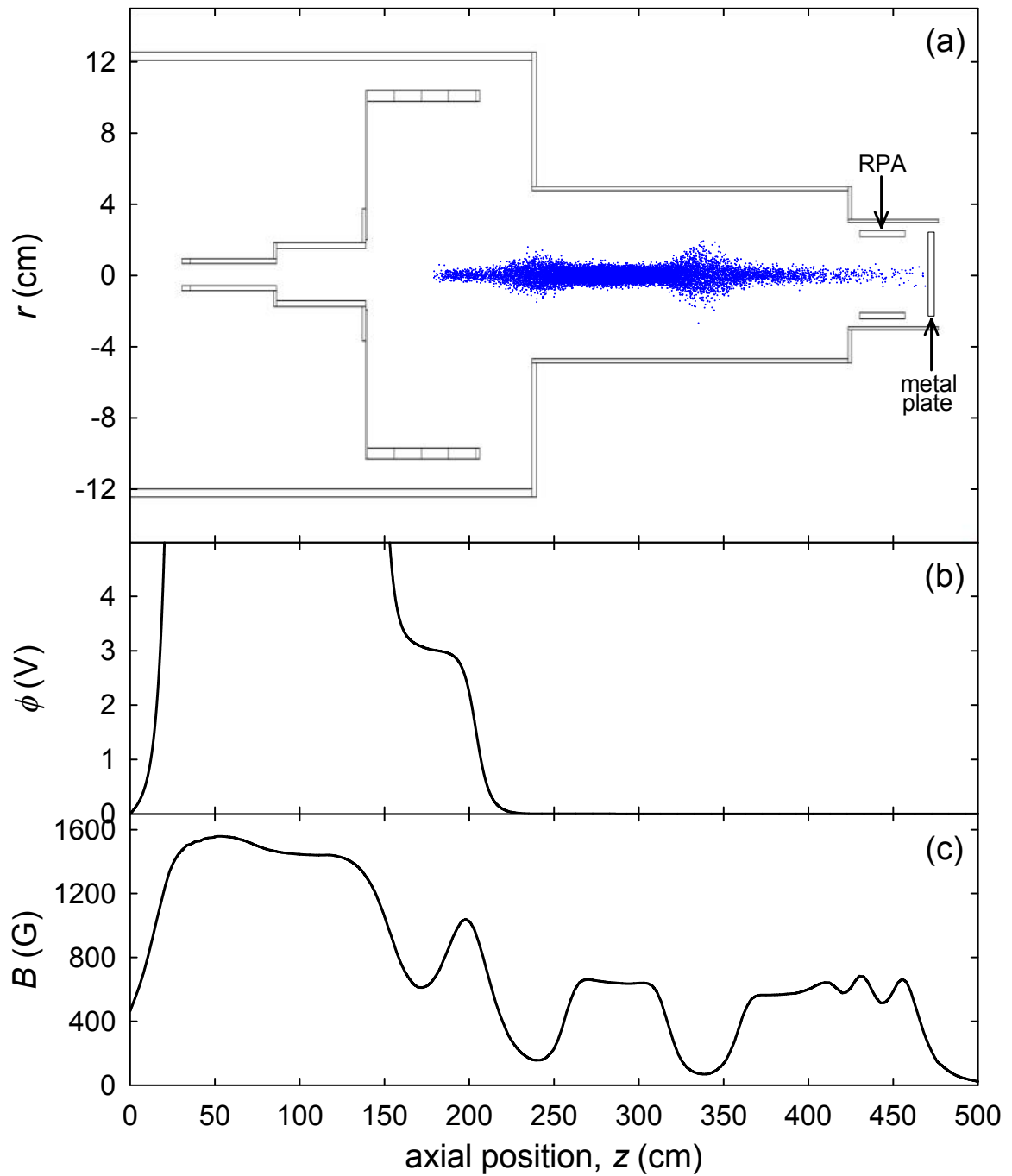


Figure 5.4: BGT-based beamline simulation beam transport. (a) electrode geometry with (•) positron axial and radial positions, (b) on-axis potential, and (c) on-axis magnetic field at $t = 22 \mu\text{s}$, under the conditions described in Fig. 5.1 and 5.2.

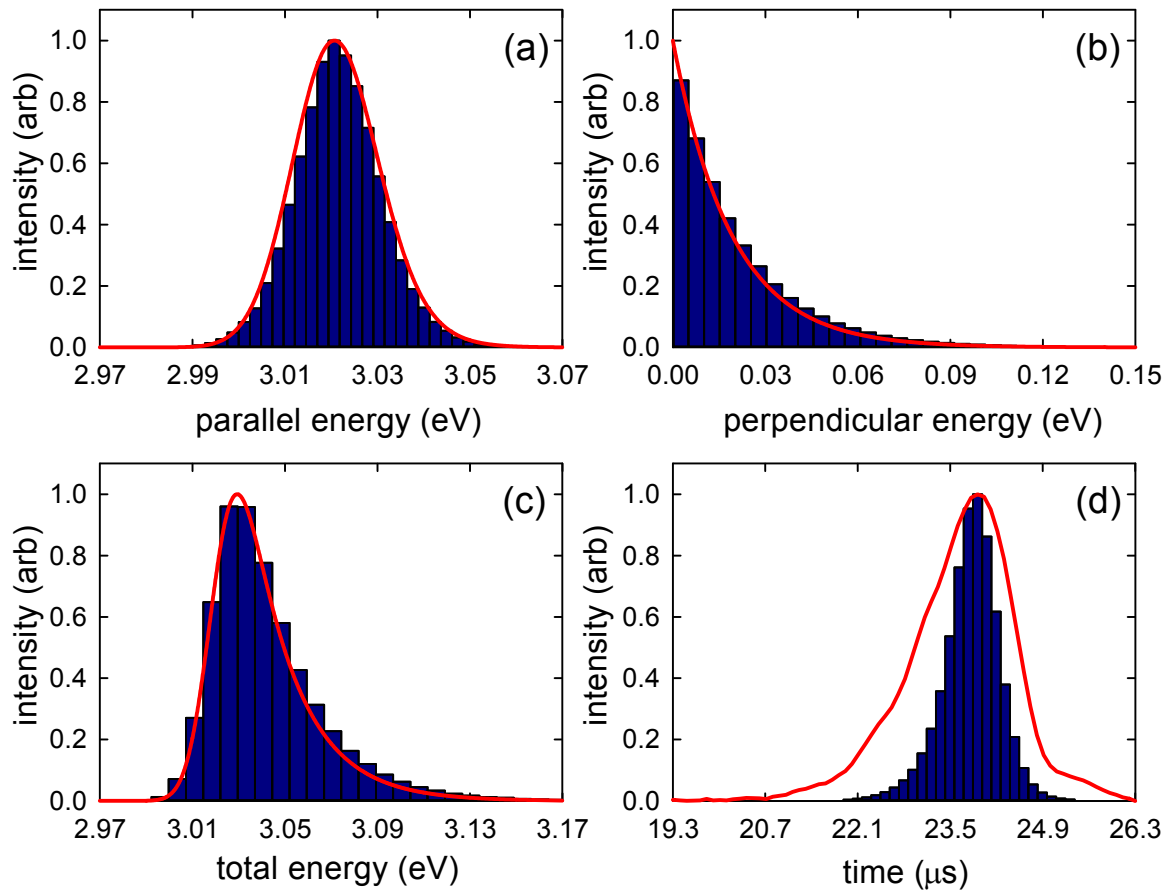


Figure 5.5: BGT distributions obtained from experiment and simulation for the conditions described by Figs. 5.1-5.4. (a) parallel energy, (b) perpendicular energy, (c) total energy, and (d) time. Blue bars represent simulation results, and red lines show experimental measurements. See text for details.

the temporal distributions are convolved with a $0.5 \mu\text{s}$ FWHM ($\sigma = 0.21 \mu\text{s}$) Gaussian distribution to account for the detector response. The consequences of these additional effects, which are relatively minor under most conditions, are discussed further below.

5.2.3 Comparisons and parameter studies

In this section experimental and simulation results for the temporal and energy distributions of the beams are compared and the effects of varying the initial conditions and ejection parameters are discussed. Since the experimental geometry is necessarily fixed (i.e., electrode dimensions and positions), the principal parameters affecting beam quality are the initial positron temperature and the imposed variation of electrode potential as a function of time in the region of the trapping well. For the experimental data shown, the error bars are based on the propagated standard error obtained from their respective fits.

Beam distributions

The beam distributions obtained under the experimental and simulation conditions described by Figs. 5.1-5.4 are shown in Fig. 5.5. As discussed in Chapter 3, due to extrinsic effects, arbitrary shifts in the energy axis are present in the experimental energy measurements. Therefore the experimental parallel and total energy measurements shown here have been shifted along the x-axis to match the peaks in the simulations. For the simulations shown in Fig. 5.5, the standard deviations are 9.0, 21, and 23 meV for the parallel, perpendicular and total energy distributions, and 0.26 μ s for the temporal distribution. For comparison, the respective experimental values are 9.7, 19.1 and 22.5 meV for the energy spreads, and 0.71 μ s for the time spread.

The simulated parallel, perpendicular, and total energy distributions agree well with the measured distributions. However, the measured temporal distribution is significantly broader than the simulation results, though the shape is qualitatively consistent. Unfortunately, the reason for this discrepancy is unclear, although a similar effect was seen by Tattersall *et al.* [49]. Experiments and simulations show that non-uniformities in the (presumed smooth) exit-gate potential can substantially broaden the time spread by reflecting some fraction of the positrons during ejection, therefore requiring them to make additional bounces within the well. Experiments were done to minimize the effects of these non-uniformities, and yielded reductions in the time spreads similar in magnitude to the discrepancies seen here. Additionally, experimental measurements show a moderate dependence of the temporal spread on the number of positrons (cf. Fig. 3.7), suggesting positron-positron effects may be important. These effects are still under investigation.

Ejection Rate

In order to study the effects of varying the *dynamics* of the ejection process, the initial well geometry is held fixed, while the time dependence of the voltage applied to the well electrode is varied. For the data presented here, the trapping and exit-gate electrodes were held at 30 and 3 V, respectively, with the well electrode initially at ground.

Referring to the ramp function given by Eq. (2.2), two parameters affect how fast the positrons are ejected from the trap without affecting the initial well geometry: the steady-state voltage V_s , and the RC time τ_r . Experimentally, τ_r is set by the resistance and capacitance of the amplifier-electrode circuit, while V_s is the steady-state voltage applied to the well electrode. The effect of varying the latter is discussed here.

While the positrons typically have long exited the trap before the ramp reaches V_s , its value changes the time at which $V_W \sim V_E$ (and therefore the slope of the voltage ramp, see Fig. 2.6). For this reason, an important quantity is the height the well is raised above the exit-gate potential, called here the ramp voltage, $\Delta V_r = V_s - V_E$.

Figure 5.6 (a) shows the standard deviation of the parallel energy distribution as the ramp voltage is varied. The simulation results agree well with the experimental measurements, with both showing a similar increase in parallel energy spread as ΔV_r is increased. This increase is due to the potential well lifting the positrons above the exit-gate potential during the last bounce before being ejected from the trap. The first positrons to be ejected leave the trap with parallel energies comparable to the exit-gate potential, while successively ejected positrons are lifted above it (cf. Fig. 5.2), adding to the parallel energy spread. This effect is more pronounced at higher ramp voltages, leading to the increase in σ_{\parallel} with Δ_r .

Because the perpendicular energies are not affected by the beam formation process, the mean perpendicular energy of the beam remains constant (~ 20 meV) as the ramp voltage is varied.

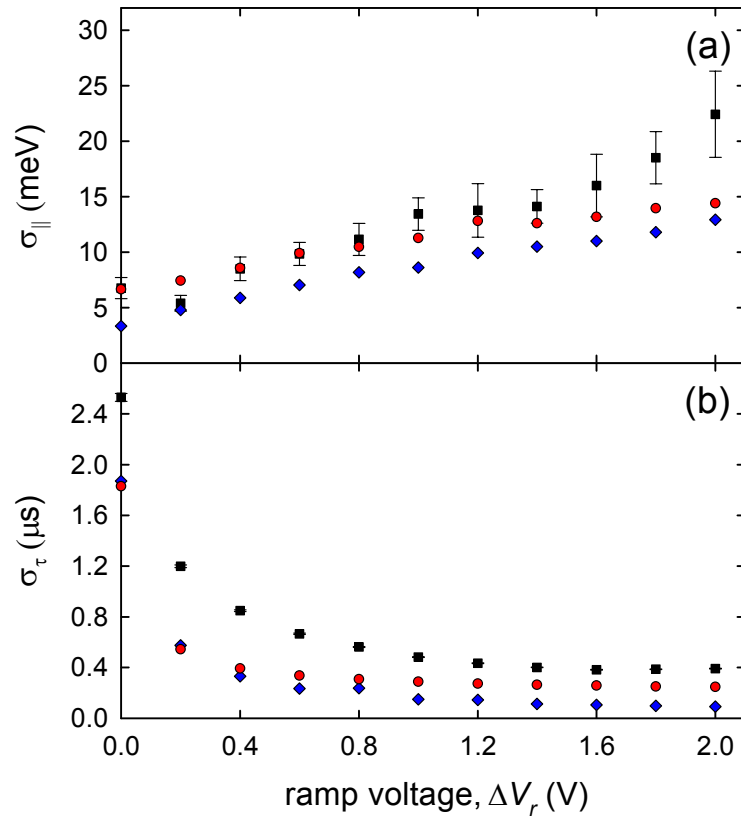


Figure 5.6: Effect of ramp voltage on the BGT beam. Standard deviations of the (a) parallel energy and (b) time distributions using various ramp voltages, $\Delta V_r = V_s - V_E$, with $V_T = 30$ V, $V_E = 3$ V, and $\tau_r = 10$ μ s. (■) experimental measurements, (●) simulation results, and (◆) simulation results without the nominal 7 mV rms electronic noise and broadened NaI detector response.

Consequently, changes in the total energy spread depend only on the parallel spread. As discussed earlier, the total energy spread may be approximated using Eq. (3.5) once the parallel and perpendicular spreads are known.

The dependence of σ_τ on the ramp voltage is shown in Fig. 5.6 (b). As discussed earlier, the simulations yield smaller time spreads than those measured experimentally. However, the simulations and measurements show a similar trend with changes in ΔV_r , namely larger ΔV_r values yield smaller time spreads. This can be explained by the mechanism described above. The later a positron is ejected from the trap, the more quickly it is accelerated out of the trap by the raising potential. Therefore, the higher the ramp voltage, the smaller the time between the first and last positron ejected, and so the smaller the time spread.

Under this mechanism, the parallel-energy and time spreads are oppositely affected. Larger ramp voltages lead to smaller time spreads and larger energy spreads; while smaller ramp voltages lead to smaller energy spreads and larger time spreads. While varying the ejection dynamics cannot improve both of these parameters simultaneously, it does allow one of these parameters (at a time) to be optimized for a particular application.

Also shown in Fig. 5.6 are the simulation results without the effects of the 7 mV rms electrical noise and detector response. Here it is seen that the contribution from the noise is typically a small fraction of the parallel energy spread, particularly at higher ramp voltages where the parallel energy spreads are larger. However, for beams generated using low ramp voltages, as much as 50% of the parallel energy spread is due to this noise, indicating that minimizing electronic noise is necessary for optimum parallel energy resolution.

The mechanism by which electronic noise broadens the parallel energy spread depends on the time scale of the noise. For electronic fluctuations on time scales short compared to positron ejection times, the noise acts to provide additional fluctuations in the parallel energy of each positron, thereby increasing the parallel energy spread of a given pulse. Alternatively, if the noise occurs on time scales long compared to the ejection time, the noise contributes the same random perturbation to the energies of *all* of the positrons in a given pulse, thus shifting the mean parallel energy. Over multiple pulses, these random shifts cause a broadening of the *average* parallel energy distribution.

While σ_τ is not affected by the presence of electronic noise, the detector response affects the temporal distribution in cases where the time spread is small. This contribution is relatively large at high ramp voltages, broadening the time spread by as much as a factor of ~ 3 ; however it is insufficient to account for the discrepancy between the measured and simulated temporal distributions [cf. Fig. 5.6 (b)]. Further, the breadth of the temporal distribution is as large or larger at low ramp voltages, where effects due to detector response are negligible.

Initial temperature

For the experiments and simulations described here, the applied trapping-gate voltage, initial well voltage, and exit-gate voltages were kept the same as above (30 V, 0 V and 3 V, respectively), with the ramp function as in Eq. (2.2) with $V_s = 3.5$ V and $\tau_r = 10$ μ s. Experimentally, the positrons were allowed to cool on N₂ for a variable amount of time. Molecular nitrogen was used as the primary cooling gas, rather than CF₄, for more precise control of the final positron temperature (due to slower cooling times with N₂). The positron temperature was then measured using the procedure described in Chapter 3 to obtain beam parameters at a variety of temperatures ≥ 300 K. In the simulations, the initial parallel and perpendicular velocity distributions are taken to be 1-D and 2-D MB distributions at the specified temperature.

As discussed earlier, simulations show that the final parallel temperature of the trapped positrons is lower than the initial parallel temperature due to the presence of adiabatic cooling during beam formation. As the initial temperature is varied, the final temperature also varies, keeping the ratio of these values approximately constant. The perpendicular temperature is unaffected by this process.

Figure 5.7 shows the energy and time spreads as the positron temperature is varied. Here, as in the case described above, the simulated and measured σ_{\parallel} are in good agreement. The increase in σ_{\parallel} with temperature can be explained by inspection of the allowed trajectories as the positrons are lifted out of the potential well. Particles with higher parallel velocities are able to explore a larger region of the potential well. This results in a wider variety of trajectories, and hence a greater variety of final energies, thereby increasing σ_{\parallel} .

At low temperatures, for example, the positrons have a small spread in parallel velocities, which also limits the axial positions that can be explored. Therefore, the distribution of axial positions when the positrons have sufficient energy to overcome the exit-gate barrier is narrower, and this results in the positrons exiting the trap with a smaller range of energies. These processes are discussed in more detail in Sec. 5.3.

The perpendicular energy spread is shown in Fig. 5.7 (b). Not surprisingly, σ_{\perp} is proportional to the positron temperature. Had the magnetic field been uniform (*i.e.*, equal in magnitude in the BGT and RPA), σ_{\perp} would be equal to $k_b T$. However, in the case considered here, the magnetic field is non-uniform, particularly in the region where the beam is formed (*cf.* Figs. 5.1 and 5.4). The result is $\sigma_{\perp} \sim 0.8 k_b T$ due to perpendicular energy transferred into parallel by invariance of the orbital magnetic moment.

As shown in Fig. 5.7 (c), the total energy spread is dominated by σ_{\perp} over the temperature range studied. This can be seen from Eq. (3.5) in the limit where $\sigma_{\perp} \gg \sigma_{\parallel}, \sigma_{\parallel, \perp}$. Thus, for beams with $\sigma_{\parallel} \ll k_b T$, reducing T is a particularly effective method for improving the total energy spread.

Finally, Fig. 5.7 (d) shows the effect of positron temperature on the temporal spread of the beam. As discussed above, the simulations under-predict σ_{τ} as compared to the experimental measurements. However, the overall trend is the same: reducing positron temperature yields a smaller time spread. The mechanism invoked to explain the dependence of σ_{\parallel} on temperature also provides a consistent explanation of the temporal behavior. At higher temperatures, more positrons have sufficient energy to be trapped higher in the potential well, thus allowing them to be ejected earlier (*i.e.*, when $V_W \lesssim V_E$). This, in turn, increases the time spread. These processes are discussed in more detail in Sec. 5.3

These results show that reducing the temperature of the initial positron cloud is an effective way to improve both the energy and time resolution. In fact, combining this result with the effects of varying the ramp voltage (discussed in the previous section), could provide an additional reduction of either the energy or time spread. In particular, adjusting the ramp voltage, such that either the time or energy spread remains constant as the temperature is reduced, will result in additional improvements to the chosen distribution beyond simply varying the temperature.

Also shown in Fig. 5.7 are simulation results without the 7 mV RMS electronic noise and minimum detector response. As in the previous section, the impact of the noise is most significant at very low parallel energy spreads, contributing $\sim 30\%$ to the parallel energy spread at 300 K. Since the total energy spread is dominated by the perpendicular spread under these conditions, and electronic noise has no effect on the perpendicular energy. In this case, the effect of electronic noise on the total energy spread σ_{τ} is quite small. Similarly, the broadening of the temporal distribution σ_{τ} due to the detector response is relatively small over the temperature range studied.

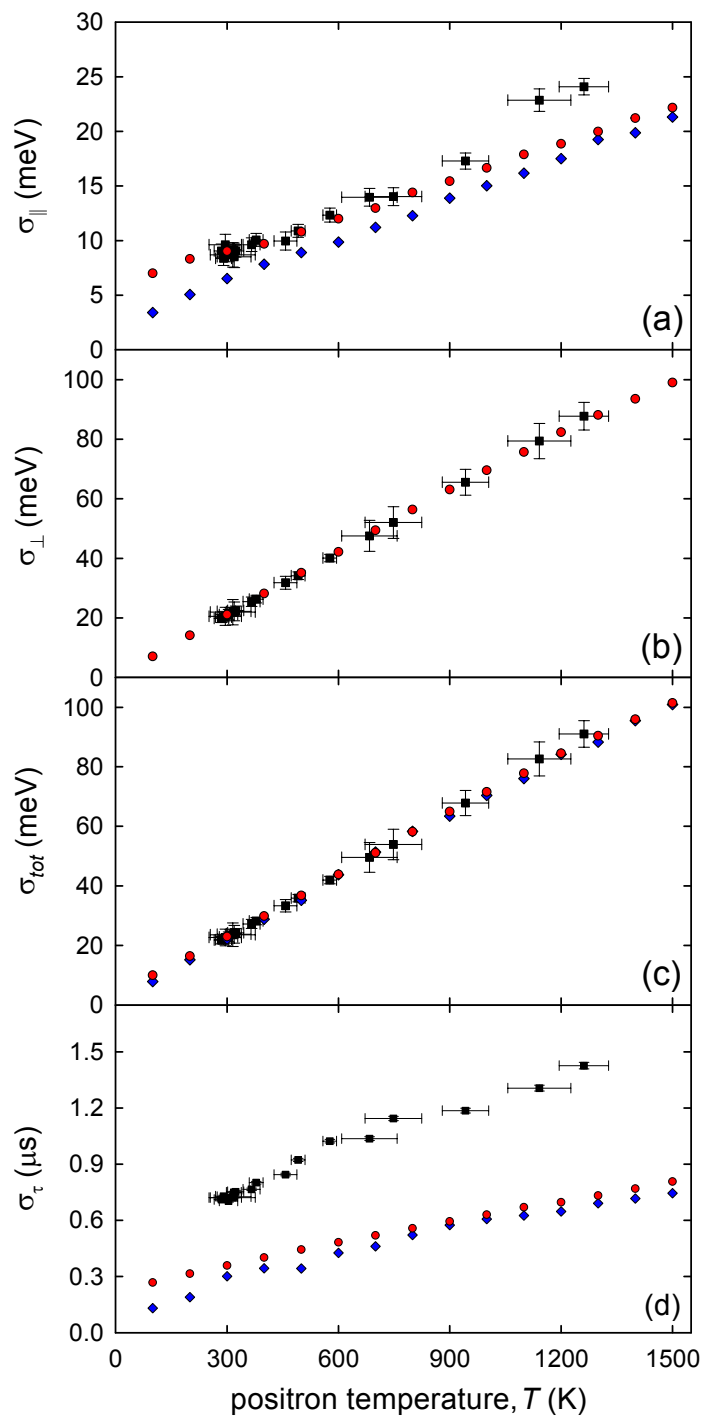


Figure 5.7: Effect of positron temperature on the BGT beam. Standard deviations of (a) parallel energy, (b) perpendicular energy, (c) total energy, and (d) time distributions of positron beam, generated at different initial positron temperatures: (■) experimental measurements; (●) simulation results and (◆) simulation results without the 7 mV RMS electronic noise and broadening due to NaI detector response.

5.3 Results: Generic geometry

Presented here are simulation results for trap-based positron beams formed using a variety of trap geometries and ejection conditions. This simulation technique was described above for the case where the parameters were chosen specifically to replicate experimental conditions, thus allowing direct comparisons with measurements of beam properties. While the previous work provided new insights into the underlying physical processes and validated the simulations, the work presented here uses the simulations to explore a larger parameter space not constrained by existing hardware

The simulation results presented in this section were obtained using the method described in Sec. 5.1, with one modification. The externally applied potentials are first calculated as a function of z , r and t on a grid of 0.05 cm, 0.25 cm, and 1 ns, respectively, using a finite-element method with the specified electrode geometry. However, for the simulations described in this section, a more precise value of $\phi(z, r, t)$ is then obtained by interpolating the grid solutions at the specific z and r positions calculated from the numerical integration at a given t . This last step is particularly important for simulating some of the narrower potential well geometries considered here. For the numerical integration, a time step δt of 1 ns was used. Reducing this time step by an order of magnitude had no significant effect on the results.

5.3.1 The generic Penning-Malmberg trap

An example of the generic trap geometry and confinement potentials used in the simulations discussed in this section are shown in Fig. 5.8. This is arguably the simplest possible PM trap, consisting of three cylindrically symmetric electrodes labeled from left to right as the trapping, well, and exit-gate electrodes, with corresponding applied voltages V_T , V_W , and V_E . Voltages V_T and V_E provide axial confinement and are held constant, with $V_E < V_T$ to give a directionality to the ejected beam. The initial well voltage $V_W(0)$ then determines the initial well depth $V_E - V_W(0)$.

The trap geometry is specified by the electrode length L and aspect ratio $\alpha \equiv L/D$, where D is the electrode inner diameter. The electrode length sets the overall length of the potential barrier (or well) provided by the electrode, while its aspect ratio determines the shape. Electrodes with small aspect ratio provide less uniform, more parabolic potentials, while large aspect ratio electrodes produce potentials with flat regions near their center in the axial direction.

As seen in Fig. 5.8, the particles are initially placed within the potential well with the initial parallel and perpendicular velocity distributions chosen to be 1-D and 2-D Maxwell-Boltzmann (MB) distributions at a given temperature. The initial radial positions are Gaussian distributed with a full-width at half-max (FWHM) of 0.5 cm. The pulse is then formed by increasing the voltage applied to the well electrode according to a specified ramp function until the particles are lifted over the exit-gate potential and ejected from the trap.

5.3.2 Beam formation regimes

As described above, the beam formation process under typical conditions is highly dynamic in nature, with each particle following a unique trajectory through phase-space as it interacts with the changing potential. The particles bounce in the well with a frequency that depends upon the shape of the trapping potential as the well voltage V_W is increased at a rate \dot{V}_W . As V_W is increased, the well width increases, and the curvature of the potential decreases. This leads to an increase in the particle bounce time and a decrease in the parallel temperature of the particles due to adiabatic

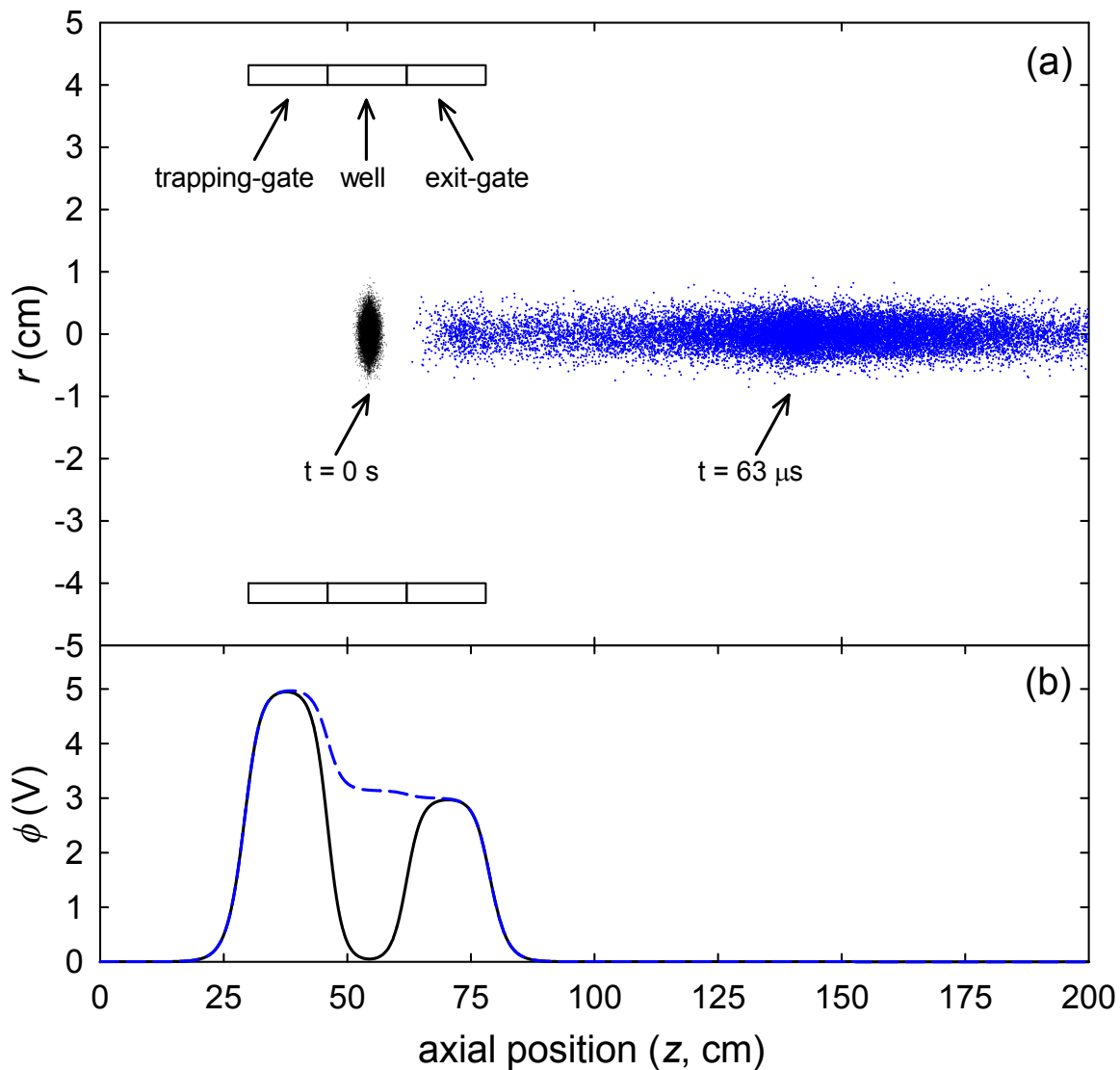


Figure 5.8: Generic PM trap simulation conditions. (a) electrode geometry showing the axial and radial positions of the particles during a typical beam pulse, and (b) the on-axis potential at (black) $t = 0$ μ s and (blue) $t = 63$ μ s. The voltages applied to the trapping and exit-gate electrodes are 5 V and 3 V, with the well voltage increased linearly from 0 V at $t = 0$ μ s at a rate of 50 mV/ μ s. All electrodes have lengths $L = 16$ cm, and aspect ratios $\alpha = 2$. Initial positron temperature is 300 K. See text for details.

cooling. Particles are first able to escape the trap only when they have sufficient kinetic plus potential energy to overcome the exit-gate barrier. This may occur at any point during the final bounce cycle depending upon the initial particle energy and phase of oscillation in the well.

In this section three distinct regimes for beam formation are discussed. The regime in which most BGTs currently operate is termed here the “full bounce” regime. Additionally, a new regime is identified which yields significantly improved beam quality. Termed the “low temperature” regime, this occurs when the positron temperature is low enough to constrain the possible positron trajectories in the well and therefore minimize the energy and time spreads of the resulting beam. Finally, there exists a third regime in which the positrons are ejected from the well on time scales in which the axial motion of the particles is negligible during beam formation. In this “non-dynamic” regime, the beam formation process is vastly simplified, and under certain conditions may provide superior beam energy resolution. The unique dynamics governing beam formation in each of these three regimes are introduced below.

In order to more clearly display the effects of beam formation on beam quality, we focus on the trajectories of the particles with the lowest and highest final parallel energies in the resulting beam, thus setting the *full* width of the parallel energy distribution. These trajectories are shown in Fig. 5.9 for typical conditions in each of the three regimes. Also shown are the on-axis potentials and corresponding particle positions at five evenly divided times during the time the particles are able to escape the trap. This interval begins when the first particle has kinetic plus potential energy greater than the maximum in the exit-gate potential at this time, ϕ_E , and ends when the final particle crosses the position of the peak in the exit-gate potential, z_E .

While only the extreme trajectories are shown in Fig. 5.9, the beam is the result of the unique trajectories of many thousands of particles. The change in parallel energy of a given particle during beam formation may be described using a basic feature of Hamiltonian systems, namely that, for the Hamiltonian $H(z,t)$ of a particle in an electrostatic potential, $dH/dt = (\partial H/\partial t)_z$ [50]. Additionally, since the particle is unable to escape the trap until $E_0 + \delta E_{\parallel} > e\phi_E$, where E_0 is its initial kinetic plus potential energy and δE_{\parallel} is its change in parallel energy during beam formation, it is useful to write the final parallel energy of a given particle in the resulting beam as

$$E_{\parallel} = e\phi_E + \int_{t_U}^{t_E} \left[\frac{\partial \phi(z,t)}{\partial t} \right]_z dt. \quad (5.6)$$

Here t_U is the time at which the particle energy equals $e\phi_E$ (and therefore becomes “untrapped”), and t_E is the time at which it crosses the position of the peak in the exit-gate potential z_E (beyond which $\partial\phi/\partial t \approx 0$), and thus is ejected from the trap.

Full bounce regime

A key feature of the full bounce regime [cf. Fig. 5.9 (a)] is that the fate of the particles in and following their final bounce in the well fixes the spread of energies and times in the resulting beam. The lowest energy particle in the beam is among the first to escape the trap. This particle obtains sufficient energy to overcome the exit-gate barrier at the *end* of a bounce cycle (i.e., $t_U \approx t_E$ in Eq. (5.6)), thus releasing it with the minimum possible energy $E_{\parallel} \sim e\phi_E$. Here, a bounce cycle is defined to begin and end upon reflection from the exit-gate barrier. In contrast, the particle ejected with the highest parallel energy is among the last to escape the trap. This particle encounters the barrier with an energy slightly less than necessary to escape. In this case, the particle is reflected such that it gains sufficient energy to escape the trap at the *beginning* of its next bounce cycle,

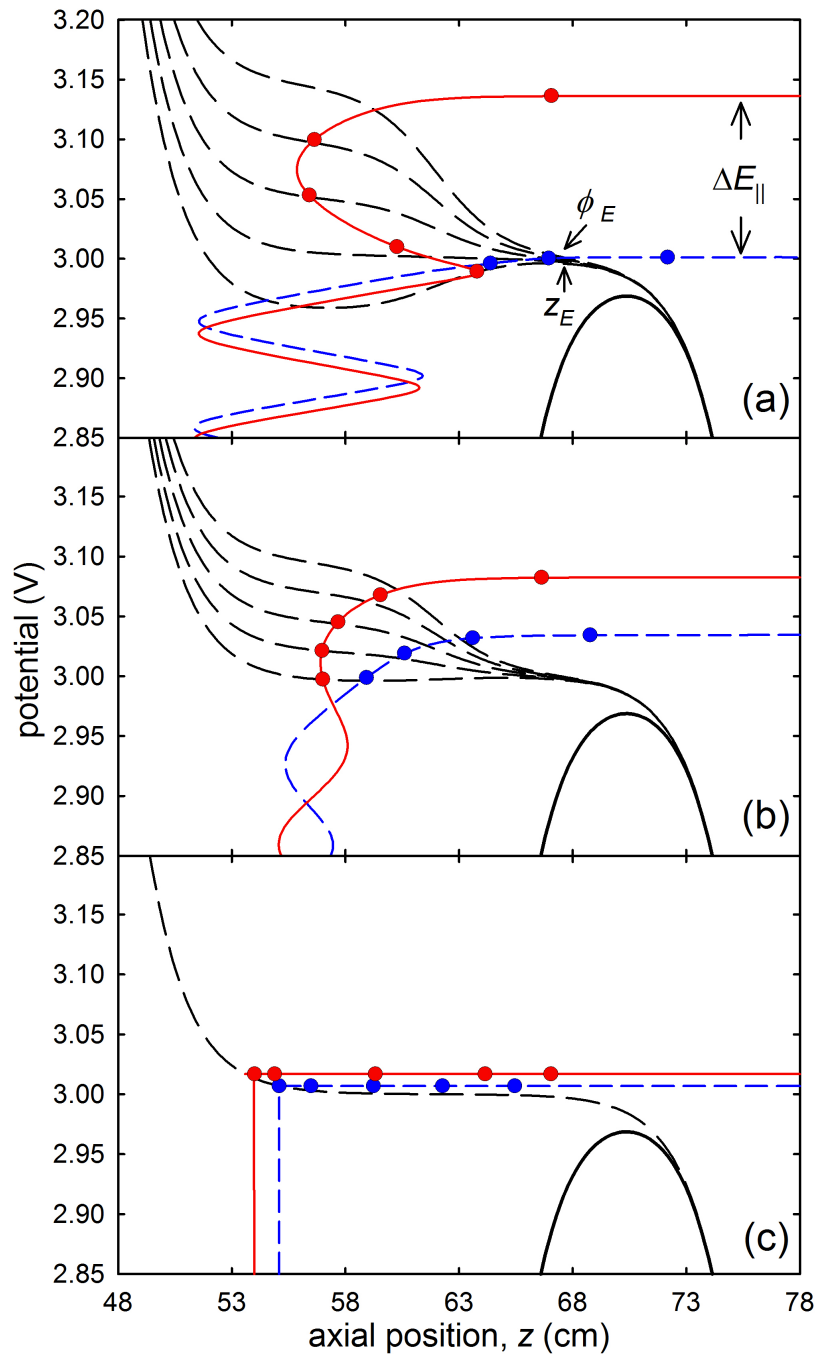


Figure 5.9: Beam formation regimes. (a) (—) Initial on-axis potential and trajectories of the particles with the (—) lowest and (—) highest final parallel energies in the simulated beam, thus setting the full width of the parallel energy distribution ΔE_{\parallel} . (—) and (•) show potentials and particle positions at 5 evenly divided times during ejection; (a) full bounce regime: $T_0 = 300$ k, (b) low temperature regime: $T_0 = 10$ K and (c) non-dynamic regime: $T_0 = 10$ K and well voltage increased linearly from 0 to 3 V in 10 ns. All other parameters as in Fig. 5.8.

but is forced to make another full pass through the rising potential region before escaping (i.e., $t_E - t_U \approx \tau_f^h$, where τ_f^h is the time required for this particle to make its final transit through the rising potential region). Therefore the highest energy particle is ejected with the maximum possible energy, $E_{\parallel} \sim e\phi_E + \tau_f^h \dot{V}_W$.

Low temperature regime

At low temperatures the initial phase-space is significantly reduced. The particles bounce within only a small region of the potential well and are therefore unable to escape the trap until $V_W \approx e\phi_E$ and the potential is nearly flat [Fig. 5.9 (b)]. This results in a majority of the particles obtaining sufficient energy to escape the trap at nearly the same time, but still having to traverse a significant portion of the rising potential region before being ejected. Because of this, all particles are lifted above the exit-gate potential before being ejected (i.e., there is no trajectory for which $T_U \approx T_E$ in Eq. (5.6)), and no particles are able to gain sufficient energy to escape at the beginning of a bounce cycle (i.e., there is no trajectory for which $T_E - T_U \approx \tau_f^h$). In this low temperature regime, particles that are ejected with the lowest (highest) parallel energies are those that have the largest parallel energy and are traveling towards (away from) the exit-gate barrier at the time they have sufficient energy to escape.

Non-dynamic regime

Finally, an example of the trajectories obtained in the non-dynamic regime are shown in Fig. 5.9 (c). Here, the well potential is raised sufficiently fast that the axial motion of the particles is negligible during beam formation, and therefore the complicated dynamical processes encountered in the other two regimes are absent. Specifically, adiabatic cooling does not occur, and the initial parallel energy distribution is unaltered by the presence of the exit-gate barrier. Further, provided the final potential is reasonably flat over the region occupied by the particles, they will simply be ejected from the trap with their initial thermal energies plus their potential energy relative to ground. Under these conditions, the parallel energy distribution is a shifted Maxwell-Boltzmann distribution with $\sigma_{\parallel} = 1/2k_bT_0$, while the perpendicular energy distribution remains MB distributed with $\sigma_{\perp} = k_bT_0$ (as is the case in all of the regimes discussed here). Using Eq. (3.5), the total energy spread may then be written simply as $\sigma_t = \sqrt{5}/2k_bT_0$. Note that an alternate method of obtaining this result would be to rapidly drop the exit-gate barrier rather than increase the potential well. In the interest of brevity, only the case of increasing the potential well is considered here.

5.3.3 Optimization and parameter studies

As discussed above, the simulations reported here are done in a uniform magnetic field, and so the spread in perpendicular energies is constant everywhere with $\sigma_{\perp} = k_bT_0$, where T_0 is the particle initial temperature. Under these conditions the total energy distribution varies only with σ_{\parallel} and may be obtained using Eq. (3.5). For this reason, only the affects of beam formation on σ_{\parallel} and σ_{τ} are discussed here.

Effect of the ejection protocol

Here, the initial well geometry is held fixed, and the time-dependence of the applied well voltage, $V_W(t)$, is varied. The particle ejection rate is quantified by the ejection ramp rate, \dot{V}_W , which

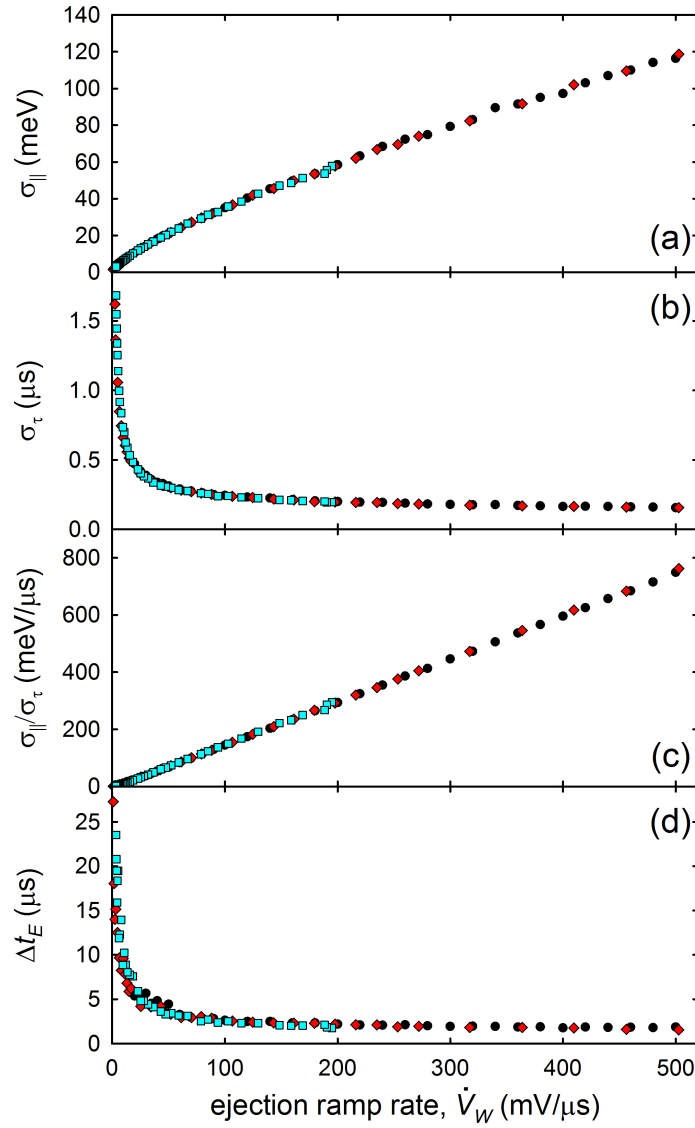


Figure 5.10: Effect of ejection protocol on simulated beam. Standard deviations of the (a) parallel energy and (b) time distributions obtained from the simulation, shown as a function of the calculated average ramp rates during the time particles escaped the trap. Also shown is the (c) ratio of the energy and temporal distributions and (d) total ejection time. The beams were generated using (●) a linear ramp with \dot{V}_W varied from 20 to 500 mV/ μ s, (◆) an RC ramp with the final voltage varied from 3.0 to 9.0 V and e-fold time fixed at 10 μ s, and (■) an RC ramp with e-fold time varied from 1 to 140 μ s and final voltage fixed at 3.5 V. All other parameters as in Fig. 5.8.

represents the average rate of change in the voltage applied to the well electrode during the time in which the particles are leaving the trap. The ramp rate is obtained by evaluating the derivative of the ramp function at the time each particle crosses the peak in the exit-gate potential, and taking the average.

Shown in Figs. 5.10 (a) and (b) are the standard deviations of the energy and time distributions as a function of their calculated average ramp rates for beams generated using three distinct protocols for varying the particle ejection rate, with all other parameters as in Fig. 5.8. Here it is seen that, at a given ramp rate, the same value for both σ_{\parallel} and σ_{τ} is obtained regardless of the protocol used to eject the beam. This indicates that the ejection rate *as the particles are raised above the end-gate potential*, \dot{V}_W , is the important quantity, and not the time dependence of $V_W(t)$ at earlier times. This simplifies greatly parameterization of the dynamical aspects of the beam formation process, allowing the ejection process to be well described by the single parameter \dot{V}_W . Thus, in the remainder of this section a linear ramp (i.e., \dot{V}_W held fixed) is used to eject the particles, allowing other parameters to be more clearly examined.

As seen in Fig. 5.10, increasing \dot{V}_W leads to an increase in σ_{\parallel} and a decrease in σ_{τ} (as also seen in the BGT, cf. Fig. 5.6). This occurs because, at higher ramp rates, the particles are given more energy during their final pass through the rising potential region, and are accelerated out of the trap more quickly due to the increased electric field, respectively. Of particular significance, as shown in Fig. 5.10 (c), is that the ratio $\sigma_{\parallel}/\sigma_{\tau}$ varies linearly with \dot{V}_W with a coefficient of order unity; namely

$$\sigma_{\parallel} = \beta \dot{V}_W \sigma_{\tau}, \quad (5.7)$$

where $\beta \approx 1.5$. This equation, which derives from the principle encapsulated in Eq. (5.6), may be understood by examining how the energy and temporal spreads are affected by the total time required to eject all particles.

The effect of the ramp rate on the total ejection time Δt_E is shown in Fig. 5.10 (d), where Δt_E is defined as the time between the first and last particle crossing the peak in the exit-gate potential, thereby escaping the trap. Comparing Figs. 5.10 (c) and (d), it is seen that $\sigma_{\tau} \propto \Delta t_E$. Further, under these conditions the parallel energy spread is primarily set by the rising potential, and so $\sigma_{\parallel} \propto \Delta t_E \dot{V}_W$. As \dot{V}_W is increased, Δt_E decreases, and this results in a decrease in temporal spread. However, the product $\Delta t_E \dot{V}_W$ increases, leading to an increase in σ_{\parallel} . These two relationships result in a coupling of the parallel energy and temporal spreads via the ramp rate, as described by Eq. (5.7).

Note that, under the conditions shown here, beam formation is in the full bounce regime. Simulations in the low temperature regime (discussed below) result in the same dependence on \dot{V}_W shown in Fig. 5.10, with both σ_{\parallel} and σ_{τ} reduced by a constant numerical scale factor which depends on the particle temperature. It should also be noted that in the non-dynamic regime $\dot{V}_W \approx 0$, since the potential is no longer changing by the time the positrons are ejected from the trap.

Effect of positron temperature

Shown in Figs. 5.11 (a) and (b) are the standard deviations of the energy and time distributions obtained using a variety of initial temperatures, T_0 , with all other parameters as in Fig. 5.8. As seen in Fig. 5.11 (a), σ_{\parallel} increases by a factor of ~ 5 as T_0 is increased from 5 to 500 K, but becomes quite insensitive to temperature as T_0 is increased further. In contrast, the temporal spread is seen to increase rapidly with T_0 at low temperatures, then asymptotes to approximately $\sigma_{\tau} \propto T_0$ at high temperatures. The measurements made using the BGT showed similar behavior, however were done over a smaller range of temperatures (cf. Fig. 5.7).

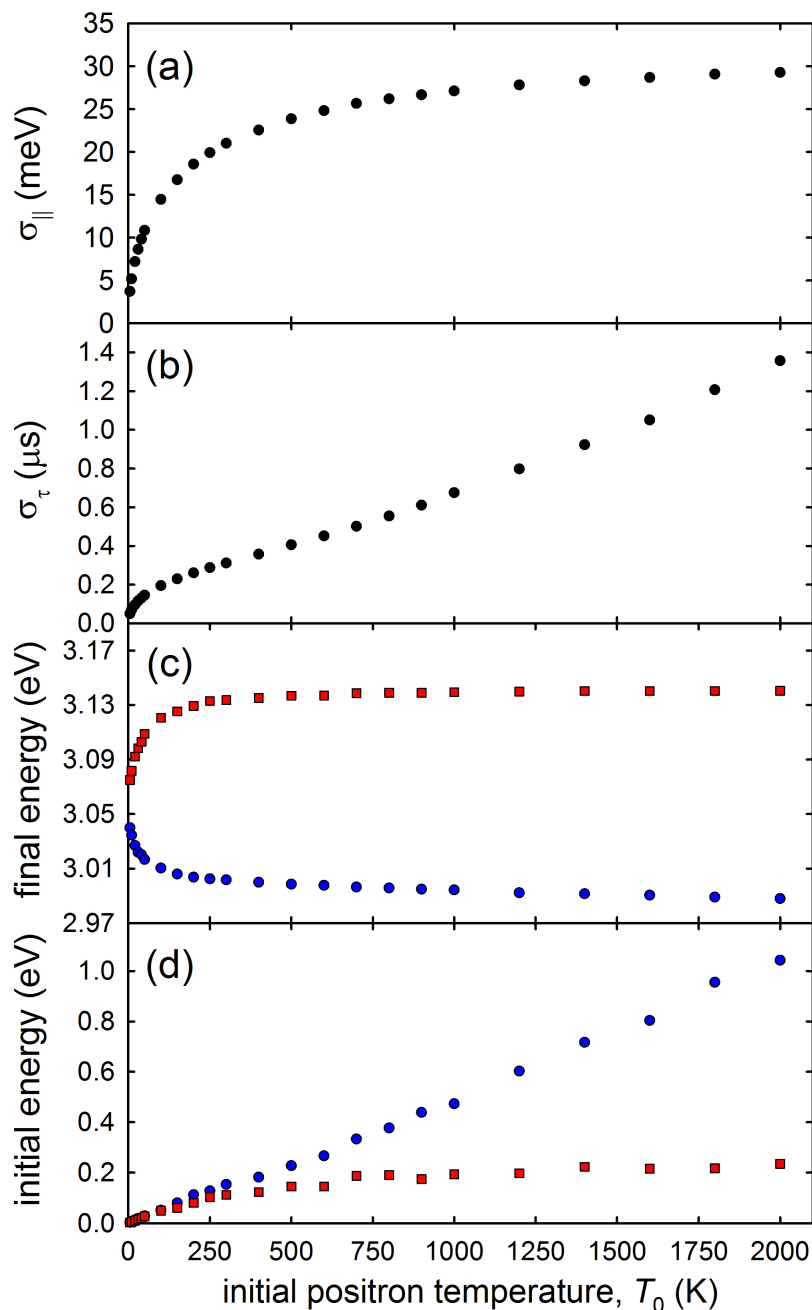


Figure 5.11: Effect of positron temperature on simulated beam. Standard deviations of the (a) parallel energy and (b) temporal distributions obtained from the simulation of beams generated using various initial particle temperatures. Also shown is the (c) final and (d) initial parallel energies of the particles which are ejected with the (●) lowest and (■) highest final parallel energies in the beam. All other parameters as in Fig. 5.8.

To better illustrate the effect of temperature on the available particle trajectories, the final and initial parallel energies of the particles that are ejected with the lowest and highest final parallel energies in the beam are shown in Figs. 5.11 (c) and (d). Here it is seen that the final energies of both extreme-energy particles are relatively constant at high temperatures; while at low temperatures, the minimum energy increases and the maximum energy decreases. This results in a relatively rapid narrowing of the full width of the parallel energy distribution.

In contrast, as seen in Fig. 5.11 (d), the initial energies of both the lowest and highest final energy particles are “selected” from specific energies in the initial thermal distribution. The particle ejected with the lowest final energy is on the high energy tail of the initial thermal distribution, and increases proportionately to the initial temperature with an energy $\sim 6k_bT_0$. At high temperatures the particle ejected with the highest final energy is one which has an initial parallel energy much lower in the thermal distribution. This optimal energy corresponds to an optimal width in the well and therefore an optimal final reflection position on the exit-gate potential. It is relatively constant as the temperature is decreased until the temperature is low enough that this initial energy state is no-longer populated. At this point, both the lowest and highest final energy particles are selected from the tail of the initial thermal distribution.

In light of the discussion above, the effects of the particle temperature on the beam distributions may be summarized as follows. At high temperatures, the initial phase space in the full bounce regime can be sufficiently populated so that the optimal well width may be obtained, and so all trajectories described by Eq. (5.6) with $0 \leq t_E - t_U \leq \tau_f$ are available. The primary effect of increasing the temperature in this regime is that particles on the tail of the initial thermal distribution are able to escape the trap at earlier times when $V_W < V_E$. This leads to an approximately linear relationship between σ_τ and T_0 at high temperatures [as seen in Fig. 5.11 (b)]. Because of the presence of the exit-gate barrier, those particles which escape the trap at earlier times are still ejected with approximately the minimum possible energy, $E_{\parallel} \sim e\phi_E$, while the particle ejected with the highest energy is the one which makes a full bounce above the exit-gate potential and is ejected with the maximum possible energy, $E_{\parallel} \sim e\phi_E + \tau_f^h \dot{V}_W$. Since the extreme particles are approximately at their minimum and maximum possible values in this regime, temperature has little effect on their ejection trajectories, and this results in σ_{\parallel} becoming insensitive to T_0 at higher temperatures [as seen in Fig. 5.11 (a)].

As the temperature is decreased the particles obtain sufficient energy to escape the trap at later times in the ejection process, resulting in a reduction in σ_τ . At very low temperatures the smaller initial phase-space results in the particles being unable to escape the trap until $V_W \approx V_E$ and the potential is nearly flat. Here the possible ejection trajectories are constrained to those where $0 \ll t_E - t_U \ll \tau_f$. This is the low temperature regime. In this regime the possible extreme energy trajectories are both set by particles on the tail of the initial energy distribution, resulting in a relatively strong reduction in both energy and temporal spreads as the temperature is reduced.

In contrast, in the non-dynamic regime $\sigma_{\parallel} \approx 1/2k_bT_0$, assuming the final potential is relatively flat over the regions the particles occupy. For this reason, at high temperatures superior energy resolution is obtained by operating in the dynamic regimes discussed above. However at low temperatures, operating in the non-dynamic regime may yield lower parallel energy spreads.

Effect of well depth

Shown in Fig. 5.12 are data for σ_{\parallel} and σ_τ when the initial well depth, defined here as $D_W \equiv V_E - V_W(0)$, is adjusted by varying the initial voltage applied to the well electrode $V_W(0)$. Here it is seen that increasing the well depth from 1 V to 50 V provides a $\sim 75\%$ improvement in

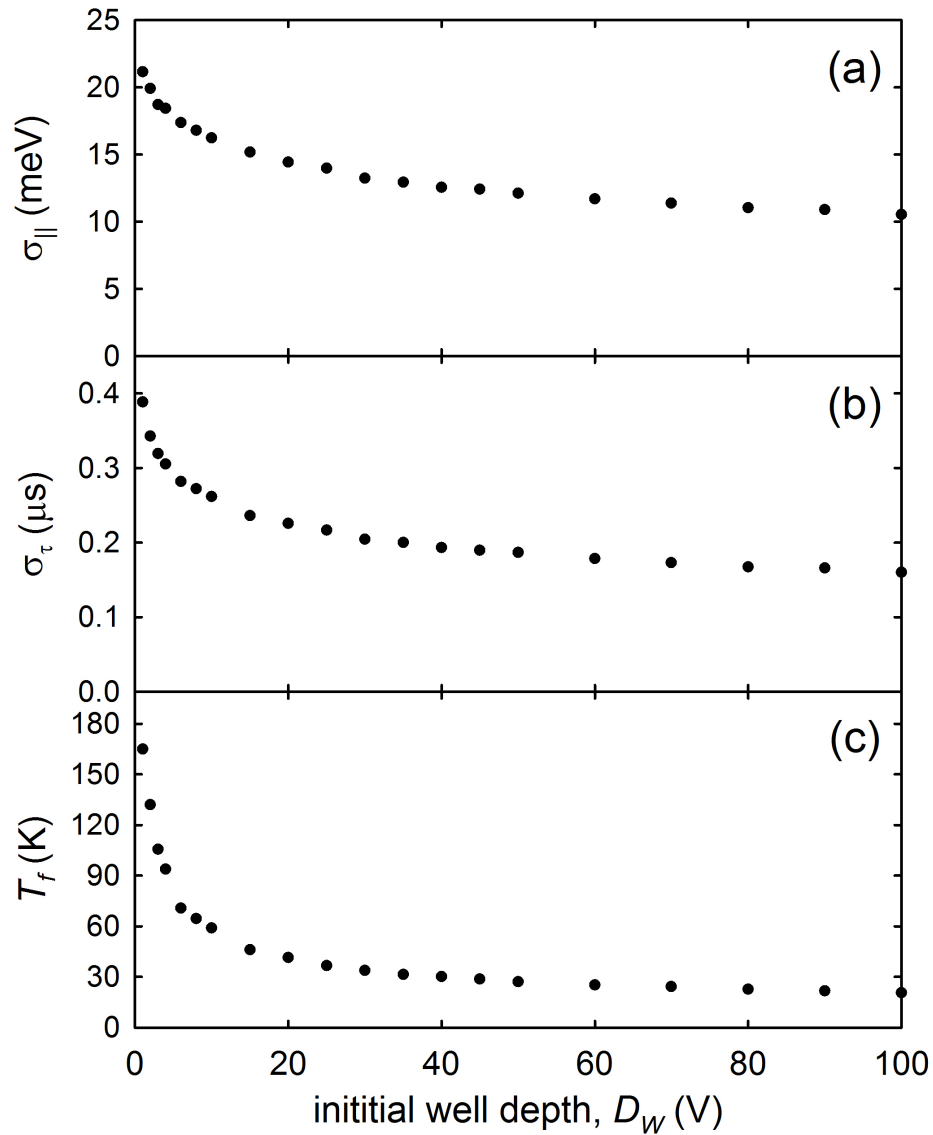


Figure 5.12: Effect of well depth on simulated beam. Standard deviation of the (a) parallel energy and (b) temporal distributions obtained from the simulation using a variety of initial well depths, $D_W \equiv V_E - V_W(0)$. Also shown in (c) is the final parallel temperature, T_f . All other parameters as in Fig. 5.8.

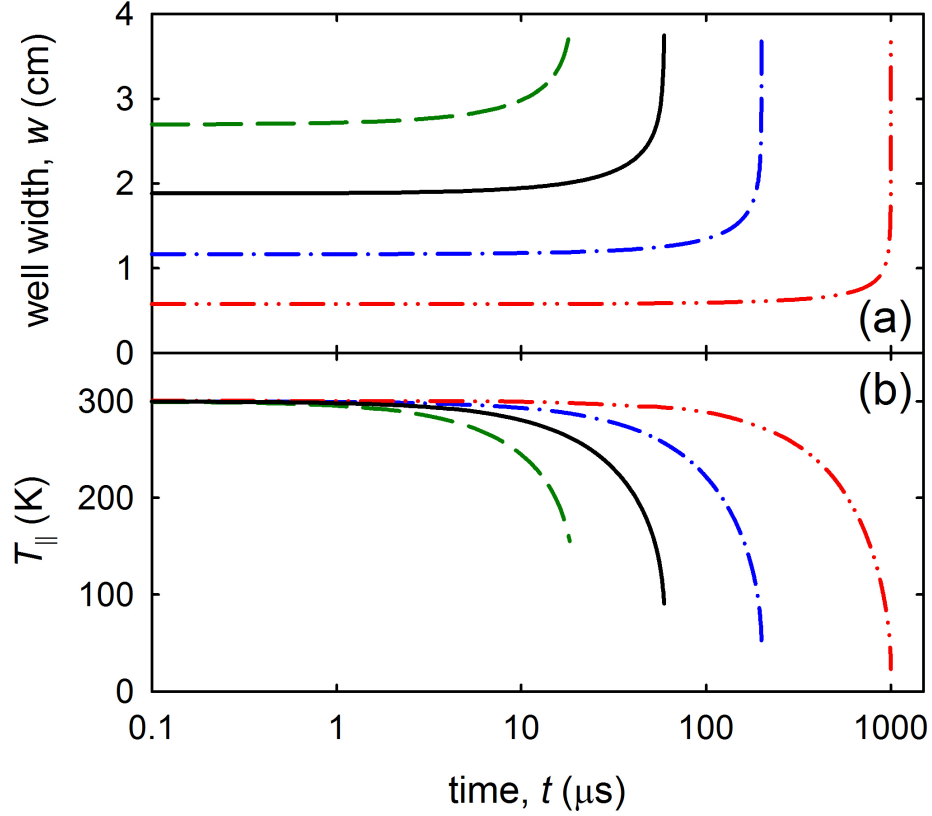


Figure 5.13: Effect of well depth on beam formation. (a) average potential well width as seen by the particles and (b) particle parallel temperature as a function of time obtained from the simulation using an initial well depth of ($- -$) 1 V, ($-$) 3 V, ($- \cdot -$) 10 V and ($- \cdot \cdot -$) 50 V.

parallel energy resolution and a factor of two improvement in σ_τ , with the improvements becoming less significant as the well depth is increased above $D_W \sim 50$ V. These improvements are due to an increase in the amount of adiabatic cooling undergone during ejection.

The time dependence of the potential well width and particle parallel temperature is shown in Fig. 5.13 for initial well depths of 1, 3, 10 and 50 V. As discussed in Sec. 5.2, the existence of a longitudinal adiabatic invariant for this system requires that the product of the parallel velocity of the particles and the spatial width of the potential well be constant. Therefore, as the well width increases during ejection, the particle parallel velocities must decrease. The amount of adiabatic cooling is proportional to the square of the ratio of the initial to final well widths (cf. Eq. (5.5)), and so the particles confined in a deeper (narrower) initial well cool to a lower final parallel temperature T_f before ejection, as seen in Fig. 5.12 (c). This yields improvements to both σ_\parallel and σ_τ via the temperature effects described in the previous section.

As discussed earlier, adiabatic cooling does not occur if the positrons are ejected on time scales significantly faster than the axial bounce time. In this non-dynamic regime, increasing the well depth does not directly affect the resulting energy distribution. However, deeper (narrower) initial potential wells reduce the axial extent of the positrons. This reduces the region over which a flat final potential must be maintained in order for the ejection process to leave the parallel energy

distribution unaltered (i.e., $\sigma_{\parallel} = 1/2k_bT_0$).

Effect of trap geometry

The trap geometry, as parameterized by the length L and aspect ratio $\alpha \equiv L/D$ of the respective electrodes, plays an important role in beam performance. Here the lengths of both the exit-gate and well electrode are independently varied in order to examine their effect the trap geometry has on beam quality. Since the electrode diameter is held constant ($D = 8$ cm), the aspect ratio also varies with the length. For small aspect ratios, the on-axis potential is approximately parabolic with a peak in potential less than the applied voltage. As α is increased, the ratio of the peak potential to the applied potential approaches unity, and the potential becomes flat near the axial center of the electrode.

Shown in Figs. 5.14 (a) and (b) are σ_{\parallel} and σ_{τ} obtained using various lengths for the exit-gate electrode L_E . Here it is seen that both σ_{\parallel} and σ_{τ} are relatively insensitive to L_E at larger lengths and aspect ratios, however for aspect ratios $\alpha_E \lesssim 1$, both spreads increase as L_E is reduced. As discussed above, the peak in the exit-gate potential sets the minimum possible parallel energy of any particle in the beam, $E_{\parallel} \gtrsim e\phi_E$, as well as the minimum time at which a particle may escape the trap. At small aspect ratios, $\phi_E < V_E$; and so, as the potential applied to the adjacent well electrode is increased to eject the particles, there is a corresponding increase in ϕ_E (i.e., the effective aspect ratio of the exit-gate electrode is increased as V_W approaches V_E). This results in a time-dependent increase in the magnitude of the exit-gate barrier during the time the particles are ejected, as shown in Fig. 5.14 (c). This, in turn, leads to an increase in both the parallel energy and time spreads of beams produced using small values of α_E .

While σ_{\parallel} is approximately flat for $\alpha_E \gtrsim 1$, σ_{τ} continues to have a weak dependence on L_E , as seen in Fig. 5.14 (b). As L_E is increased, the time to pass over the exit barrier becomes comparable to the time required to eject the remaining particles. This, in turn, allows later-ejected particles to partially catch up with earlier ones, further reducing σ_{τ} . As L_E is increased, the time required for the earlier (low energy) particles to cross the exit-gate barrier becomes sufficiently long for them to be overtaken by the later-released (higher energy) particles. This leads to an increase in σ_{τ} . This effect is more dramatic for beams generated using higher ramp rates (not shown).

The effects of the well electrode length L_W on σ_{\parallel} and σ_{τ} are shown in Fig. 5.15 (a) and (b). In this case, both spreads increase significantly as L_W is increased, with σ_{\parallel} increasing by more than a factor of 130 between $L_W = 4$ cm and 32 cm. This strong dependence on L_W is due to the effect that the width and shape of the potential well has on the axial bounce times of the particles.

Shown in Fig. 5.15 (c) is the mean time required for the particles to make their final axial bounce within the well, $\bar{\tau}_f$. Here it is seen that $\bar{\tau}_f$ increases significantly as L_W is increased, and in a similar manner to both σ_{\parallel} and σ_{τ} . At small values of α_W , the well potential is approximately parabolic in shape, and so the bounce time is less sensitive to changes in L_W in this regime. However, for values of $\alpha_W \gtrsim 2$, where the potential well is relatively flat, increasing L_W leads to a rapid increase in the bounce times.

As discussed above, the time spread is largely set by the time required for the particles to overcome the exit-gate barrier and be ejected from the trap, while the parallel energy spread is predominantly set by the change in energy imparted to the particles during their last bounce, and so both processes are sensitive to $\bar{\tau}_f$.

It should be noted that both the beam and electrode diameters are held constant at 0.5 cm FWHM and 8 cm, respectively. Under these conditions, radial effects due to gradients in the axial potential are small and do not contribute significantly to the energy and time spreads of the resulting

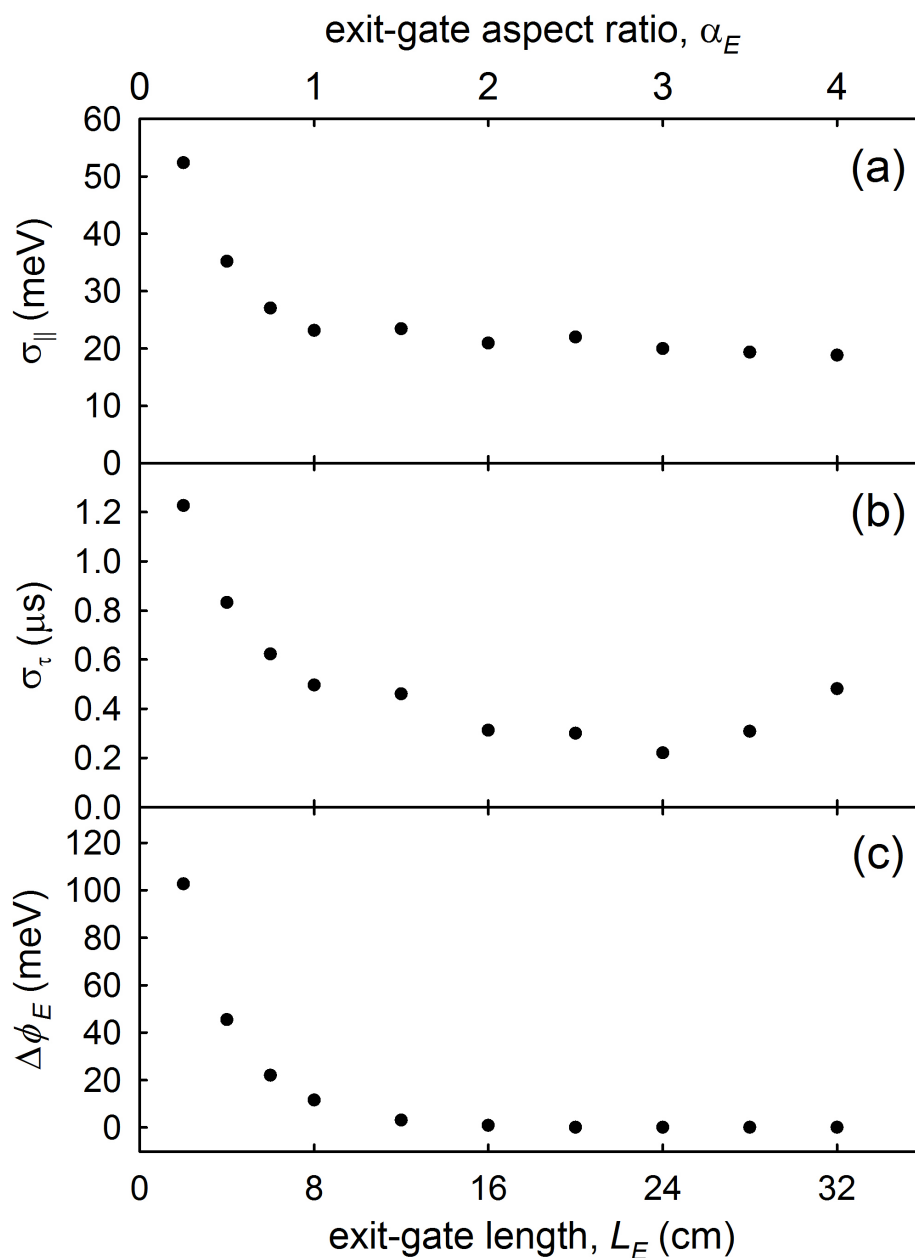


Figure 5.14: Effect of exit-gate length on simulated beam. Standard deviation of the (a) parallel energy and (b) time distributions obtained from the simulation of beams produced by traps with a variety of exit-gate electrode lengths. Also shown in (c) is the change in magnitude of the peak in exit-gate potential during particle ejection. All other parameters as in Fig. 5.8.

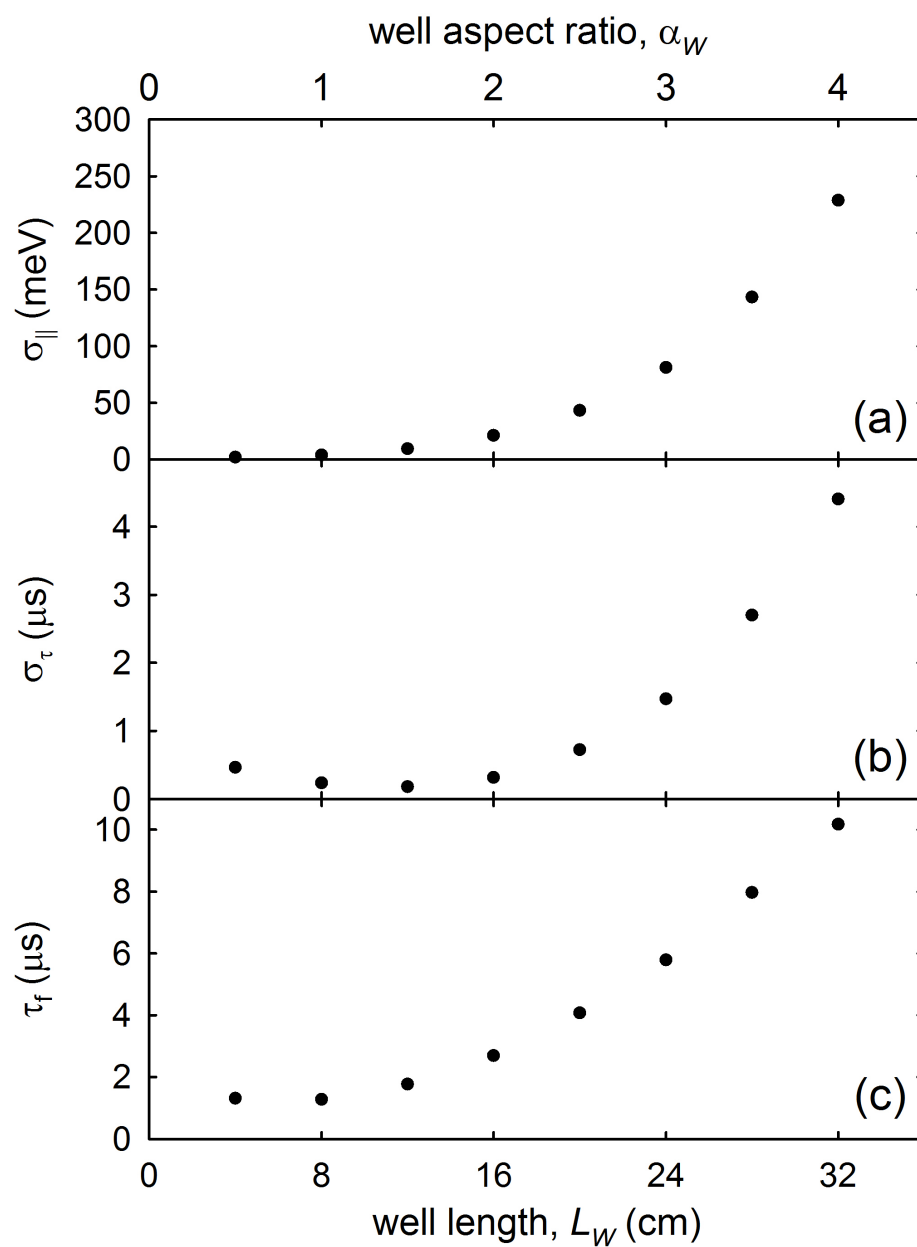


Figure 5.15: Effect of well length on simulated beam. Standard deviation of the (a) parallel energy, and (b) time distributions obtained from the simulation of beams produced by traps with a variety of well electrode lengths. Shown in (c) is the average final bounce time during particle ejection. All other parameters as in Fig. 5.8.

beam. However, conditions where the radial variation in the applied potentials across the beam becomes comparable to the parallel energy spread (e.g., $\alpha \lesssim 1$ with beam diameters approaching the electrode diameter) will lead to a broadening of the parallel energy spread.

Factors affecting the shape of the beam distributions

Beyond the impact of beam formation conditions on the spreads in the parallel energy and time distributions, it is also of interest to examine how these conditions affect the *shapes* of the distributions. Shown in Fig. 5.16 are the beam distributions obtained under three qualitatively different conditions. Figures. 5.16 (a) and (b) show the distributions for a beam formation protocol using a roughly parabolic potential well and typical ramp rate ($V_T = 5$ V, $V_E = 3$ V, $V_0 = 0$ V, and $\dot{V}_W = 50$ mV/ μ s, with aspect ratios 2, 1, and 2 for the trapping, well and exit-gate electrodes, respectively). Under these conditions, both the parallel energy and time distributions can be roughly described by Gaussians, and therefore are well described by the detailed analysis presented in Sec. 5.2.

Shown in Figs. 5.16 (c) and (d) are the distributions using the same parameters as in (a) and (b), but with the well aspect ratio increased from 1 to 4 (i.e., a long flat trapping well). In this case, both the energy and time distributions deviate significantly from Gaussians. This suggests that the Gaussian-like distributions that have been observed in many experiments are associated with (roughly) parabolic potential wells.

Shown in Figs. 5.16 (e) and (f) are the distributions for the case of an ultra-fast release, which corresponds to beam formation in the non-dynamic regime. The parameters are $V_T = 3.3$ V and $V_E = 3$ V, with the well voltage increased linearly from 0 to 3 V in 0.1 μ s (vs. 60 μ s in the dynamical case), using electrodes with aspect ratios $\alpha = 2$. While the initial well is approximately parabolic, the final potential is reached on time scales fast compared to the axial bounce time, and so adiabatic cooling does not occur and the initial parallel energy distribution is unaltered by the presence of the exit-gate barrier. Further, provided the final potential is reasonably flat over the axial extent of the particles, they are ejected with their initial thermal velocities plus their potential relative to ground. Under these conditions, the parallel energy distribution is a shifted Maxwell-Boltzmann distribution with $\sigma_{\parallel} = 1/2k_bT_0$.

5.4 Summary: Optimal conditions for beam-formation

The studies described above elucidates the process of beam formation, especially concerning its impact on beam quality. This understanding can be used, in turn, to find optimum conditions for beam formation, with emphasis on situations in which a high energy resolution beam is desired, delivered in pulses of microsecond duration or shorter. These results show three distinct regimes in which beam formation occurs; the full bounce and low temperature dynamic regimes, and the fast-ejection non-dynamic regime.

Beam formation in the two dynamic regimes may be summarized as follows. As the well voltage is increased to eject the particles, the well width increases. This results in a decrease in the parallel temperature (due to adiabatic cooling) and an increase in the axial bounce time. The particles are first able to escape the trap when the sum of their kinetic and potential energy exceeds the peak in the exit-gate potential.

In the full bounce regime, the first particles to escape are those on the high energy tail of the initial thermal distribution which gain sufficient energy to overcome the exit-gate barrier at the end of their final bounce cycle. These particles are ejected with the minimum parallel energy.

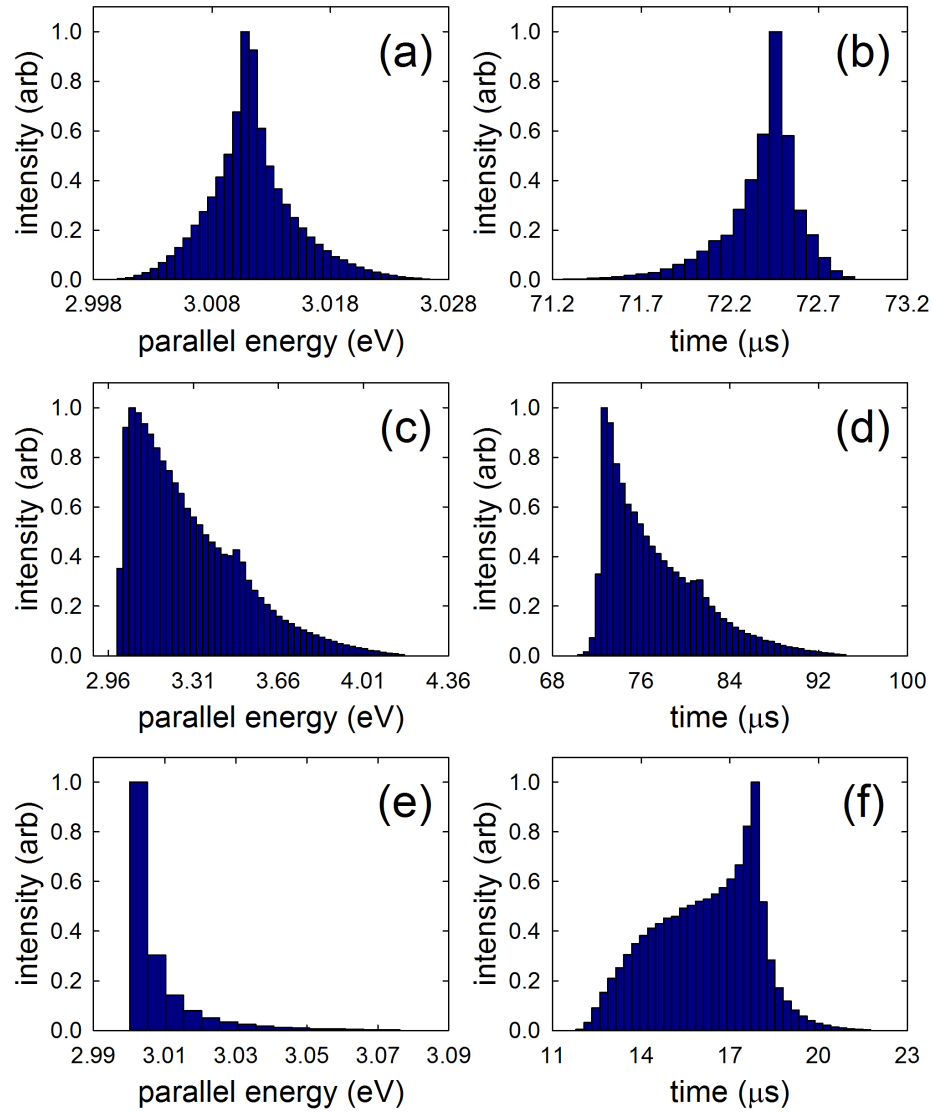


Figure 5.16: Effect of beam formation on the shape of the beam distributions. (left) parallel energy and (right) temporal distributions obtained from the simulation for three specific trapping geometries and ejection protocols: (a) and (b), parabolic potential well and typical ejection protocol; (c) and (d) long flat potential well and typical ejection protocol; and (e) and (f), parabolic potential well with ultra-fast ejection protocol. The σ_{\parallel} values for (a), (c), and (e) are 3.7, 223 and 12.6 meV respectively; and the corresponding σ_{τ} values are 0.23, 4.3 and 1.7 μs . See text for details.

In contrast, the final particles to leave are those which obtain sufficient energy to escape at the beginning of their final bounce cycle. These particles are therefore required to make a full pass through the rising potential (above the energy of the exit-gate potential), and so they are ejected with the maximum parallel energy.

In contrast, in the low temperature regime, both the first and last particles to escape are those on the tail of the initial thermal distribution that are moving towards and away from the exit-gate barrier, respectively, as they obtain sufficient energy to escape the trap. This results in a raising of the minimum and a lowering of the maximum possible final parallel energies, thus resulting in improved temporal and energy resolution.

The effects on beam quality of other factors was also studied. The average ramp rate during the time the particles escape the trap is a critical parameter, while the time dependence of the ramp at earlier times is not. Large ramp rates cause the particles to be accelerated out of the trap more quickly, and to higher energies, than low ramp rates. Additionally, both the parallel energy and time resolution improve as the temperature is reduced. This is due to the reduction of phase-space at low temperatures, which leads to a restriction on the possible extreme trajectories and results in narrower energy and time distributions. Since reducing the positron temperature also decreases the perpendicular energy spread, this provides a very effective method of improving the total energy resolution of the beam, provided the parallel energy spread (set by the other dynamics during beam formation) does not dominate the perpendicular spread.

The effects of the potential well depth and trap geometry were also shown to impact beam quality. The amount of adiabatic cooling during ejection can be increased by increasing the initial well depth (due to the corresponding decrease in the initial well width). Additionally, narrow, parabolic potential wells result in shorter positron bounce times. Both of these effects can be used to improve the energy and temporal spreads of the resulting beam. Finally, the compact Gaussian-like parallel energy and time distributions that have frequently been experimentally observed correspond to approximately parabolic trapping potential wells and moderate ramp rates.

Using the results presented here, the optimal trap geometry and ejection parameters for producing beams with high energy resolution and reasonable temporal resolution may be described as follows. An ideal trap geometry will have exit-gate and well aspect ratios of $\alpha_E \gtrsim 1$ and $\alpha_W \lesssim 1$, respectively, while maintaining the shortest lengths possible. The initial voltage applied to the well electrode should be made small compared to the voltage applied to the exit-gate electrode to ensure the positrons are trapped within a narrow parabolic potential well, and the positrons should be cooled to the lowest possible temperature before the start of beam formation. The positrons should then be ejected by increasing the well voltage at the lowest possible rate that still yields satisfactory temporal resolution for the desired application.

Some of the work and discussion in Chapter 5 is taken from “Formation of buffer-gas-trap based positron beams,” M. R. Natisin, J. R. Danielson and C. M. Surko, *Phys. Plasmas* **22**, 033501 (2015) [26] and “Formation mechanisms and optimization of trap-based positron beams,” M. R. Natisin, J. R. Danielson and C. M. Surko, *Phys. Plasmas*, **23**, 023505 (2016) [27]. The author of this dissertation led the research and was the principle author of these papers.

Chapter 6

Positron cooling through interactions with a molecular gas

A better understanding of low energy positron-molecule collisions and thermalization processes will aid in the development of novel experimental techniques and technology. In particular, such processes are central to a number of techniques used in creating high-density positron plasmas and tailored positron beams. Prominent examples include the use of molecular gases as an inelastic energy loss mechanism for buffer gas positron accumulators (cf. Chapter 2), and as the requisite cooling mechanism when rotating electric fields are used to radially compress trapped plasmas [the “rotating wall” (RW) technique] [51, 52, 53]. Additionally, the results of these atomic physics studies will aid in the development of techniques to cool positrons to lower temperatures (< 300 K). These cold positrons, in turn, can then be used to produce positron beams with improved energy resolution as compared to those currently available (cf. Chapter 5).

Positron thermalization in a molecular medium proceeds in several stages. When the positron temperature is large, the positrons cool rapidly through high energy processes such as electronic excitation and ionization. Once the positron energy falls below the thresholds for these higher energy processes (e.g., a few electron volts), the cooling rate slows dramatically, and the lower energy processes of vibrational and rotational excitation dominate. It is these lower energy processes that are the focus of this chapter.

Presented here are measurements and calculations for positron cooling from temperatures $\geq 1,200$ K through inelastic collisions with either CF_4 , N_2 or CO gases at 300 K. These molecules were chosen for study to compare the effectiveness in cooling positrons *via* vibrational and rotational excitation. By symmetry, the permanent dipole and quadrupole moments of CF_4 are zero, leaving vibrational excitation as the dominant cooling channel. For N_2 , the cross section for vibrational excitation is small (due to the mode being IR-inactive), and the molecule has no permanent dipole moment, leaving rotational excitation by coupling to the quadrupole moment to dominate. Carbon monoxide has a dipole-active vibrational mode, as well as non-zero dipole and quadrupole moments, allowing it to cool through all three types of vibrational and rotational excitation.

A model is presented that describes the evolution of the positron temperature due to inelastic interactions with a molecular gas. The model predictions, which are calculated using simple cross sections under the Born approximation, are then compared to experimental measurements, allowing estimates of the magnitudes of the relevant cross sections to be made. For the vibrational excitations in CF_4 and CO , these estimates are compared to direct experimental measurements, while for

rotational excitations in N_2 and CO, they yield new information, since no direct measurements of the cross sections exist.

6.1 Model of positron thermalization with a molecular gas

The model presented is general, in that it describes the thermalization of positrons (or electrons) with a gas through a variety of inelastic collisions (e.g., vibrational or rotational excitation and de-excitation, etc.), provided acceptably accurate forms for the relevant cross sections are available.

The mean positron-molecule collision rate is

$$\langle \Gamma \rangle = n \sqrt{\frac{2}{m}} \langle \sigma(\epsilon) \sqrt{\epsilon} \rangle, \quad (6.1)$$

where n is the molecule number density, m is the positron mass, $\sigma(\epsilon)$ is the collisional cross section, ϵ is the incident positron energy, and $\langle \dots \rangle$ indicates averaging over the positron energy distribution. Since the mass of the molecule is large compared to that of the positron, the molecule is assumed to be stationary, and so the positron velocity is assumed to be the relative velocity.

Using Eq. (6.1), the mean collision rate for excitation from, or de-excitation to $(+, -)$ the i^{th} mode can be written

$$\langle \Gamma_i^{(+,-)} \rangle = n_i \sqrt{\frac{2}{m}} \int_0^\infty \sigma_i^{(+,-)}(\epsilon) \sqrt{\epsilon} f(\epsilon, T) d\epsilon, \quad (6.2)$$

where the cross sectional average has been written as an integral over the positron energy distribution, $f(\epsilon, T)$, and n_i is the population density of state i .

If the various states in the molecule are assumed to be Boltzmann distributed, then the population density can be written as

$$n_i \equiv n \frac{g_i \exp\left[-\frac{E_i}{k_b T_g}\right]}{\sum_j g_j \exp\left[-\frac{E_j}{k_b T_g}\right]} \quad (6.3)$$

where g is the mode degeneracy, E is the mode energy, and T_g is the temperature of the molecular gas.

The total power transferred to or from the positrons is equal to a sum over all processes which can de-excite or excite the molecule,

$$P_{c,h} = \sum_i |\Delta E_i| \langle \Gamma_i^{(+,-)} \rangle. \quad (6.4)$$

Here the subscripts c and h represent cooling (excitation) and heating (de-excitation) of the positrons, and ΔE_i is the change in energy of the molecule by excitation from, or de-excitation to, state i . The mean rate of energy change of the positrons can then be written

$$\left\langle \frac{d\epsilon}{dt} \right\rangle = -P_{\text{tot}} = \frac{3}{2} k_b \frac{dT}{dt}, \quad (6.5)$$

where

$$P_{\text{tot}} \equiv P_c - P_h \quad (6.6)$$

is the total *cooling* power acting on the positrons.

Using Eqs. (6.4)-(6.6), the first order differential equation describing the evolution of the positron temperature as a function of time is

$$\frac{dT}{dt} = -\frac{2}{3k_b} \sum_i |\Delta E_i| \left(\langle \Gamma_i^{(+)} \rangle - \langle \Gamma_i^{(-)} \rangle \right). \quad (6.7)$$

Assuming the cross sections satisfy detailed balance, the excitation and de-excitation collision rates for each mode will equilibrate at the gas temperature. Above this temperature, excitation dominates, thus cooling the positrons; while below, de-excitation dominates, heating the positrons.

Unfortunately, the solution to Eq. (6.7) cannot be expressed analytically if realistic cross sections are used, and so the solution must be found numerically. For all of the cases considered here, the solutions were found by numerically integrating Eq. (6.7) using a 10 μs time step. Reducing the time step by three orders of magnitude (10 ns) yields a change in the results of less than 1%, indicating that stable numerical solutions are reached using 10 μs time steps.

For simplicity, it is assumed that the positron energy distribution, $f(\epsilon, T)$, remains Maxwell-Boltzmann at all times. While no effort is made here to justify this assumption theoretically, the measured positron energy distributions at each temperature (see below) indicate that it is a reasonable approximation.

For the results discussed here, generic formulae for cross sections in the Born approximation are used for vibrational and rotational excitation and de-excitation. The dominant CF_4 and CO vibrational cross sections are available from experimental measurements, and fit well to simple scalings of the theoretical Born-dipole cross sections [41]. This indicates that the use of these theoretical cross sections is appropriate. No direct measurements of the rotational cross sections exist for positron impact; however data for rotational excitation of N_2 by *electron* impact suggest that the so-called ‘‘Gerjuoy-Stein’’ cross sections are reasonably accurate [54].

6.2 Description of the experiments

The experimental apparatus was described in detail in Chapter 2. For these experiments, N_2 is injected into the first stage of the BGT and maintained at lower pressures in the other two stages by differential pumping. The cooling gas is injected into the third stage to interact with the trapped positrons, eventually cooling them to the gas temperature (~ 300 K). For all experiments discussed here, the N_2 trapping gas was maintained at significantly lower pressure in the third stage as compared with that of the cooling gas, so that the positrons cooled predominantly through interactions with the cooling gas. Data were taken at two different N_2 pressures to verify this.

Once the trapped positrons have cooled to the ambient gas temperature of 300 K, Gaussian noise with an amplitude of 150-500 mV peak-to-peak and a bandwidth of 9 MHz is applied to one of the confining electrodes for 100-200 ms. It is then shut off, at which point the positron temperature is between $\sim 1,200$ and 1,800 K, depending on the molecule being studied. The peak temperature reached during this process is determined by a competition between the rf heating and gas cooling rates. The initial conditions were varied for each gas in an attempt to reach reasonably similar peak temperatures. The temperature of the positrons is then measured as a function of time as they relax to the ambient gas temperature.

The positron temperature was measured using the techniques described in Sec. 3.3. The positrons are ejected from the BGT and passed through a retarding potential analyzer (RPA), where the beam parallel energy distribution is measured. This measurement is then repeated with the RPA in a different magnetic field. Then, the two measured energy distributions are fit to an exponentially-modified Gaussian (EMG) distribution function to obtain the mean parallel energy of the beam at each magnetic field (see Sec. 3.2). Equation (3.20) is then used to obtain the positron mean perpendicular energy from the two measured mean parallel energies.

The mean perpendicular energy of the positrons in the BGT, \bar{E}_\perp^t , can then be obtained from the measured \bar{E}_\perp in the RPA region by

$$\bar{E}_\perp^t = \bar{E}_\perp \frac{B^t}{B}, \quad (6.8)$$

where B^t and B are the magnetic fields in the BGT and RPA regions, respectively. Combining (3.20) and (6.8) and using the fact that $T_\parallel = T_\perp \equiv T = \bar{E}'_\parallel / k_b$ in the BGT before the beam is formed gives the temperature of the positrons in the trap,

$$T = \frac{\bar{E}'_\parallel - \bar{E}_\parallel}{k_b (1 - B'/B)} \left(\frac{B^t}{B} \right). \quad (6.9)$$

Equation (6.9) is the basis for the temperature measurements presented here.

Examples of measured parallel energy distributions used to determine the positron temperature are shown in Fig. 6.1. The points show the measured integrated parallel energy distributions with the RPA in a magnetic field of $B \sim 800$ Gauss and $B' = B/4$. The dashed lines show fits to the data, providing the mean parallel energies \bar{E}_\parallel and \bar{E}'_\parallel , which are represented by the vertical dotted lines in Fig. 6.1 (a) and (b), respectively. For the example shown, Eq. (6.9) gives a temperature of 717 ± 20 K. Also shown by the solid lines are the derivatives of the fits, which represent the respective parallel energy distributions.

These and similar measurements are found to be consistent with the assumption of the model that the positron energy distribution remains Maxwell-Boltzmann, even while the positrons are being heated or cooled. The beam formation process removes most of the information regarding the original parallel positron energies, but leaves the perpendicular energies intact. As seen in Fig. 6.1 (a), when the RPA magnetic field is comparable to that of the buffer gas trap, the parallel energy distribution resembles a Gaussian. As the RPA field is lowered, some positron perpendicular energy is transferred into the parallel component due to the invariance of the orbital magnetic moment. This results in an increase in the mean parallel energy, as well as the development of a high energy tail in the parallel energy distribution [cf. Fig. 6.1 (b)]. At all temperatures discussed here, the measured distributions fit well with the EMG distribution function. This indicates that the positrons equilibrate rapidly to a Maxwell-Boltzmann distribution even while being heated or cooled.

For the results presented here, $\sim 20,000$ positrons were used with a magnetic field ratio $B'/B = 1/4$. The pressure measurements were done using an ion gauge calibrated to a capacitance manometer placed *in situ* in the trapping region, with an overall uncertainty of $\pm 10\%$. Measurements with each gas at half pressure were also done at several temperatures to ensure that the cooling rates varied linearly with the gas pressure, indicating that there were no gas-independent cooling mechanisms present. Since the time required for each temperature measurement is significant (~ 1 hour per data point), multiple measurements of each data point was not practical. For this reason, the error bars shown for each molecule represent the standard deviation of five measurements of the

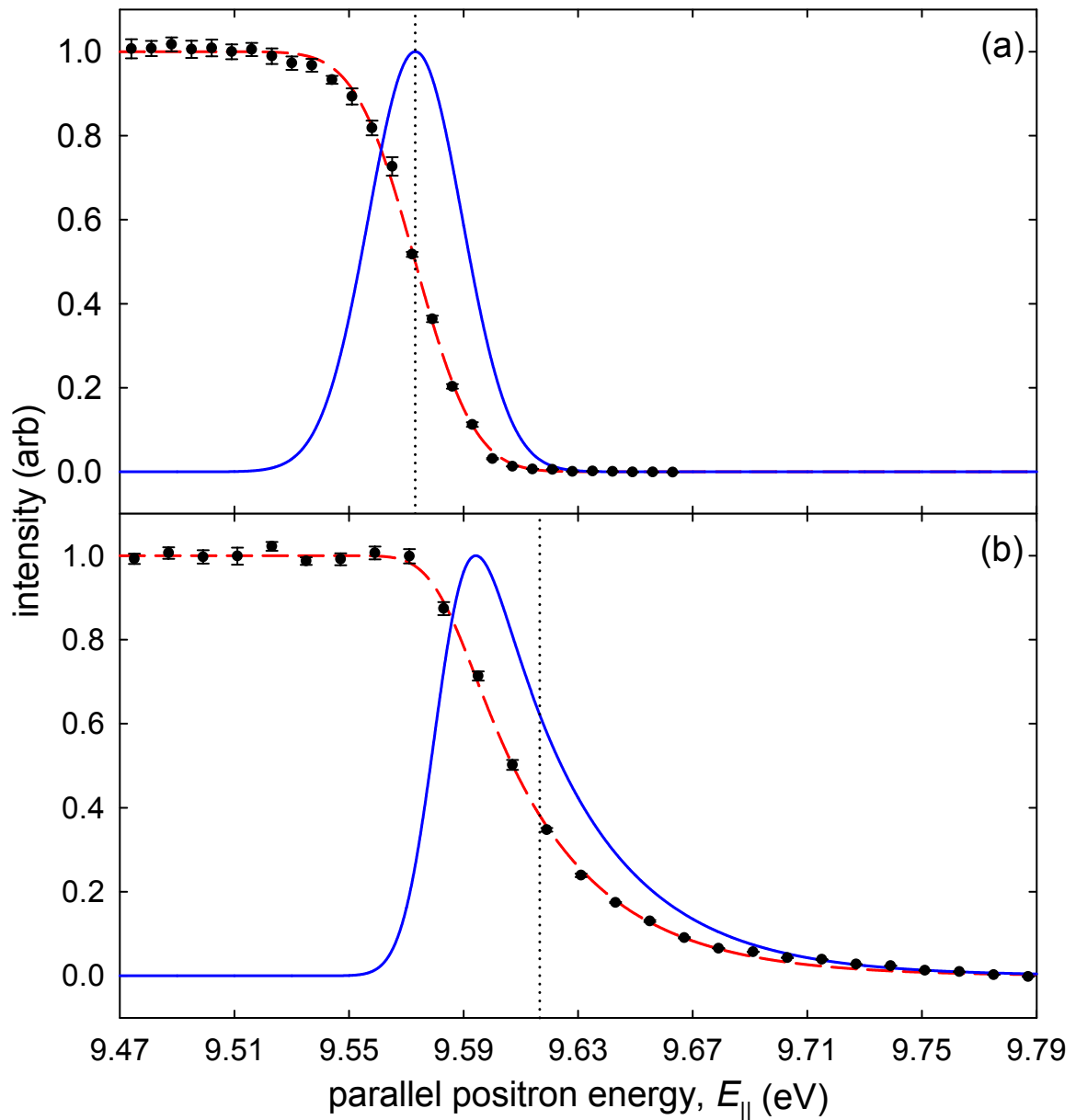


Figure 6.1: Example cutoffs used to obtain positron temperature. Parallel energy distribution measured at (a) $B \sim 800$ G, and (b) $B' \sim 200$ G; (\bullet) measured integrated parallel energy distributions, ($- -$) fits to data, and ($-$) derivatives of fits that represent the positron energy distributions. Dotted vertical lines represent fitted mean parallel energies \bar{E}_{\parallel} and \bar{E}'_{\parallel} .

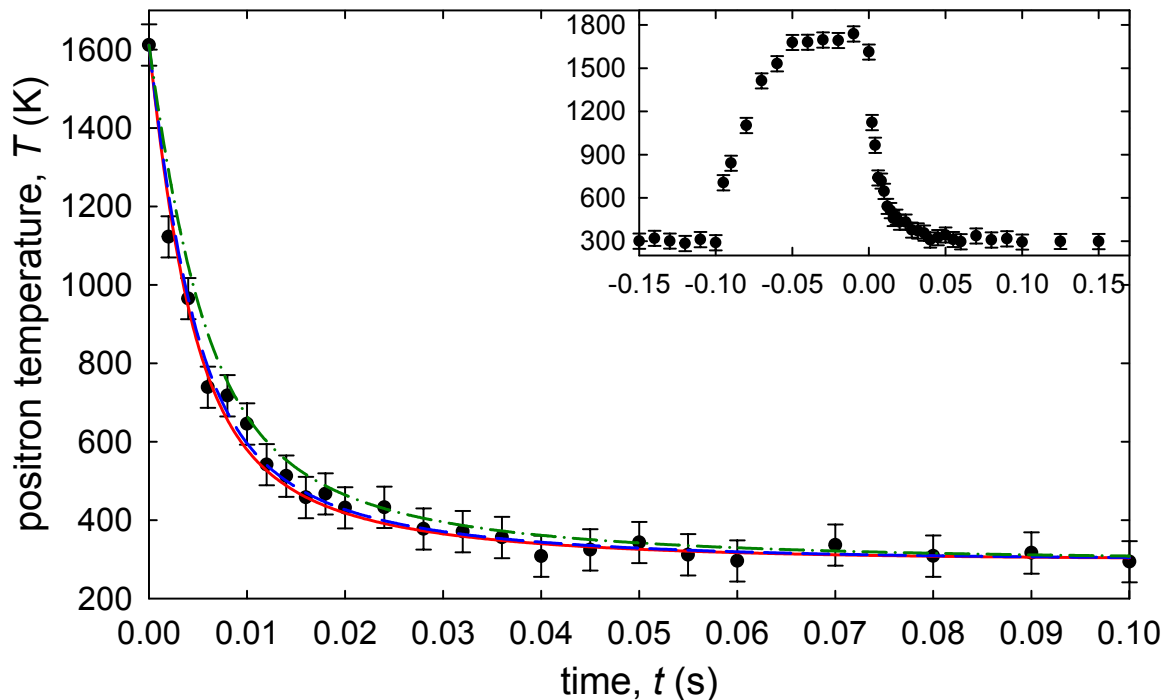


Figure 6.2: Positron cooling using $0.51 \pm 0.05 \mu\text{torr}$ of CF_4 at 300 K: (●) measured data, (—) solution to Eq. (6.7) for vibrational excitation and de-excitation of the ν_3 mode, (---) solution to (6.7) with cross sections scaled by a fitting factor $\eta = 0.95$ and (-·-) solution to Eq. (6.7) with cross sections scaled by $\eta = 0.75$ to match the direct measurement given in Ref. [41]. Inset shows the full heating and cooling cycle.

$t = 0$ s point (i.e., where the error is expected to be largest).

6.3 Measurements and model predictions

6.3.1 Carbon tetrafluoride

The first case considered is positron cooling through interactions with CF_4 at a pressure of $0.51 \pm 0.05 \mu\text{Torr}$. The measured positron temperature during the heating and cooling cycle is shown in the inset of Fig. 6.2. The positrons were trapped and initially allowed to cool to the gas temperature of ~ 300 K, after which rf heating noise was applied for 100 ms. The positrons reached a peak temperature of $\sim 1,700$ K, at which point the noise was switched off, and the positrons were allowed to relax back to the gas temperature.

Both the permanent electric dipole and quadrupole moments of CF_4 are zero by symmetry, leaving vibrational excitation by coupling to the transition dipole moments as the dominant cooling channel. The cross section used is the Born-dipole cross section [55], with the de-excitation cross

section obtained by requiring detailed balance,

$$\sigma_{0,v} = \frac{8\pi a_0^2}{3} g_v \left(\frac{\mu_v}{ea_0} \right)^2 \left(\frac{R_y}{\varepsilon} \right) \ln \left[\frac{\sqrt{\varepsilon} + \sqrt{\varepsilon - \varepsilon_v}}{\sqrt{\varepsilon} - \sqrt{\varepsilon - \varepsilon_v}} \right] \quad (6.10)$$

$$\sigma_{v,0} = \frac{8\pi a_0^2}{3} g_0 \left(\frac{\mu_v}{ea_0} \right)^2 \left(\frac{R_y}{\varepsilon} \right) \ln \left[\frac{\sqrt{\varepsilon + \varepsilon_v} + \sqrt{\varepsilon}}{\sqrt{\varepsilon + \varepsilon_v} - \sqrt{\varepsilon}} \right], \quad (6.11)$$

where a_0 is the Bohr radius, R_y is the Rydberg energy (13.6 eV), ε is the incident positron energy, μ_v is the transition dipole moment with dimensions of ea_0 , and g_v and ε_v are the degeneracy and energy of mode v . Here, $\sigma_{0,v}$ describes excitation from the ground state to the first excited state v , and $\sigma_{v,0}$ represents de-excitation from state v to the ground state. Excitation from excited states is neglected.

There are two triply degenerate, dipole-active CF_4 vibrations; the ν_3 degenerate stretch mode at $\varepsilon_v = 159$ meV, and the ν_4 degenerate deformation mode at $\varepsilon_v = 78.4$ meV. The transition dipole moments for these modes, which are calculated using the absolute integrated intensities and procedures given by Bishop and Cheung in Ref. [56], are found to be $0.12 ea_0$ and $0.02 ea_0$ for the ν_3 and ν_4 modes, respectively. Since the cross sections scale as μ_v^2 , the contribution from the weak ν_4 mode is small, and so only (de-)excitation of the ν_3 mode is considered here.

As shown in Fig 6.2, even at the low gas pressure of $0.51 \mu\text{torr}$, the positrons thermalize with the CF_4 remarkably quickly, reaching 300 K in under 50 ms. Also shown as a solid line is the solution to Eq. (6.7) for the case of excitation and de-excitation of the ν_3 vibrational mode using the cross sections given by Eq. (6.11). In this case, the simple model is in excellent agreement with the measured data.

The measured positron cooling curve also provides some information regarding the cross sections for the relevant interactions. The fact that the model prediction matches well for CF_4 suggests that the Born-dipole cross section is a good approximation to the actual cross section. Applying a constant empirical scale factor, η , to both the excitation and de-excitation cross sections given by Eq. (6.11) enables an estimate of the vibrational cross section. For the case of CF_4 , the best fit is found by scaling the Born-dipole cross sections by a factor $\eta = 0.95 \pm 0.10$, resulting in the curve shown by the dashed line in Fig. 6.2.

For comparison, the ν_3 vibrational excitation cross section for positron impact on CF_4 has been directly measured experimentally and found to be a factor of $\sim 0.75 \pm 0.2$ times the Born-dipole model prediction [41]. The positron cooling curve obtained from the model using this scale factor is shown by the dot-dashed curve in Fig. 6.2. The fact that the two measurements lie within their respective error bars confirms that the positron cooling curves may be used to estimate the underlying cross sections. While this technique does not provide as detailed cross section information as direct measurement, it is a useful alternative, particularly in cases where direct measurement is not currently possible.

6.3.2 Molecular nitrogen

Data for N_2 at a pressure of $15 \pm 1.5 \mu\text{Torr}$ are shown in Fig. 6.3. Since N_2 is a homonuclear diatomic molecule, it has no permanent dipole moment, and the vibrational mode is dipole-inactive. Thus, the lowest order coupling is rotational excitation via the non-zero quadrupole moment. In this case, the selection rules allow only rotational transitions with $\Delta j = \pm 2$, where j is the rotational quantum number. In the Born approximation, the cross sections for excitation from and de-excitation to

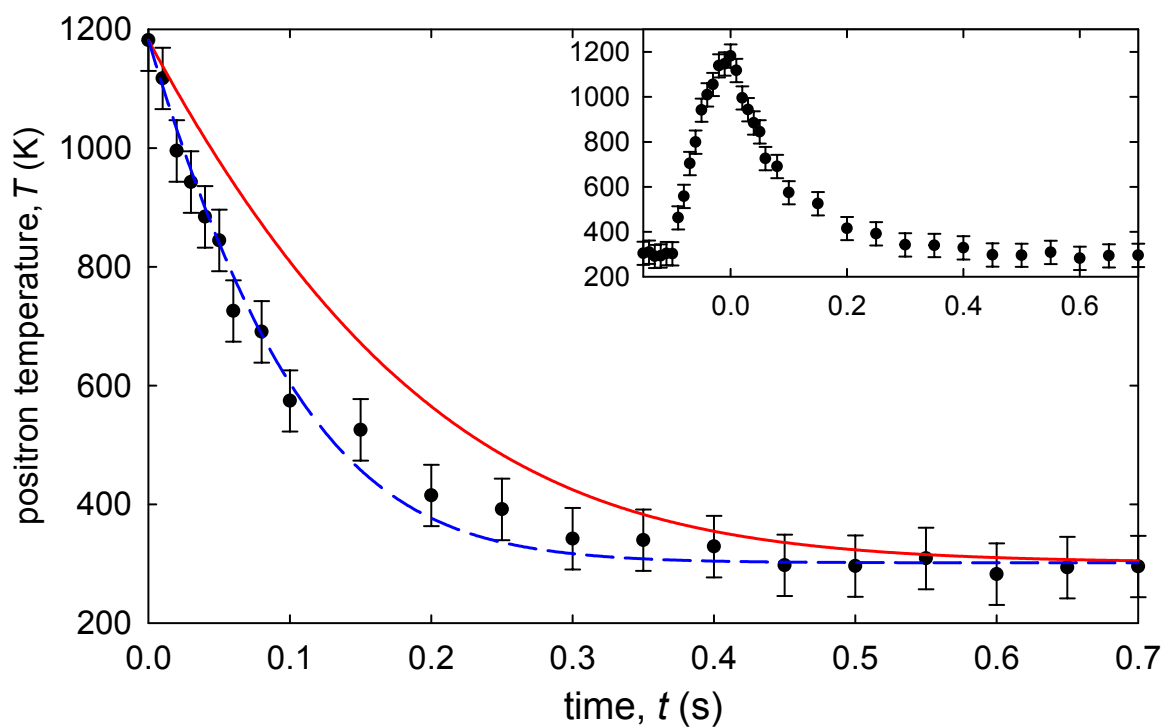


Figure 6.3: Positron cooling using $15 \pm 1.5 \mu\text{torr}$ of N_2 at 300 K: (\bullet) measured data; ($—$) solution to Eq. (6.7) for quadrupole rotational excitation and de-excitation of all contributing j rotational states; and ($- -$) solution to Eq. (6.7) with cross sections scaled up by $\eta = 1.8$. The inset shows the full heating and cooling cycle.

state j are described by the Gerjuoy-Stein equations [57],

$$\sigma_{j,j+2} = \frac{8\pi a_0^2}{15} \left(\frac{Q}{ea_0^2} \right)^2 \frac{(j+2)(j+1)}{(2j+3)(2j+1)} \sqrt{1 - \frac{\Delta\varepsilon_j}{\varepsilon}} \quad (6.12)$$

$$\sigma_{j+2,j} = \frac{8\pi a_0^2}{15} \left(\frac{Q}{ea_0^2} \right)^2 \frac{(j+2)(j+1)}{(2j+3)(2j+5)} \sqrt{1 + \frac{\Delta\varepsilon_j}{\varepsilon}}, \quad (6.13)$$

where Q is the quadrupole moment with dimensions of ea_0^2 . The energies of the rotational states are $\varepsilon_j = B_r j(j+1)$, where B_r the rotational constant of the molecule. Thus the energy transferred to and from the positron following a collision is $\Delta\varepsilon_j = B_r(4j+6)$.

As shown in Fig. 6.3, the positrons thermalize with N_2 much more slowly than for CF_4 , even at significantly higher gas pressure and lower initial positron temperature, taking ~ 0.5 s to reach 300 K. The prediction from (6.7), using the cross sections given by Eq. (6.13) with $Q = 1.27 ea_0^2$ and $B_r = 0.25$ meV [58, 59], is shown by the solid curve. Rotational states up to $j = 60$ are included in the calculation, although the contributions from $j \gtrsim 30$ are negligible. The degeneracy is taken to be $6(2j+1)$ and $3(2j+1)$ for even and odd j , respectively.

For N_2 , the calculated cooling rate is lower than the measured data, suggesting that the Gerjuoy-Stein formula underestimates the rotational excitation cross sections for N_2 by positrons. Since the Born approximation includes only long range effects, this may indicate that short range effects, such as polarization, are important in describing positron collisions with N_2 [60]. It should be noted that, while the N_2 vibrational mode is dipole-inactive and therefore has a cross section of zero in the Born approximation, more sophisticated calculations predict a non-zero vibrational excitation cross section. However, the magnitude of the predicted cross section is small, approximately three orders of magnitude smaller than that for CF_4 [61, 62]. Including this process in the model does not significantly affect the positron cooling rate.

Adjusting the magnitude of the rotational excitation and de-excitation cross sections given by Eq. (6.13) yields a best fit scale factor $\eta = 1.8 \pm 0.2$ (cf. dashed curve in Fig. 6.3). This fit yields a magnitude for the $j = 0 \rightarrow 2$ rotational excitation cross section which is in reasonable agreement with more recent theoretical calculations [63]. However it should be noted that the energy dependence of the Gerjuoy-Stein formulae are markedly different than those predicted in Ref. [63]. Since no direct measurements of the rotational excitation cross section for positrons on N_2 exist, the indirect measurements shown in Fig. 6.3 represent a potentially important benchmark for comparison with future theoretical predictions.

6.3.3 Carbon monoxide

Cooling data for CO at a pressure of $1.7 \pm 0.2 \mu\text{Torr}$ are shown in Fig. 6.4. Unlike the previous two cases, CO has both non-zero permanent dipole and quadrupole moments, as well as a dipole active vibrational mode. The solution to Eq. (6.7) then involves both the vibrational and quadrupole rotational interactions given by Eqs. (6.11) and (6.13), as well as additional cross sections describing rotational interactions by coupling to the permanent electric dipole moment. For dipole-coupled rotations, the allowed transitions are $\Delta j = \pm 1$. Again using the Born approximation,

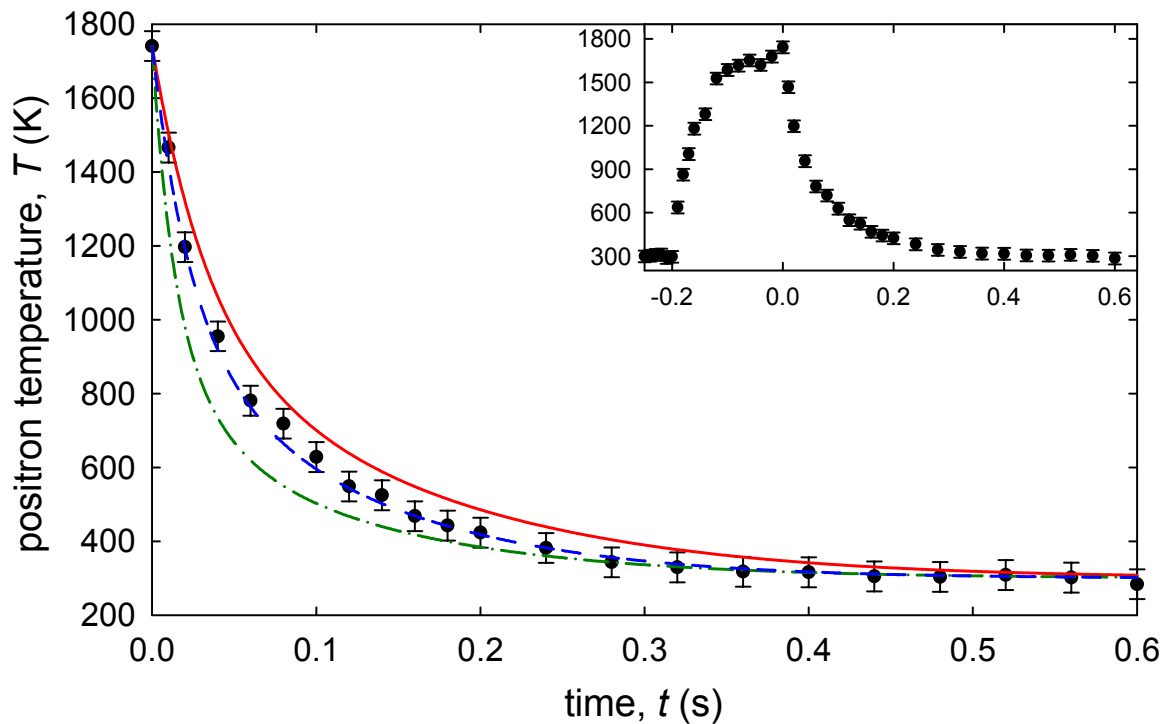


Figure 6.4: Positron cooling using $1.7 \pm 0.2 \mu\text{torr}$ of CO at 300 K: (•) measured data; (—) solution to Eq. (6.7) for vibrational, dipole rotational and quadrupole rotational excitation and de-excitation of the ν_1 mode and all contributing j rotational states; (— · —) solution to Eq. (6.7) with vibrational cross sections scaled by $\eta = 2.8$ to match direct measurement given in ref [41]; and (— —) solution to Eq. (6.7) with vibrational, dipole and quadrupole rotational cross sections scaled by $\eta = 1.5, 1.5$ and 1, respectively.

they are [64]

$$\sigma_{j,j+1} = \alpha \left(\frac{R_y}{\varepsilon} \right) \left(\frac{j+1}{2j+1} \right) \ln \left[\frac{\sqrt{\varepsilon} + \sqrt{\varepsilon - \Delta\varepsilon_j}}{\sqrt{\varepsilon} - \sqrt{\varepsilon - \Delta\varepsilon_j}} \right] \quad (6.14)$$

$$\sigma_{j+1,j} = \alpha \left(\frac{R_y}{\varepsilon} \right) \left(\frac{j+1}{2j+3} \right) \ln \left[\frac{\sqrt{\varepsilon + \Delta\varepsilon_j} + \sqrt{\varepsilon}}{\sqrt{\varepsilon + \Delta\varepsilon_j} - \sqrt{\varepsilon}} \right], \quad (6.15)$$

with

$$\alpha \equiv \frac{8\pi a_0^2}{3} \left(\frac{\mu}{ea_0} \right)^2, \quad (6.16)$$

where μ is the permanent dipole moment with dimensions of ea_0 . Here, the energy exchanged with the positron in each collision is $\Delta\varepsilon_j = 2B_r(j+1)$.

For CO, the rotational constant B_r is 0.24 meV [59], and the permanent dipole and quadrupole moments are $0.044 ea_0$ and $2.59 ea_0^2$, respectively [65, 58]. The only vibrational mode is the dipole-active C-O stretch mode, occurring at $\varepsilon_v = 266$ meV with a transition dipole moment of $0.042 ea_0$ [56].

Shown in Fig. 6.4 by a solid line is the prediction of Eq. (6.7) using the cross sections given by Eqs. (6.11), (6.13) and (6.15). For this calculation all states up to $j = 60$ were included for both the dipole and quadrupole coupled rotations. The predicted cooling rate is surprisingly close to that measured, given the simplicity of the model and the variety of open cooling channels.

The total cooling power for each of the three processes is plotted in Fig. 6.5. Note that it switches sign from > 0 to < 0 when the positron temperature decreases below the gas temperature (300 K). Not surprisingly, the cooling power is dominated by vibrational excitation at high temperatures. However, at $T \sim 600$ K, the contribution from quadrupole-coupled rotations becomes comparable. Interestingly, due to the large quadrupole moment of CO and the fact that the allowed transitions for quadrupole coupling are $\Delta j = \pm 2$, quadrupole rotational excitations contribute more to the positron cooling than do the dipole-coupled rotations over the entire temperature range studied.

While no measurements exist for rotational excitation of CO by positron impact, the vibrational excitation cross section has been measured and found to be 2.8 ± 0.6 times larger than that predicted by Born-dipole coupling [41]. The dot-dashed curve shown in Fig. 6.4 shows the calculated cooling rate with this scaling applied to the Born-dipole cross section, leaving the rotational cross sections unscaled.

Unlike the previous cases of CF_4 and N_2 , CO involves multiple interactions, and so determining the magnitudes of the underlying cross sections by fitting the measured data using a single scale factor is more complicated. However, the large difference in the strengths and energies of the vibrational interactions relative to that of the rotational interactions allows rough estimates of their respective magnitudes to be made based on the shape of the cooling curve.

Fitting the measured data in the range of temperatures above 800 K, where the positron cooling is dominated by vibrational excitation, suggests that the Born-dipole vibrational cross section should be scaled by $\eta \sim 1.5$. Given the additional uncertainties in this factor due to potential contributions from the rotational modes, this result is roughly consistent with the direct measurement of 2.8. Since the dipole and quadrupole rotational interactions occur at similar energies, the scale factors for their cross sections cannot be determined individually. Nevertheless, relatively crude estimates of the ranges of cross section values can be made. If the dipole rotations are assumed to be completely absent, then the quadrupole rotational cross sections must be enhanced by a factor of ~ 1.5 to agree with the data. Alternatively, if the quadrupole interactions were assumed absent, then

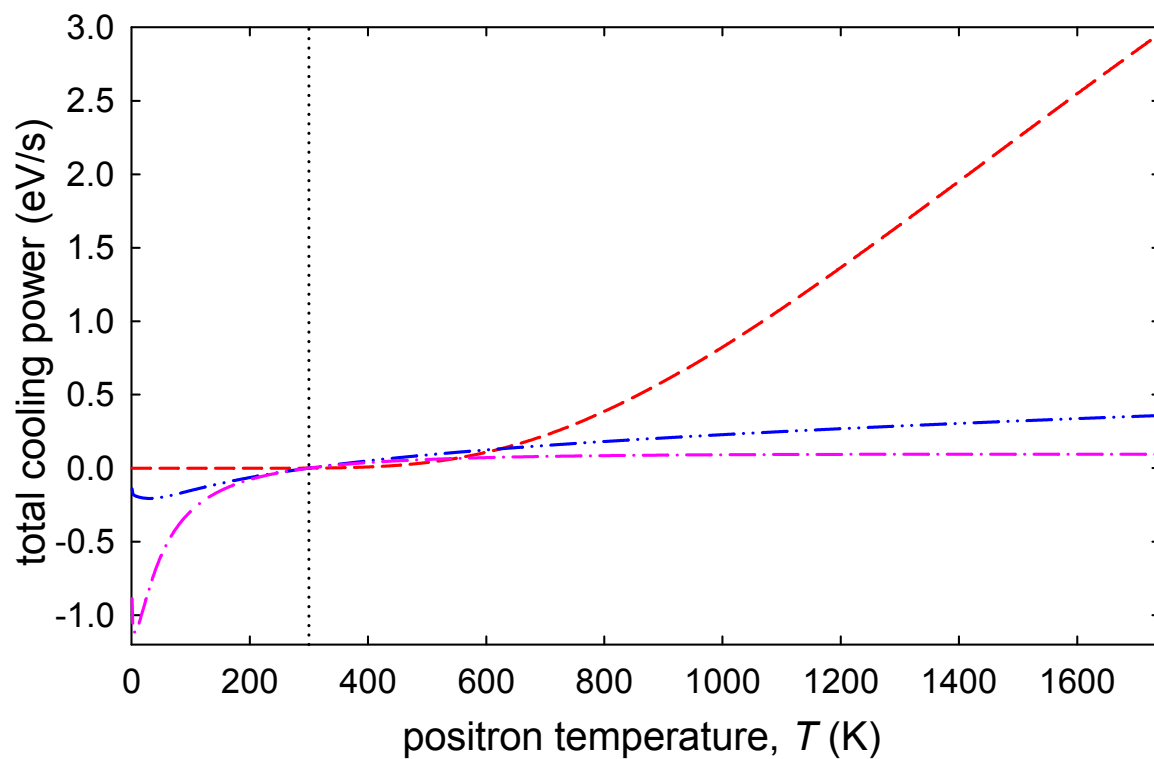


Figure 6.5: Positron-CO cooling power per channel. Total cooling power [defined in Eq. (6.6)] as a function of the positron temperature for $1.74 \mu\text{Torr}$ of CO at a gas temperature of 300 K (vertical dotted line) for (---) vibrational excitation, (-·-) dipole coupled rotations and (-·-) quadrupole coupled rotations.

Table 6.1: Buffer gas cooling parameters for the three molecules studied here: B_r is the rotational constant; μ and Q are the permanent electric dipole and quadrupole moments; ϵ_v and μ_v are the vibrational mode energies and transition dipole moments; τ_p is the pressure normalized 1/e time constant from Fig. 6.6; η are empirical scale factor(s) for the relevant theoretical cross sections required to obtain agreement with experiment. For the case of CO, η is given for the vibrational/dipole rotational/quadrupole rotational cases, respectively. See text for details.

molecule	B_r (meV)	μ (ea_0)	Q (ea_0^2)	ϵ_v (meV)	μ_v (ea_0)	τ_p (ms μ Torr)	η
CF ₄	-	0	0	159	0.12	4.8	0.95 ± 0.1
N ₂	0.25	0	1.27	-	-	1500	1.8 ± 0.2
CO	0.24	0.044	2.59	266	0.042	130	$\sim 1.5/0-3.5/0-1.5$

the dipole rotational cross sections would need to be scaled up by a factor ~ 3.5 .

Therefore, these data suggest that the Born-dipole rotational cross sections given by Eq. (6.15) should be scaled by $\eta \sim 0-3.5$, while the quadrupole rotational cross sections given by Eq. (6.13) require $\eta \sim 0-1.5$. Indeed, calculations from Refs. [66, 67] indicate that the dipole rotational excitation cross section should be scaled by a factor of $\sim 1-2$, while the quadrupole rotational excitation cross section should be scaled by a factor of ~ 0.3 . As an example, the dashed curve in Fig. 6.4 represents the solution with the cross section for vibrations, dipole rotations and quadrupole rotations scaled by $\eta = 1.5, 1.5$ and 1 , respectively.

6.3.4 Positron cooling comparisons

The time scales over which the positrons thermalize with a particular molecular gas clearly depends strongly on the type of gas and the cooling channels available. For comparison, Fig. 6.6 shows the measured cooling curves for the three molecules studied, normalized to a gas pressure of 1μ Torr. Also shown are exponential fits over this temperature range for each of the molecules. While the cooling curves are not quite exponential in shape, these fits allow estimates of the pressure-normalized 1/e times for these gases.

The model parameters used and the characteristic cooling times for the three molecules studied are listed in Table 6.1. By far the most effective cooling gas over the temperature range studied is CF₄, with a pressure-normalized 1/e time, τ_p , of just 4.8 ms- μ Torr; a factor of ~ 300 times faster than that of N₂. The total cooling power for CF₄ is significantly larger than that of either N₂ or CO over all temperatures studied (i.e., above 300 K). This is due to the very large transition dipole moment of the ν_3 vibrational mode, as well as the relatively high energy of this mode, which acts to remove significant energy from the positrons with each collision.

With a 1/e time of 1.5 s at 1μ Torr, N₂ is the least effective cooling gas studied. Both the cross sections and the amount of energy transferred are significantly smaller in the case of quadrupole rotational excitation than for that of vibrational excitation, resulting in far slower positron cooling. In addition, the quadrupole moment of N₂ is more than a factor of two smaller than that of CO, resulting in a smaller cooling power even at low temperatures where the CO vibration becomes insignificant.

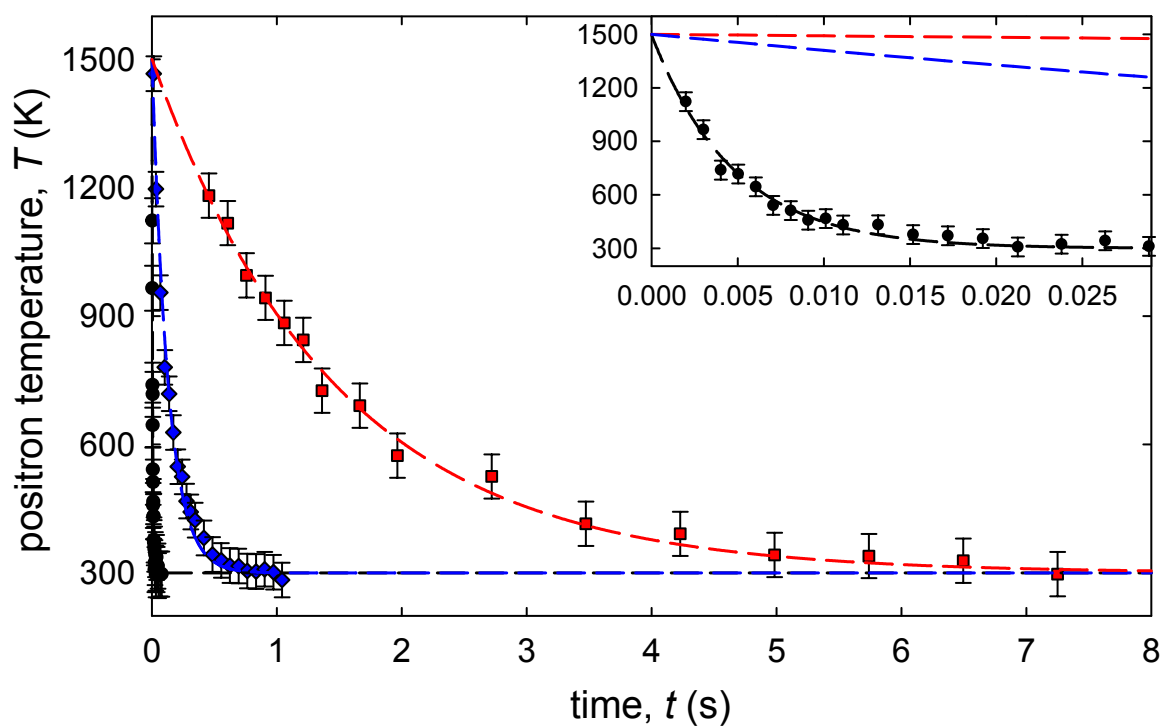


Figure 6.6: Positron cooling comparisons at 300 K using (●) CF₄, (◆) CO, and (■) N₂ gases normalized to 1 μ torr and shifted to line up at t=0 s; and (---) an exponential fit for each case. The inset shows CF₄ in more detail.

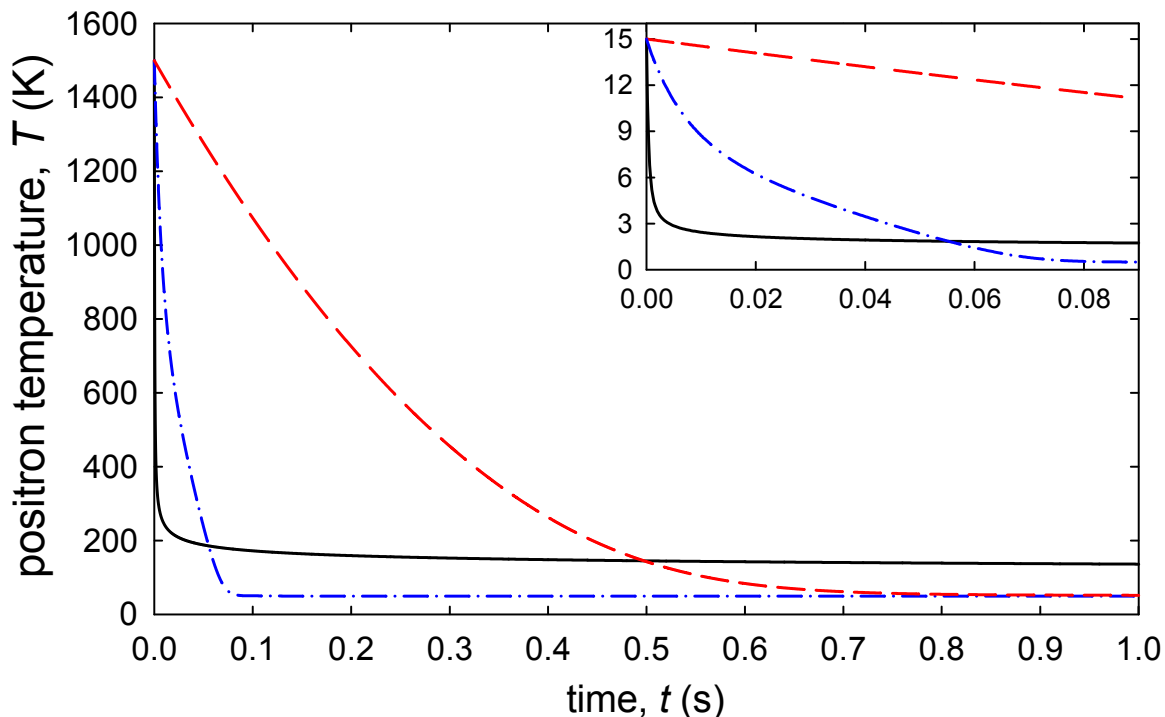


Figure 6.7: Positron cooling comparisons at 50 K. Solutions to Eq. (6.7) for a gas pressure of $1 \mu\text{Torr}$ and a temperature of 50 K using cross sections scaled by the empirically determined scale factors, η , listed in Table 6.1 for (—) CF_4 , (---) N_2 and (-·-) CO . Inset shows CF_4 and CO curves in more detail. See text for details.

The CO molecule cools through both vibrational and rotational excitation, and so it is expected to maintain reasonable cooling power over a broader range of temperatures than either CF_4 or N_2 . However, the non-degenerate CO stretch vibration has a transition dipole moment which is ~ 3 times smaller than that of the triply degenerate CF_4 stretch mode. This results in a vibrational excitation cross section ~ 27 times smaller than that for CF_4 .

6.4 Model predictions using cryogenic buffer-gases

While the measurements discussed in Sec. 6.3 were done with a gas temperature ~ 300 K, they provide insight into the effectiveness of these gases in cooling positrons to cryogenic temperatures. The data suggest that vibrational excitation is by far the most effective method of cooling positrons to 300 K. However, as the positron temperature decreases, so does the effectiveness of this cooling channel, due to the relatively high energies of vibrational modes. This raises the question as to whether rotational excitations are able to cool positrons to low temperatures on reasonable time scales.

Figure 6.7 shows the solution to (6.7) for positron cooling on CF_4 , N_2 and CO at a pressure of $1 \mu\text{Torr}$ and a temperature of 50 K. Note that fixing the gas pressure at $1 \mu\text{Torr}$ and reducing the temperature from 300 K to 50 K results in a factor of 6 increase in the gas number density, yielding far faster cooling rates. For these calculations, the Born approximation scale factors listed in Table 6.1 for CF_4 and N_2 were applied to the respective cross sections; while for CO , a factor

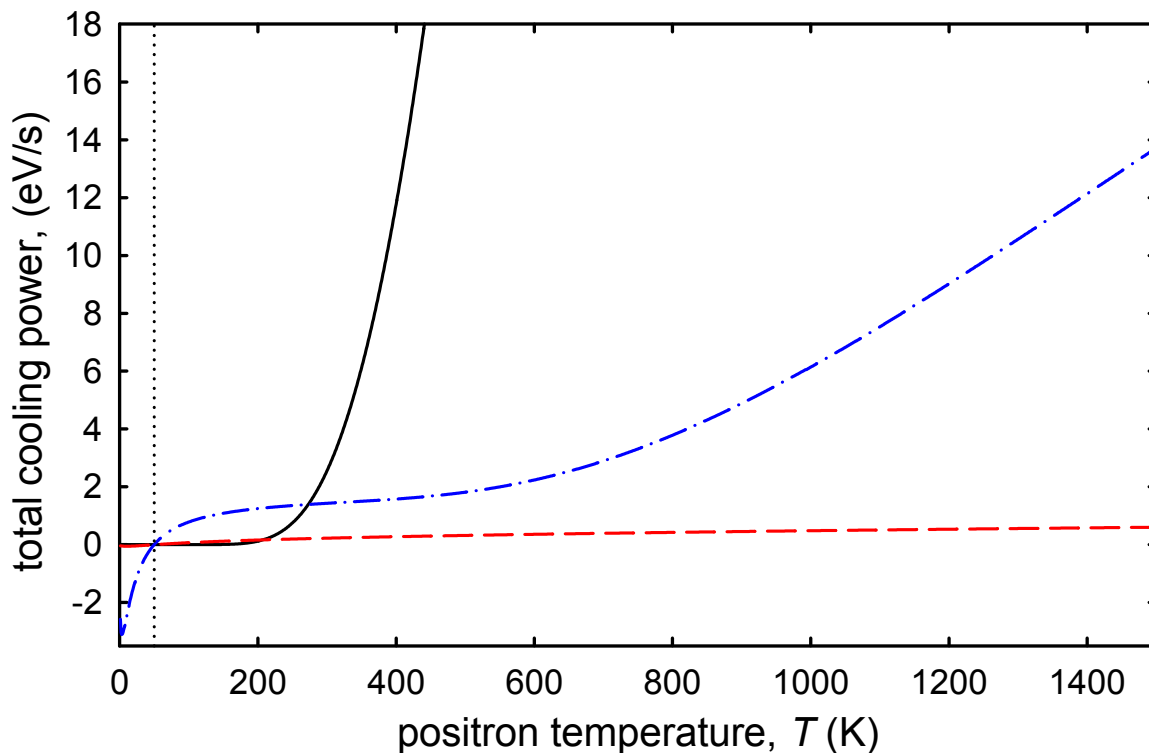


Figure 6.8: ositron cooling power at 50 K. Calculated total cooling power, defined as in Eq. (6.6), for the conditions described in Fig. 6.7 for (—) CF_4 , (- -) N_2 and (- · -) CO . Vertical dotted line shows gas temperature. See text for details.

of 1.5 was applied to the vibrational and dipole rotational cross sections, leaving the quadrupole rotational cross sections unscaled. Figure 6.7 shows the total cooling power, as defined by Eq. (6.6), for these conditions.

As in the 300 K case (Fig. 6.6), the positrons cool remarkably rapidly through interactions with CF_4 . However, due to the relatively high energy of the ν_3 vibrational mode in CF_4 , the cooling power drops off rapidly as the positron temperature falls. By 130 K the cooling power has dropped below 1 meV/s, making cooling below this temperature impractical on reasonable time scales. It should be noted that the lower energy ν_4 degenerate deformation mode, occurring at 78.4 meV, will make a non-negligible contribution to the cooling curve at very low temperatures. This mode was neglected due to having an excitation cross section ~ 20 smaller than that of the ν_3 mode. However at temperatures below ~ 230 K it becomes the dominant cooling mechanism, allowing the positrons to cool to $\lesssim 100$ K on reasonable time scales (not shown). However, it should be noted that due to the relatively low vapor pressure of CF_4 , it begins to freeze at temperatures below ~ 100 K and μTorr pressures.

Referring to Fig. 6.8, N_2 again shows a comparatively weak cooling power over a majority of the temperature range. However, because of the low energies of the rotational modes ($\epsilon_j = 1.5$ meV for the lowest excited rotational state), its cooling power continues to low temperatures. Below ~ 210 K, N_2 becomes a better cooling gas than CF_4 , and it appears possible to cool the positrons to 50 K in ~ 1 s using 1 μTorr of N_2 .

As was seen in Fig. 6.5 and can also be seen by the change in slope of the CO curve

in Figs. 6.7 and 6.8, CO transitions from cooling predominantly through vibrational to rotational excitation at ~ 600 K, and becomes the most effective cooling gas of the three discussed here at temperatures $\lesssim 270$ K. Due to its larger quadrupole and dipole moments, and its dipole-active vibrational mode, CO maintains a larger cooling power than N_2 over all temperatures considered here. For these reasons, it appears possible to cool positrons to 50 K in $\lesssim 100$ ms using 1 μTorr of CO.

Some of the work and discussion in Chapter 6 is taken from “Positron cooling by vibrational and rotational excitation of molecular gases,” M. R. Natisin, J. R. Danielson and C. M. Surko, *J. Phys. B* **47**, 225209 (2014) [25]. The author of this dissertation led the research and was the principle author of the paper.

Chapter 7

The cryogenic beam-tailoring trap

As described in the previous chapters, the processes of positron beam formation and cooling have been studied in detail. Under typical conditions, beam formation is intrinsically dynamical. In particular, the particle dynamics just before ejection are crucial in setting beam quality. It was also shown that cooling the positrons to low temperatures prior to ejection is expected to yield significantly improved energy and temporal resolution, and that trap geometries which create narrow, parabolic trapping potentials result in optimal beam quality. Using these results, a new trap-based beam system was designed and built, with the goal of achieving significantly improved energy resolution together with improved spatial and temporal resolution.

A schematic diagram of the upgraded beamline is shown in Fig. 7.1. The source, moderator and buffer gas trap (BGT) regions are unchanged from the previous experimental configuration and operate as described in Chapter 2. The pulsed, room temperature positron beam ejected from the BGT is magnetically guided into a new apparatus called the cryogenic beam-tailoring trap (CBT). The CBT is placed after the BGT, where it re-traps the incident, room-temperature positrons, compresses them both radially and axially, and further cools them through interactions with a cryogenically cooled buffer gas before re-ejecting them as a pulsed beam with superior beam characteristics.

7.1 Overview of CBT design

A schematic diagram of the region surrounding the primary CBT electrodes is shown in Fig. 7.2. The CBT is attached to a high-power cryocooler (Cryomech AL-325) via a cold finger. The cryocooler is maintained at ~ 12 K, as measured by a temperature sensor on the cold head. The cold finger is made of oxygen-free high-conductivity (OFHC) copper with a large cross sectional area to maximize thermal conductivity. The cold finger is attached to the CBT through a high thermal conductivity flexible thermal strap, which isolates the CBT electrodes from the strong vibrations produced by the cryocooler. A room-temperature buffer gas is introduced through a PID controlled piezoelectric valve and into a long metal tube which feeds the gas into the trap. The trap is pumped on both sides by cryogenic pumps.

The CBT electrode design is shown in Fig. 7.3. The primary CBT electrodes consist of eight cylindrically symmetric electrodes surrounded by a cylindrical shell. The electrodes are made of OFHC copper. They were originally plated with a $50 \mu\text{in}$ silver diffusion barrier followed by a $50 \mu\text{in}$ gold overlayer. However, for improved electrode performance, the inner diameter surfaces of the electrodes were subsequently coated with a colloidal graphite solution commonly known as

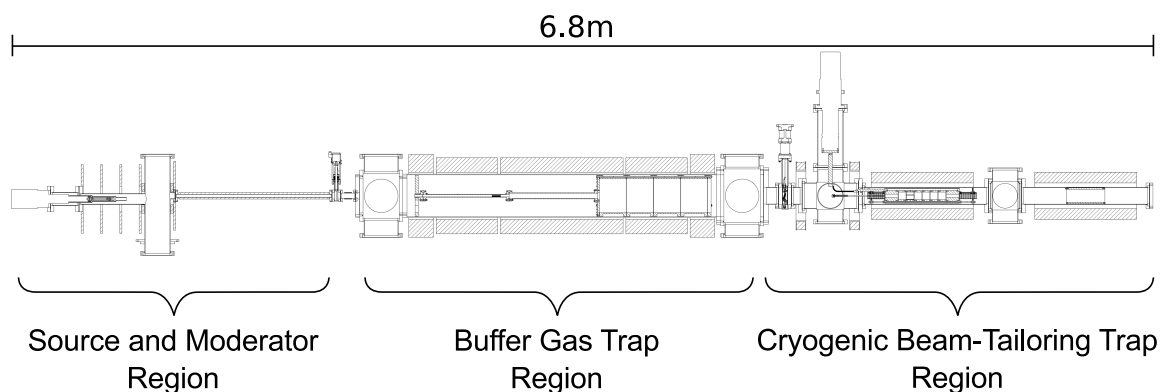


Figure 7.1: Schematic diagram of the CBT-based beamline. A steady-state positron beam is produced in the source and moderator region and guided into the buffer gas trap region, where it is converted into a high resolution pulsed beam. This pulsed beam is then guided into the cryogenic beam-tailoring trap region, where it is further tailored into a pulsed beam with superior characteristics.

Aquadag for improved electrical uniformity, as discussed below.

The electrodes are maintained at a temperature between 46 K and 54 K, as measured by temperature sensors placed on baffle electrodes at each end of the trap. Room-temperature buffer gas is injected through a long metal tube into the region between the inside of the outer shell and the outside of the electrodes. The buffer gas cools to the ~ 50 K electrode temperature through collisions with the cold surfaces before entering the inner cavity through slots in one of the electrodes. The 50 K buffer gas has an estimated typical pressure of ~ 1 μ Torr in the inner cavity, where it is able to interact with the trapped positrons.

7.2 Experimental methods with the CBT

The CBT operates in six phases, as shown in Fig. 7.4. Initially, the potentials are set to catch the incident BGT pulse, during which time the BGT fill, cool and eject phases are completed. Approximately 10 μ s after the BGT eject phase is triggered, the incident pulse is “caught” by gate-switching electrode B1. The re-trapped positrons are compressed radially for ~ 0.2 s using the so-called “rotating wall” technique in the single-particle regime by applying an azimuthally rotating electric field to the 4-segmented electrode labeled RW [68, 69].

After the radial compression phase, the positrons are axially compressed by applying a negative voltage to R1, thus pulling them into a narrow parabolic potential well. This is done to induce a strong magnetron motion for better radial confinement during cooling, and to increase the amount of adiabatic cooling during ejection (as discussed in Chapter 5). At this point, the positrons are cooled through interactions with the 50 K CO buffer gas for ~ 0.2 s. They are subsequently ejected by increasing the R1 electrode voltage, which lifts them over the potential barrier generated by R2 and R3 and ejects them as a pulsed, cryogenic positron beam.

Under typical conditions, the total shot-to-shot time (including BGT phases) is ~ 0.8 s for $\sim 10^4$ positrons per pulse from the CBT. The re-trapping efficiency (i.e., BGT to CBT) is $\sim 60\%$. This represents a 40% loss which appears to be due to the following two effects. The first is that the incident BGT beam diameter is comparable to the inner diameter of the CBT baffle electrodes

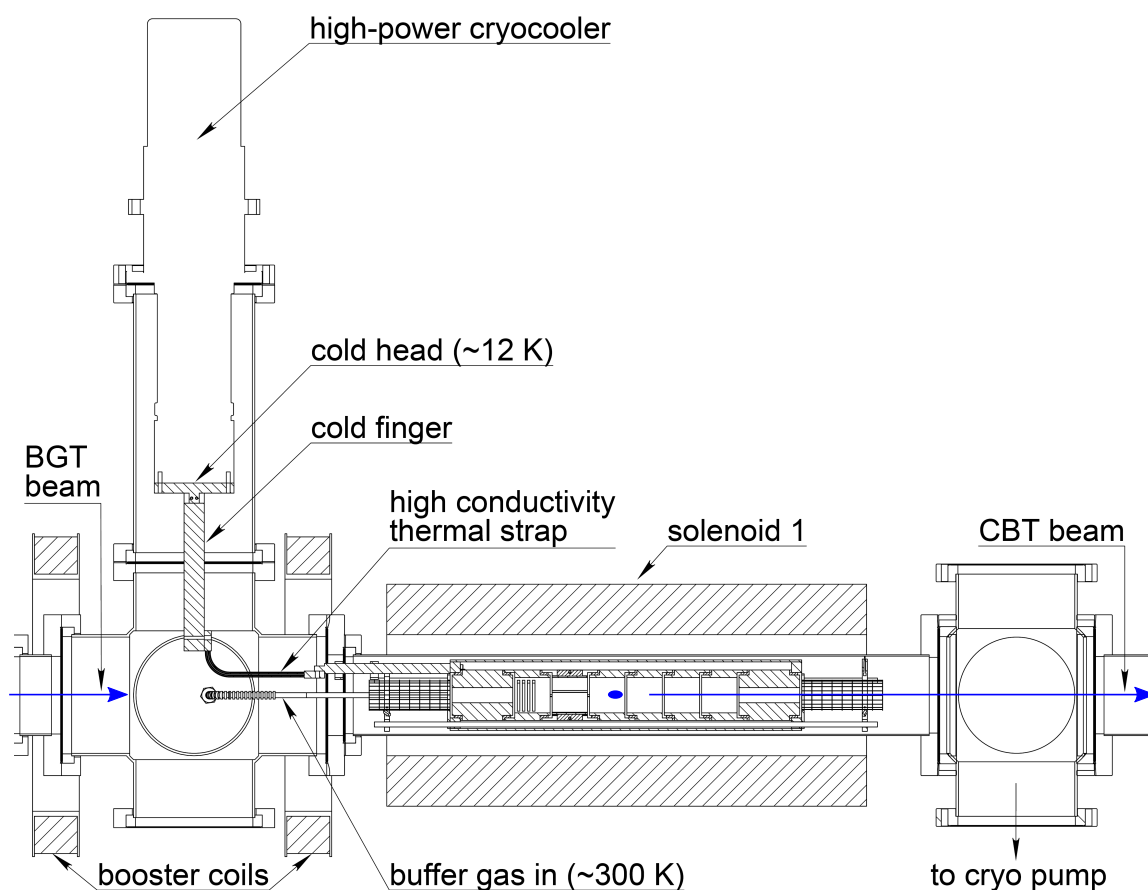


Figure 7.2: Schematic diagram of the CBT region. The pulsed BGT beam is magnetically guided into the CBT by a pair of booster coils and a solenoidal magnet, providing a magnetic field of ~ 650 G. A high-power cryocooler maintained at 12 K is attached to the CBT electrodes via a cold finger. A thermal strap isolates the CBT electrodes from the vibrations produced by the cryocooler. The CBT buffer gas is injected into the trap at through as gas line and pumped on both sides of the trap by cryogenic pumps.

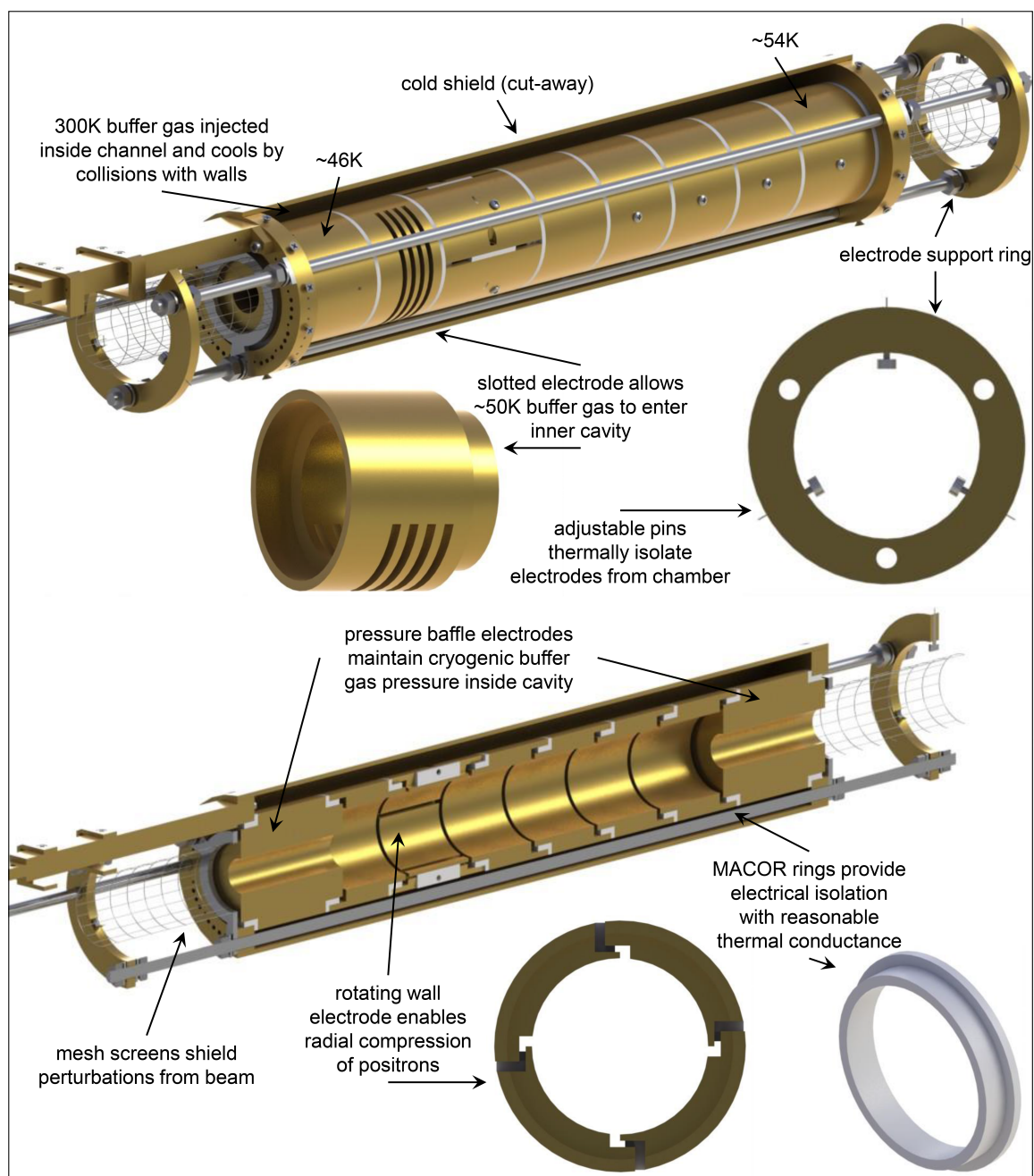


Figure 7.3: Overview of CBT electrodes.

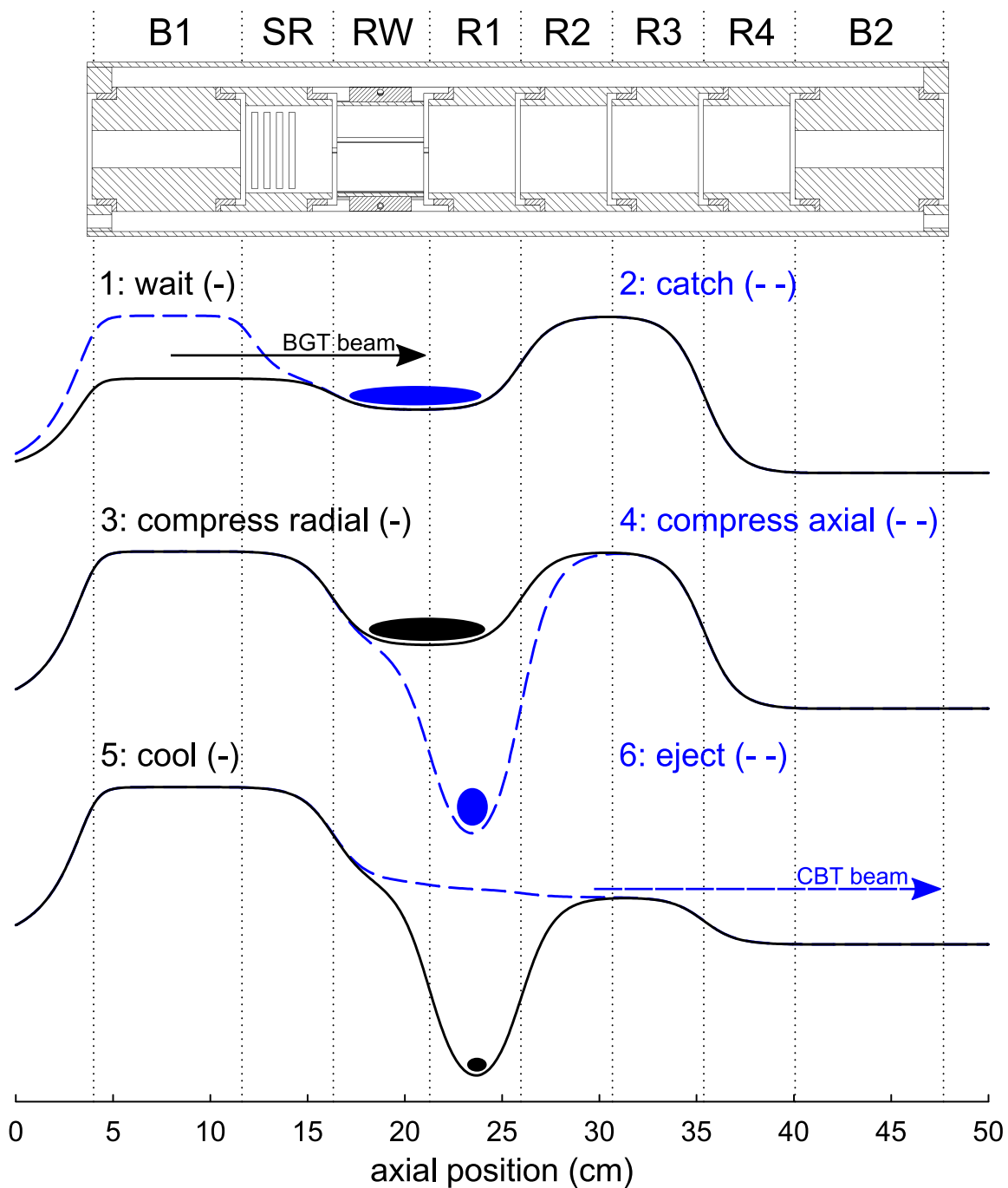


Figure 7.4: Schematic diagram of the CBT electrodes and potentials produced during each of its six phases of beam formation. Electrodes from left to right are the baffle B1, slotted ring SR, rotating wall RW, cylindrical rings R1 - R4, and baffle B2. Phases are labeled according to the order in which they proceed, (—) shows phases 1,3 and 5 and (---) shows phases 2,4 and 6. Shaded regions and arrows represent the positrons in the various phases. See text for details.

[baffle ID = 1.9 cm, cf. Fig. 7.7 (b) inset for BGT beam *radial* profile]. Secondly, there is significant asymmetry-induced radial expansion of the positrons before they are compressed by the rotating wall.

When trapping in an approximately parabolic potential well in the region beyond the SR and RW electrodes (i.e., the electrodes with azimuthal asymmetries), $\sim 100\%$ re-trapping has been obtained. This is the expected result based on simulations of the re-trapping process. However, the re-trapping efficiency is reduced when using non-parabolic trapping potentials or trapping in a region which includes the SR or RW electrodes, both of which are required for operation of the rotating wall. The buffer gas and pressure also affect the efficiency, but to a lesser extent. These results indicate that radial compression of the incident BGT beam would likely result in a near-unity re-trapping efficiency.

Using this technique, positrons have been cooled to 50 K with either a CO or N₂ buffer gas. In the case of CO, the positrons are cooled primarily through vibrational excitation of the CO stretch mode at high temperatures, then rotational excitation at low temperatures by coupling to both the CO dipole and quadrupole moments. In the case of N₂, positron cooling is significantly slower due to quadrupole-coupled rotational excitation being the dominant cooling channel (cf. Chapter 6). It should be noted that, while positrons were cooled to 50 K using either a CO or N₂ buffer gas, radial compression was only significant when CO was used. No appreciable radial compression was achieved when using N₂. For this reason, and due to CO yielding significantly faster cooling rates, the beam results discussed here were all obtained using a CO buffer gas.

Once the beam is ejected from the CBT, it is magnetically guided into another solenoidal magnet where the beam characteristics are measured. The measured magnetic field for the CBT-based beamline under typical conditions is shown in Fig. 7.5. Here, an RPA electrode is used to measure the positron energy distributions using the techniques described in Chapter 3. Additionally, a phosphor screen, mounted to the end flange of the beamline ($B \sim 320$ G), enabled measurement of the beam radial distribution.

7.3 Characterization of the CBT beam

The resulting parallel, perpendicular, and total energy distributions obtained from the CBT are shown in Fig. 7.6. For these data, the positrons are ejected by raising the well voltage to 0.1 V above the exit-gate voltage. The methods used to obtain these distributions have been described in detail in Chapter 3. The parallel energy distribution is well fit by a Gaussian with $\Delta E_{\parallel} = 4.0 \pm 0.2$ meV FWHM and a standard deviation $\sigma_{\parallel} = 1.7 \pm 0.1$ meV. The perpendicular energy distribution is a Maxwell-Boltzmann with $\sigma_{\perp} = 4.5 \pm 0.3$ meV, corresponding to a positron temperature of 52.4 ± 3.7 K. Finally, the total energy distribution is a convolution of the parallel and perpendicular components, resulting in an exponentially modified Gaussian (EMG) distribution with an energy resolution $\Delta E_t = 6.9 \pm 0.7$ meV ($\sigma_t = 4.8 \pm 0.3$ meV). This is a factor of ~ 5 better than that obtained by the previous state-of-the-art positron beam, as shown in the inset to Fig. 7.6 (c).

While the primary goal of the CBT was to provide significantly improved energy resolution as compared with previously existing techniques, other characteristics of the resulting beam were also improved. Shown in Fig. 7.7 are the measured temporal and radial distributions, obtained under the same conditions as those shown in Fig. 7.6. The temporal distribution is approximately Gaussian with $\Delta\tau = 0.88 \pm 0.01$ μ s FWHM ($\sigma_{\tau} = 0.4 \pm 0.004$ μ s); this corresponds to a factor of ~ 2 improvement over the previous state-of-the-art energy resolution beam. As discussed in Chapter 3, the response time of the detector and associated electronics was ~ 0.5 μ s FWHM, and so provides

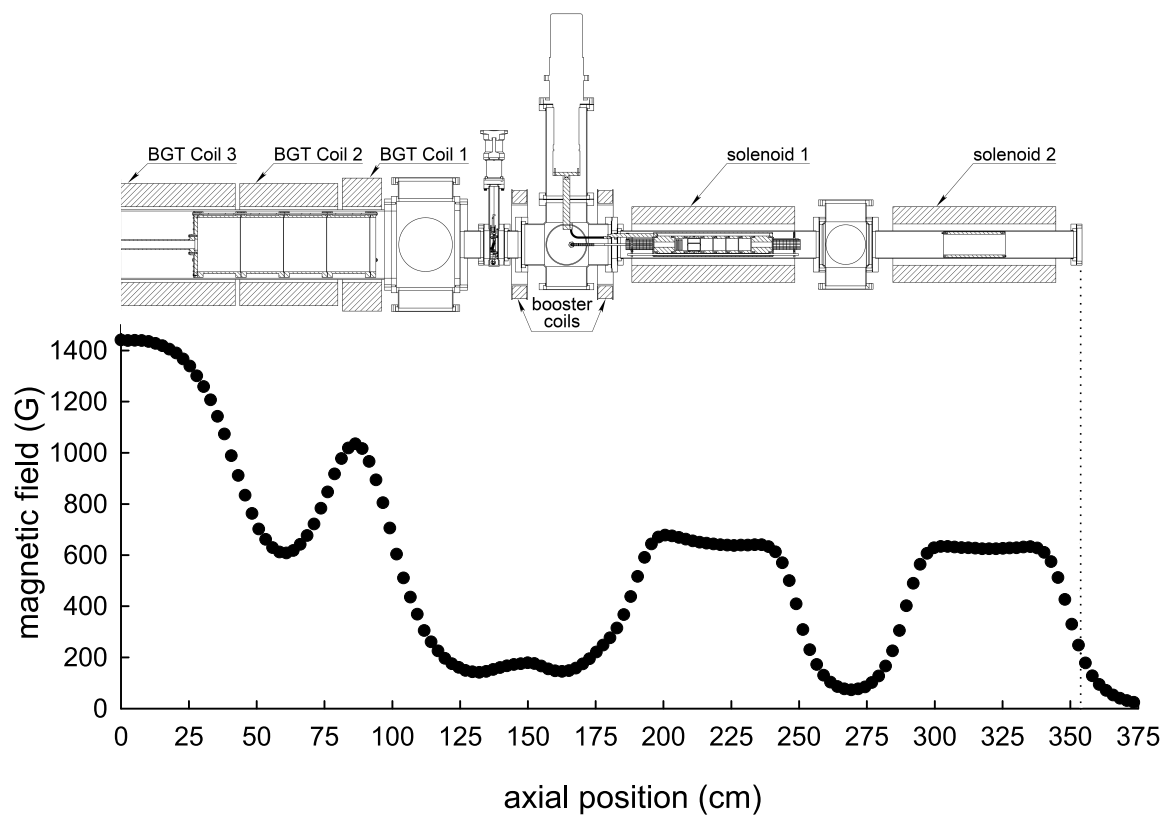


Figure 7.5: Measured magnetic field of CBT-based beamline. (Top) schematic diagram of the beamline from the second stage of the BGT to the RPA region and (bottom) measured on-axis magnetic field over the same region under typical conditions. Vertical dashed line indicates relative position of end of beamline.

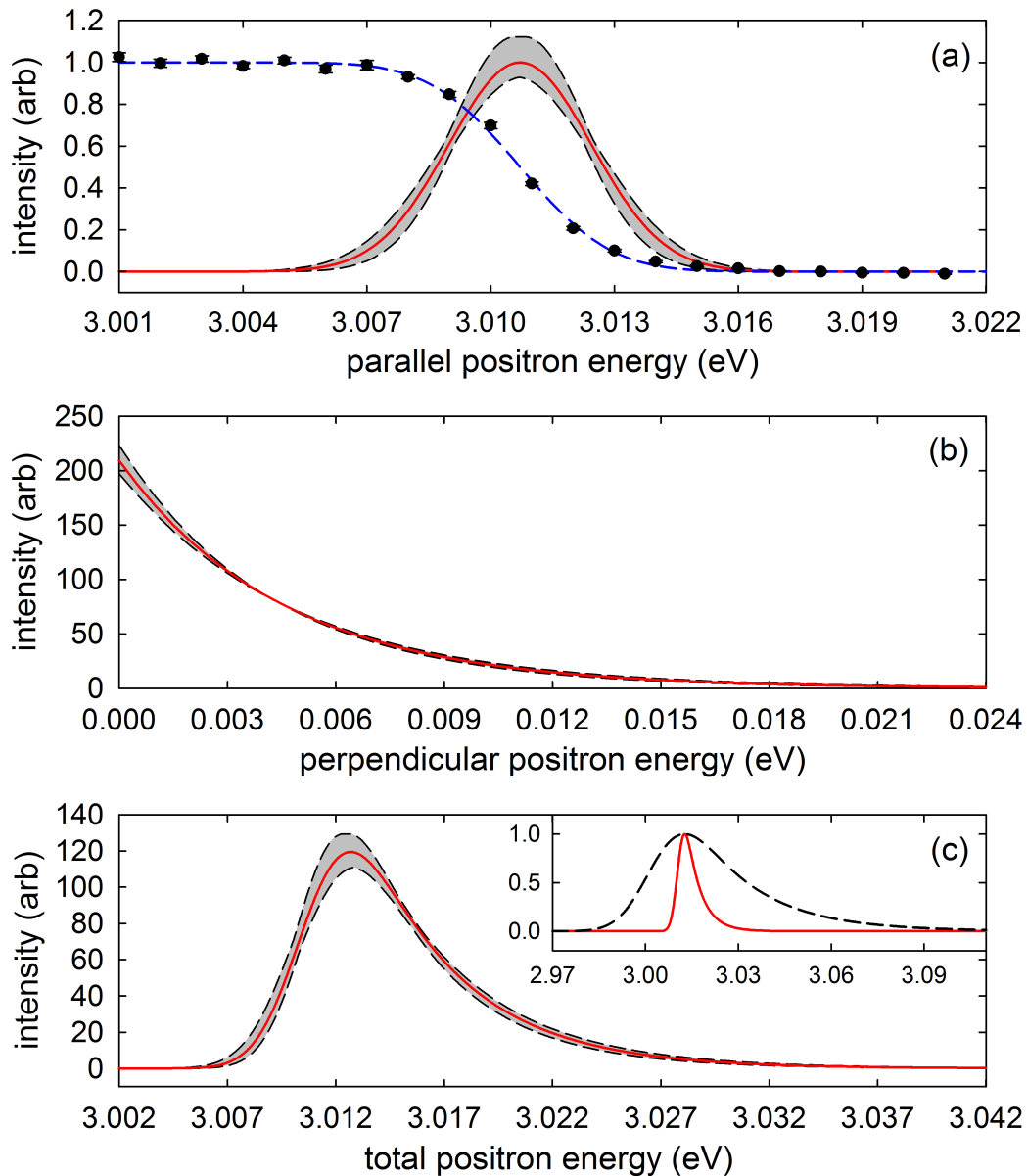


Figure 7.6: Measured energy distributions obtained from CBT (—): (a) (•) measured cumulative parallel energy distribution, (—) Gaussian fit to data yielding $\Delta E_{\parallel} = 4.0 \pm 0.2$ meV FWHM ($\sigma_{\parallel} = 1.7 \pm 0.1$ meV), (b) Maxwell-Boltzmann perpendicular energy distribution corresponding to a measured mean perpendicular energy of 4.5 ± 0.3 meV (52 ± 3.7 K), and (c) convolution of curves in (a) and (b), yielding $\Delta E_t = 6.9 \pm 0.7$ meV FWHM ($\sigma_t = 4.8 \pm 0.3$ meV). Shaded regions show 95 % confidence intervals estimated from the fits. The inset in (c) shows the total energy distribution obtained from (—) CBT, and (---) state-of-the-art BGT [cf. Fig. 3.4(c)].

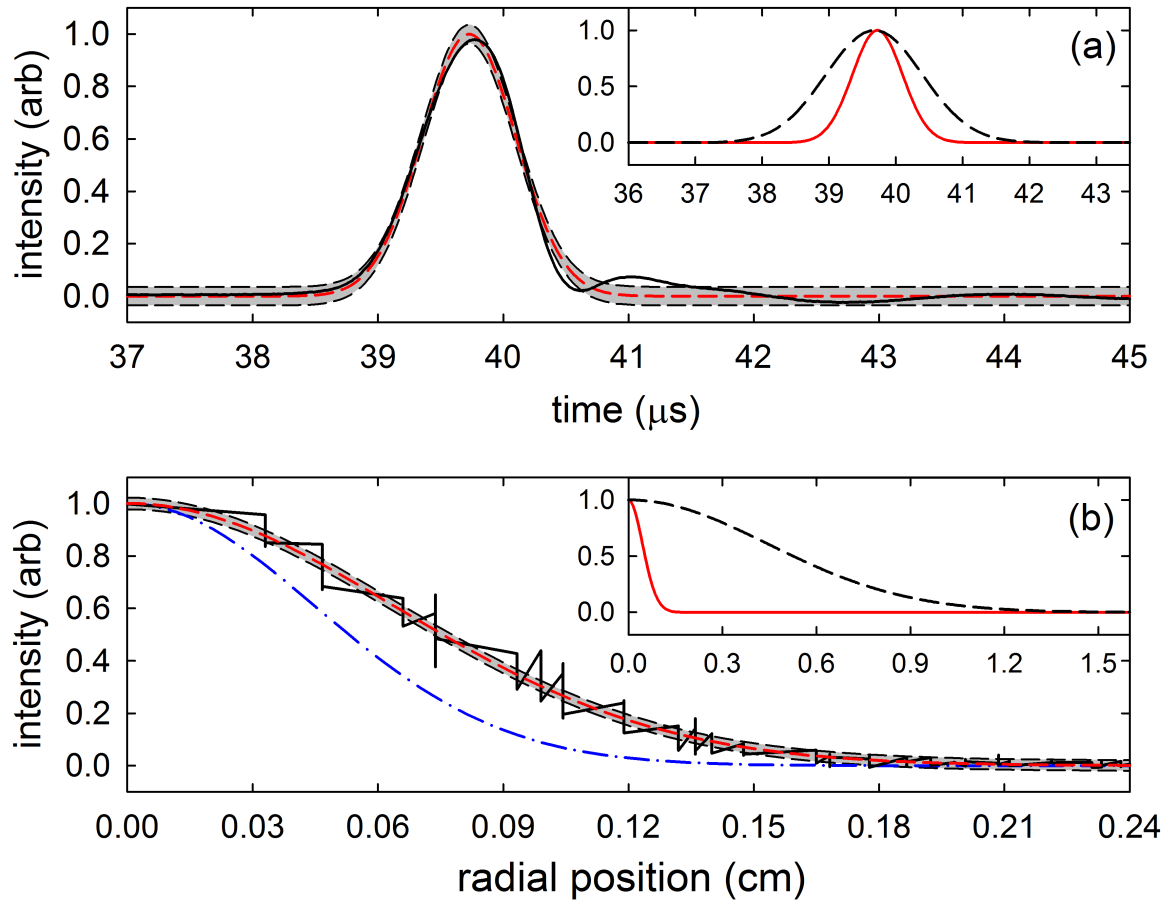


Figure 7.7: Measured time and radial distributions obtained from CBT (—): (a) temporal and (b) radial beam distributions from the CBT as measured at the phosphor screen (32 mT). (---) Gaussian fits to data yielding $\Delta\tau = 0.88 \pm 0.01 \mu$ FWHM ($\sigma_\tau = 0.4 \pm 0.004 \mu$ s) and $\Delta R = 0.15 \pm 0.001$ cm FWHM, respectively. (---) Estimated radial distribution in CBT (650 G) with $\Delta R \approx 0.1$ cm FWHM. Shaded regions show the 95 % confidence intervals estimated from the fits. Insets show fits to the (a) temporal distribution obtained from (—) CBT and (---) state-of-the-art BGT and (b) radial distribution at 650 G obtained from (—) CBT and (---) state-of-the-art BGT (cf. Fig. 3.5).

a non-negligible contribution to the measured temporal distribution. Therefore this measurement represents an upper bound. Under different conditions (e.g., increasing the positron ejection rate), significantly narrower temporal spreads may be obtained at the cost of energy resolution. However, due to the limitations of the current detection apparatus, the ultimate limit of the temporal resolution has not yet been measured.

The radial distribution, shown in Fig. 7.7 (b), is measured by accelerating the beam to -10 kV and allowing it to impinge on a phosphor screen. The resulting light is recorded with a CCD camera and the data averaged azimuthally. The measured radial distribution is fit to a Gaussian, yielding a beam diameter of $\Delta R = 0.15 \pm 0.001$ cm FWHM at the phosphor screen. Taking into consideration the fact that the screen is in a lower magnetic field than the CBT (320 G vs. 650 G, respectively), the measurements indicate that the beam diameter in the CBT is approximately 1 mm. This is a full order of magnitude improvement over the 300 K BGT beam. For reference, without the radial compression using the RW, the beam diameter in the CBT is approximately 1 cm FWHM.

7.4 CBT beam results under various conditions

The results presented in the previous section demonstrate the CBT beam characteristics under conditions such that the highest energy resolution is obtained. In this section the behavior of the beam distributions under other conditions are briefly discussed.

Shown in Fig. 7.8 are the measured FWHM of the parallel energy, total energy and temporal distributions obtained from the CBT using various ramp voltages, defined as $\Delta V_r = V_s - V_E$ (i.e., final ramp voltage V_s above exit-gate voltage V_E), shown for the cases where the CBT is operated at both 300 K and 50 K, respectively. This has the effect of varying the positron ejection rate. Here it is seen that at all ramp voltages both the parallel energy and temporal spreads are reduced in the lower temperature case, due to the effects of positron temperature on beam formation described in Chapter 5. Moreover, the total energy spreads are further reduced in the low temperature case due to the lower perpendicular spread.

As the ramp voltage is decreased, the parallel energy spread trends towards smaller values and the temporal spread trends towards larger values, as expected from the analysis in Chapter 5. However, at low ramp voltages, ΔE_{\parallel} is seen to begin to increase with decreasing ramp voltage in the 300 K case. This is due to beam reflections during the measurement process (cf. Sec. 3.5), where the “secondary beam” signal overlaps with that of the primary beam, thus broadening the measured energy distribution. In contrast, in the 50 K case the greatly reduced temporal spread allows the primary beam to remain sufficiently isolated in time from these secondary beams, allowing accurate measurement down to $\Delta V_r \sim 0.1$ V. It should also be noted that the measured temporal spread is limited by the minimum detector response of $\sim 0.5 \mu\text{s}$ FWHM, and so these values represent upper bounds. This is especially unfortunate in the 50 K case, where $\Delta\tau \lesssim 0.5$ at all but the lowest ramp voltages.

The effect of positron number on the measured temporal spread is shown in Fig. 7.9. For this data, the ramp voltage is set to 0.3 V. The data are taken with the CBT at both 300 K and 50 K, each with the radial compression both on and off. Here it is seen that in all cases, $\Delta\tau$ increases with positron number. However this effect is relatively weak, particularly below 10^4 positrons. Further, the radial compression has no significant effect at low positron numbers. However, above $\sim 10^5$ positrons, the radial compression results in $\Delta\tau$ increasing more rapidly with positron number. This effect is more pronounced in the 50 K case.

These effects are thought to be due to the positron space-charge potential, which increases

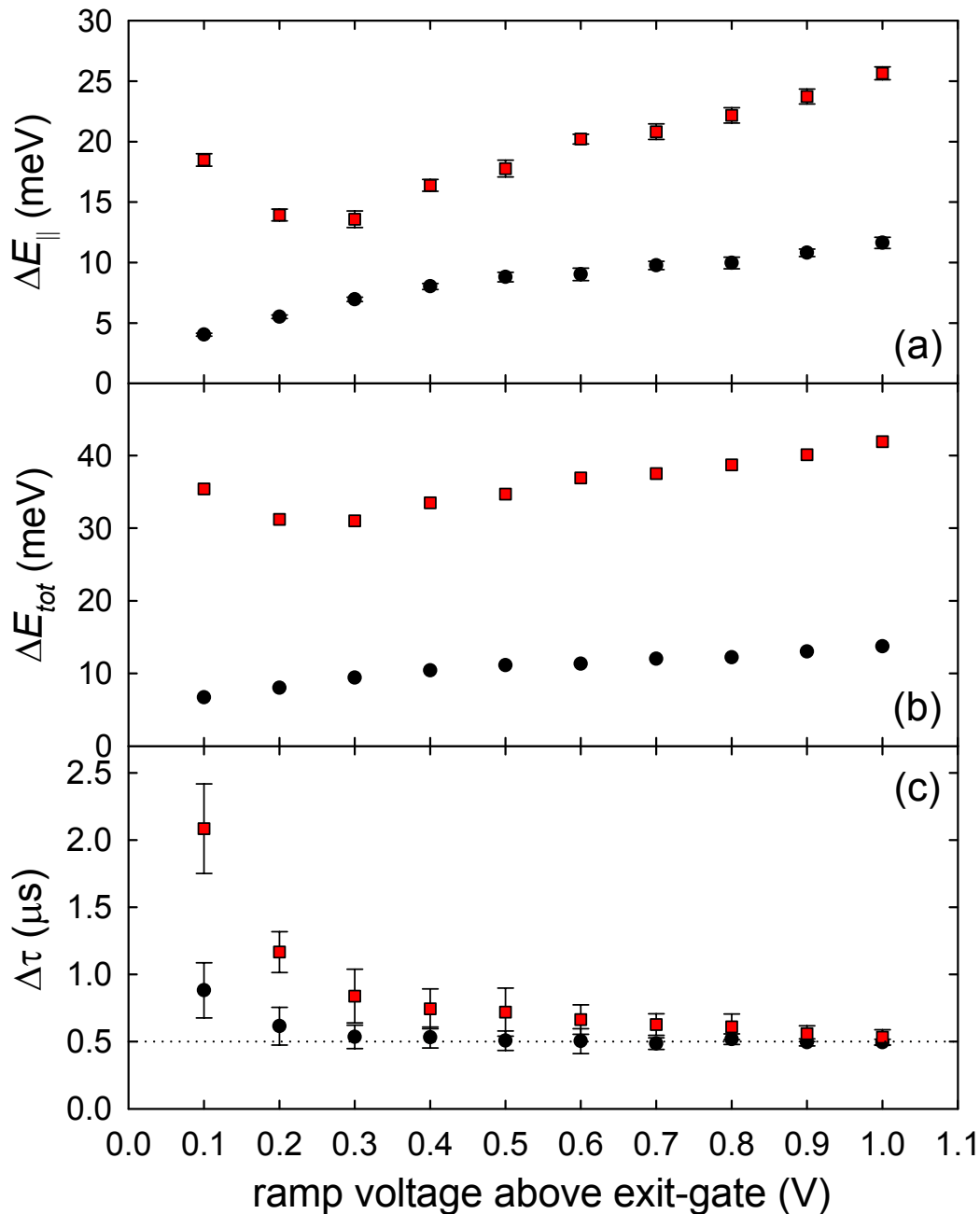


Figure 7.8: Effect of ramp voltage on the CBT beam. FWHM of the (a) parallel energy, (b) total energy [calculated using Eq. (3.9)], and (c) time distributions using various ramp voltages, $\Delta V_r = V_s - V_E$. (\bullet) CBT at ~ 300 K and (\blacksquare) CBT at ~ 50 K. Note that in (b) the detector response limits the temporal spread measurement to ~ 0.5 μ s FWHM (shown by dotted line), and so these values represent upper bounds.

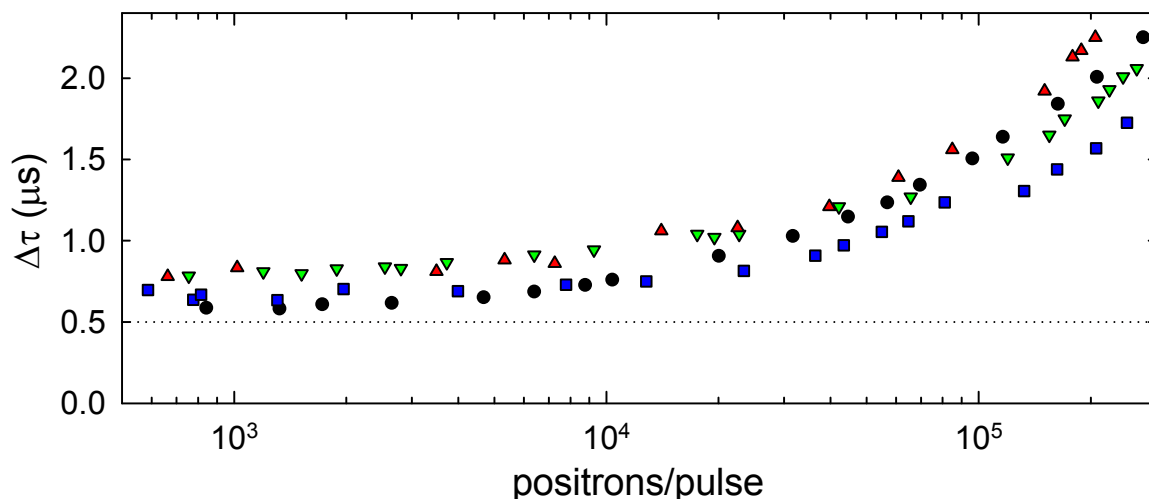


Figure 7.9: CBT temporal spread dependence on positrons number. (●) measured FWHM of the temporal distribution obtained as the number of positrons per pulse is varied. (▲) CBT at 300 K, radial compression on, (▼) CBT at 300 K, radial compression off, (●) CBT at 50 K, radial compression on, (■) CBT at 50 K, radial compression off. Dotted line shows minimum detector response ($\sim 0.5 \mu\text{s}$ FWHM).

as the number of positrons per unit length (along the magnetic axis) increases, and as the positron diameter decreases (relative to the electrode diameter). This is consistent with the data shown in Fig. 7.9. Specifically, $\Delta\tau$ increases more rapidly at smaller beam diameters, and at lower temperatures (i.e., where the number of positrons per unit length is increased due to the reduced axial extent of the positrons).

7.5 CBT Utility in future research

The significantly narrower total energy distribution obtained from the CBT has several practical advantages. This narrower energy spread allows features approximately five times more densely packed in energy to be resolved, as compared with previous capabilities. This is, for example, particularly useful for studying annihilation processes such as intramolecular vibrational redistribution. It is also expected to be sufficient to enable the first direct measurements of positron-induced multimode excitations. Additionally, it is sufficient to permit measurements of features down to approximately five times lower energy, potentially enabling the first state-resolved measurements of rotational excitation by positron impact. Finally, the narrower total energy distribution yields approximately five times better signal-to-noise ratios for narrow spectral features as compared to those obtained previously. This allows smaller signals to be adequately measured with less averaging. Several specific examples of new measurements made possible by this technology are discussed below.

7.5.1 Positron annihilation on molecules

As described in Chapter 4, the primary motivation for the development of the CBT was to enable the study of a variety of positron-molecule annihilation processes that appear to be present

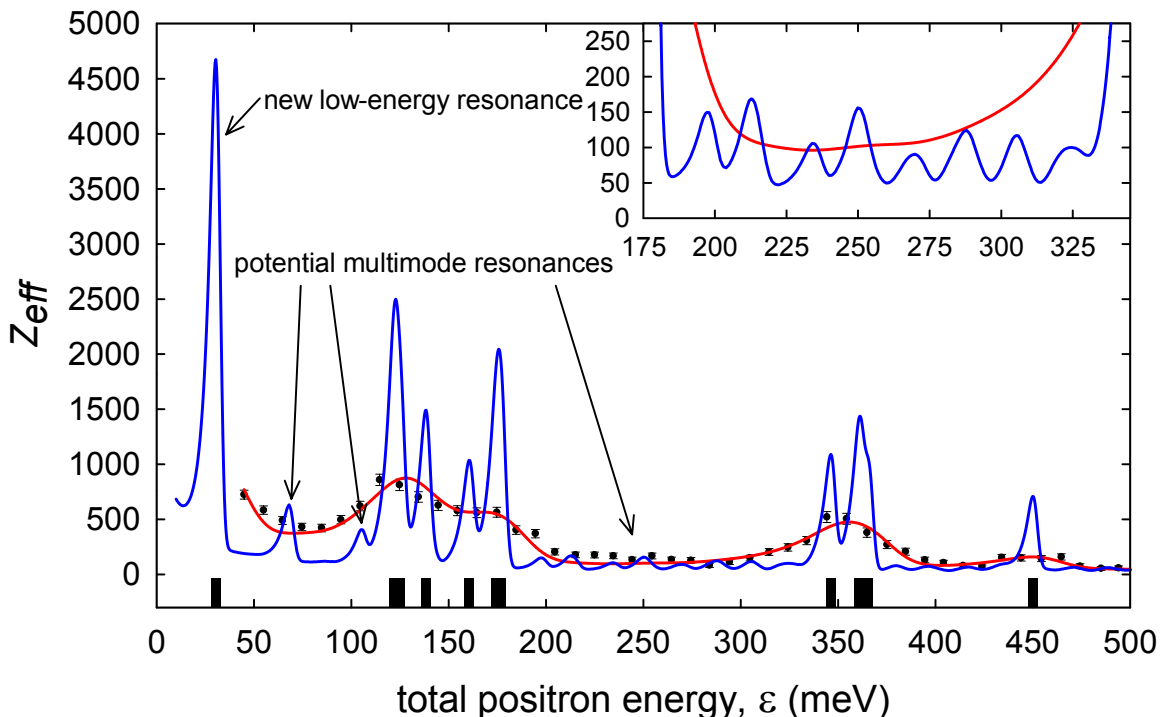


Figure 7.10: BGT vs. CBT annihilation spectrum for methanol (CH_3OH): (\bullet) measured Z_{eff} , ($—$) total model from Eq. (A.16) fit to data with BGT beam distribution (cf. Table B.12), and ($—$) total model using same fit parameters but with CBT beam distribution. Vertical bars show vibrational mode energies downshifted by binding energy. Inset shows low Z_{eff} resonance in more detail.

within measurements made using the BGT-based beamline, but could not be studied in sufficient detail due to the limitations of the available beam-energy resolution. These open questions include the study of previously unseen low-energy ($\lesssim 50$ meV) vibrational Feshbach resonances (VFRs), the effects of infrared-inactive vibrational modes, the contribution from multimode resonant annihilation (MRA), and the effects of intramolecular vibrational redistribution (IVR) on the measured annihilation spectra. These processes are described in more detail in the appendix.

Presented here are examples where additional physics beyond the standard Gribakin-Lee (GL) model can now be studied. The measured data are fit to the “total model” (Eq. (A.16)), which includes the predictions from the GL and MRA models, where the magnitudes of the resonances predicted by GL are scaled by factors β_{ν} and the MRA prediction is scaled by a numerical factor η to best fit the data. Equation (A.16) is then used with these same fitted factors to best predict the annihilation spectra which would be measured using the CBT beam.

The first example, shown in Fig.7.10, is the annihilation spectrum for methanol (CH_3OH). Here, the benefits of the narrower energy spread of the CBT beam is immediately apparent in the splitting of the previously resonances into multiple peaks. For the fundamental VFRs, this allows the effects of IVR on individual vibrational modes to be examined. It also allows for more accurate measures of the positron-molecule binding energy to be obtained. The improved energy resolution also allows the measurement of previously unobserved low energy VFRs. Also shown here is an example where the CBT beam has the potential to make the first state-resolved measurements of

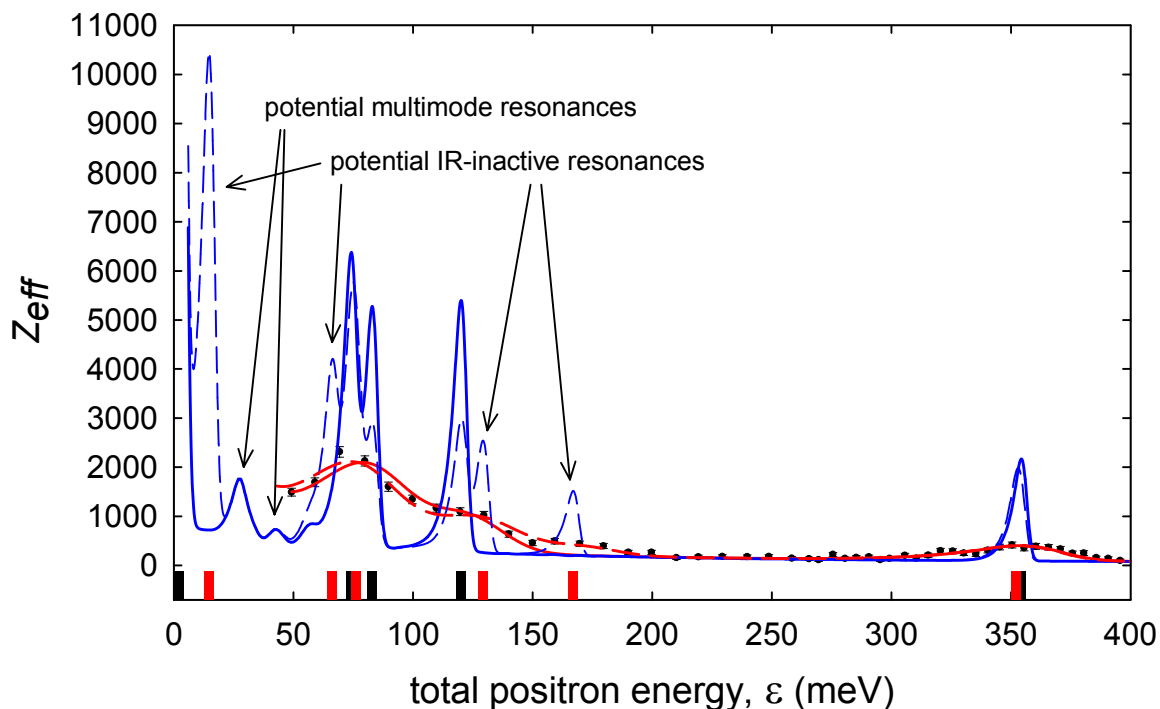


Figure 7.11: BGT vs. CBT annihilation spectrum for 1,2-trans-dichloroethylene ($C_2H_2Cl_2$): (\bullet) measured Z_{eff} , ($-$) total model from Eq. (A.16) fit to data with BGT beam distribution (see Table B.17), and ($-$) total model using same fit parameters but with CBT beam distribution. Dashed curves show the total model predictions including IR-inactive modes. Vertical bars show vibrational mode energies downshifted by binding energy, where black and red indicate IR-active and IR-inactive modes, respectively.

multimode VFRs. These measurements will confirm whether or not the broad background of annihilations seen in virtually all measured data to date is due to multimode resonant annihilation, and if so, they will provide important information towards understanding the discrepancies between the MRA model and the measured data (as discussed in Appendix A).

The annihilation spectrum for 1,2-trans-dichloroethylene ($C_2H_2Cl_2$) is shown in Fig. 7.11. Also shown is the fitted total model solutions for the case where only infrared-active vibrational modes are included (i.e., as intended in the GL model), as well as the case where *all* vibrational modes are included. Here it is seen that, while the measured data shows some indication that IR-inactive modes contribute to the annihilation rate, the CBT beam is expected to be able to resolve several independent IR-inactive resonances. If measured, these features would be the first fully resolved VFRs mediated by IR-inactive vibrational excitations. This information could aid in the development of new theoretical models that can describe the excitation of VFR in the absence of dipole-coupling. This molecule is also another example in which the CBT beam is expected to be able to resolve resonances due to multimode excitations.

As a final example, the annihilation spectrum for 1,1-dichloroethylene ($C_2H_2Cl_2$) is shown in Fig. 7.12. The measured data show considerable enhancement above the GL model predictions at low energies and considerable suppression below the GL predictions at high energies (cf. Fig. 4.4). Due to the density of fundamental modes, it is difficult to identify if the effects are due to large

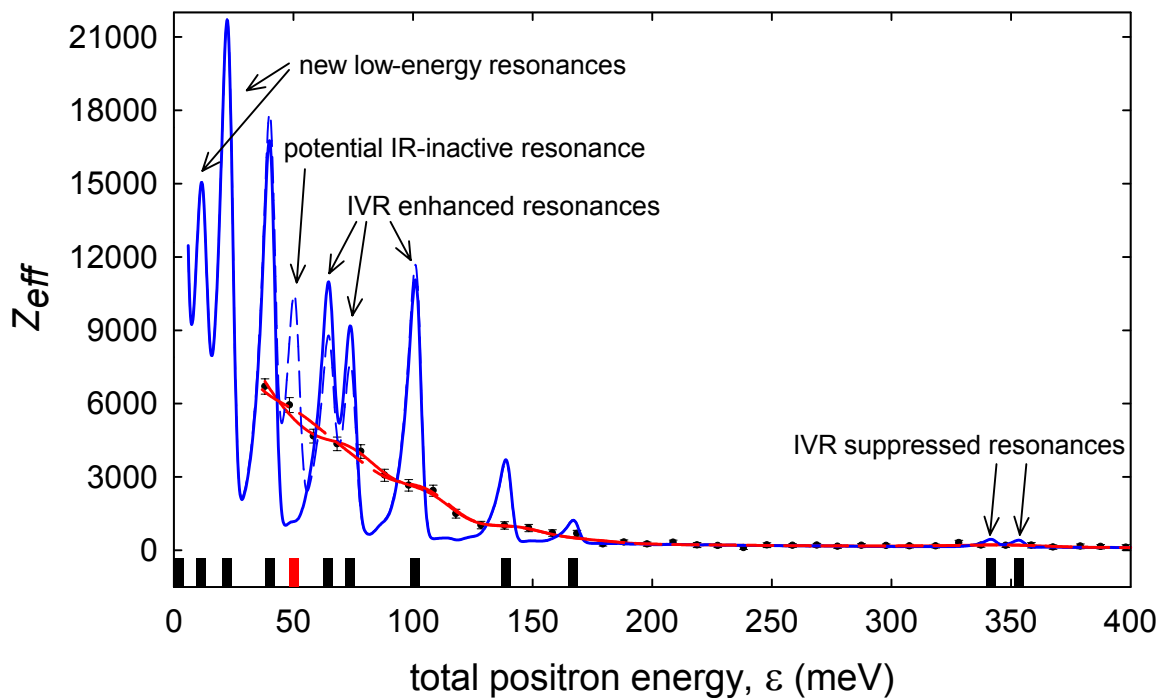


Figure 7.12: BGT vs. CBT annihilation spectrum for 1,1-dichloroethylene ($C_2H_2Cl_2$): (•) measured Z_{eff} , (—) total model from Eq. (A.16) fit to data with BGT beam distribution (cf. Table B.2), and (—) total model using same fit parameters but with CBT beam distribution. Dashed curves show total model predictions now including IR-inactive modes. Vertical bars show vibrational mode energies downshifted by binding energy, where black and red indicate IR-active and IR-inactive, respectively.

enhancement/suppression of a few modes or a smaller effect on many of the modes with the BGT beam. Using the CBT beam, it is expected that each of the modes can be independently resolved, allowing the effects of IVR on a each mode to be examined. This molecule is also another example in which the CBT beam may be able to resolve previously unseen low-energy modes, as well as an IR-inactive mode.

7.5.2 Inelastic positron scattering

Another area of study where the narrower energy spread of the CBT beam will be useful is in the measurement of inelastic positron scattering cross sections. As described in Chapter 4, low energy scattering measurements can be done using high resolution beams from BGTs [28]. This technique has been used to measure inelastic scattering cross sections for a variety of processes, such as ionization and electronic excitation [22]. Measurements of lower energy processes such as vibrational excitation have also been done for a small selection of molecules [16, 41]. However, no measurements of rotational excitation cross sections have yet been done.

Using the CBT-based beam described here, vibrational excitation cross sections could be measured for a significantly larger number of molecules. The ~ 7 meV FWHM total energy resolution is sufficient to resolve any vibrational excitation cross section with a threshold energy and mode separation $\gtrsim 7$ meV, and this requirement is satisfied for most small molecules. This resolution is even sufficient to make the first measurements of state-resolved rotational excitation cross sections.

As in the case of positron annihilation, it is worth investigating the ability of the CBT to measure such a low-energy, densely packed feature as rotational excitation. Results are presented here of calculations which simulate the measurement of rotational excitation cross sections in order to investigate if these measurements would be possible using this new beam technology. Experimentally, these measurements would be done by passing the beam through a scattering cell in which the positrons interact with the target molecule, and measuring the cumulative total energy distribution of the scattered beam relative to the incident beam to obtain the positron energy loss.

The scattered beam total energy distribution function $f'(\epsilon)$ obtained from this process may be written as

$$f'(\epsilon) = \sum_j n_j \sigma_j^+ f(\epsilon + \Delta E_j) L + \sum_j n_j \sigma_j^- f(\epsilon - \Delta E_j) L, \quad (7.1)$$

where the first term describes the effects of inelastic rotational excitation and the second term represents superelastic rotational de-excitation. Here, n_j is the population density of the j^{th} rotational mode, L is the length of the scattering region, and $\sigma_j^{(+,-)}$ and ΔE_j are the cross sections and energy exchanged for excitation from, and de-excitation to, the j^{th} rotational mode. Equation (7.1) may then be integrated to obtain the resulting scattered beam cumulative distribution function, analogous to the data obtained experimentally.

The results of Eq. (7.1) using the Gerjuoy-Stein cross sections (Eq. (6.13)) for 1 mTorr of H_2 at 300 K and a scattering length of 40 cm is shown in Fig. 7.13. These results show that the rotational excitation cross sections from the $j = 0, 1, 2$ and 3 states are expected to be resolvable with the CBT beam. Note that none are resolvable with the BGT beam. Therefore, the CBT is expected to enable the first state-resolved rotational excitation measurements. Further, the effects due to de-excitation from the $j = 2, 3$ and 4 states are also potentially resolvable, enabling the first rotational de-excitation cross section measurement. The largest difficulty associated with this measurement would not be due to the low energies involved, but rather with the small magnitude of these cross sections, which would require significant averaging to obtain precision measurements.

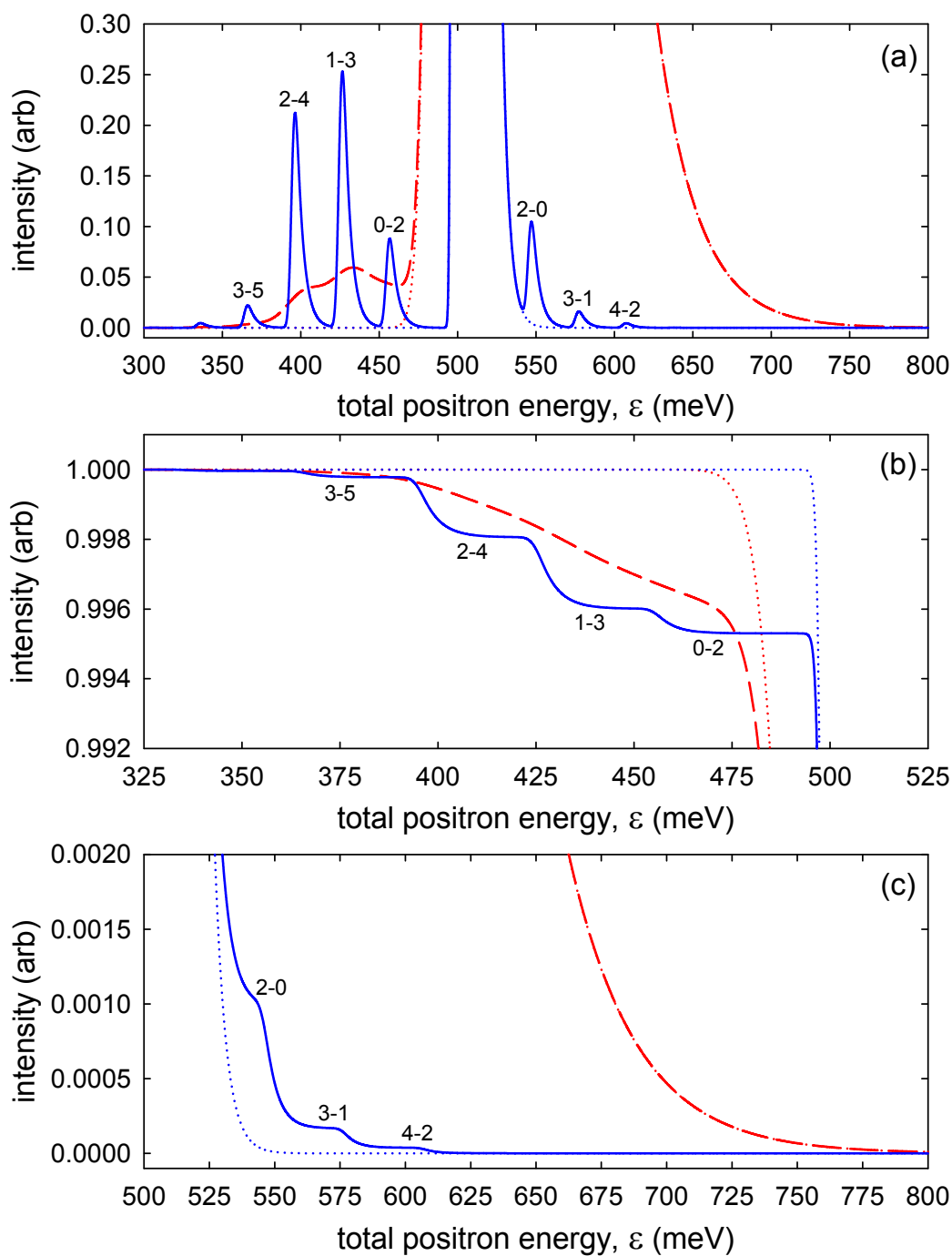


Figure 7.13: Simulated results of H₂ rotational scattering: (a) scattered beam distributions from Eq. (7.1); (b) and (c) show integrated scattered beam distributions, thus replicating experimental measurement. (—) results using BGT beam distribution and (—) results using CBT beam distribution. Dotted curves show un-scattered beam distributions. Labels show initial and final j state. See text for details.

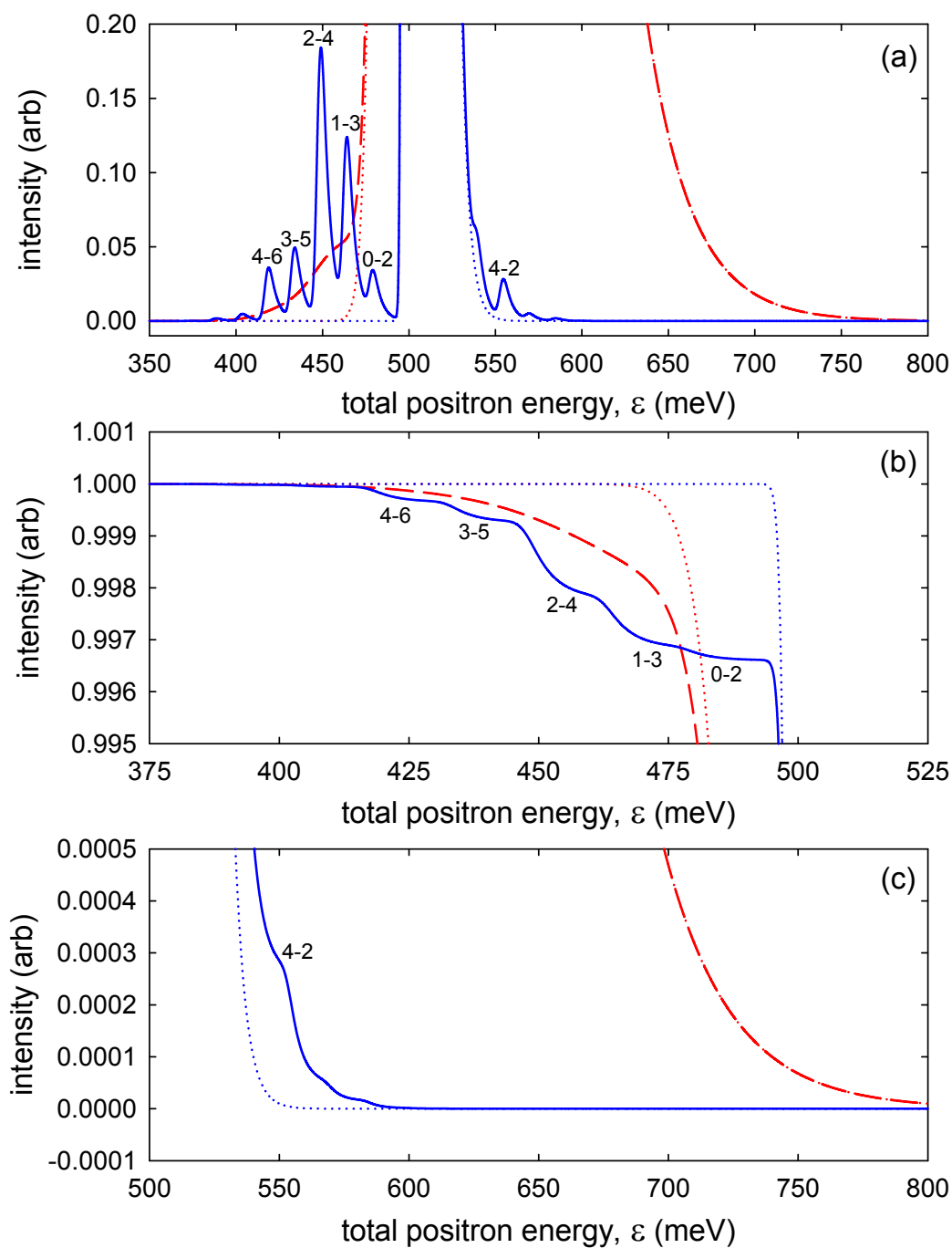


Figure 7.14: Simulated results of D_2 rotational scattering: (a) scattered beam distributions from Eq. (7.1); (b) and (c) show integrated scattered beam distributions, thus replicating experimental measurement. (---) results using BGT beam distribution and (—) results using CBT beam distribution. Dotted curves show un-scattered beam distributions. Labels show initial and final j state. See text for details.

The results for scattering on a D_2 gas under the same conditions as those described above are shown in Fig. 7.14. As for H_2 , the rotational excitation cross sections of D_2 are resolvable with the CBT beam, including at least one de-excitation cross section. However, in this case, the modes are more closely spaced, and the expected cross sections smaller, making this measurement more difficult than that for H_2 .

Some of the work and discussion in Chapter 7 is taken from “A cryogenically cooled, ultra-high-energy-resolution, trap-based positron beam,” M. R. Natisin, J. R. Danielson and C. M. Surko, *App. Phys. Lett.* **108**, 024102 (2016)[70]. The author of this dissertation led the research and was the principle author of the paper.

Chapter 8

Summary and concluding remarks

8.1 Summary of the dissertation¹

The primary topic of this dissertation was the development of an understanding of physical processes underlying positron cooling and beam formation in state-of-the-art, trap-based beam systems. Such systems begin with positrons emitted from a ^{22}Na radioactive source. The positrons are then moderated using a solid neon moderator, producing a steady-state positron beam which is then magnetically guided into a three-stage buffer gas trap (BGT). In the BGT the positrons are trapped and cooled using N_2 and CF_4 buffer gases. Once the positrons are cooled to the ambient (e.g., ~ 300 K) gas temperature, they are ejected from the trap by raising the potential well, lifting them over an exit-gate barrier and forming a high resolution, pulsed beam.

The characteristics of these magnetized beams were analyzed using a variety of experimental and analytically techniques. An analytic model was presented that described the transformation of the beam energy distributions as the beam propagates through non-uniform magnetic fields. Experimental techniques for measuring the energy, temporal and radial beam distributions were also described. Using these techniques, the resulting beam obtained from the BGT-based beamline was characterized. This beam had total energy spreads as low as $\Delta E_{tot} = 33$ meV FWHM, a temporal spread of $\Delta\tau = 1.7$ μs FWHM, and a radial spread of $\Delta R = 1.0$ cm FWHM. These beam characteristics, referred to as the “state-of-the-art” beam, was the highest energy-resolution beam available at the time.

The utility of high-resolution positron beams for atomic physics studies was also discussed. Here it was shown that, while the state-of-the-art positron beam was sufficient for the study of a variety of processes, many open questions regarding positron annihilation on molecules and inelastic scattering remained outside the reach of current beam technology. Specifically, the effects of infrared-inactive vibrational excitations, multimode resonant annihilation, intramolecular vibrational redistribution, and low-energy scattering processes such as rotational excitation are prohibitively difficult to study without improved beam-energy resolution.

As a necessary prerequisite to the development of higher resolution positron beams, detailed studies of the physical phenomena operative during beam formation were carried out. Experiments with the BGT-based beamline and Monte-Carlo-type simulations were done to better understand these processes, with a focus on the mechanisms responsible for setting the energy resolution of the

¹Not summarized here are the Appendices, which discuss related atomic physics studies done by the author of this thesis.

resulting beam. Parameters such as the positron ejection rate, positron temperature, well depth, and trap geometry were investigated.

These simulations also revealed three distinct regimes for beam formation. Besides the regime in which current traps typically operate, there exists a regime at low positron temperatures in which the possible positron trajectories become constrained, resulting in significant improvements in both energy and temporal resolution. Finally, a third regime was discussed in which the positrons are ejected on time scales over which their axial motion is negligible, and this results in the beam formation process becoming essentially non-dynamic as compared with the other two regimes.

These studies highlighted the potential role of positron cooling in obtaining high resolution beams. As a result, mechanisms related to positron cooling were investigated in further detail. Experimental measurements and theoretical calculations for positron cooling through vibrational and rotational excitation of the molecular gases CF_4 , N_2 and CO were presented. These results showed that, while positrons cooled to 300 K significantly faster through interactions with CF_4 due to the strong vibrational excitation, they can be cooled to significantly lower temperatures through interactions with N_2 and CO due to the lower energy rotational excitations.

The detailed information gained from these studies was then used to design, construct and operate a next-generation, high-energy-resolution, trap-based beam system. The pulsed positron beam ejected from the BGT was magnetically guided into a new apparatus called the cryogenic beam-tailoring trap (CBT). The CBT is placed after the BGT, where it re-traps the incident, 300 K positrons. The trapped positrons are compressed both radially and axially, and further cooled through interactions with a cryogenic 50 K buffer gas before re-ejecting them as a pulsed beam.

Using these techniques, positron beams with total energy spreads as low as $\Delta E_{tot} = 6.9$ meV FWHM were produced. This represents a factor of ~ 5 improvement over the previous state-of-the-art. These beams also have temporal spreads of $\Delta\tau = 0.9$ μs FWHM and radial spreads of $\Delta R = 0.1$ cm FWHM, representing improvements by factors of ~ 2 and ~ 10 over the previous state-of-the-art, respectively. Future experimental applications for this new technology were also discussed.

8.2 Future progress in positron beam development

While the advancements in producing high resolution positron beams described in this dissertation have opened up a variety of new processes for experimental study, many processes are of sufficiently low energy, or have a sufficiently high density of spectral features, that their investigation still remains problematic. Positron beam technology must continue to evolve toward higher energy resolution in order that these processes can eventually be studied.

Described here are a few examples of alternative positron cooling and beam formation techniques that potentially may be used to produce positron beams with narrower energy spreads. Also described here is a likely impediment to further progress in developing higher energy resolution positron beams, regardless of the techniques used to produce them.

8.2.1 Alternative cooling techniques

While the buffer-gas cooling technique used in the CBT allowed positron temperatures as low as 50 K to be obtained, further reduction in positron temperature would allow additional gains in beam-energy resolution. Simulations show that with a positron temperature of 1 K, total energy spreads of ~ 0.5 meV could be obtained using methods for beam-formation identical to those described here for the CBT. Unfortunately, the positron temperature obtainable using the buffer-gas

cooling techniques used in the CBT is limited by the vapor pressure of the molecules used to cool them. For N_2 and CO , this limits the temperature to a minimum of ~ 30 K. Using H_2 would allow buffer gas temperatures of ~ 5 K, however calculations show that positron cooling on H_2 is limited to ~ 30 K due to the relatively high energy of the lowest rotational excitation. For this reason, alternative positron cooling techniques will likely need to be used to obtain significantly lower positron temperatures. Listed here are several possible cooling techniques to accomplish this.

Cyclotron cooling

The cyclotron orbits of positrons in a strong magnetic field results in large particle accelerations that, in turn, results in the emission of radiation. This results in positron cooling [71]. In this case, the positrons come to equilibrium to the temperature of the surrounding electrode structure, thus allowing temperatures as low as ~ 4 K (liquid helium temperatures) to be obtained. Unfortunately, this technique requires large magnetic fields, and even then the cooling rate can be relatively slow compared to buffer-gas cooling.

Controlled evaporation

The depth of the confining potential well is reduced on a time scale slow with respect to the trapped particle thermal equilibration time, allowing the highest energy particles to be released while the remaining particles are left to equilibrate at a lower temperature. Using this technique, trapped antiprotons have been cooled to temperatures as low as 9 K [44]. The drawbacks of this technique are the obvious loss of a potentially significant fraction of the trapped positions, as well as the potentially large time required for efficient evaporation. Note that the evaporation must be done on time scales fast compared to cyclotron cooling to prevent re-heating of the positrons to the surrounding electrode temperature.

Sympathetic cooling

In the example of this technique, ${}^9\text{Be}^+$ ions were produced and laser-cooled to milli-Kelvin temperatures in a Penning trap, then the cold ion plasma used to cool positrons through Coulomb collisions. Using this technique, positron temperatures of ~ 5 K have been obtained [72]. Unfortunately, the presence of the ${}^9\text{Be}^+$ ions will likely have a negative affect on beam formation, making it necessary to remove them prior to positron ejection. Alternatively, a different beam formation technique could possibly be used (e.g., small diameter beam extraction from a plasma, as discussed below).

8.2.2 Alternative beam formation techniques

The focus of this dissertation was on positron beams formed by raising the potential well until the positrons had sufficient energy to overcome an exit-gate barrier and escape the trap. However, there are other possible techniques for producing positron beams, some of which may allow for better energy resolution. Note that, while the beam formation process discussed in this dissertation took place in the single-particle regime, many other techniques require the positrons to be in the plasma regime.

Ultra-fast ejection

As discussed in Chapter 5, if the positrons are ejected using the same methods discussed here, but on time scales over which positron axial motion is negligible, beam formation is simplified. In this “non-dynamic” regime of beam formation, the total energy spread is more sensitively dependent on the temperature. For example, simulations show that operating the CBT in this regime with a positron temperature of 1 K would yield total energy spreads as low as ~ 0.1 meV.

Extraction of small diameter beams

This technique first involves the creation of a positron plasma within a Penning-Malmberg (PM) trap, after which the end-gate potential is reduced for a time long compared to the axial bounce time to allow all particles with sufficient energy to escape, and then increased back to its original value. This technique exploits the fact that, in a PM trap, the plasma space-charge potential is largest at the radial center, and so the first particles to escape are those from this region, allowing beam diameters as small as $50 \mu\text{m}$ to be produced [73]. Additionally, for small beams in which the plasma potential does not vary significantly across the beam, the parallel energy spread is approximately equal to the temperature [74]. The disadvantage of this technique is that it requires radial compression of the plasma before each beam extraction, and so maintaining low positron temperatures would require relatively long periods of cyclotron cooling between pulses.

Autoresonant ejection

In this case, an oscillating drive electric field is applied to a quasi-harmonic potential which confines a single-component plasma. The time-dependent drive is initially applied at a frequency above the longitudinal bounce frequency of the plasma, and subsequently swept to lower frequencies. During this process, the center-of-mass longitudinal motion of the plasma becomes phase-locked to the drive, allowing the particles to be driven out of the well with little excess longitudinal energy [75]. Unfortunately, the utility of this technique to produce positron beams with low energy spreads has not yet been studied.

8.2.3 A final obstacle to future progress

As discussed in Chapters 3 and 7, the ability to produce or even measure positron beams with small energy spreads is made difficult by perturbations in the produced electric potentials. These effects, which appear to be primarily due to electrode surface conditions (e.g., molecular interactions with electrode surfaces, material or plating imperfections), result in a broadening of the measured parallel energy distribution of the beam. Unfortunately, all of the cooling and beam formation techniques discussed above rely on potentials produced by metal electrodes for confinement and manipulation of the positrons, and so they are susceptible to these effects.

Experience suggests that these effects can be minimized by placing the confinement and measurement electrodes at distances far from the positrons. However this solution is neither practical nor entirely effective. The colloidal graphite coating applied to the CBT electrodes (discussed in Chapter 7) appears to minimize these effects considerably as compared to the gold-plating that it replaced. However it is unknown whether this coating is actually more effective, or if the previous gold-plating was especially sub-optimal. Before positron beams with energy spreads $\lesssim 1$ meV can be developed and used for scientific applications, systematic investigation into these effects will likely have to be done.

This places us at a unique juncture in the evolution of positron beam technology. As stated in the introduction to this dissertation, positron beam development has been largely serial, with the modern beamline sequentially manipulating positrons toward ever increasing energy resolution. It may be that the next leap in beam technology will be unable to follow this trend. Instead, it may be that limitations fundamental to the way in which the present beams are produced will need to be addressed.

8.3 Concluding remarks

The work presented here represents the most detailed description of trap-based positron beams to date. Many aspects of these beams have been discussed; from the positron cooling and beam formation processes, to the evolution of the resulting beam distributions. It is hoped that this work will enable optimization and refinement of the many BGT-based beam systems that are currently used around the world, as well as provide the requisite knowledge for the development of the next generation of positron beam technology. The CBT is the first step towards this end, and the leap in beam quality it provides demonstrates the effectiveness of this approach. The continued development of high resolution positron beams has enabled the experimental study of a wide variety of new processes. As the technology continues to improve, their utility for scientific applications will only increase in scope.

Appendix A

Positron annihilation on molecules: experimental and theoretical methods

This appendix, and the one that follows, describe new experiments and analysis conducted by the author to study resonant positron annihilation on a variety of molecules. This work elucidates the roles of Feshbach resonances, multimode resonant annihilation (MRA), and intramolecular vibrational energy redistribution (IVR) in determining annihilation rates. These studies, and the difficulties encountered in their investigation, were the primary motivation for the positron beam development described in this dissertation.

A.1 Description of an annihilation experiment

The experimental apparatus used for the atomic physics research presented in this appendix is the BGT-based beamline described in Chapter 2. The beam emitted from the BGT is magnetically guided into the annihilation region, where the annihilation rate is measured as the positrons interact with the target molecular gas.

A schematic of the annihilation region is shown in Fig. A.1. A solenoid and pair of Helmholtz coils provide a magnetic field which varies between $\sim 500 - 700$ G (cf. Fig. 2.7). The

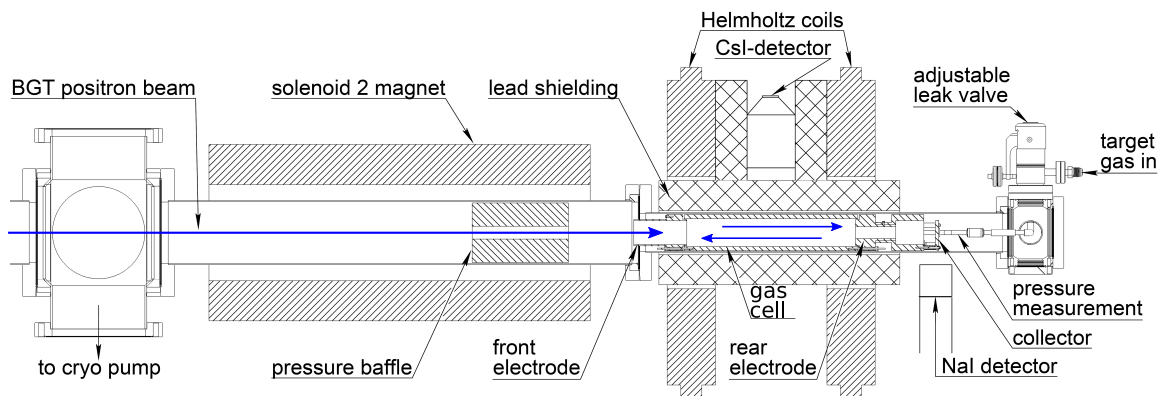


Figure A.1: Schematic diagram of the annihilation region as used for positron annihilation studies. See text for details.

target molecular gas is introduced into the chamber through an adjustable cantilever leak valve, and maintained at a typical pressure of 1 – 10 μ Torr in the gas cell, as measured by a capacitance manometer fed through the rear electrode and into the gas cell region. A small copper baffle aperture is placed between the measurement region and a pump to ensure a nearly constant pressure profile inside the measurement region, as well as a rapid drop in pressure outside of the gas cell.

The molecular delivery technique depends on the phase of the substance at room temperature. For gases, the molecule is injected directly into the vacuum chamber through a piezoelectric valve. For solids, it is placed within a water bath controlled at an elevated temperature, allowing the vapor to enter the chamber through a leak-valve. For liquids, the liquid is repeatedly frozen with liquid nitrogen and pumped on to remove contaminants, then placed in a water bath controlled at 300 K, allowing the vapor to enter the chamber through a leak-valve. The majority of the molecules discussed in this appendix were in the liquid phase.

The so-called “annihilation electrodes,” which were designed and used for the more recent positron annihilation experiments discussed here, are used to manipulate the beam during an annihilation measurement. The rear electrode is biased to reflect the incident BGT beam, allowing it to make multiple passes through the measurement region, during which time the number of annihilations occurring within a 15 μ s window are counted. The measurement region is spanned by a long cylindrical electrode, referred to as the annihilation cell, which allows the incident beam energy to be adjusted. By repeating this measurement process with the annihilation cell at differing potentials, the number of annihilations as a function of incident positron energy is obtained.

The gamma rays emitted from the annihilations are detected using a CsI crystal attached to a photodiode, which produces a pulse with a magnitude proportional to the detected gamma ray energy. These pulses are then analyzed using a single-channel analyzer, which identifies the pulse amplitudes that correspond to those expected for a 511 keV gamma ray. This process, in addition to the lead shielding, copper baffle, and small detector field of view, ensure that the measured annihilation counts are due to the annihilation of the positrons with the target gas, minimizing other contribution from extrinsic sources.

A.2 Calculating annihilation rates

The experimental procedures described above allow the number of annihilations at a given incident positron energy to be measured within a fixed time window. However, this number implicitly depends upon various aspects of the measurement process (e.g., the number of positrons in the beam, the target gas density, etc.). In order to allow proper comparisons between differing measurements, the effects of these experimental parameters must be removed, thus allowing the fundamental annihilation rates due to the the processes themselves to be examined directly.

The experimentally measured total annihilation cross section σ_{exp} may be written as

$$\sigma_{exp}(\epsilon) = \frac{I_{\gamma}(\epsilon)}{I_0 N_p \eta_D \ell n_g}, \quad (\text{A.1})$$

where I_{γ} is the number of detected annihilations, I_0 is the number of positrons in a single pulse, N_p is the number of passes each pulse makes through the annihilation cell during the measurement time window, ℓ is the length of the annihilation cell, η_D is the integrated detector efficiency, and n_g is the molecular gas density.

The number of passes made by the beam through the annihilation cell at a given cell voltage,

within the fixed measurement time window, may be written as

$$N_p = 2 \frac{t_w}{\delta t_p}, \quad (\text{A.2})$$

where t_w is the measurement time window and

$$\delta t_p = 2\sqrt{m/2} \left[\frac{d}{\sqrt{\bar{E}_\parallel}} + \frac{\ell}{\sqrt{\bar{E}_\parallel - eV}} \right] \quad (\text{A.3})$$

is the time required for the beam to be reflected and make a full round trip between the buffer gas trap and rear electrode (cf. Fig. A.1). Here, m is the positron mass, d is the distance from the BGT to the cell, \bar{E}_\parallel is the mean parallel energy of the positron beam and V is the voltage applied to the annihilation cell. Note that the beam makes two passes through the annihilation cell during each round trip (one downstream and the other upstream).

Using Eq. (A.1), the measured annihilation rate may then be written as

$$\Gamma_{exp}(\varepsilon) = n_g \sigma_{exp}(\varepsilon) v \quad (\text{A.4})$$

$$= \sqrt{\frac{2}{m}} n_g \sigma_{exp}(\varepsilon) \sqrt{\varepsilon}, \quad (\text{A.5})$$

where v and ε are the positron velocity and energy, respectively. The positron-molecule annihilation rate is conventionally described in terms of the dimensionless quantity Z_{eff} [32], which is the measured annihilation rate normalized to the Dirac rate Γ_D for two-gamma annihilation in a free-electron gas,

$$Z_{eff}(\varepsilon) \equiv \frac{\Gamma(\varepsilon)}{\Gamma_D} = \frac{\Gamma(\varepsilon)}{\pi r_0^2 c n_g}, \quad (\text{A.6})$$

where, r_0 is the classical electron radius and c is the speed of light.

A.3 Theoretical overview

A.3.1 Vibrational Feshbach resonances

The most notable feature discovered with the first energy-resolved measurements of Z_{eff} was the existence of resonances associated with the molecular vibrational modes [31]. These resonances are the result of a vibrational Feshbach resonances (VFR) mediated by a positron-molecule bound state.

The process of VFR excitation and positron attachment is shown schematically in Fig. A.2. If an incident positron approaches the molecule with an energy ε_v such that

$$\varepsilon_v = \omega_v - \varepsilon_b, \quad (\text{A.7})$$

the positron may excite the vibrational mode and become trapped within the molecular potential, forming a positron-molecule bound state. Here ω_v is the energy of a molecular vibration, and ε_b is the positron-molecule binding energy, with the convention that $\varepsilon_b > 0$ represents a bound state. Once this occurs, the positron may then be detached and ejected from the molecule by the de-excitation of the vibrational mode, or it may annihilate with one of the molecular electrons.

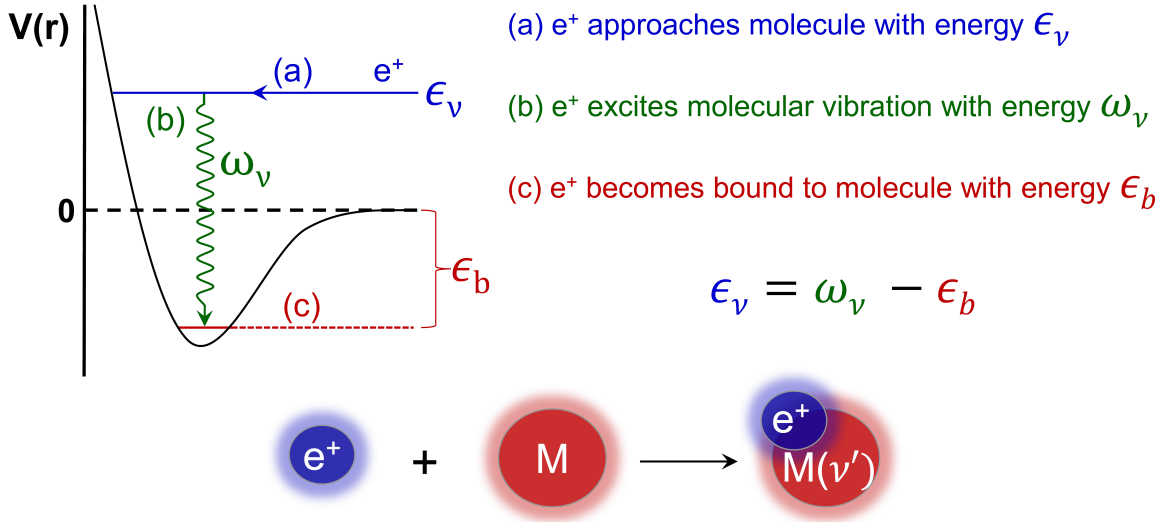


Figure A.2: Overview of the vibrational Feshbach resonance and positron attachment. The positron approaches the molecule with an energy ϵ_v and excites a molecular vibration of energy ω_v , forming a (temporary) positron-molecule bound state with binding energy ϵ_b .

The presence of the temporary positron-molecule bound state results in an increase in the probability of annihilation at the resonant energy ϵ_v , and therefore a corresponding increase in the measured Z_{eff} at that energy. Equation (A.7) may also be re-written to allow the binding energy to be calculated for a given measured annihilation spectrum based on the positions of the resonances relative to the known vibrational energies. Using this technique, the binding energies of more than 60 molecules have now been measured [17].

A.3.2 The Gribakin-Lee Model

Theoretical description of energy-resolved positron-molecule annihilation is largely due to the work of Gleb Gribakin and collaborators at Queens University. The so-called ‘‘Gribakin-Lee’’ (GL) model of positron annihilation on molecules separates Z_{eff} into ‘‘direct’’ and ‘‘resonant’’ components,

$$Z_{eff}^{(GL)}(\epsilon) = Z_{eff}^{(Dir)}(\epsilon) + Z_{eff}^{(Res)}(\epsilon). \quad (\text{A.8})$$

Here, $Z_{eff}^{(Dir)}$ represents annihilation ‘‘in-flight’’ due to the temporary overlap of the positron and electron wave functions, while $Z_{eff}^{(Res)}$ represents the resonant annihilation due to VFRs.

The direct term in Eq. (A.8) describes positron annihilation due to s-wave scattering and, at low positron energies, may be written as [76]

$$Z_{eff}^{(Dir)}(\epsilon) \approx \frac{F}{2(\epsilon + |\epsilon_b|)}, \quad (\text{A.9})$$

where ϵ is the incident positron energy, ϵ_b is the positron-molecule binding energy and F is a factor related to the electron-positron contact density. Calculations of positron annihilation on atoms have shown $F \approx 18$ eV [77]. Here it is seen that $Z_{eff}^{(Dir)}$ is enhanced if a low-lying virtual state ($\epsilon_b < 0$)

or a weakly bound state ($\epsilon_b > 0$) exist. However, a key point is that the direct annihilation rate for thermal positrons at 300 K is limited to $Z_{eff}^{(Dir)} \lesssim 10^3$ [76].

The resonant annihilation term in Eq. (A.8) may be written explicitly if it is assumed that the resonances are due to isolated VFRs of infrared-active fundamental vibrational modes. In this case, positron capture is mediated by long-range dipole coupling, and the resonant annihilation rate may be written as a sum over all infrared-active vibrational modes [30],

$$Z_{eff}^{(Res)}(\epsilon) \approx \pi F \sum_{\nu} g_{\nu} \sqrt{\frac{\epsilon_b}{\epsilon_{\nu}}} \frac{\Gamma_{\nu}^e}{\Gamma_{\nu}} f(\epsilon_{\nu} - \epsilon). \quad (\text{A.10})$$

Here, g_{ν} and Γ_{ν} are the degeneracy and elastic relaxation rate of mode ν , and $f(\epsilon_{\nu} - \epsilon)$ is the beam energy distribution function. The total positron loss rate can be written $\Gamma_{\nu} = \Gamma_{\nu}^e + \Gamma^a$, where Γ^a is the bound positron annihilation rate. The rates Γ_{ν}^e and Γ^a may be calculated explicitly, and typically $\Gamma_{\nu}^e \gg \Gamma^a$. This simplification results in $\Gamma_{\nu}^e / \Gamma_{\nu} \approx 1$. Therefore, under these conditions, $Z_{eff}^{(Res)} \propto g_{\nu} \sqrt{\epsilon_b / \epsilon_{\nu}}$. In most cases, $Z_{eff}^{(Res)} \gg Z_{eff}^{(Dir)}$.

A.3.3 Multimode resonant annihilation

The resonant term in the GL model describes positron attachment mediated by isolated VFRs of infrared-active fundamental vibrational modes, however it does not account for the contributions due to multimode excitations (i.e., combination modes and overtones of the fundamentals). Another model, developed by Gribakin and Lee [34], and later applied to the measured spectra [35], describes the effects of positron attachment due to multimode excitations.

The multimode resonant annihilation (MRA) model assumes that the positron can attach to all energetically allowed multimode vibrational excitations, and that all modes and combinations with sufficient energy to detach the positron can act subsequently as inelastic escape channels. Finally, the MRA model assumes that the positron couples to all vibrational excitations with the same strength. Under these assumptions, the MRA contribution to Z_{eff} can be written as [34]

$$Z_{eff}^{(MRA)}(\epsilon) \approx \pi F \sqrt{\frac{\epsilon_b}{\epsilon}} \frac{\rho(\epsilon + E_{\nu} + \epsilon_b)}{N(\epsilon + E_{\nu})}, \quad (\text{A.11})$$

where E_{ν} is the thermal energy in the target molecule, $\rho(\epsilon + E_{\nu} + \epsilon_b)$ is the energy density of entrance-channel multimode states populated at positron energy ϵ , and

$$N(\epsilon + E_{\nu}) = \int_0^{\epsilon + E_{\nu}} \rho(E') dE' \quad (\text{A.12})$$

is the total number of open inelastic escape channels.

An example of the vibrational density of states ρ is shown in Fig. A.3. Shown here are all of the modes in 1,1-dichloroethylene ($\text{C}_2\text{H}_2\text{Cl}_2$) up to 500 meV, as calculated in the harmonic approximation. Each mode is represented by a horizontal bar at the given energy and mode order, where mode order is defined as the total number of constituent fundamentals in the multimode vibration (e.g., fundamentals are mode order 1, first overtones are mode order 2, etc.). Here it is seen that at higher energies the multimode spectrum becomes quite dense.

Experiments have shown that virtually all molecules studied to date show signs of MRA, typically taking the form of a broad background of annihilations which decreases at higher energies (see Appendix B). However, the results predicted by Eq. (A.11) overestimate the contribution in

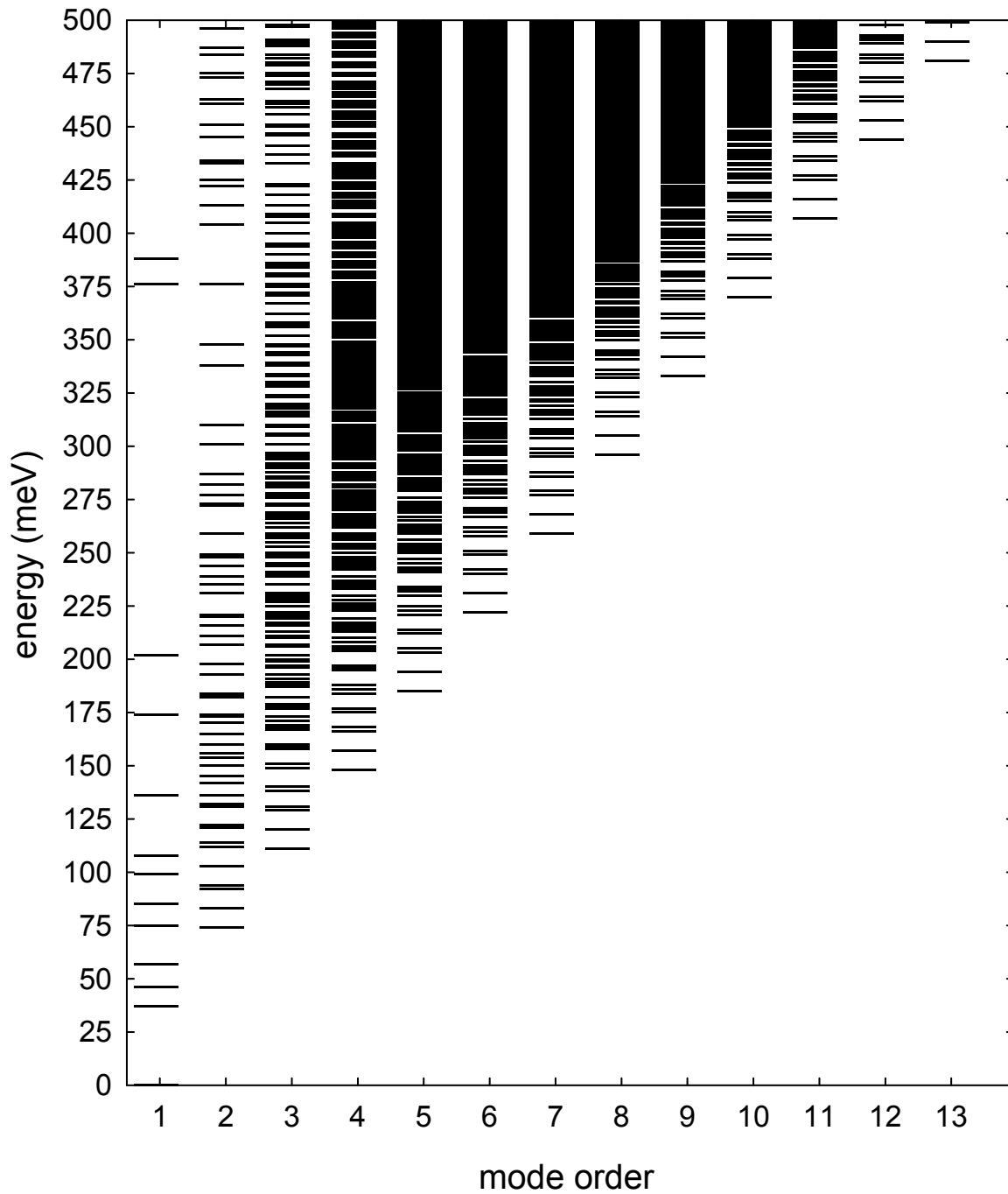


Figure A.3: Multimode structure of 1,1-dichloroethylene (C₂H₂Cl₂) up to 500 meV. Horizontal bars represent vibrational multimode of a given energy and mode order, where the mode order is the number of constituent fundamentals in the multimode vibration. Also shown are the calculated relaxations rates for the fastest mode, shown in GHz.

almost all cases. It is believed that this overestimate is due to the failure of one of the assumptions of the model, namely, that the positron couples to all vibrational excitations with the same strength. It is more likely that the positron couples to higher order multimode states more weakly than to lower order states, thus resulting in smaller contributions than predicted by Eq. (A.11). Indeed, adjusting the density of states so that higher order multimodes contribute less by applying “tapering” factor of the form $\rho \rightarrow \rho'/x^{n-1}$, where x is a numerical constant and n is the multimode mode order, yields results consistent with most measurements, further supporting this hypothesis.

In order to quantify the discrepancy between theory and measurement, and to allow for a similar procedure to quantify discrepancies in the magnitudes of the resonances (see below), the result of Eq. (A.11) is typically scaled by a constant numeral factor η which best fits the measured data. This factor is found by first subtracting the (typically small) $Z_{eff}^{(Dir)}$ component (Eq. (A.9)) from the measured data, and then fitting the resulting data to the MRA model in the regions *between* the resonances (i.e., where the MRA contribution is dominant).

A.3.4 Intramolecular vibrational energy redistribution

Another feature seen in virtually all annihilation spectra is that the magnitudes of the measured resonances differ from those predicted by the GL model. These discrepancies vary from the complete absence of a predicted resonance, to the enhancement of resonances by 10-100 times their predicted magnitudes [17]. This process is thought to be due to intramolecular vibrational redistribution (IVR), where the vibrational energy of a molecule is redistributed into near-resonant multimode vibrational states [36, 37, 38]. This energy redistribution may occur on sub-picosecond time scales [78], which can be considerably faster than the time for elastic emission of the positron due to relaxation of a fundamental. This allows time for coupling to many modes before positron loss occurs (e.g. via ejection from the molecule or annihilation).

Unfortunately, aside from a simple model which describes the effects of IVR on positron-molecule annihilation in certain limits [40], the effects of IVR cannot yet be predicted quantitatively. However, a qualitative description of the process may be made by analyzing the relative relaxations rates of the vibrational modes involved, as calculated from the IR-spectra [30].

The impact of IVR on positron annihilation rates depends on three processes: mode coupling between the excited fundamental and nearby multimode states, positron ejection from the fundamental, and positron ejection from the multimode states. For simplicity, it is assumed that the escape rate from a multimode state is dominated by the constituent mode with the largest elastic rate. Additionally, for IVR to be relevant, the mode coupling rates must be comparable to or larger than the elastic rate. By analyzing the relaxation times of the multimode states relative to that of a nearby entrance fundamental, the qualitative effects of IVR (i.e., enhancement or suppressor as compared to GL predictions) can be estimated.

Two examples of this analysis are shown in Fig. A.4. Shown in Fig. A.4 (a) are the vibrational modes near the CO stretch mode in acetaldehyde (C_2H_4O), along with the calculated relaxation rates of the fastest constituent modes (in GHz). Here it is seen that the relaxation rate of the CO stretch mode is by far the *largest* of any of the nearby multimode states. Therefore, IVR coupling into *any* nearby multimode will only increase the positron attachment time, and so also the probability of annihilation. For this reason, it is expected that the VFR associated with the CO stretch mode in acetaldehyde would be enhanced above the GL model prediction if IVR is present, as is observed [39].

As a second example, the modes near the CD stretch mode in chloroform-D ($CDCl_3$) are shown in Fig. A.4 (b). In this case, the relaxation rate of the CD stretch mode is by far the *smallest* of

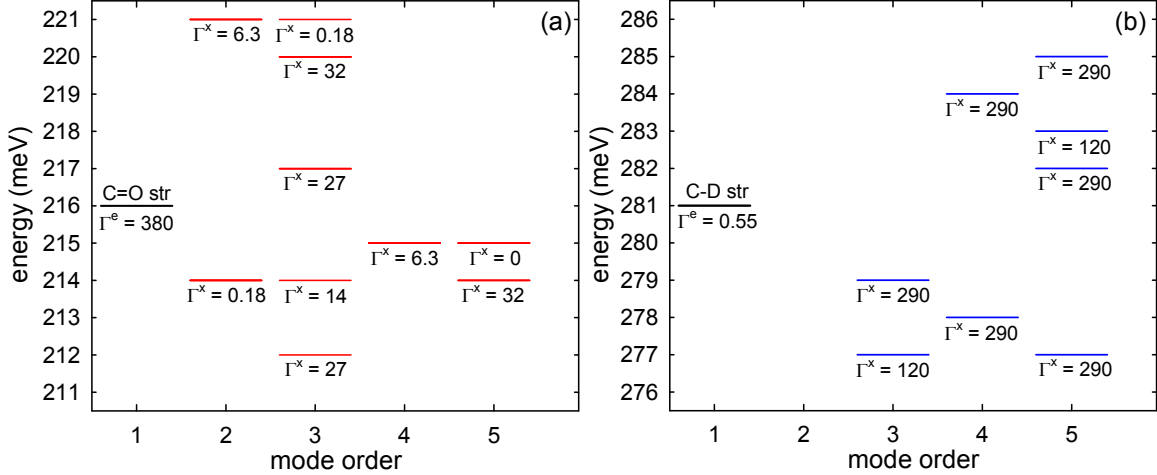


Figure A.4: Example of IVR Analysis. (a) mode structure of acetaldehyde (C₂H₄O) within ± 5 meV of the CO stretch mode, and (b) mode structure of chloroform-D (CDCl₃) within ± 5 meV of the CD stretch mode up to mode order 5. Horizontal bars represent vibrational mode of a given energy and mode order, where mode order is the number of constituent fundamentals that the mode is composed of. Also shown are the calculated relaxation rates for the fastest mode, shown in GHz.

any nearby multimode state. In addition, all of these multimodes contain a constituent fundamental which is of sufficient energy to eject the positron (i.e., $\omega_v > \epsilon_b$). Therefore, IVR coupling into *any* nearby multimode will only decrease the positron attachment time through de-excitation of the constituent fundamental in the IVR coupled multimode. This process may be schematically written as

$$e^+(\epsilon) + M \longrightarrow e^+M(v_{\text{fund}}) \longrightarrow e^+M(v_{\text{multi}}) \longrightarrow e^+(\epsilon') + M(v'). \quad (\text{A.13})$$

For this reason, it is expected that the VFR associated with the CD stretch mode on chloroform-D would be suppressed below GL model prediction if IVR is present, as is observed [39].

In order to quantify the potential effects of IVR on the measured annihilation rate, the measured data is fit using a procedure designed to isolate the discrepancies between the GL model prediction and the experimental results. First, the binding energy is estimated and the associated predictions from the GL (Eq. (A.8)) and MRA (Eq. (A.11)) models are calculated. The MRA scale factor η is then found as described above, and the scaled MRA contribution subtracted from the data. The resulting data is now approximately that of the resonant component only. It is now fit to a modified version of $Z_{\text{eff}}^{(\text{Res})}$ (Eq. (A.10)), where the magnitudes of the VFRs are now allowed to be adjusted to match the data:

$$Z_{\text{eff}}^{(\text{Res})}(\epsilon, \beta_v) \equiv \pi F \sum_v \beta_v g_v \sqrt{\frac{\epsilon_b}{\epsilon_v}} f(\epsilon_v - \epsilon). \quad (\text{A.14})$$

Here, the fitted VFR scale factors indicate the level of enhancement ($\beta_v > 1$) and suppression ($\beta_v < 1$) for the corresponding VFR. This entire fit process is then iterated until a stable solution is found. Combining this equation with the $Z_{\text{eff}}^{(\text{Dir})}$ term yields the modified GL model,

$$Z_{\text{eff}}^{(\text{GL})}(\epsilon, \beta_v) = Z_{\text{eff}}^{(\text{Dir})}(\epsilon) + Z_{\text{eff}}^{(\text{Res})}(\epsilon, \beta_v). \quad (\text{A.15})$$

A.3.5 The overall model

The theoretical and empirical techniques described in this section may be summarized as a semi-empirical model for the measured annihilation spectra:

$$Z_{eff}^{(Tot)}(\epsilon, \beta_v, \eta) = Z_{eff}^{(Dir)}(\epsilon) + Z_{eff}^{(Res)}(\epsilon, \beta_v) + \eta Z_{eff}^{(MRA)}(\epsilon). \quad (\text{A.16})$$

This equation includes the predicted contributions from the Gribakin-Lee model ($Z_{eff}^{(Dir)}$ and $Z_{eff}^{(Res)}$) and the multimode resonant annihilation model ($Z_{eff}^{(MRA)}$), along with the empirically fitted scale factors η and β_v which quantify the discrepancies between the predicted components and the measured data.

Appendix B

Measured annihilation spectra

In this Appendix some of the measured annihilation spectra obtained by the author of this dissertation are presented. The measurements were done using the BGT-based beamline discussed in Chapter 2 using the experimental techniques described in Appendix A. These measurements are compared to the theoretical models discussed in Appendix 4. All vibrational mode energies were obtained from the “NIST Chemistry WebBook” [81], unless otherwise stated. The relevant fit factors obtained for the binding energy ϵ_b , multimode resonant annihilation (MRA) scale factor η , and vibrational Feshbach resonance (VFR) magnitude scale factors β_v are listed for each molecule. The binding energies and MRA scale factors are also summarized in Table B.1.

As described in Chapter 3, it was found that under certain conditions the measured annihilation spectra has been seen to be shifted in energy compared to that of previous measurements, resulting in an incorrect binding energy (and so also incorrect fitted scale factors, due to the energy dependence of the fitted models). These effects are assumed to be related to perturbations in the potential generated by the annihilation cell electrode due to surface effects such as molecular adsorption and material or plating defects. For this reason, most of the measurements shown here were immediately followed by the repeat measurement of a known molecule (typically hexane) to ensure no shifts in the data were present. This practice was not used for some of the earlier measurements shown here, and so for these data possible shifts may be present. Data where shifts may be present are noted in the figure and table captions where applicable. For all spectra shown in the appendix, the curves are as discussed in Fig. B.1.

Table B.1: Summary of molecular fit parameters. The parameters ϵ_b and η represent the binding energy and MRA scale factors obtained from fitting the measured data to Eq. (A.16). For the case of the binding energies, the respective standard error obtained from the fits is also shown. Molecules denoted with (*) indicate measurements where possible energy shifts are present. See text for details.

molecule	formula	ϵ_b (meV)	η
1,1-dichloroethylene	$C_2H_2Cl_2$	35 ± 3	0.31
1H-perfluorooctane	$C_8F_{17}H$	19 ± 3	0.70
chloroform ¹	$CHCl_3$	40 ± 1	0.31
chloroform-d ²	$CDCl_3$	42 ± 3	0.34
dichloromethane	CH_2Cl_2	31 ± 1	0.28
dichloromethane-d2	CD_2Cl_2	27 ± 1	0.36
ethanol ³	CH_3CH_2OH	30 ± 1	0.83
ethanol-d1	CH_3CH_2OD	28 ± 2	1.2
ethanol-d5	CD_3CD_2OH	41 ± 1	0.64
ethanol-d6	CD_3CD_2OD	32 ± 1	0.94
methanol ⁴	CH_3OH	6 ± 1	0.51
methanol-d1	CH_3OD	4 ± 1	0.49
methanol-d3	CD_3OH	6 ± 2	0.73
methanol-d4	CD_3OD	8 ± 2	0.34
1,2-cis-dichloroethylene*	$C_2H_2Cl_2$	76 ± 1	0.17
1,2-trans-dichloroethylene*	$C_2H_2Cl_2$	29 ± 2	0.24
bromoform*	$CHBr_3$	121 ± 2	0.07
bromoform-d*	$CDBr_3$	125 ± 10	0.07
tetrachloroethylene*	C_2Cl_4	65 ± 2	0.13
trichloroethylene*	C_2HCl_3	60 ± 1	0.16
carbon tetrabromide*	CBr_4	115	0.13
carbon tetrachloride*	CCl_4	57 ± 1	0.09

¹ Previously reported $\epsilon_b = 40$ meV using current data [39]. Fits to previous data yielded $\epsilon_b = 50$ meV [35].

² Previously reported $\epsilon_b = 43$ meV using current data [39].

³ Results obtained using new data. Fits to previous data yielded $\epsilon_b = 45$ meV [33] and 43 meV [79].

⁴ Results obtained using new data. Fits to previous data yielded $\epsilon_b = 2$ meV [80] and 20 meV [79].

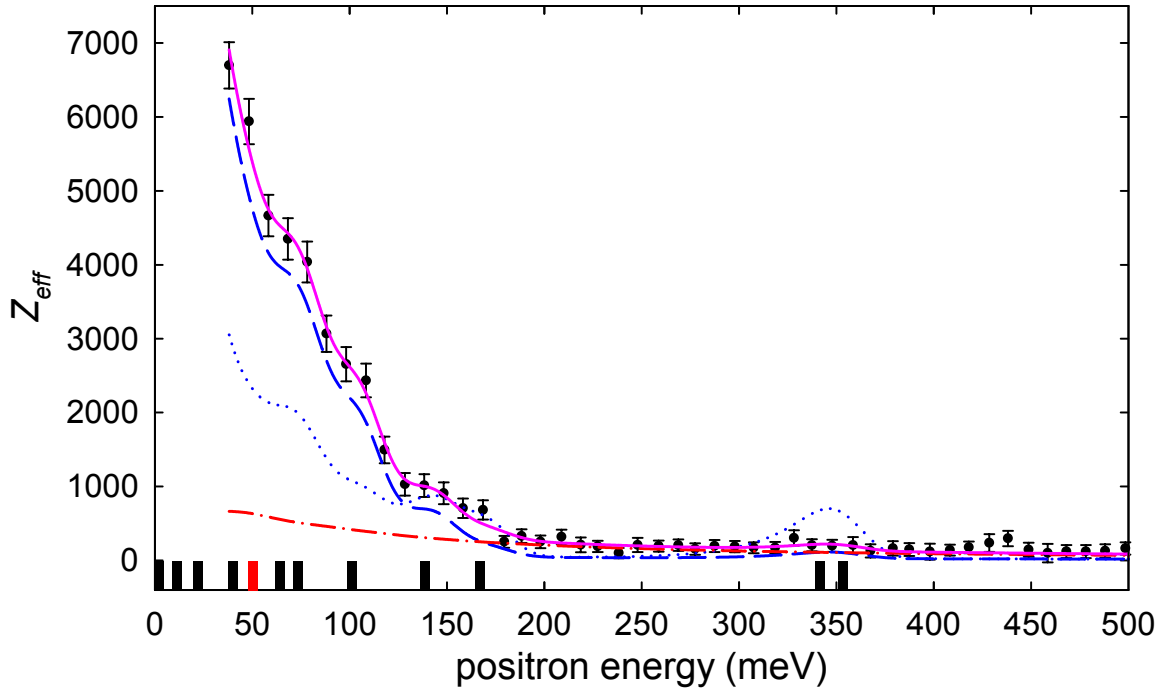


Figure B.1: Annihilation spectrum for 1,1-dichloroethylene ($\text{C}_2\text{H}_2\text{Cl}_2$): $\epsilon_b = 35 \pm 2.9$ meV and $\eta = 0.31$. (●) measured Z_{eff} from Eq. (A.6); (···) unscaled Gribakin-Lee (GL) model from Eq. (A.8); (---) scaled GL model from Eq. (A.15); (-.-) scaled multimode resonant annihilation (MRA) model from Eq. (A.11) multiplied by the fit factor η ; and (—) scaled total model from Eq. (A.16)). Black and red vertical bars represent the resonant vibrational mode energies given by Eq. (A.7) for the cases of either an infrared-active or inactive mode, respectively.

Table B.2: Mode fit parameters for 1,1-dichloroethylene ($\text{C}_2\text{H}_2\text{Cl}_2$).

ω_v (cm^{-1})	ω_v (meV)	ϵ_v (meV)	g_v	IR-Active	β_v
299	37	2	1	yes	1
372	46	11	1	yes	1
460	57	22	1	yes	2.4
603	75	40	1	yes	2.4
686	85	50	1	no	0
800	99	64	1	yes	1.8
875	108	74	1	yes	1.8
1095	136	101	1	yes	2.6
1400	174	139	1	yes	0.96
1627	202	167	1	yes	0.30
3035	376	341	1	yes	0.13
3130	388	353	1	yes	0.13

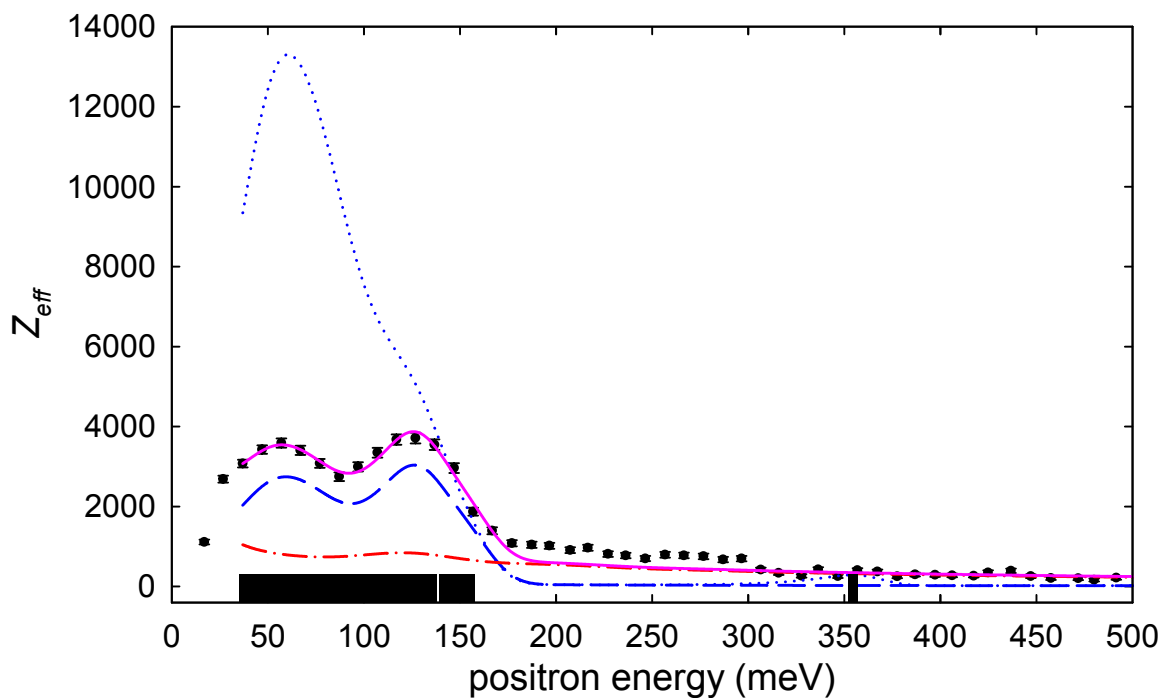


Figure B.2: Annihilation spectrum for 1H-perfluorooctane ($C_8F_{17}H$): $\epsilon_b = 19 \pm 3$ meV and $\eta = 0.70$.

Table B.3: Mode fit parameters for 1H-perfluorooctane ($C_8F_{17}H$). Vibrational modes obtained from IR-spectra. For brevity, ranges of modes are listed rather than each individual mode.

ω_v (cm^{-1})	ω_v (meV)	ϵ_v (meV)	g_v	IR-Active	β_v
453-747	56	37	1	yes	0.20
778-1054	96	78	1	yes	0.11
1086-1361	135	116	1	yes	0.65
1405	174	155	1	yes	1.6
3012	373	355	1	yes	~ 0

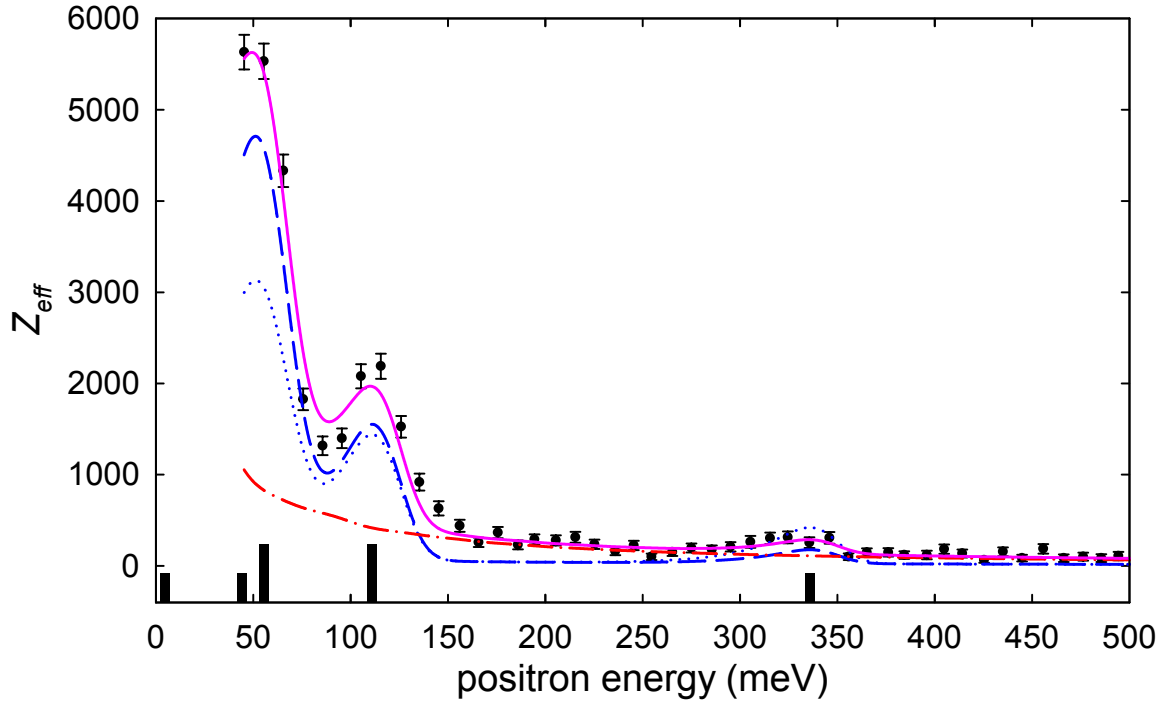


Figure B.3: Annihilation spectrum for chloroform (CHCl_3): $\varepsilon_b = 40 \pm 1.0$ meV and $\eta = 0.31$.

Table B.4: Mode fit parameters for chloroform (CHCl_3).

ω_v (cm^{-1})	ω_v (meV)	ε_v (meV)	g_v	IR-Active	β_v
261	32	-8	2	yes	N/A
363	45	5	1	yes	1
680	84	44	1	yes	1.6
774	96	56	2	yes	1.6
1220	151	111	2	yes	1.1
3034	376	336	1	yes	0.39

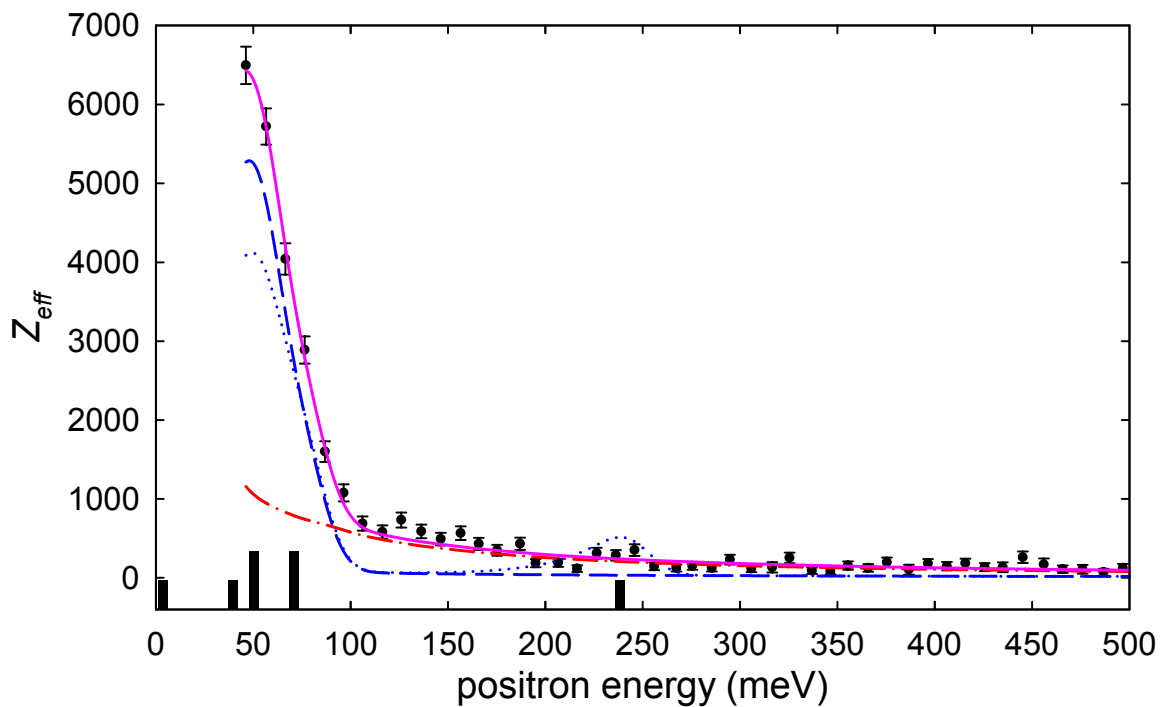


Figure B.4: Annihilation spectrum for chloroform-d (CDCl_3): $\varepsilon_b = 42 \pm 3$ meV and $\eta = 0.34$.

Table B.5: Mode fit parameters for chloroform-d (CDCl_3).

ω_v (cm^{-1})	ω_v (meV)	ε_v (meV)	g_v	IR-Active	β_v
262	32	-10	2	yes	N/A
369	46	3	1	yes	1
659	82	39	1	yes	1.4
749	93	51	2	yes	1.4
914	113	71	2	yes	0.91
2266	281	239	1	yes	~ 0

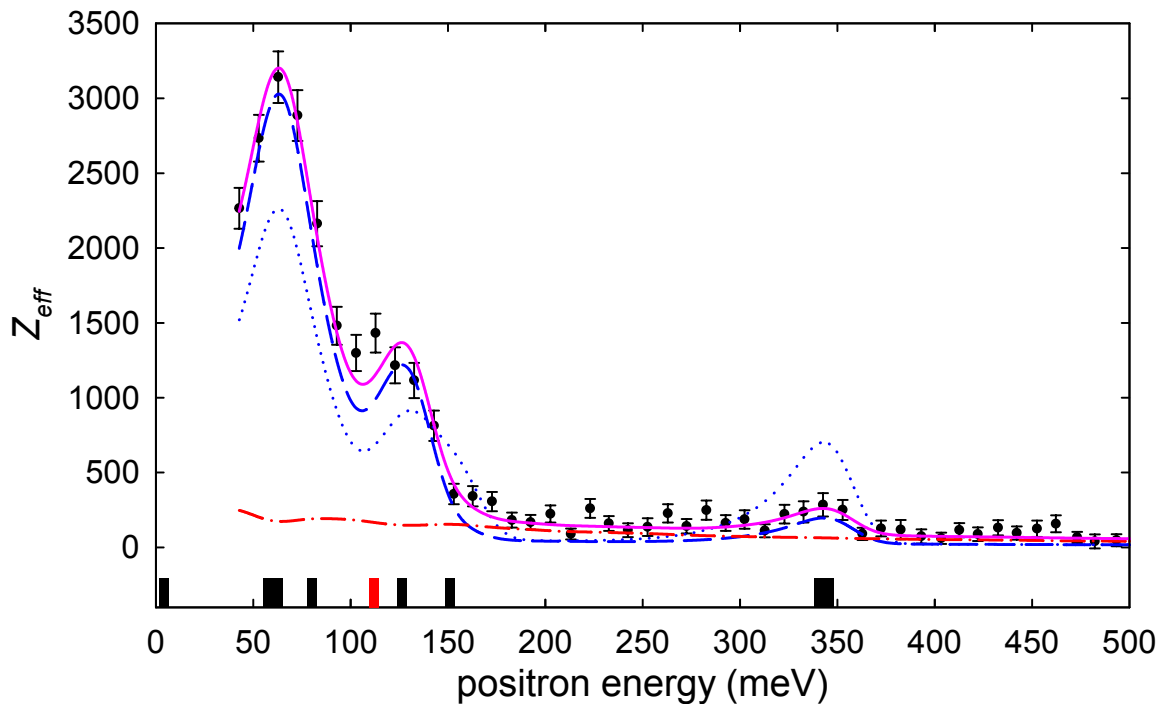


Figure B.5: Annihilation spectrum for dichloromethane (CH_2Cl_2): $\varepsilon_b = 31 \pm 1$ meV and $\eta = 0.28$.

Table B.6: Mode fit parameters for dichloromethane (CH_2Cl_2).

ω_v (cm^{-1})	ω_v (meV)	ε_v (meV)	g_v	IR-Active	β_v
282	35	4	1	yes	1
717	89	58	1	yes	1.4
758	94	63	1	yes	1.4
898	111	80	1	yes	1.4
1153	143	112	1	no	0
1268	157	126	1	yes	2.0
1467	182	151	1	yes	0.15
2999	372	341	1	yes	0.25
3040	377	346	1	yes	0.25

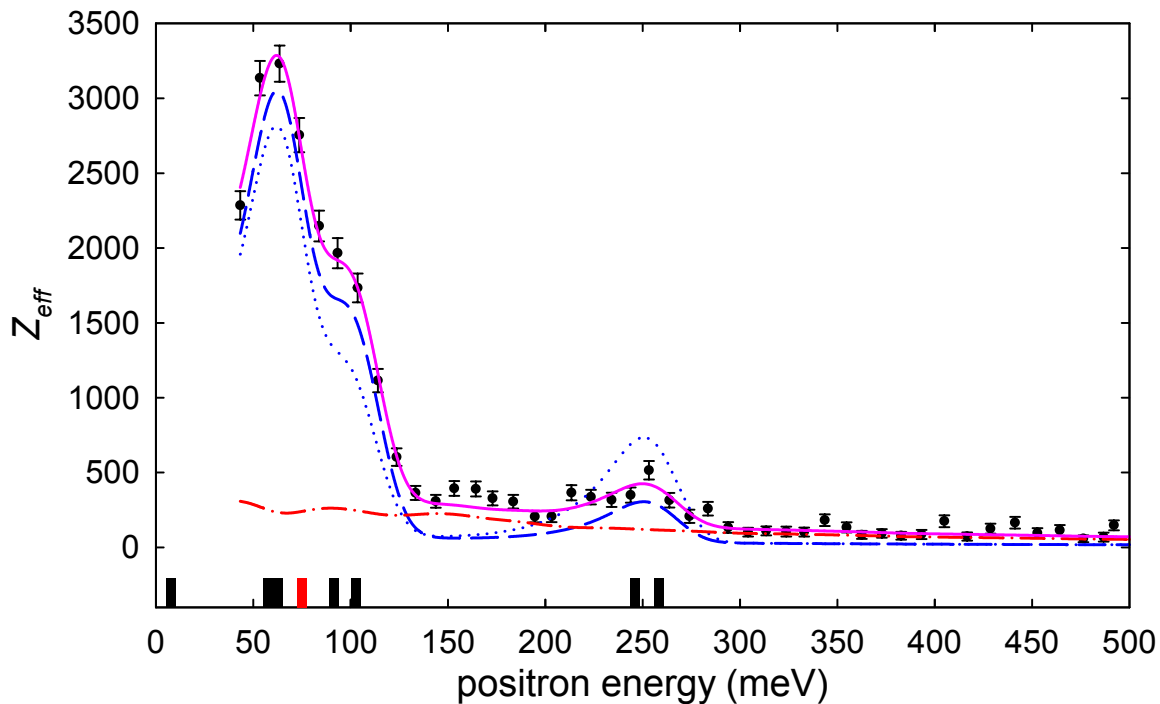


Figure B.6: Annihilation spectrum for dichloromethane-d2 (CD_2Cl_2): $\varepsilon_b = 27 \pm 1$ meV and $\eta = 0.36$.

Table B.7: Mode fit parameters for dichloromethane-d2 (CD_2Cl_2).

ω_v (cm^{-1})	ω_v (meV)	ε_v (meV)	g_v	IR-Active	β_v
282	35	8	1	yes	1
687	85	58	1	yes	1.1
712	88	61	1	yes	1.1
727	90	63	1	yes	1.1
826	102	75	1	no	0
957	119	91	1	yes	1.1
1052	130	103	1	yes	1.6
2205	273	246	1	yes	0.39
2304	286	258	1	yes	0.39

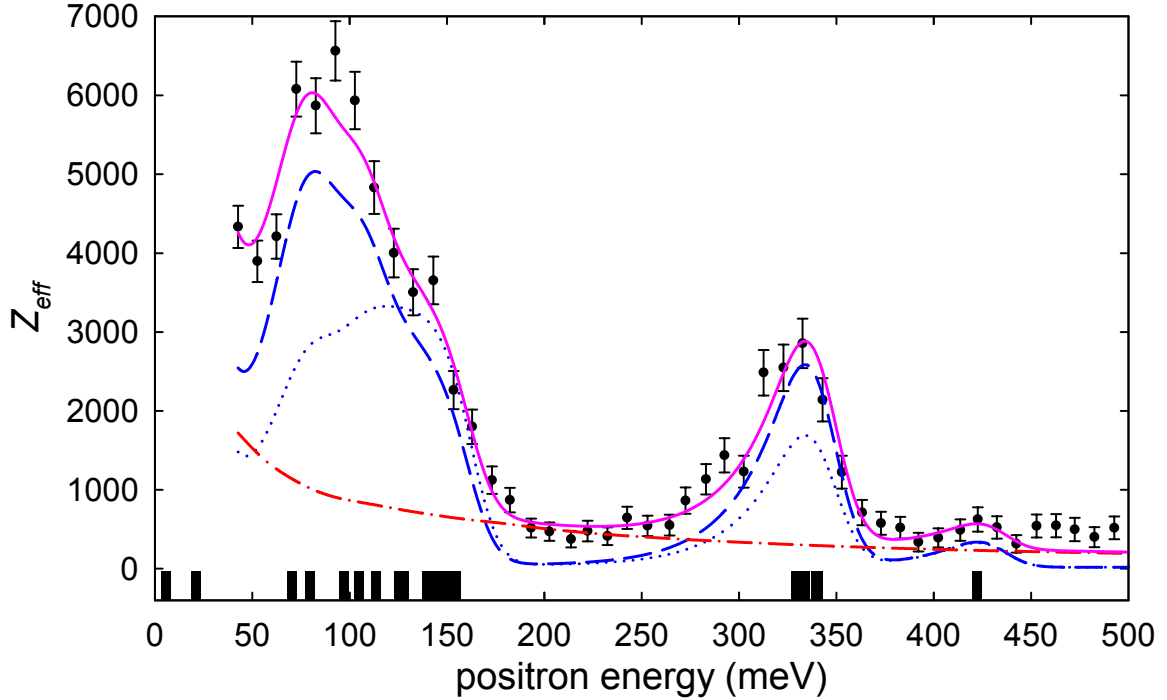


Figure B.7: Annihilation spectrum for ethanol ($\text{CH}_3\text{CH}_2\text{OH}$): $\varepsilon_b = 30 \pm 1$ meV and $\eta = 0.83$. Data shown here represent new measurements. Original measurements are shown in Ref. [33].

Table B.8: Mode fit parameters for ethanol ($\text{CH}_3\text{CH}_2\text{OH}$). For brevity, ranges of modes are listed rather than each individual mode.

ω_v (cm^{-1})	ω_v (meV)	ε_v (meV)	g_v	IR-Active	β_v
241	30	-1	1	yes	N/A
290	36	6	1	yes	1
417	52	21	1	yes	1.7
812-1091	101	70	1	yes	2.1
1161-1446	144	114	1	yes	0.96
1464-1490	182	151	1	yes	0.53
2900-2991	360	329	1	yes	1.5
3653	453	422	1	yes	1.0

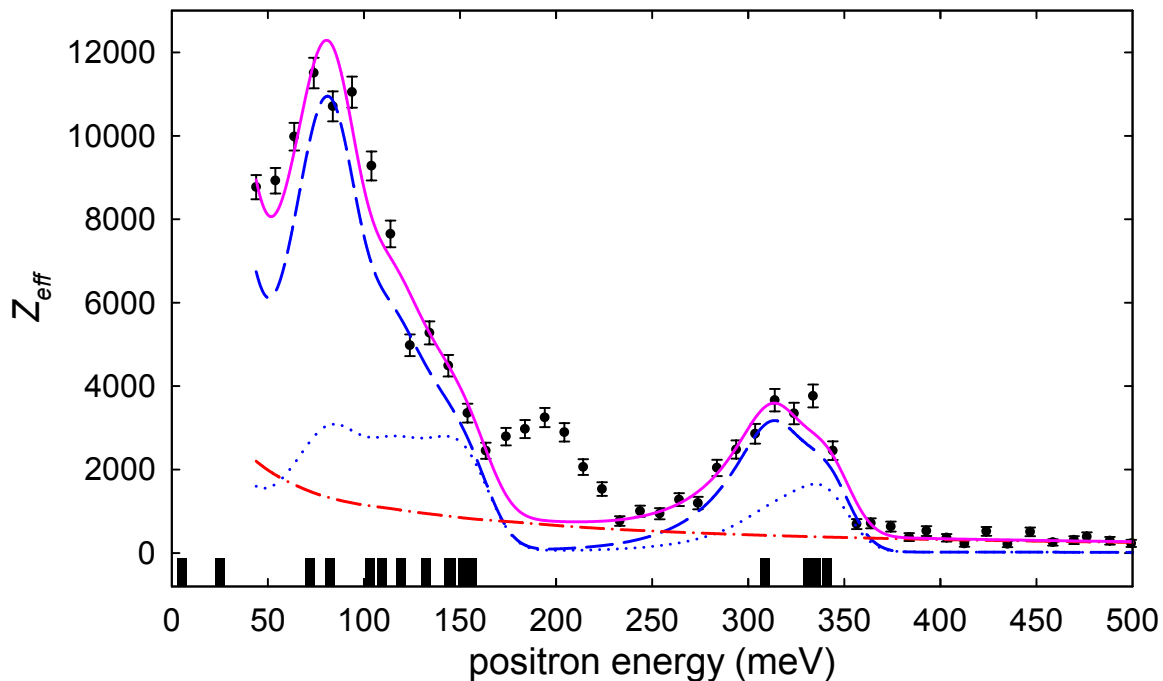


Figure B.8: Annihilation spectrum for ethanol-d1 ($\text{CH}_3\text{CH}_2\text{OD}$): $\epsilon_b = 28 \pm 2$ meV and $\eta = 1.17$.

Table B.9: Mode fit parameters for ethanol-d1 ($\text{CH}_3\text{CH}_2\text{OD}$). For brevity, ranges of modes are listed rather than each individual mode. Vibrational mode energies obtained from Ref. [56]

ω_v (cm^{-1})	ω_v (meV)	ϵ_v (meV)	g_v	IR-Active	β_v
214	27	-1	1	yes	N/A
266	33	5	1	yes	1
423	52	25	1	yes	6.2
802-885	99	72	1	yes	4.5
1055-1290	131	103	1	yes	2.6
1386-1482	172	144	1	yes	1.0
2713	336	309	1	yes	6.0
2893-2795	359	331	1	yes	1.4

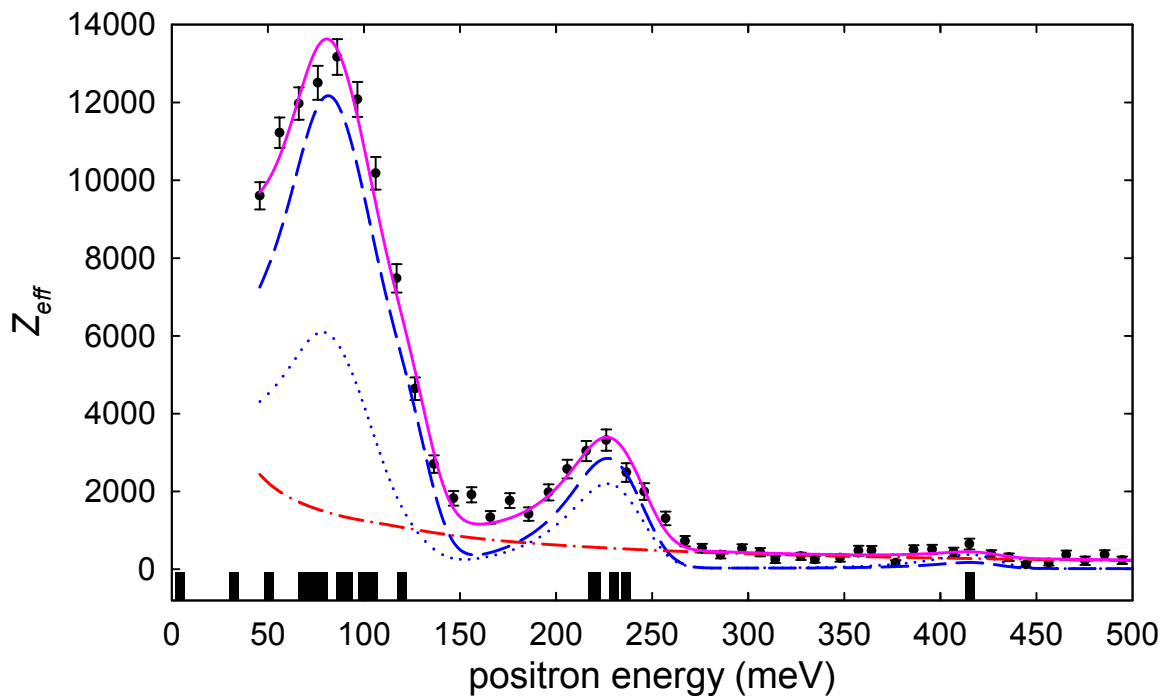


Figure B.9: Annihilation spectrum for ethanol-d5 ($\text{CD}_3\text{CD}_2\text{OH}$): $\varepsilon_b = 41 \pm 1$ meV and $\eta = 0.64$.

Table B.10: Mode fit parameters for ethanol-d5 ($\text{CD}_3\text{CD}_2\text{OH}$). For brevity, ranges of modes are listed rather than each individual mode. Vibrational mode energies obtained from Ref. [56].

ω_v (cm^{-1})	ω_v (meV)	ε_v (meV)	g_v	IR-Active	β_v
193	24	-17	1	yes	N/A
291	36	-4	1	yes	N/A
360	45	4	1	yes	1
589-878	73	33	1	yes	1.4
897-1172	111	71	1	yes	2.0
1291	160	120	1	yes	5.6
2095-2233	260	219	1	yes	1.3
3676	456	415	1	yes	0.43

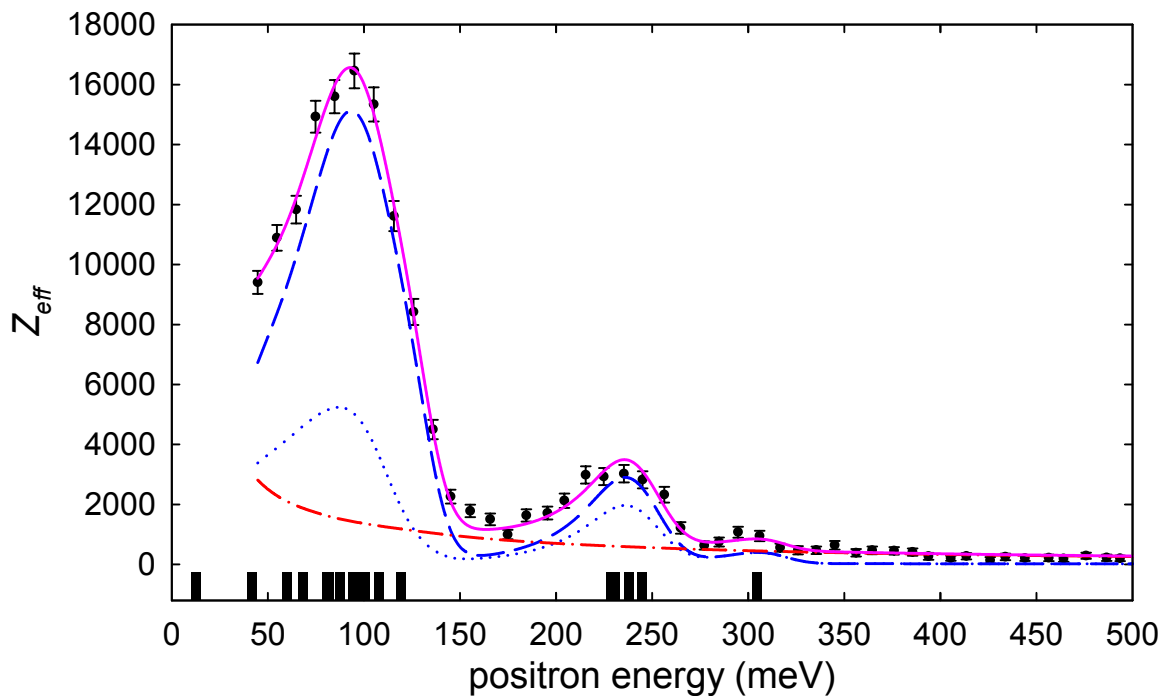


Figure B.10: Annihilation spectrum for ethanol-d6 ($\text{CD}_3\text{CD}_2\text{OD}$): $\varepsilon_b = 32 \pm 1$ meV and $\eta = 0.94$.

Table B.11: Mode fit parameters for ethanol-d6 ($\text{CD}_3\text{CD}_2\text{OD}$). For brevity, ranges of modes are listed rather than each individual mode. Vibrational mode energies obtained from Ref. [56].

ω_v (cm^{-1})	ω_v (meV)	ε_v (meV)	g_v	IR-Active	β_v
190	24	-8	1	yes	N/A
218	27	-4	1	yes	N/A
354	44	12	1	yes	~ 0
588-804	73	41	1	yes	1.6000
904-1121	112	81	1	yes	2.6
1215	151	119	1	yes	11
2098-2229	260	229	1	yes	1.5
2713	336	305	1	yes	1.0

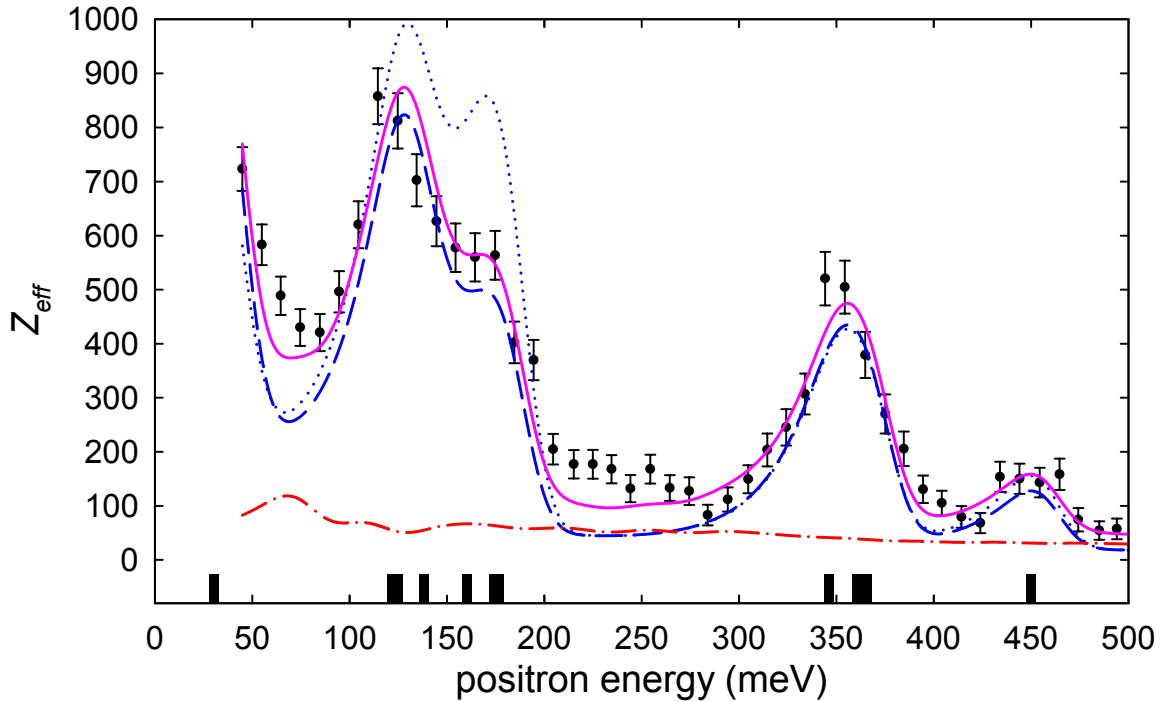


Figure B.11: Annihilation spectrum for methanol (CH_3OH): $\varepsilon_b = 6 \pm 1$ meV and $\eta = 0.51$. Data shown here represent new measurements. Original measurements are shown in Ref. [80].

Table B.12: Mode fit parameters for methanol (CH_3OH).

ω_v (cm^{-1})	ω_v (meV)	ε_v (meV)	g_v	IR-Active	β_v
295	37	30	1	yes	1.4
1033	128	122	1	yes	0.90
1060	131	125	1	yes	0.90
1165	144	138	1	yes	0.90
1345	167	160	1	yes	0.55
1455	180	174	1	yes	0.55
1477	183	177	2	yes	0.55
2844	353	346	1	yes	1.0
2960	367	361	1	yes	1.0
3000	372	366	1	yes	1.0
3681	456	450	1	yes	0.79

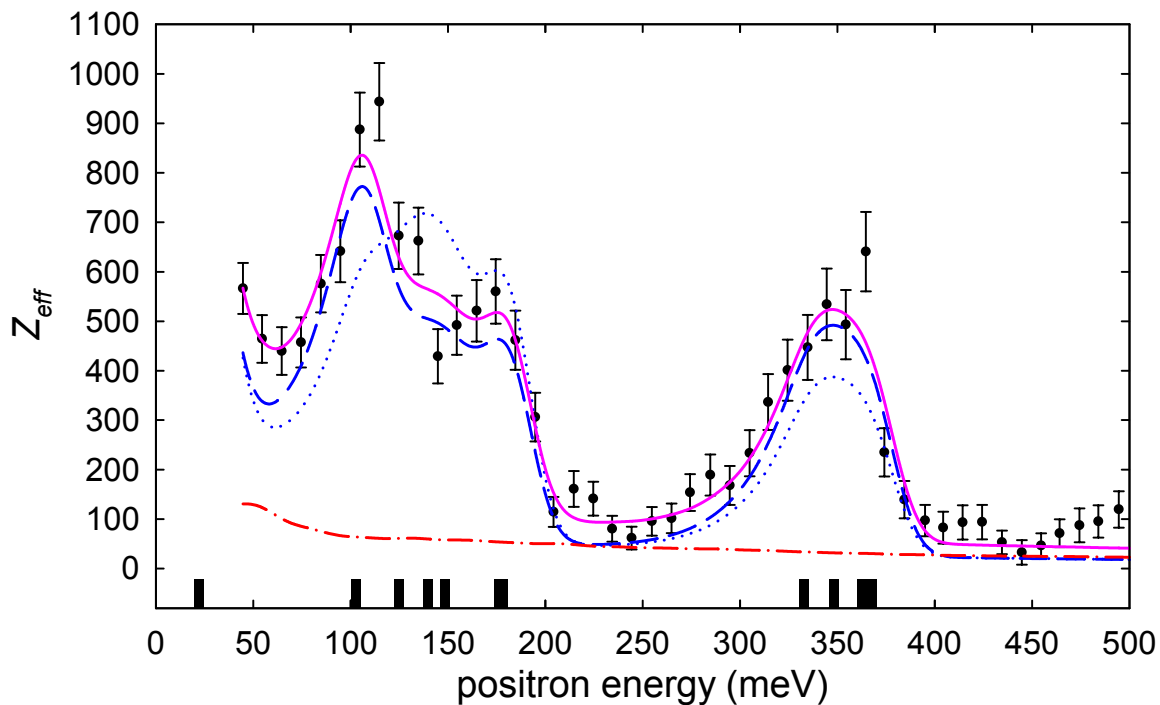


Figure B.12: Annihilation spectrum for methanol-d1 (CH_3OD): $\varepsilon_b = 4 \pm 1$ meV and $\eta = 0.49$.

Table B.13: Mode fit parameters for methanol-d1 (CH_3OD).

ω_v (cm^{-1})	ω_v (meV)	ε_v (meV)	g_v	IR-Active	β_v
213	26	22	1	yes	0.87
864	107	103	1	yes	2.2
1040	129	125	1	yes	0.63
1160	144	140	1	yes	0.63
1230	152	148	1	yes	0.63
1456	181	176	1	yes	0.75
1473	183	178	2	yes	0.75
2718	337	333	1	yes	1.3
2843	352	348	1	yes	1.3
2960	367	363	1	yes	1.3
3000	372	368	1	yes	1.3

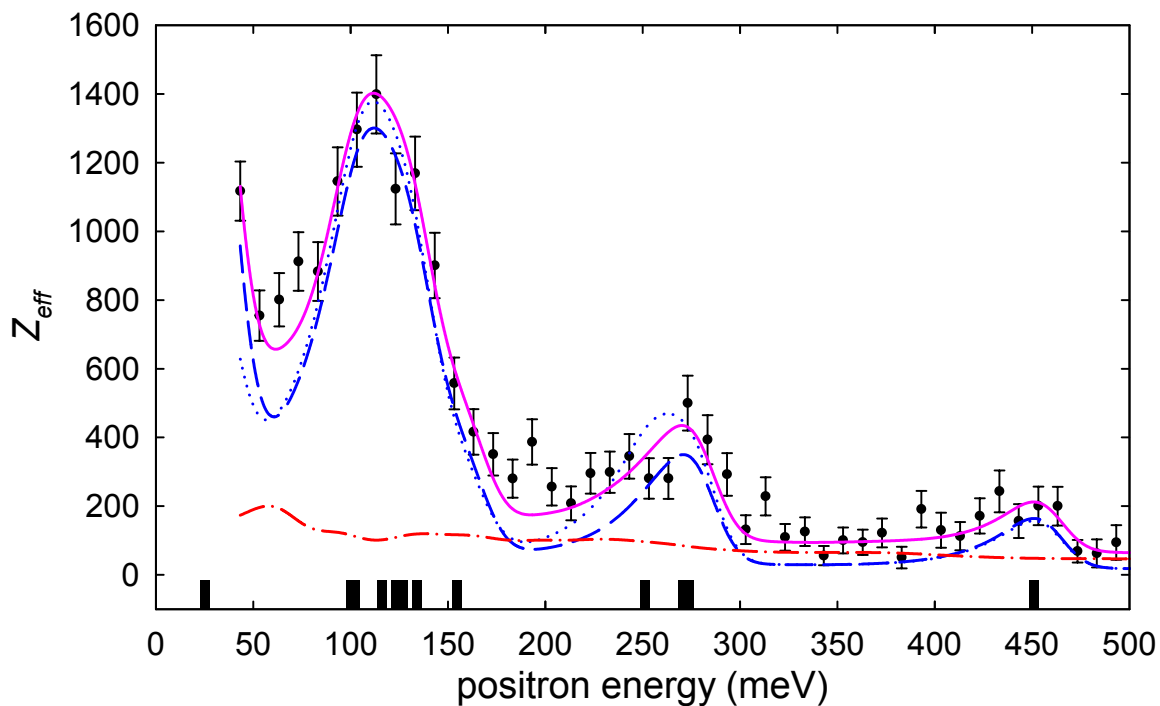


Figure B.13: Annihilation spectrum for methanol-d3 (CD_3OH): $\varepsilon_b = 7 \pm 2$ meV and $\eta = 0.73$.

Table B.14: Mode fit parameters for methanol-d3 (CD_3OH).

ω_v (cm^{-1})	ω_v (meV)	ε_v (meV)	g_v	IR-Active	β_v
256	32	25	1	yes	2.4
858	106	100	1	yes	0.93
877	109	102	1	yes	0.93
988	122	116	1	yes	0.93
1047	130	123	1	yes	0.93
1075	133	127	1	yes	0.93
1134	141	134	1	yes	0.93
1297	161	154	1	yes	1.2
2077	258	251	1	yes	0.18
2235	277	271	1	yes	0.87
2260	280	274	1	yes	0.87
3690	457	451	1	yes	1.1

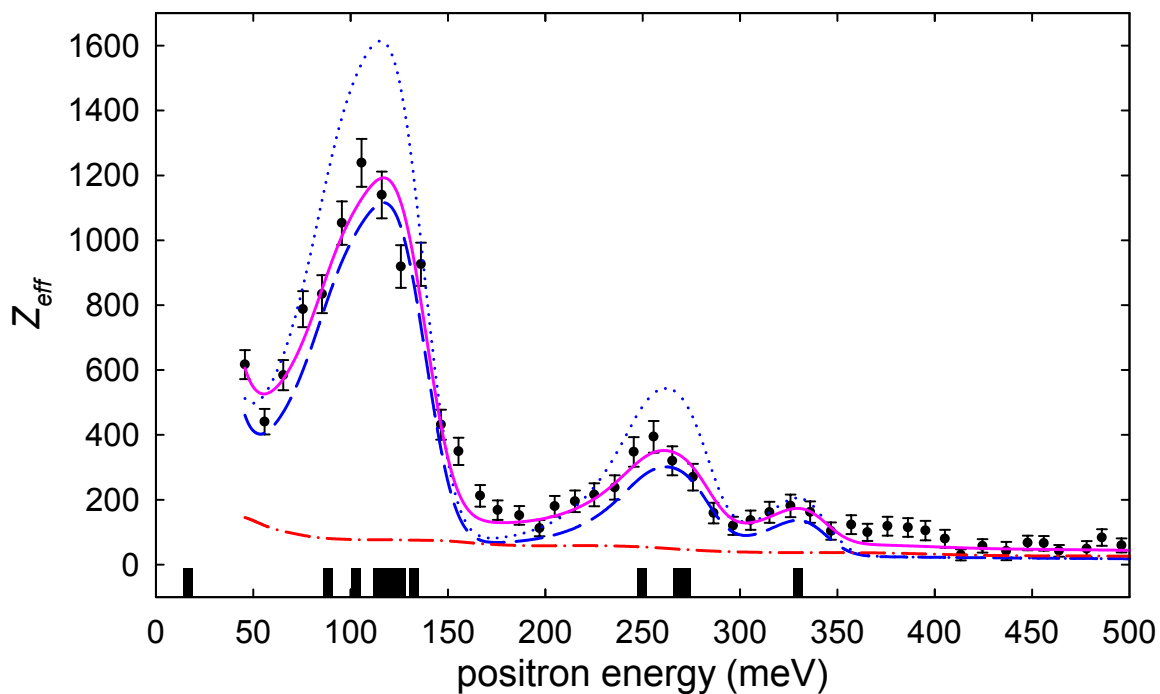


Figure B.14: Annihilation spectrum for methanol-d4 (CD_3OD): $\varepsilon_b = 8 \pm 2.2$ meV and $\eta = 0.34$.

Table B.15: Mode fit parameters for methanol-d4 (CD_3OD).

ω_v (cm^{-1})	ω_v (meV)	ε_v (meV)	g_v	IR-Active	β_v
196	24	16	1	yes	1.5
776	96	88	1	yes	0.62
892	111	103	1	yes	0.62
983	122	114	1	yes	0.62
1024	127	119	1	yes	0.62
1060	131	123	1	yes	0.62
1080	134	126	1	yes	0.81
1135	141	133	1	yes	0.81
2080	258	250	1	yes	0.52
2228	276	268	1	yes	0.52
2260	280	272	1	yes	0.52
2724	338	330	1	yes	0.61

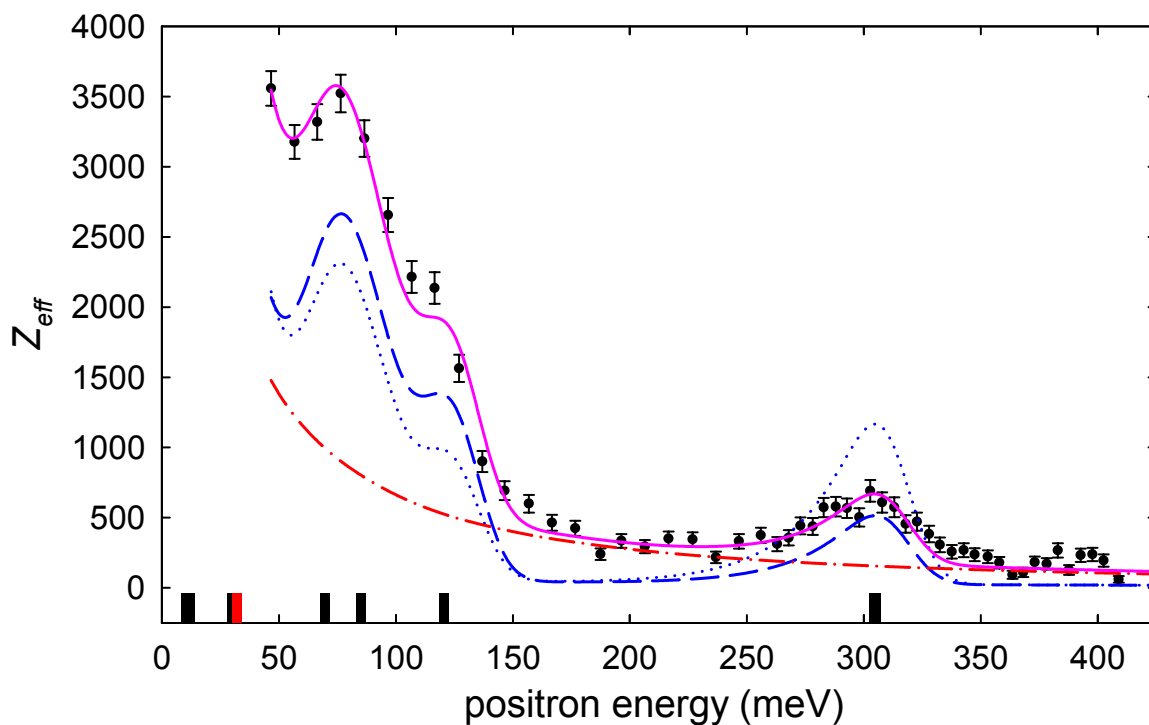


Figure B.15: Annihilation spectrum for 1,2-cis-dichloroethylene ($C_2H_2Cl_2$): $\epsilon_b = 76 \pm 1$ meV and $\eta = 0.17$. Possible energy shifts present.

Table B.16: Mode fit parameters for 1,2-cis-dichloroethylene ($C_2H_2Cl_2$). Possible energy shifts present.

ω_v (cm^{-1})	ω_v (meV)	ϵ_v (meV)	g_v	IR-Active	β_v
173	21	-55	1	yes	N/A
406	50	-26	1	no	0
571	71	-6	1	yes	N/A
697	86	10	1	yes	1
711	88	12	1	yes	0.80
857	106	30	1	yes	0.80
876	109	32	1	no	0
1179	146	70	1	yes	1.1
1303	162	85	1	yes	1.1
1587	197	120	1	yes	1.4
3072	381	305	1	yes	0.43
3077	381	305	1	yes	0.43

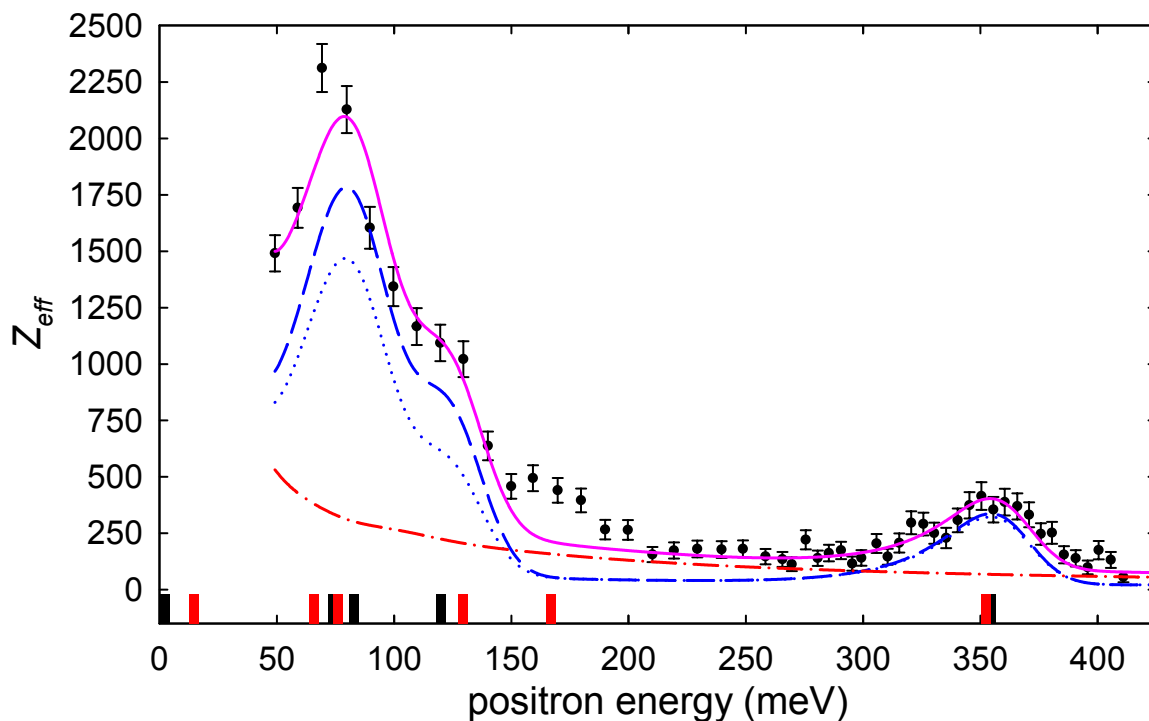


Figure B.16: Annihilation spectrum for 1,2-trans-dichloroethylene ($C_2H_2Cl_2$): $\epsilon_b = 29 \pm 2$ meV and $\eta = 0.24$. Possible energy shifts present.

Table B.17: Mode fit parameters for 1,2-trans-dichloroethylene ($C_2H_2Cl_2$). Possible energy shifts present.

ω_v (cm^{-1})	ω_v (meV)	ϵ_v (meV)	g_v	IR-Active	β_v
227	28	-1	1	yes	N/A
250	31	2	1	yes	1
350	43	15	1	no	0
763	95	66	1	no	0
828	103	74	1	yes	1.2
846	105	76	1	no	0
900	112	83	1	yes	1.2
1200	149	120	1	yes	1.5
1274	158	129	1	no	0
1578	196	167	1	no	0
3073	381	352	1	no	0
3090	383	354	1	yes	1.0

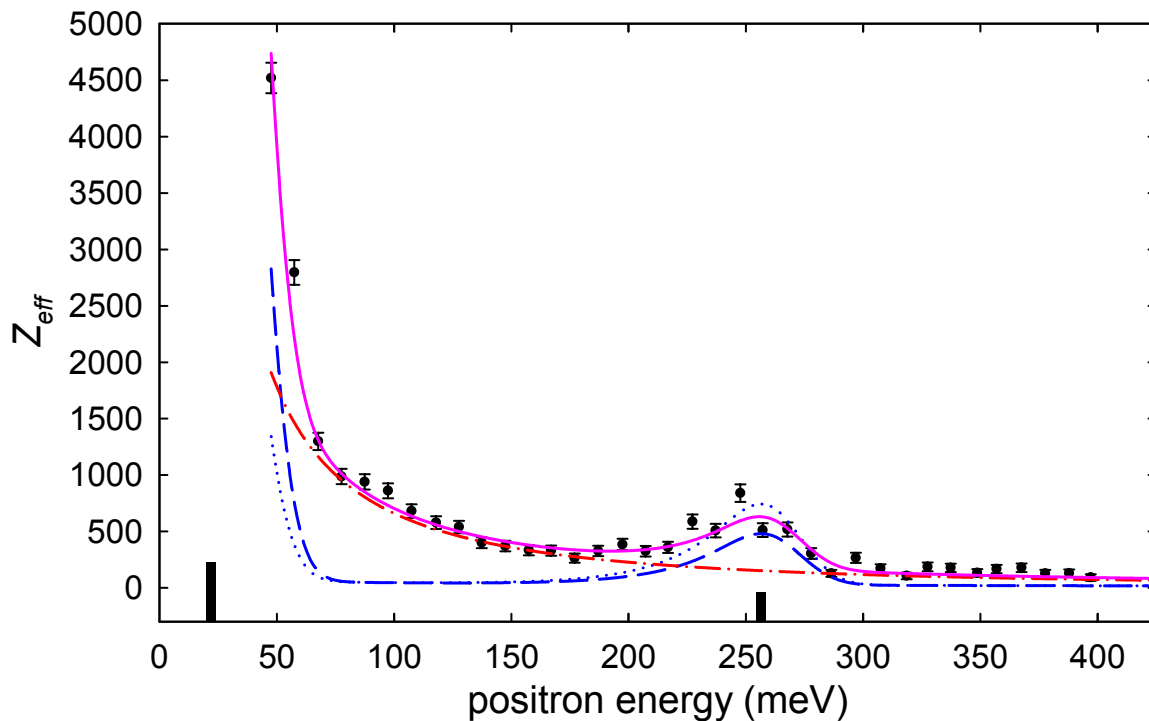


Figure B.17: Annihilation spectrum for bromoform (CHBr_3): $\epsilon_b = 121 \pm 2$ meV and $\eta = 0.07$. Possible energy shifts present.

Table B.18: Mode fit parameters for bromoform (CHBr_3). Possible energy shifts present.

ω_v (cm^{-1})	ω_v (meV)	ϵ_v (meV)	g_v	IR-Active	β_v
155	19	-101	2	yes	N/A
222	28	-93	1	yes	N/A
541	67	-54	1	yes	N/A
669	83	-38	2	yes	N/A
1149	142	22	2	yes	2.2
3042	377	256	1	yes	0.63

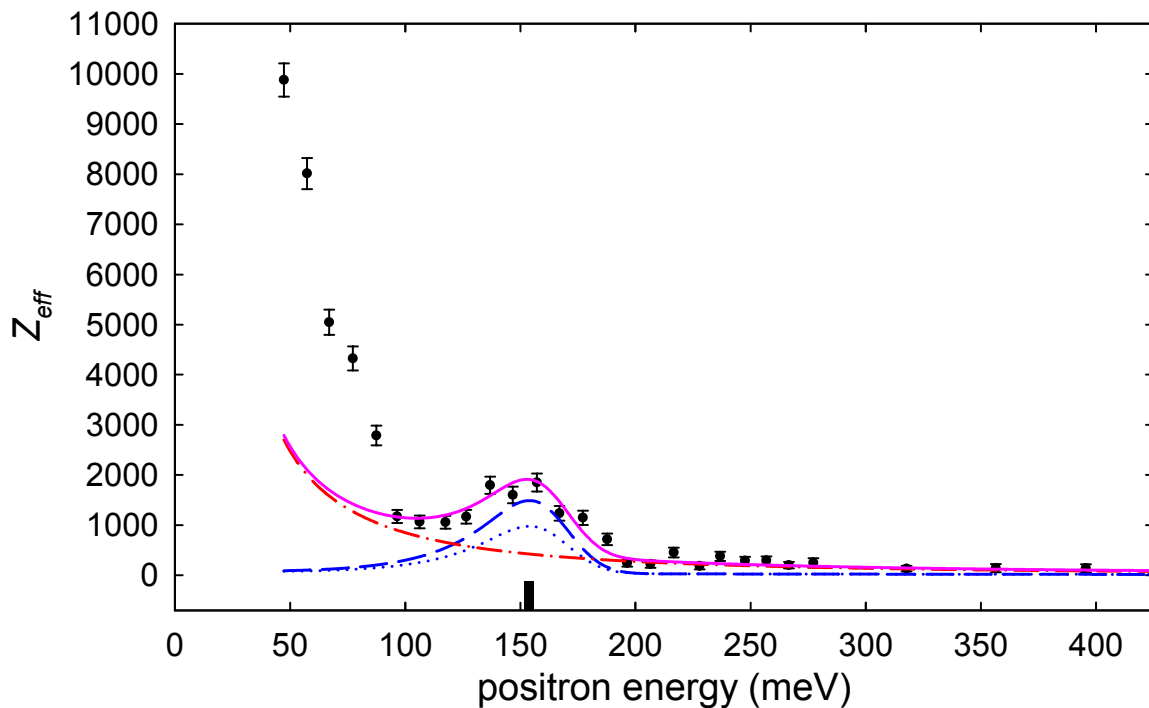


Figure B.18: Annihilation spectrum for bromoform-d (CDBr_3): $\varepsilon_b = 125 \pm 10$ meV and $\eta = 0.07$. Possible energy shifts present.

Table B.19: Mode fit parameters for bromoform-d (CDBr_3). Possible energy shifts present.

ω_v (cm^{-1})	ω_v (meV)	ε_v (meV)	g_v	IR-Active	β_v
153	19	-106	2	yes	N/A
222	28	-98	1	yes	N/A
521	65	-61	1	yes	N/A
632	78	-47	2	yes	N/A
850	105	-20	2	yes	N/A
2251	279	154	1	yes	1.5

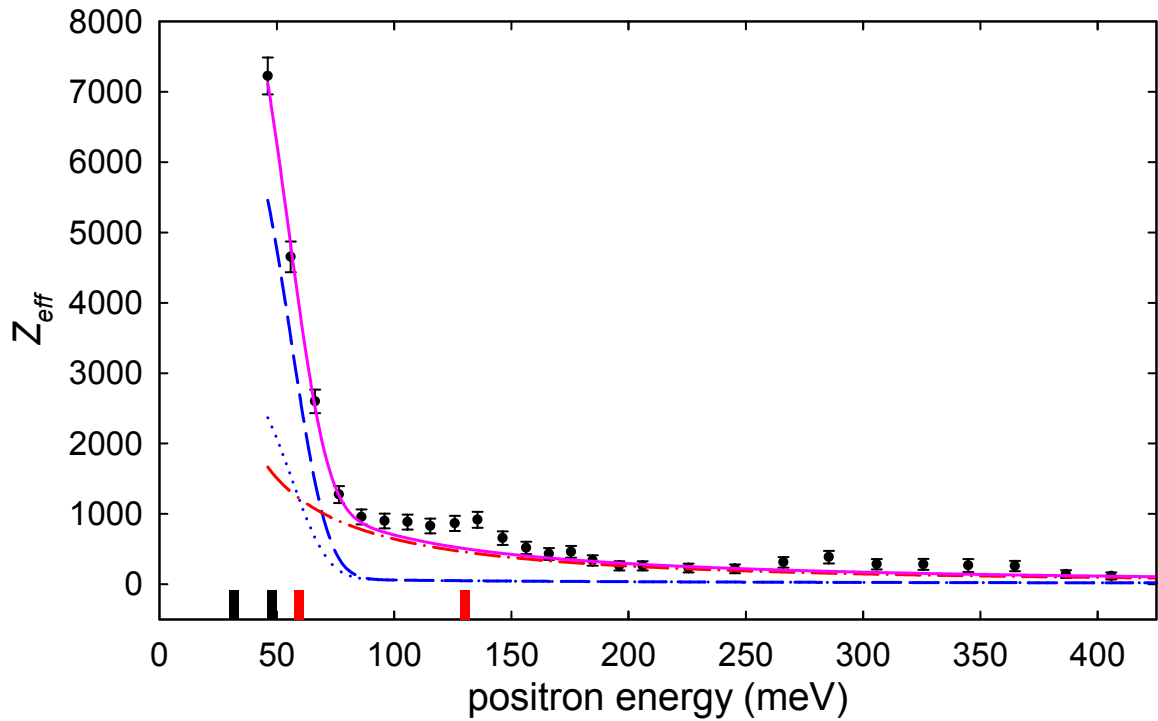


Figure B.19: Annihilation spectrum for tetrachloroethylene (C_2Cl_4): $\epsilon_b = 65 \pm 2$ meV and $\eta = 0.13$. Possible energy shifts present.

Table B.20: Mode fit parameters for tetrachloroethylene (C_2Cl_4). Possible energy shifts present.

ω_v (cm^{-1})	ω_v (meV)	ϵ_v (meV)	g_v	IR-Active	β_v
110	14	-51	1	no	0
176	22	-43	1	yes	N/A
237	29	-35	1	no	0
288	36	-29	1	yes	N/A
310	38	-26	1	yes	N/A
347	43	-22	1	no	0
447	55	-9	1	no	0
512	63	-1	1	no	0
777	96	32	1	yes	2.4
908	113	48	1	yes	2.4
1000	124	59	1	no	0
1571	195	130	1	no	0

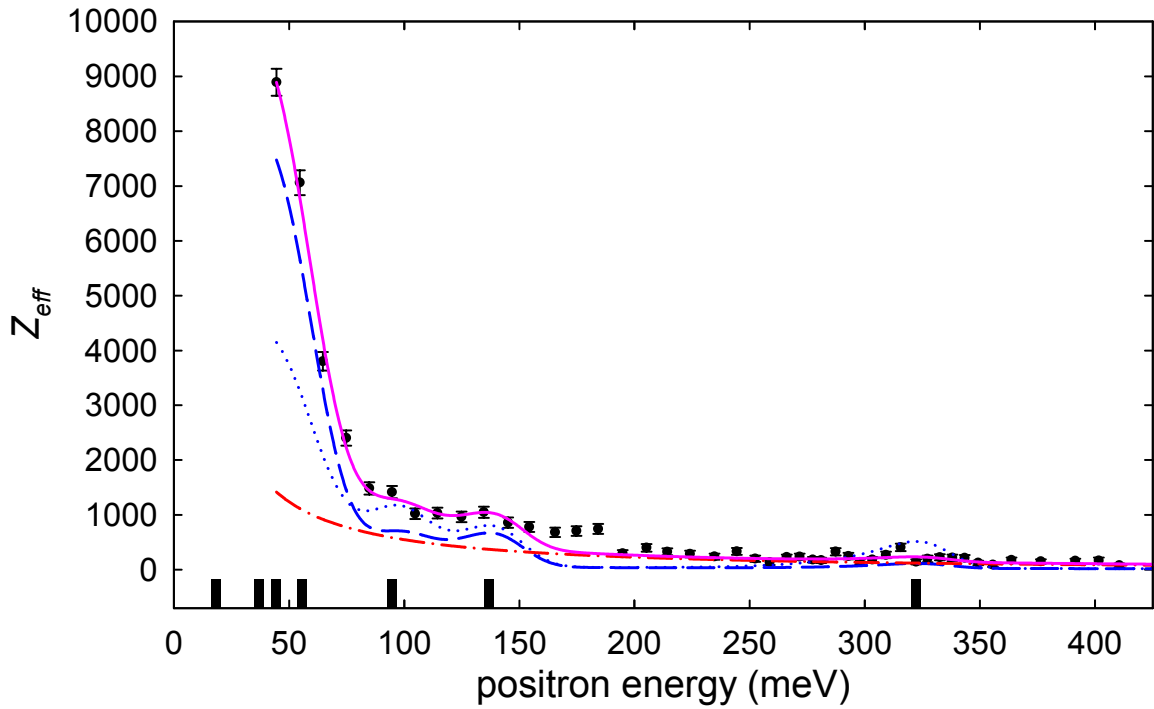


Figure B.20: Annihilation spectrum for trichloroethylene (C_2HCl_3): $\varepsilon_b = 60 \pm 1$ meV and $\eta = 0.16$. Possible energy shifts present.

Table B.21: Mode fit parameters for trichloroethylene (C_2HCl_3). Possible energy shifts present. Vibrational mode energies obtained from experimentally measured values listed in Ref. [82].

ω_v (cm^{-1})	ω_v (meV)	ε_v (meV)	g_v	IR-Active	β_v
178	22	-38	1	yes	N/A
215	27	-33	1	yes	N/A
277	34	-25	1	yes	N/A
384	48	-12	1	yes	N/A
451	56	-4	1	yes	N/A
630	78	18	1	yes	1.9
780	97	37	1	yes	1.9
840	104	44	1	yes	1.9
931	115	56	1	yes	1.9
1247	155	95	1	yes	0.52
1586	197	137	1	yes	0.82
3082	382	322	1	yes	0.18

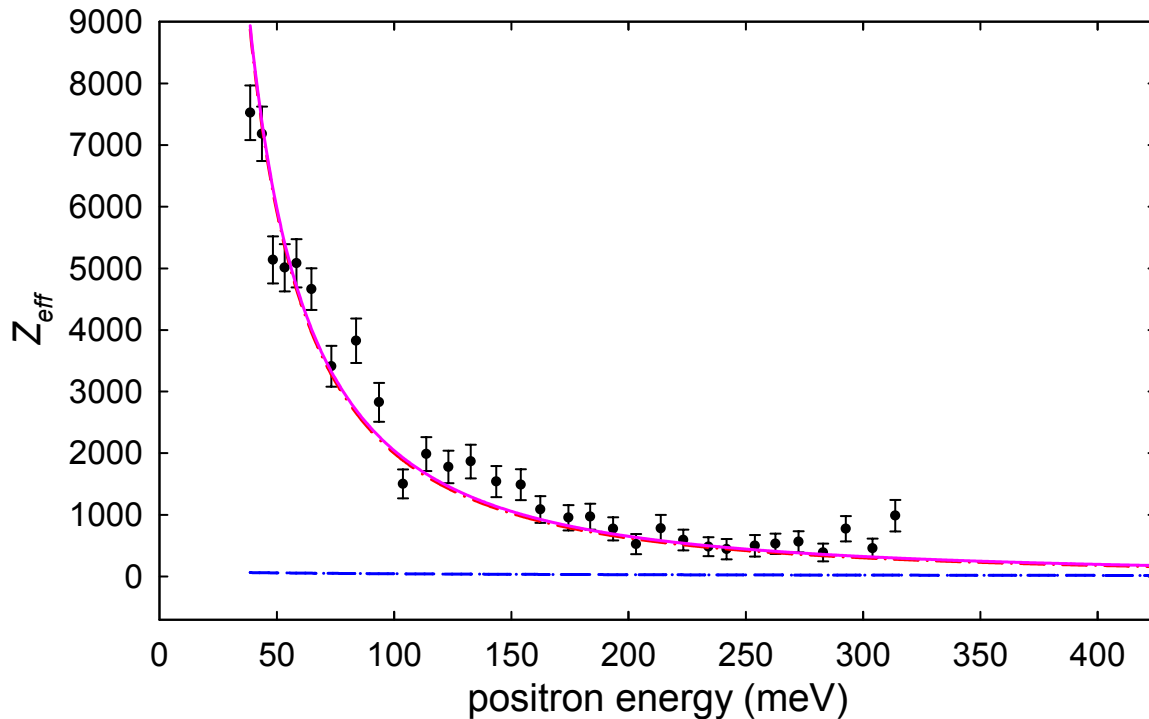


Figure B.21: Annihilation spectrum for carbon tetrabromide (CBr_4): $\epsilon_b = 115$ meV and $\eta = 0.13$. Due to lack of resonances, the binding energy is estimated using Eq. 5 of Ref. [83]. Possible energy shifts present.

Table B.22: Mode fit parameters for carbon tetrabromide (CBr_4). Possible energy shifts present.

ω_v (cm^{-1})	ω_v (meV)	ϵ_v (meV)	g_v	IR-Active	β_v
122	15	-100	2	no	0
182	23	-92	3	yes	N/A
267	33	-82	1	no	0
672	83	-32	3	yes	N/A

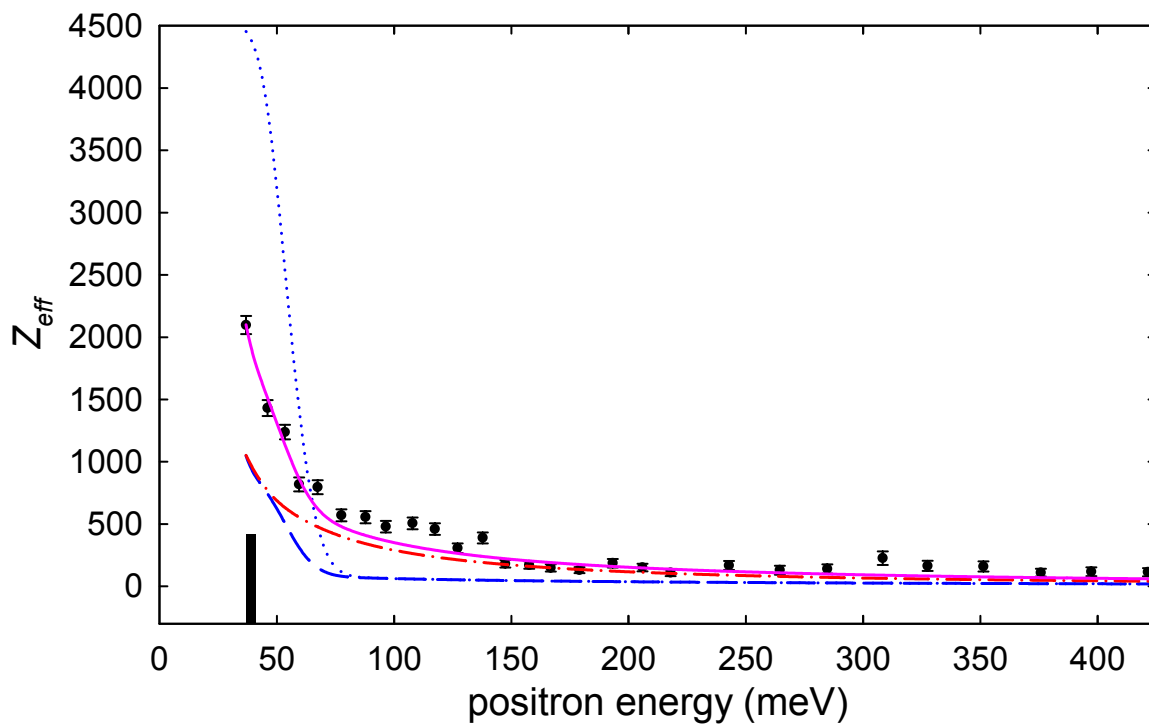


Figure B.22: Annihilation spectrum for carbon tetrachloride (CCl_4): $\varepsilon_b = 57 \pm 1$ meV and $\eta = 0.09$. Possible energy shifts present.

Table B.23: Mode fit parameters for carbon tetrachloride (CCl_4). Possible energy shifts present.

ω_v (cm^{-1})	ω_v (meV)	ε_v (meV)	g_v	IR-Active	β_v
217	27	-30	2	no	0
314	39	-18	3	yes	N/A
459	57	0	1	no	0
776	96	39	3	yes	0.17

Bibliography

- [1] P. Dirac, “The quantum theory of the electron,” in *Proceedings of the Royal Society of London A: Mathematical, Physical and Engineering Sciences*, vol. 117, p. 610, 1928.
- [2] P. Dirac, “A theory of electrons and protons,” in *Proceedings of the Royal Society of London A: Mathematical, Physical and Engineering Sciences*, vol. 126, p. 360, 1930.
- [3] P. Dirac, “On the annihilation of electrons and protons,” in *Mathematical Proceedings of the Cambridge Philosophical Society*, vol. 26, p. 361, 1930.
- [4] P. Dirac, “Quantised singularities in the electromagnetic field,” in *Proceedings of the Royal Society of London A: Mathematical, Physical and Engineering Sciences*, vol. 133, p. 60, 1931.
- [5] C. D. Anderson, “The positive electron,” *Phys. Rev.*, vol. 43, p. 491, 1933.
- [6] I. Curie and F. Joliot, “Un nouveau type de radioactivité,” *CR Acad Sci Paris*, vol. 198, p. 254, 1934.
- [7] D. G. Costello, D. E. Groce, D. F. Herring, and J. W. McGowan, “Evidence for the negative work function associated with positrons in gold,” *Phys. Rev. B*, vol. 5, p. 1433, 1972.
- [8] A. P. Mills and E. M. Gullikson, “Solid neon moderator for producing slow positrons,” *App. Phys. Lett.*, vol. 49, p. 1121, 1986.
- [9] D. A. Fischer, K. G. Lynn, and D. W. Gidley, “High-resolution angle-resolved positron reemission spectra from metal surfaces,” *Phys. Rev. B*, vol. 33, p. 4479, 1986.
- [10] K. F. Canter, P. G. Coleman, T. C. Griffith, and G. R. Heyland, “Measurement of total cross sections for low energy positron-helium collisions,” *J. of Phys. B*, vol. 5, p. L167, 1972.
- [11] P. G. Coleman and J. T. Hutton, “Excitation of helium atoms by positron impact,” *Phys. Rev. Lett.*, vol. 45, p. 2017, 1980.
- [12] D. Fromme, G. Kruse, W. Raith, and G. Sinapius, “Partial-cross-section measurements for ionization of helium by positron impact,” *Phys. Rev. Lett.*, vol. 57, p. 3031, 1986.
- [13] C. M. Surko, M. Leventhal, and A. Passner, “Positron plasma in the laboratory,” *Phys. Rev. Lett.*, vol. 62, p. 901, 1989.
- [14] R. G. Greaves and C. M. Surko, “Solid neon moderator for positron-trapping experiments,” *Can. J. Phys.*, vol. 74, p. 445, 1996.

- [15] S. J. Gilbert, C. Kurz, R. G. Greaves, and C. M. Surko, "Creation of a monoenergetic pulsed positron beam," *App. Phys. Lett.*, vol. 70, p. 1944, 1997.
- [16] J. P. Sullivan, S. J. Gilbert, and C. M. Surko, "Excitation of molecular vibrations by positron impact," *Phys. Rev. Lett.*, vol. 86, p. 1494, 2001.
- [17] G. F. Gribakin, J. A. Young, and C. M. Surko, "Positron-molecule interactions: Resonant attachment, annihilation, and bound states," *Rev. Mod. Phys.*, vol. 82, p. 2557, 2010.
- [18] D. Chaudhary, M. R. Went, K. Nakagawa, S. J. Buckman, and J. P. Sullivan, "Molecular pore size characterization within chitosan biopolymer using positron annihilation lifetime spectroscopy," *Mat. Lett.*, vol. 64, p. 2635, 2010.
- [19] M. Amoretti, C. Amsler, G. Bonomi, A. Bouchta, P. Bowe, C. Carraro, C. L. Cesar, M. Charlton, M. J. T. Collier, M. Doser, V. Filippini, K. S. Fine, A. Fontana, M. C. Fujiwara, R. Funakoshi, P. Genova, J. S. Hangst, R. S. Hayano, M. H. Holzscheiter, L. V. Jorgensen, V. Lagomarsino, R. Landua, D. Lindelof, E. L. Rizzini, M. Macri, N. Madsen, G. Manuzio, M. Marchesotti, P. Montagna, H. Pruys, C. Regenfus, P. Riedler, J. Rochet, A. Rotondi, G. Rouleau, G. Testera, A. Variola, T. L. Watson, and D. P. van der Werf, "Production and detection of cold antihydrogen atoms," *Nature*, vol. 419, p. 456, 2002.
- [20] R. Krause-Rehberg, N. Van der Walt, L. Büttner, and F. Börner, "A ^{22}Na positron source for use in uhv," *Nucl. Instr. and Meth. Phys. Res. B*, vol. 221, p. 165, 2004.
- [21] J. A. Young, *Energy-resolved annihilation studies: Vibrational Feshbach resonances and positron-molecule bound states*. ProQuest, 2007.
- [22] J. P. Marler and C. M. Surko, "Positron-impact ionization, positronium formation, and electronic excitation cross sections for diatomic molecules," *Phys. Rev. A*, vol. 72, p. 062713, 2005.
- [23] S. J. Gilbert, *A new ultra-cold positron beam and applications to low-energy positron scattering and electron-positron plasmas*. PhD thesis, University of California, San Diego, 2000.
- [24] T. Murphy and C. Surko, "Positron trapping in an electrostatic well by inelastic collisions with nitrogen molecules," *Phys. Rev. A*, vol. 46, p. 5696, 1992.
- [25] M. R. Natisin, J. R. Danielson, and C. M. Surko, "Positron cooling by vibrational and rotational excitation of molecular gases," *J. Phys. B*, vol. 47, p. 225209, 2014.
- [26] M. R. Natisin, J. R. Danielson, and C. M. Surko, "Formation of buffer-gas-trap based positron beams," *Phys. Plasmas*, vol. 22, p. 033501, 2015.
- [27] M. R. Natisin, J. R. Danielson, and C. M. Surko, "Formation mechanisms and optimization of trap-based positron beams," *Phys. Plasma*, vol. 23, p. 023505, 2016.
- [28] J. P. Sullivan, S. J. Gilbert, J. P. Marler, R. G. Greaves, S. J. Buckman, and C. M. Surko, "Positron scattering from atoms and molecules using a magnetized beam," *Phys. Rev. A*, vol. 66, p. 042708, 2002.
- [29] C. M. Surko, G. F. Gribakin, and S. J. Buckman, "Low-energy positron interactions with atoms and molecules," *J. Phys. B*, vol. 38, p. R57, 2005.

- [30] G. F. Gribakin and C. M. R. Lee, "Positron annihilation in molecules by capture into vibrational feshbach resonances of infrared-active modes," *Phys. Rev. Lett.*, vol. 97, p. 193201, 2006.
- [31] S. J. Gilbert, L. D. Barnes, J. P. Sullivan, and C. M. Surko, "Vibrational-resonance enhancement of positron annihilation in molecules," *Phys. Rev. Lett.*, vol. 88, p. 043201, 2002.
- [32] P. A. Fraser, "Positrons and positronium in gases," *Adv. At. Mol. Phys.*, vol. 4, p. 63, 1968.
- [33] J. A. Young and C. M. Surko, "Feshbach-resonance-mediated positron annihilation in small molecules," *Phys. Rev. A*, vol. 78, p. 032702, 2008.
- [34] G. F. Gribakin and C. M. R. Lee, "Positron annihilation in large polyatomic molecules. The role of vibrational feshbach resonances and binding," *Euro. Phys. J. D*, vol. 51, p. 51, 2009.
- [35] A. C. L. Jones, J. R. Danielson, M. R. Natisin, C. M. Surko, and G. F. Gribakin, "Ubiquitous nature of multimode vibrational resonances in positron-molecule annihilation," *Phys. Rev. Lett.*, vol. 108, p. 093201, 2012.
- [36] D. J. Nesbitt and R. W. Field, "Vibrational energy flow in highly excited molecules: Role of intramolecular vibrational redistribution," *J. Chem. Phys.*, vol. 100, p. 12735, 1996.
- [37] R. Bigwood, M. Gruebele, D. M. Leitner, and P. G. Wolynes, "The vibrational energy flow transition in organic molecules: Theory meets experiment," *PNAS*, vol. 95, p. 5960, 1998.
- [38] M. Gruebele and P. G. Wolynes, "Vibrational energy flow and chemical reactions," *Acc. Chem. Res.*, vol. 37, p. 261, 2004.
- [39] A. C. L. Jones, J. R. Danielson, M. R. Natisin, and C. M. Surko, "Role of vibrational dynamics in resonant positron annihilation on molecules," *Phys. Rev. Lett.*, vol. 110, p. 223201, 2013.
- [40] J. R. Danielson, A. C. L. Jones, M. R. Natisin, and C. M. Surko, "Modeling enhancement and suppression of vibrational feshbach resonances in positron annihilation on molecules," *Phys. Rev. A*, vol. 88, p. 062702, 2013.
- [41] J. Marler, G. F. Gribakin, and C. M. Surko, "Comparison of positron-impact vibrational excitation cross sections with the born-dipole model," *Nucl. Instrum. Meth. B*, vol. 247, p. 87, 2006.
- [42] M. Kimura, M. Takekawa, Y. Itikawa, H. Takaki, and O. Sueoka, "Mode dependence in vibrational excitation of a co₂ molecule by electron and positron impacts," *Phys. Rev. Lett.*, vol. 80, p. 3936.
- [43] G. Gabrielse, N. S. Bowden, P. Oxley, A. Speck, C. H. Storry, J. N. Tan, M. Wessels, D. Grzonka, W. Oelert, G. Schepers, T. Sefzick, J. Walz, H. Pittner, T. W. Hänsch, and E. A. Hessels, "Background-free observation of cold antihydrogen with field-ionization analysis of its states," *Phys. Rev. Lett.*, vol. 89, p. 213401, 2002.
- [44] G. B. Andresen, M. D. Ashkezari, M. Baquero-Ruiz, W. Bertsche, P. D. Bowe, E. Butler, C. L. Cesar, S. Chapman, M. Charlton, A. Deller, S. Eriksson, J. Fajans, T. Friesen, M. C. Fujiwara, D. R. Gill, A. Gutierrez, J. S. Hangst, W. N. Hardy, M. E. Hayden, A. J. Humphries, R. Hydromako, M. J. Jenkins, S. Jonsell, L. V. Jorgensen, L. Kurchaninov, N. Madsen, S. Menary,

- P. Nolan, K. Olchanski, A. Olin, A. Povilus, P. Pusa, F. Robicheaux, E. Sarid, S. S. e. Nasr, D. M. Silveira, C. So, J. W. Storey, R. I. Thompson, D. P. van der Werf, J. S. Wurtele, and Y. Yamazaki, "Trapped antihydrogen," *Nature*, vol. 468, p. 673, 2010.
- [45] G. Gabrielse, R. Kalra, W. S. Kolthammer, R. McConnell, P. Richerme, D. Grzonka, W. Oelert, T. Sefzick, M. Zielinski, D. W. Fitzakerley, M. C. George, E. A. Hessels, C. H. Storry, M. Weel, A. Müllers, and J. Walz, "Trapped antihydrogen in its ground state," *Phys. Rev. Lett.*, vol. 108, p. 113002, 2012.
- [46] D. B. Cassidy and A. P. Mills, "The production of molecular positronium," *Nature*, vol. 449, p. 195, 2007.
- [47] W. C. Swope, H. C. Andersen, P. H. Berens, and K. R. Wilson, "A computer simulation method for the calculation of equilibrium constants for the formation of physical clusters of molecules: Application to small water clusters," *J. Chem. Phys.*, vol. 76, p. 637, 1982.
- [48] D. H. E. Dubin and T. M. O'Neil, "Trapped nonneutral plasmas, liquids, and crystals (the thermal equilibrium states)," *Rev. Mod. Phys.*, vol. 71, p. 87, 1999.
- [49] W. Tattersall, R. D. White, R. E. Robson, J. P. Sullivan, and S. J. Buckman, "Simulations of pulses in a buffer gas trap," *J. Phys.: Conf. Ser.*, vol. 262, p. 012057, 2011.
- [50] H. Goldstein, *Classical Mechanics*. Addison Wesley, 1980.
- [51] R. G. Greaves and C. M. Surko, "Radial compression and inward transport of positron plasmas using a rotating electric field," *Phys. Plasmas*, vol. 8, pp. 1879–1885, 2001.
- [52] J. R. Danielson and C. M. Surko, "Radial compression and torque-balanced steady states of single-component plasmas in penning-malmberg traps," *Phys. Plasmas*, vol. 13, p. 055706, 2006.
- [53] D. B. Cassidy, R. G. Greaves, V. E. Meline, and A. P. Mills, "Strong drive compression of a gas-cooled positron plasma," *Appl. Phys. Lett.*, vol. 96, pp. 101502–101502, 2010.
- [54] A. G. Robertson, M. T. Elford, R. W. Crompton, and M. A. Morrison, "Rotational and vibrational excitation of nitrogen by electron impact," *Aust. J. Phys.*, vol. 50, pp. 441–472, 1997.
- [55] Y. Itikawa, "The born cross section for vibrational excitation of a polyatomic molecule by electron collisions," *J. Phys. Soc. Jpn.*, vol. 36, p. 1121, 1974.
- [56] D. M. Bishop and L. M. Cheung, "Vibrational contributions to molecular dipole polarizabilities," *J. Phys. Chem. Ref. Data*, vol. 11, pp. 119–133, 1982.
- [57] E. Gerjuoy and S. Stein, "Rotational excitation by slow electrons," *Phys. Rev.*, vol. 97, pp. 1671–1679, 1955.
- [58] C. Graham, D. A. Imrie, and R. E. Raab, "Measurement of the electric quadrupole moments of CO_2 , CO , N_2 , Cl_2 and BF_3 ," *Mol. Phys.*, vol. 93, p. 49, 1998.
- [59] K. P. Huber and G. Herzberg, eds., *Molecular Spectra and Molecular Structure. IV. Constants of Diatomic Molecules*. New York, N.Y.: Van Nostrand Reinhold Co., 1979.

- [60] K. Takayanagi and M. Inokuti, "On the scattering of slow positrons by molecules," *J. Phys. Soc. Jap.*, vol. 23, p. 1412, 1967.
- [61] K. T. Mazon, W. Tenfen, S. E. Michelin, F. Arretche, M.-T. Lee, and M. M. Fujimoto, "Vibrational cross sections for positron scattering by nitrogen molecules," *Phys. Rev. A*, vol. 82, p. 032704, 2010.
- [62] F. A. Gianturco and T. Mukherjee, "Dynamical coupling effects in the vibrational excitation of H₂ and N₂ colliding with positrons," *Phys. Rev. A*, vol. 55, p. 1044, 1997.
- [63] T. Mukherjee, A. S. Ghosh, and A. Jain, "Low-energy positron collisions with h₂ and n₂ molecules by using a parameter-free positron-correlation-polarization potential," *Phys. Rev. A*, vol. 43, p. 2538, 1991.
- [64] R. D. Hake and A. V. Phelps, "Momentum-transfer and inelastic-collision cross sections for electrons in O₂, CO, and CO₂," *Phys. Rev.*, vol. 158, p. 70, 1967.
- [65] R. D. Nelson, D. R. Lide, and A. A. Maryott, eds., *Selected Values of electric dipole moments for molecules in the gas phase*. Washington, D.C.: U.S. National Bureau of Standards, 1967.
- [66] A. Jain, "A treatment of low-energy positron-co collisions using a new parameter-free positron correlation polarisation (pcop) potential," *J. Phys. B*, vol. 23, pp. 863,, 1990.
- [67] A. S. Ghosh and T. Mukherjee, "Positron-molecule scattering at low and medium energies," *Can. J. Phys.*, vol. 74, p. 420, 1996.
- [68] R. G. Greaves and J. M. Moxom, "Compression of trapped positrons in a single particle regime by a rotating electric field," *Phys. Plasmas*, vol. 15, p. 072304, 2008.
- [69] C. A. Isaac, C. J. Baker, T. Mortensen, D. P. van der Werf, and M. Charlton, "Compression of positron clouds in the independent particle regime," *Phys. Rev. Lett.*, vol. 107, p. 033201, 2011.
- [70] M. R. Natisin, J. R. Danielson, and C. M. Surko, "A cryogenically cooled, ultra-high-energy-resolution, trap-based positron beam," *App. Phys. Lett.*, vol. 108, p. 024102, 2016.
- [71] T. M. O'Neil, "Cooling of a pure electron plasma by cyclotron radiation," *Phys. Fluids*, vol. 23, p. 725, 1980.
- [72] B. M. Jelenković, A. S. Newbury, J. J. Bollinger, W. M. Itano, and T. B. Mitchell, "Sympathetically cooled and compressed positron plasma," *Phys. Rev. A*, vol. 67, p. 063406, 2003.
- [73] J. R. Danielson, T. R. Weber, and C. M. Surko, "Extraction of small-diameter beams from single-component plasmas," *Appl. Phys. Lett.*, vol. 90, p. 081503, 2007.
- [74] T. R. Weber, J. R. Danielson, and C. M. Surko, "Energy spectra of tailored particle beams from trapped single-component plasmas," *Phys. Plasmas*, vol. 16, p. 057105, 2009.
- [75] G. B. Andresen, M. D. Ashkezari, M. Baquero-Ruiz, W. Bertsche, P. D. Bowe, E. Butler, P. T. Carpenter, C. L. Cesar, S. Chapman, M. Charlton, J. Fajans, T. Friesen, M. C. Fujiwara, D. R. Gill, J. S. Hangst, W. N. Hardy, M. E. Hayden, A. J. Humphries, J. L. Hurt, R. Hydromako,

- S. Jonsell, N. Madsen, S. Menary, P. Nolan, K. Olchanski, A. Olin, A. Povilus, P. Pusa, F. Robicheaux, E. Sarid, D. M. Silveira, C. So, J. W. Storey, R. I. Thompson, D. P. van der Werf, J. S. Wurtele, and Y. Yamazaki, "Autoresonant excitation of antiproton plasmas," *Phys. Rev. Lett.*, vol. 106, p. 025002, 2011.
- [76] G. F. Gribakin, "Mechanisms of positron annihilation on molecules," *Phys. Rev. A*, vol. 61, p. 022720, 2000.
- [77] G. F. Gribakin, "Theory of positron annihilation on molecules," in *New Directions in Antimatter Chemistry and Physics*, p. 413, 2001.
- [78] S. Twagirayezu, X. Wang, D. S. Perry, J. L. Neill, M. T. Muckle, B. H. Pate, and L.-H. Xu, "IR and FTMW-IR spectroscopy and vibrational relaxation pathways in the CH stretch region of CH₃OH and CH₃OD," *J. Phys. Chem. A*, vol. 115, p. 9748, 2011.
- [79] A. C. L. Jones, J. R. Danielson, J. J. Gosselin, M. R. Natisin, and C. M. Surko, "Positron binding to alcohol molecules," *New J. Phys.*, vol. 14, p. 015006, 2012.
- [80] J. A. Young, G. F. Gribakin, C. M. R. Lee, and C. M. Surko, "Role of combination vibrations in resonant positron annihilation," *Phys. Rev. A*, vol. 77, p. 060702, 2008.
- [81] "NIST chemistry webbook." <http://webbook.nist.gov>.
- [82] "NIST computational chemistry comparison and benchmark database." <http://cccbdb.nist.gov>.
- [83] J. R. Danielson, J. A. Young, and C. M. Surko, "Dependence of positron-molecule binding energies on molecular properties," *J. Phys. B*, vol. 42, p. 235203, 2009.